EXCELENCIA
MARÍA
DE MAEZTU

IFISC

Universitat de les Illes Balears

CSIC

PROCEEDINGS OF THE 2025 SURF@IFISC FELLOWSHIPS

Proceedings of the 2025 SURF@IFISC Fellowships

The SURF (Summer Undergraduate Research Fellowships) Program is offered by IFISC since 2013 (only interrupted in 2020 due to the Covid-19 pandemic) with the goal of attracting excellent undergraduate students with majors compatible with IFISC research lines and offers summer research fellowships at IFISC, typically during the month of July, advised by members of IFISC.

SURF attracted for the summer of 2025 a total of 43 candidates (31 male and 12 female), out of which 7 candidates were selected, 6 of them male and 1 female candidates. The candidates came from 22 different universities belonging to 7 different countries, while the candidates were citizens of 8 different countries. The universities with more candidates were the Universidad Yachay Tech with 5 applicants, and the University of Padua, the University of Salamanca, and the University of Valencia, each with 4 applicants. More than half of the applicants, 26, were Spanish citizens, followed by Italy and Ecuador with 5 applicants.

These are the proceedings:

1. Marc Rosendo Cerveró, (Supervisor: Antonio Fernández Peralta), *Network Geometry and Path Lengths*
2. Alberto Mateos Roig, Felipe Esteban Olivares Zamora, *Ordinal language of Non-Gaussian distributed data*
3. Álvaro Iturbe Jabaloyes, Javier Osca, Llorenç Serra, *Transport Properties of Quantum Anomalous Hall and QAH-Superconductor Junctions*
4. Miguel Cerdán Ortuño, Daniel Ruiz-Reynés, Damià Gomila, *Spatiotemporal dynamics of vegetation patterns*
5. Pau Rocabert, Silvia Ortín, *Exploring a Simple Neural Network Inspired by the Brain*
6. Nuria Balbás, Dimitrios Chalkiadakis, Leonardo Lyra Gollo, *Decoding the Brain: How Neuronal Morphology Shapes Dynamics and Function*
7. Ismaele Visentini, Nathan Silvano, *Spatiotemporal Dynamics of a Two-Species Model in a Flowing Environment*

Network Geometry and Path Lengths

Marc Rosendo Cerveró, Antonio Fernández Peralta
Instituto de Física Interdisciplinar y Sistemas Complejos, IFISC (CSIC-UIB)
Campus Universitat de les Illes Balears, E-07122 Palma de Mallorca, Spain

Abstract

The following work explores the path length distribution (PLD) in spatial networks with a focus on urban roadmaps to analyse how efficiently information or flow propagates through these systems and how the notion of *large-world* network can be defined and contrasted to the more traditional concept of *small-world*. By comparing empirical data from several cities against two different types of graph (the Random Geometric Graph and gravity models) we examine the degree to which the spatial structure shapes network connectivity. Our results reveal distinct PLD profiles corresponding to different urban layouts, ranging from lattice-like to more complex clustered structures with varying curvature. Furthermore, the Gravity model, incorporating both node importance in the network and spatial decay, captures critical aspects of real city roadmaps despite some limitations. The study highlights the interplay between spatial embedding and connectivity in defining large-world characteristics across diverse urban contexts, incorporating metrics for quantifying network *smallness* and how they relate to results for different models.

1 Introduction

Many complex systems, both man-made and present in nature, can be modeled in several different ways. One of the more powerful approaches to describe these systems of interacting components (with ”interaction” defined very broadly) is through graphs, the system being viewed as a network composed of nodes and edges that connect them. Under this paradigm, a node can represent almost anything (road intersections in roadmaps, power stations in power grids, people in social networks, etc.). Edges generally have a more straightforward interpretation: in spatial networks, they usually represent a literal connection between two particular points in space. As these kinds of systems will be the main focus of this paper, we won't delve into more general networks. In any case, edges represent an interaction of some type between nodes.

We aim to characterise some cities' roadmaps by their *small-worldness*, that is, whether there is a short path between(almost) any pair of nodes. This concept is generally used to characterise, among other quantities, ease of flow in a network. It can also be used as a qualitative description, as this label encompasses many things (such as short average paths, as mentioned, and large clustering, which means that most nodes have many connections). The most representative *small-world* graph is the random (Erdös-Rényi) graph, and the most common examples of *large-world* networks are regular lattices, which usually have very long average distances and diameters. We will, to an extent, identify *large-worldness* and similarity to a lattice. This will become clearer when presenting our results, but suffice to say that the path length, in a lattice, scales in a very particular manner [Tho11]: it follows the relationship $N(l) \propto l^{d-1}$, where l is the path length and d the dimension of the lattice. For the sake of convenience, will present all our PLD plots in log-log form, so the relationship will be linear: $log(N) \propto log(l) \cdot (d-1)$. It will be usually identified, then, a linear growth in the (log-log) PLD with a grid-like structure.

The present work explores one particular statistic of a graph: the **path length distribution**, $N(l)$ (from now on, PLD). It is, in a very broad sense, a measure of how fast information can be transmitted through a certain network, as modelled by a graph. It is defined as the all-pairs distribution of shortest graph distances between said pairs; that is, the least number of edges between them. We will use it to analyse the similarity of our data and certain classical graph models. Although analytical expressions for these models are generally not available, some approximations or asymptotic limits can be obtained for certain graphs. In any case, numerical simulations are relatively easy to perform.

The models that we will use can be described as a collection of nodes with fixed positions (given by the data) and a certain distribution that governs the probability of edges existing between nodes. The distributions that we will consider, which we will call $P_{i,j}$, depend on the spatial distance between nodes (R) and the number of neighbours of each node (that is, the number of nodes k_i for which $N(l_{i,r}) = 1$, called its "degree"). The dependence on R is easy to justify: interactions between members of a spatial network generally decrease with distance. The dependence in k is related to a frequent property of real-world networks: the existence of extremely connected nodes. These nodes, called "hubs", are integral to the system and tend to attract many more edges than the rest of nodes; thus, it is natural to consider a model in which the probability of a node being connected to another depends itself on its connectedness.

2 Theoretical models

Graph models, for our purposes, can be divided in two: spatial and non-spatial, which precede the former. In spatial models, the nodes have a defined position and $P_{i,j}$ depends on this "geographic" distribution. Non-spatial models, however, are defined only by their connectivity and not where the nodes might be located (in general, they have no particular location). Since our focus is on eminently spatial networks, such as roadmaps, spatial models will be of main interest. Nevertheless, classical non-spatial models will be reviewed too, given that they do display some key properties of the more complex spatial graphs and are simpler to analyse.

The first graph model to appear was devised by Paul Erdös and Alfred Rényi, in their seminal 1959 paper [ER59]. It can be described as a fixed set of nodes, each connected with a probability p to any other node in the graph independently of other edges. It can be proven that its degree distribution is poissonian and, if p is high, the average distance between nodes is small compared with the network size. This last property is a benchmark of what are known as "small-world" networks: those that are so interconnected that the average distance is much shorter than what could be generally expected. This is commonly summed up as the average distance growing logarithmically with N instead of linearly, which would be more intuitive.

A second classic graph model, the Barabási-Albert model, is an extension of the former. It is a constructive model as well, in which nodes are added sequentially, but it differs from the ER model in that it incorporates *preferential attachment*, the very common occurrence of some nodes that are more important to the network (they are **central**, more connected) than others. Its implementation is simple: every time a node is added, a sample of a fixed number of nodes is made and the new node has a probability of being attached to each of these, with this probability being linear with the degree of the node in the network. This way, the *connectedness* of certain nodes in the network will keep escalating, and they will become completely fundamental for the behaviour of the system. Of course, they tend to have much smaller average distances than other graphs (lattice graphs, for example, and even ER graphs), as most nodes are connected to a very small subset of components of the network. In any case, these graphs were the first that could explain the tendency of many systems to have some members with much greater influence and connectivity than others.

As was commented before, a relatively modern innovation in the field of network science are spatial graphs. These incorporate a metric, and so the graph is embedded in a certain space, almost invariably 2D Euclidean or hyperbolic space. In our case, the graphs considered use the Euclidean norm and are in the Cartesian plane. Spatial maps add a layer of complexity to graph theory because they cannot be described only by their topology, but they expand the realm of applications to real-life network modelling enormously, given that infrastructure networks, international trade and travel fluxes and local-level transportation, just to name a few examples, are all fundamentally spatial networks.

One of the more general families of spatial graphs are the *random geometric graph* (RGG) and its derivates. As their name suggests, they usually describe networks in which the nodes are in random positions embedded in a certain space. Of course, since their connectivity depends on the relative positions of the nodes, the geometric distribution is fundamental to connectivity. However, this does not mean its application to a set of already positioned nodes is not possible: since the important thing is the connectivity of the graph and not geometry (for example, a lattice graph is defined by a uniform k, not the reticular structure), we will just consider our nodes' positions set and apply the algorithm to those. Of course, this geometry will impact which edges are formed, but the models are useful to assess the dependencies of the edge probability. At any rate, the original RGG is a **disk** model; the probability of a node being connected to another is a constant p if they are closer than a certain distance and zero if they are not. It can be expressed as $P_{i,j} = p \cdot \Theta(R - r_{i,j})$, for some tunable R. Depending on the geometry of the problem, it can lead to a lattice network, an essentially random one or an intermediate behaviour. In fact, they can be seen as interpolations between these two extremes. The "soft" version of this model, the SRGG, is similar in the sense that connection probability decays with distance, but it differs in that the distribution describing this decay is now continuous and non-zero everywhere. This lack of a sudden decrease translates into the existence of some long-range edges that cannot exist in standard RGGs.

The *gravity model* is, in a way, an "extension" of the SRGG model. The idea of this model is to account for both distance between nodes and their connectivity. That way, the edge probability is higher not only between closer nodes, but also between **more important** nodes. This is crucial for some systems, like international trade (for which this model is the standard) where the presence of hubs is fundamental. It mimics Newton's law of gravitation, but substituting mass by degree, thus allowing for already connected nodes to have even more edges. The resulting distribution is:

$$P_{i,j} \propto \frac{k_i \cdot k_j}{f(R_{i,j})} \tag{2.1}$$

The function f can take several forms; it is usually taken to be a power of R or an exponential (as in the SRGG model). Of course, much like the other models, it may not be suitable for all graphs; particularly large-world networks and those without large hubs. Note that it is a descriptive model, used to describe the system *a posteriori*.

One drawback of this characteristic is that it necessitates using the data from the real network to generate the model; while for the RGG family the only real requirement are the relative positions of all nodes and the values of some tunable parameters, the gravity model requires using the data on the connectivity of each individual node to simulate what that connectivity *would be* under the model. That makes for some computational complications. Another obstacle is how to tackle the normalization of the probability distribution, as the sum $\sum_{i,j} G\frac{k_i \cdot k_j}{R_{i,j}}$ would have to be calculated over the original graph, which is quite difficult to do accurately due to numerical issues. The approach chosen to solve these complications is to use weighted random sampling with a reservoir (WRSR) [ES05]. Reservoir sampling goes through the data in one pass and only stores in memory a number of elements equal to the size of the sample (to be determined before performing the analysis). This set, the reservoir, is updated constantly taking into account *ratios* of weights. This peculiarity allows us to bypass normalization, avoid memory overhead issues and fast-track the weight calculation dramatically.

3 Results and discussion

We will start presenting the path length distribution results for some real roadmaps, then compare them to each model. For a direct visual reference for these layouts, see Figure 8.

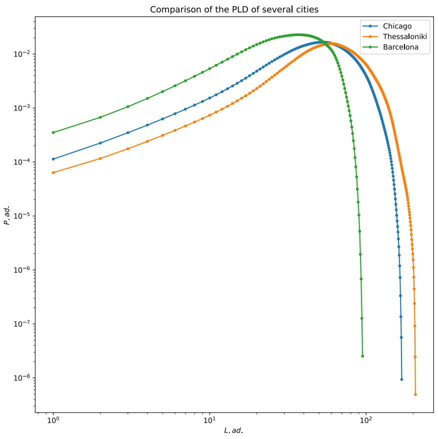

Figure 1: Distributions of some cities with linear growth.

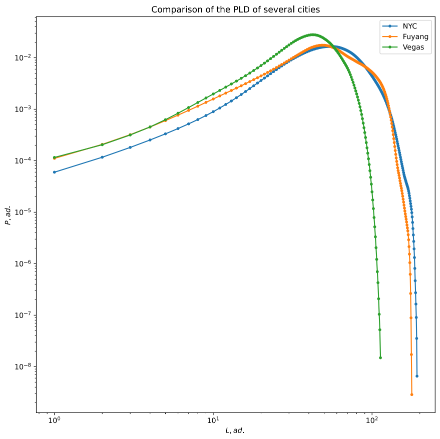

Figure 2: Distributions of some cities with larger curvature.

As can be seen in Figure 1 and Figure 2, cities present PLDs with similar shapes. They can often be separated in two categories depending on their growth: fully linear or linear in a small-scale regime but exponential for larger scales.

Fully linear PLDs come from power-law functional dependences; that is, self-similar structures, akin to lattices (as mentioned in the introduction). Their layouts are usually reticular at all levels, which in this case means that the whole roadmap is made of ”squares”, thus the self-similarity. The most famous example, Chicago (Figure 8d), reflects this perfectly: at a local level, almost all intersections have four edges and form squares but, zooming out, the agglomeration of the whole city in one block (permitted by the very level and regular terrain, as the city sits on the Midwest prairie) allows for the regular pattern to continue until the confines of the city, thus making it an almost perfect lattice. The slight curvature at the top might be due to the coastline, which increases border effects, making some paths longer. Barcelona is similar in the sense that the whole city is one compact block, and so it follows a linear pattern too. Thessaloniki, on the other hand, is a highly irregular city with two very large population centers around the coast and several smaller communities inland. This part of the city lies just below Mount Chortiatis and is thus a very rocky and rough terrain. Those suburban neighbourhoods do not account for a large portion of the total nodes, which is why the PLD starts linear and only acquires a slight curvature near its peak.

The cases of New York, Fuyang (China) and Las Vegas are markedly different. New York is often grouped with some famously grid-like cities such as Chicago, but that paints an incomplete picture of the city. It is composed of five ”boroughs”, of which only one is actually like a grid: Manhattan. It is an uninterrupted, regular patch of land and can thus be modelled quite well as a rectangular grid. The other four, while always locally resembling a grid (like many other cities), are highly irregular in shape. Even Manhattan itself isn’t wholly reticular: Lower Manhattan, which is much older than the rest and was the US capital in the 1790’s, was not planned beforehand like Upper Manhattan and is much more unevenly distributed. The same is true for the other four boroughs, so some curvature of the graph is to be expected. Las Vegas does not have many distinct features (save for Summerlin, and, of course, the Strip); it just has some large irregularities and a long road crossing the whole city. The road was used for logistics during WWII and thus couldn’t be destroyed to plan the rest of the city, so it does not fit the layout. Fuyang, however, does have a very distinct structure. Like most prefectural cities in China, it is sort of a higher-level formation, actually made up of several cities, so it is actually a relatively sparse arrangement of many dense clusters. Most of them are grid-like, to a certain extent, but not as much as other big cities, and the connection between different clusters results in a large deviation from the PLD of a grid.

In the interest of contextualising these results, we proceed to quantify the degree to which these cities are large-world networks. Given the shape of their PLDs (generally linear, to a certain extent) and layouts, as was explained before, the expectation is that they will be large-worlds. To test this, we will use the Small World Index, following an analogous procedure to the one described by Z.P. Neal [Nea17]. The SWI was chosen over other common measures, such as the small-world coefficient ω, because of its more accurate integration of lattice-like elements. It is calculated with the following formula, with d_l and d_r being the average distances in comparable (with a similar number of edges and nodes) lattice and random graphs:

$$SWI = \frac{d_l - d}{d_r - d_l} \cdot \frac{C - C_r}{C_l - C_r} \tag{3.1}$$

SWI close to 1 are small-worlds, with large clustering and small average distances.
The results obtained are presented in the following table ($pSWI \equiv -log_{10}(SWI)$):

City	Roadmap		Random		Lattice		pSWI
	<d>	C	<d>	C	<d>	C	
Vladivostok	28.45	-1.58	7.44	-2.84	21.22	-0.61	∞ ($SWI \approx 0$)
Vegas	48.4	-1.48	11.84	-4	74.92	-0.71	1.147
NYC	61.85	-1.56	11.82	-4.34	112.9	-0.65	1.210
Paris	47.4	-1.3	14.08	-3.69	48.19	-0.78	2.156
Fuyang	64.7	-1.43	10.4	-4	77.95	-0.65	1.488
Barcelona	46.8	-1.4	14.6	-3.68	49.1	-0.78	1.798
Stockholm	51.4	-1.39	11.35	-3.78	61.3	-0.0776	2.017
Chicago	65.6	-1.75	10.63	-4.05	82.3	-0.65	1.735

Table 1: Parameters for each roadmap and their equivalent lattice and random graphs.

Note that $SWI \approx 1$, representing a small-world, corresponds to $pSWI \approx 0$. Since $pSWI$ is positive and relatively large for all cities, it can be concluded that none of them resemble a small-world network (all have $SWI \approx 0$). Given the criterion used, it appears that they have lattice characteristics. Also of note is that the cities whose PLDs are the most linear (more grid-like structures), Vladivostok and Paris, have the two highest SWI, though Stockholm seems to be an outlier. In any case, this calculation confirms that most, if not all, city roadmaps cannot be described by traditional small-world models.

3.1 Gravity model

With the data for the city layouts, we can now move on to testing the chosen models on them. The gravity model will be reviewed first. As was seen in the "theoretical models" section, the gravity model gives path length distributions with large and changing curvature, a relatively sharp peak and, in general, small-world characteristics. Their most distinct feature is the remarkable similarity of all results with the model. Almost all have the exact same shape and end around the same value, $L \approx 10$. Their global maximum values are also at much lower L values than the city PLDs, which is to be expected in small-world networks (many distances are relatively short). Given all this, the gravity model is expected to present some issues when used to represent real cities; chiefly, its tendency to give very small graph diameters and maximum-probability distances. This is exactly what we find when computing the PLD of some of the cities shown in the former section. The first three, Chicago, Thessaloniki and Barcelona, all have distributions with similar curvature and very close endpoints and maximum values. Aside from the fact that these three cities are not that alike (with Chicago being much larger than Barcelona), these curves do not look or behave like those of the real roadmaps. Their curvature is too pronounced and the maximums are all about a full order of magnitude apart. The same is true for the second batch of cities: even if the original curvatures were larger than for the first three, the gravity model way overestimates them. The location of the maximum and the diameter also have the same issues, and in fact Fuyang and Las Vegas' maximums do not even reach $L = 10$.

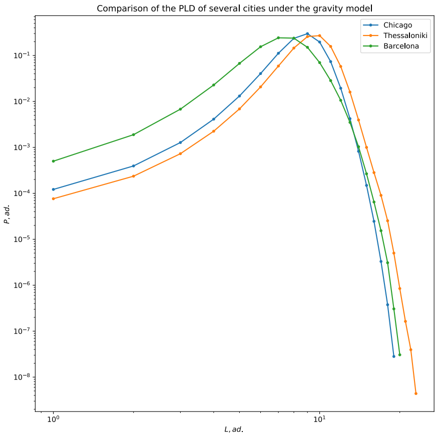

Figure 3: Gravity model distributions of some cities with linear growth.

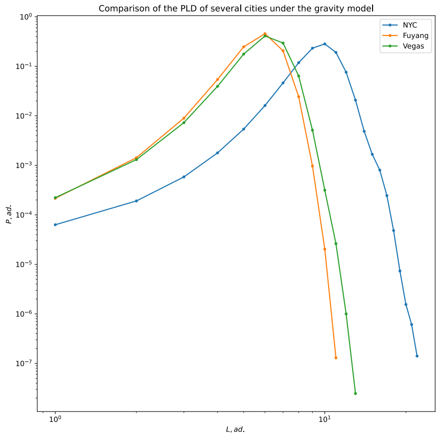

Figure 4: Gravity model distributions of some cities with larger curvature.

However, for all its failures, the gravity model can actually incorporate curvature and the effect of node connectivity. One of the advantages of this model is that it is quite easy to tune; the distance decay function can take many different forms (for example, a power law with different exponents) and some changes can be made to the connectivity term. The main issue is that this term, since the model gives a non-zero probability for any value of R, can create some long distance connections that would generally not exist in an actual city.

One way to tackle this is, then, reducing its importance in the equation: a modified version of the model can be used in which P grows with the *square root* of $k_i \cdot k_j$. Furthermore, the decay with distance can be accelerated so that the fitted graph is not a small-world. Some examples are shown in the following figure:

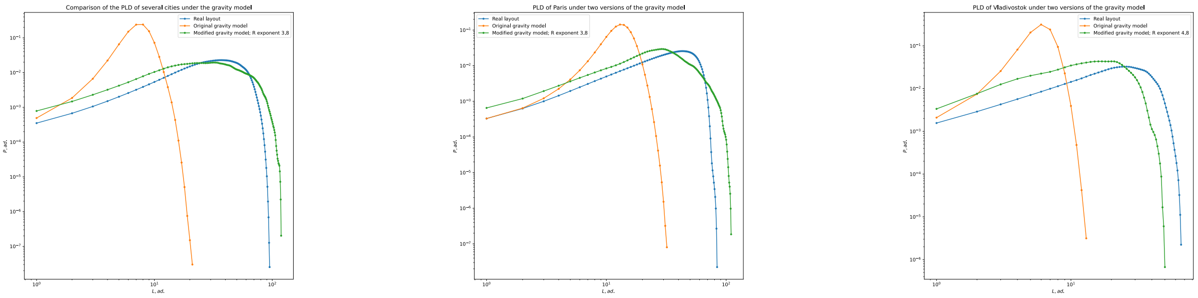

(a) Barcelona (b) Paris (c) Vladivostok

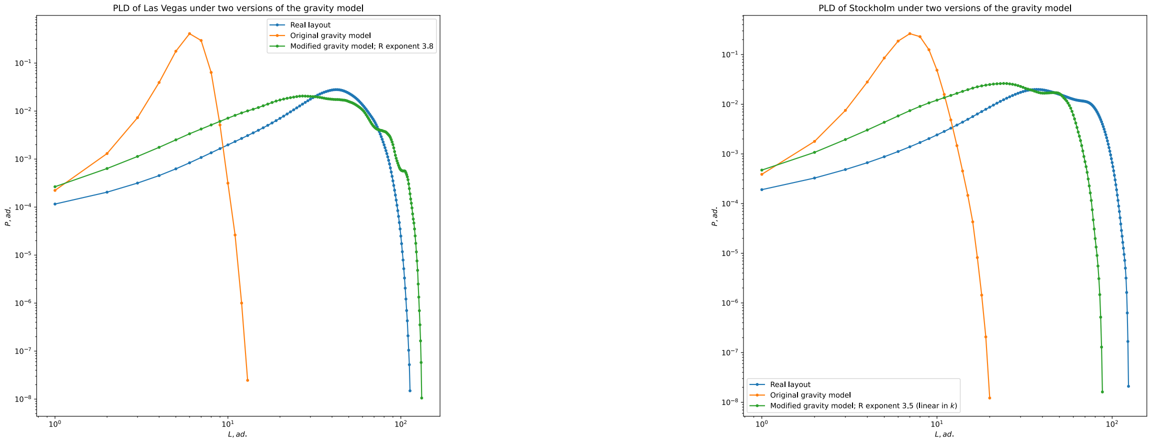

(d) Las Vegas (e) Stockholm

Figure 5: Superposition of PLDs for some city maps and their original and modified gravity fits.

It is apparent from the figure that this modification yields much better results when compared against the base model. It can be concluded, then, that even though the gravity model probability distribution has a smooth decay and is never zero, making this a fundamentally small-world model, it can capture some crucial features of city roadmaps, chiefly the difference between more and less important nodes, and be tweaked to approximate relatively well the real PLD.

3.2 Random Geometric Graph model

As mentioned in the ”theoretical models” section, the Random Geometric Graph is, in principle, better suited to describe large-world networks like the ones we are analysing. These graphs also have, of course, parameters to tune; the radius of the connection disk, R, and the connection probability, p. Since its effect is more or less homogeneous over all the nodes, this probability is not as important to the shape of the distribution as R. This interaction radius is actually the parameter that shapes the curve. It very directly controls how similar to a small-world network the fitted network behaves. Of course, a large radius promotes bonding between nodes that are further apart, and so direct connections between zones that would usually not be connected. Of note is that these types of edges are never present in pure lattices, which is why they are the eminent example of a large-world network.

We will use as a "measure" for the radius the parameter R_0, which is the disk radius at which the fitted model has the same number of edges as the actual network. The best fits have been obtained by doing a sweep over many values of R_0 but, since this is for the most part a qualitative study, no least-squares fitting has been performed.

The results obtained vary widely by city. Evidently, some cities are better suited for this model.

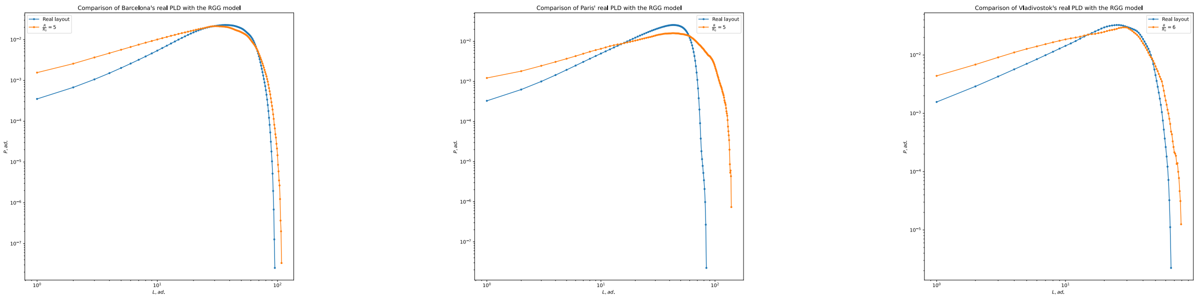

(a) Barcelona (b) Paris (c) Vladivostok

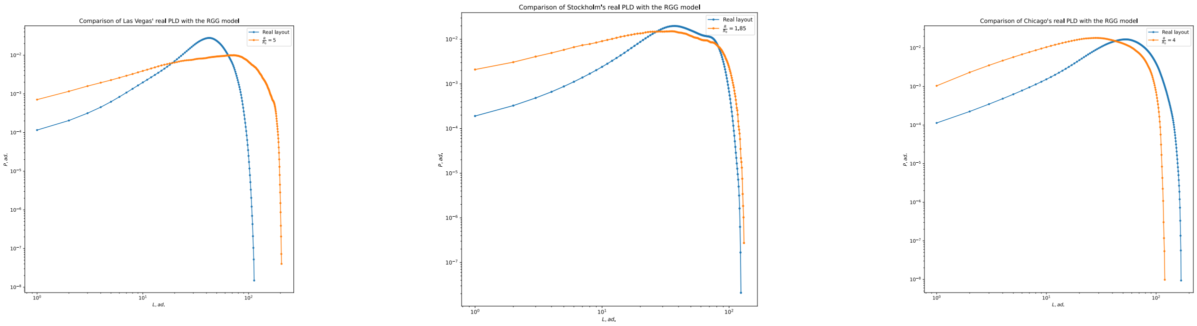

(d) Las Vegas (e) Stockholm (f) Chicago

Figure 6: Superposition of PLDs for some city maps and their RGG fits.

As can be seen clearly in Figure 6, it is those cities with less curvature in their PLD that are better approximated by the RGG model (here, Paris, Barcelona and Vladivostok). Even in those that are relatively well represented by the model, it fails to capture any slight curvature they may have, like in the case of Paris. In cities where the initial growth is nonlinear (Las Vegas and Stockholm) the model completely fails and it just resembles a 2D grid. The case of Chicago is quite interesting. Its growth is very clearly linear at first and has some curvature only near the maximum. The RGG model simulates almost perfectly the slope of the first region (and it is the slope that matters when comparing a map to a grid, as was seen when reviewing the theory on grid PLDs), but fails to curve to a concave shape, so that section is not well approximated. What is remarkable about this result is that a graph that presents two different behaviours at different scales (grid-like at a local level and a slight deviation at high distances) can be accurately modelled as an RGG on a certain range, even if it can't be outside that region.

3.3 Model comparison

Having seen both models and their performance at simulating cities, a more direct comparison between both is in order. For this purpose, some cities have been selected by their properties and the shape of their distributions and compared against the best fit found, presented in the last two sections.

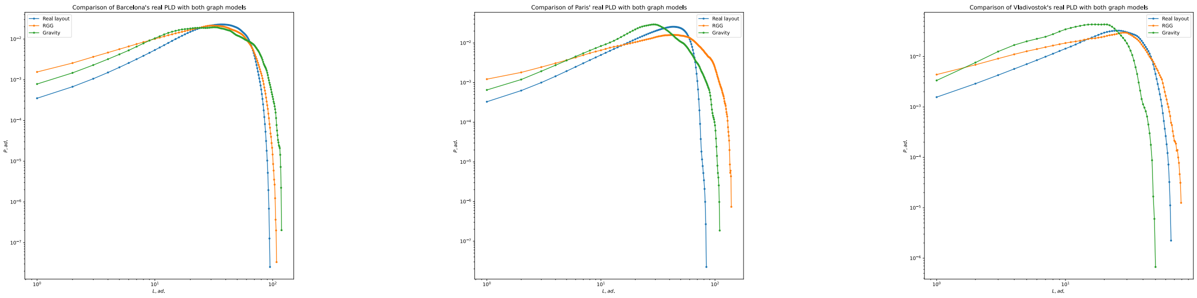

(a) Barcelona (b) Paris (c) Vladivostok

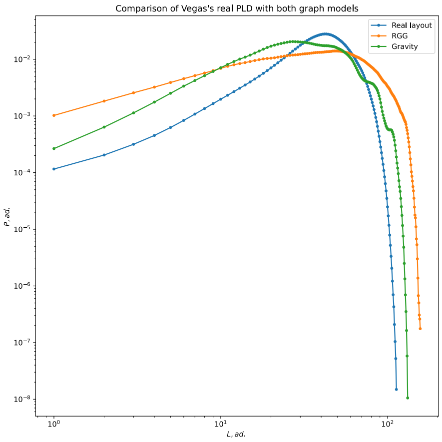

(d) Las Vegas

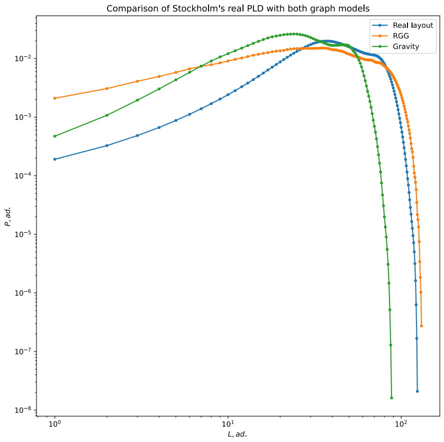

(e) Stockholm

Figure 7: Superposition of PLDs for selected city maps and both their RGG and gravity fits.

Two general trends can be seen. On one hand, some graphs that are large-world (linear growth) and are relatively well approximated by both RGG and modified gravity models, even if the RGG, clearly the performs better in all cases. These would be Paris, Vladivostok and Barcelona. The cities on other group, which includes Las Vegas and Stockholm, deviate notably from linearity so as to be represented by a grid-like network. The modified gravity model, which is far more flexible and can incorporate curvature, is much better suited to fit these cities. Notably, these two groups coincide almost perfectly with the division marked by their SWI values (Table 1), save for Stockholm: there is, then, a direct link between *large-worldness* and the type of model that better represents a network. The suitability of grid-like (and non-continuous, non-zero in $P_{i,j}$, more generally) seems to decrease quite steeply with *small-worldness*, while gravity-like models are more versatile.

4 Conclusions

With the two models and the original graphs presented and analysed, we can extract several conclusions. Chiefly, that there is a very clear association between *large-worldness*, lattice structure and the suitability of some models to represent certain graphs. This implies that when modelling infrastructure networks like, for example, power grids, to look for the possibility of cascading failures, the geometry of the network must be carefully considered alongside its topology for, as was demonstrated in the article, the former is completely fundamental for the description of spatial maps. The fine-grained analysis of several roadmaps has provided an intuitive relationship between certain traits of a city's layout (such as their coastlines or the ruggedness of the terrain) and the shape of their PLDs and, more generally, their connectivity.

We would like to emphasise that the methods used in this work to generate model graphs to fit roadmaps could be extrapolated directly to create the best possible fits, within the possibilities of the *large-world* framework, potentially for any type of spatial network. Furthermore, spectral analysis and modularity techniques can be applied to enhance the study of some more particular *large-world* networks, such as larger-scale maps or airport traffic flows.

A City maps

For reference, we show the roadmap graphs generated from datasets obtained with OpenStreetMap.

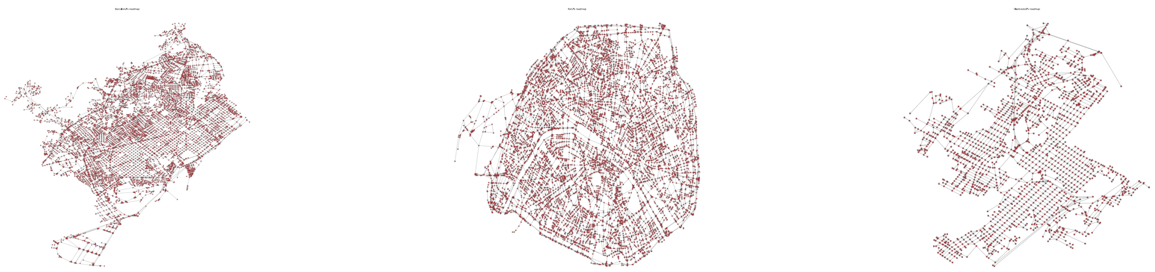

(a) Barcelona (b) Paris (c) Vladivostok

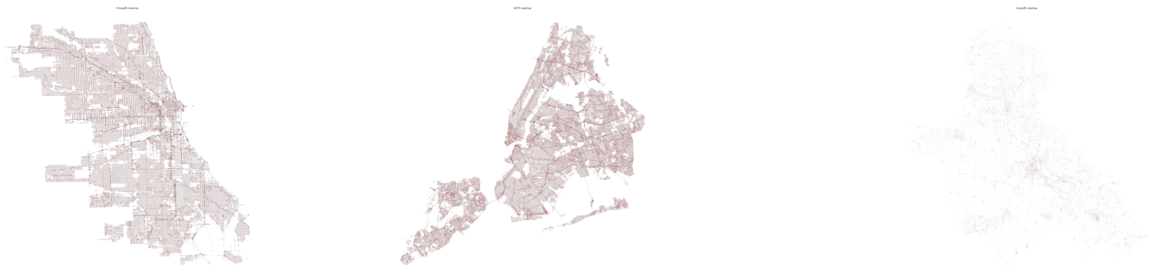

(d) Chicago (e) NYC (f) Fuyang

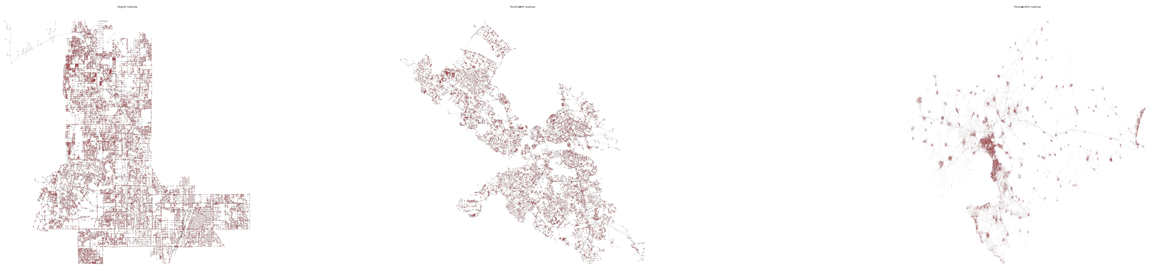

(g) Las Vegas (h) Stockholm (i) Thessaloniki

Figure 8: Selected city roadmaps.

Acknowledgments

The author would like to acknowledge Prof. Fernández Peralta for his help on bringing about and aiding this investigation, and Daniel Ruiz Reynés and Manuel Matías for organizing the SURF program and making this investigation possible.

References

[ALW16] Thomas C. van Dijk Andre Löffler and Alexander Wolff. Snapping graph drawings to the grid optimally. 2016.

[BBDD+21] Marián Boguñá, Ivan Bonamassa, Manlio De Domenico, Shlomo Havlin, Dmitri Krioukov, and M. Ángeles Serrano. Network geometry. *Nature Reviews Physics*, 3:114–35, 2021.

[ea15] Eytan Katzav et al. Analytical results for the distribution of shortest path lengths in random networks. *Europhysics Letters*, 111, 2015.

[ER59] P. Erdös and A. Rényi. On random graphs i. *Publicationes Mathematicae Debrecen*, 6, 1959.

[ES05] P. Efraimidis and P. Spirakis. Weighted random sampling with a reservoir. *Information Processing Letters*, 97, 2005.

[Nea17] Zachary P. Neal. How small is it? comparing indices of small worldliness. *Network Science*, 5(1):30–44, 2017.

[Tho11] Kevin P. Thompson. The nature of length, area, and volume in taxicab geometry. 2011.

[vS10] M. van Steen. *Graph Theory and Complex Networks: An Introduction*. 2010.

Ordinal Language of Non-Gaussian Distributed Data

Student: Alberto Mateos Roig
Tutor: Felipe Esteban Olivares Zamora
Instituto de Física Interdisciplinar y Sistemas Complejos, IFISC (CSIC-UIB)
Campus Universitat de les Illes Balears, E-07122 Palma de Mallorca, Spain

July 2025

Abstract

This monograph addresses the question: *Are ordinal patterns capable of capturing the underlying distribution of a time series?* We develop theoretical and numerical analysis of pattern probability integrals for various distributions, introduce an optimized algorithm (ORDPAT), study the impact of distributional asymmetry and temporal correlation (Hurst exponent H), and demonstrate applications to financial indices (NASDAQ, S&P 500, cross-country comparisons).

1 Introduction

Many real-world time series —from physical systems to financial markets— exhibit non-Gaussian features such as heavy tails, asymmetries, and long-range correlations. Traditional statistical tools, based on moments or spectral densities, often struggle to capture such complexity, especially in the presence of noise or nonlinearity.

Ordinal pattern analysis, introduced by Bandt and Pompe 2002, provides a symbolic framework to encode time series through the relative order of values in short sliding windows. This approach is robust to noise, invariant under monotonic transformations, and captures temporal structures in a way that is both intuitive and computationally efficient. Furthermore, it has been found very useful in various contexts, as shown in works such as Massimiliano Zanin et al. 2012, Leyva et al. 2022, Burgos Atencia, Agarwal, and Culcer 2021, and Amigó and Rosso 2023, where it is applied to characterize complexity, detect dynamical changes, and analyze non-Gaussian features in time series.

In this work, we focus on analyzing the distribution of increments (i.e., first differences) of a time series, rather than the raw values themselves. This approach aligns with common practices in fields like finance or turbulence, where returns or velocity differences are of primary interest. Consequently, to construct meaningful comparisons, we will typically generate independent and identically distributed (i.i.d.) random data with a given distribution, and then integrate them to simulate the original process before applying ordinal pattern analysis. This procedure allows us to disentangle distributional effects from temporal correlation structure.

To model the underlying distributions, we make use of the family of q-Gaussian distributions, a generalization of the normal distribution that emerges naturally in the framework of nonextensive statistical mechanics Tsallis 2009. q-Gaussians are particularly well-suited for modeling heavy-tailed behavior and have been successfully applied across diverse fields, including finance, biology, and physics (see e.g., Tsallis 2009). Their flexibility makes them a natural choice for analyzing real-world data that depart from Gaussian assumptions.

Despite its success in autocorrelation L. Zunino et al. 2008, the use of ordinal patterns as a tool to identify or reconstruct underlying distributions remains underexplored. Some studies have made initial steps in this direction Azami and Escudero 2016, Fadlallah et al. 2013, but a comprehensive theoretical and numerical analysis is still lacking. This research seeks to bridge that gap by addressing the fundamental question: *Are ordinal patterns capable of capturing the underlying distribution of a time series?*

To explore this question, we adopt both theoretical and empirical approaches. We derive integral expressions for pattern probabilities, implement efficient numerical algorithms, and test the framework on both synthetic and empirical data, including financial time series and physical experiments. For comparing the different data, it will be used the Permutation Jensen-Shannon distance developed by Luciano Zunino, Felipe Olivares, Ribeiro, et al. 2022. The effectiveness and versatility of this methodology have been demonstrated in diverse contexts, such as Luciano Zunino, Porte, and Soriano 2024, Luciano Zunino 2024, and F. Olivares, L. Zunino, and M. Zanin 2023, highlighting its applicability to areas ranging from biomedical signals to landing flow dynamics.

The structure of this monograph is as follows. In Section 2, we provide theoretical insights into the relation between pattern probabilities and the underlying distribution. Section 3 introduces a novel computational algorithm and validates it numerically. Section 4 explores the role of asymmetry in ordinal analysis. Section 5 examines the effect of temporal correlations using fractional Brownian motion and q-Gaussian processes. Section 6 presents real-world applications, and Section 7 concludes with a discussion of implications and future directions.

2 Theoretical Insights

2.1 Ordinal Pattern Probability Integrals

Consider a time series $\{X_t\}_{t=1}^{N}$. For an embedding dimension D and delay $\tau = 1$, each subsequence $\mathbf{X}_t = (X_t, X_{t+1}, \ldots, X_{t+D-1})$ gives rise to an ordinal pattern π determined by the relative rankings of its components. For a first impression, Figure 1 shows the six order patterns of length 3.

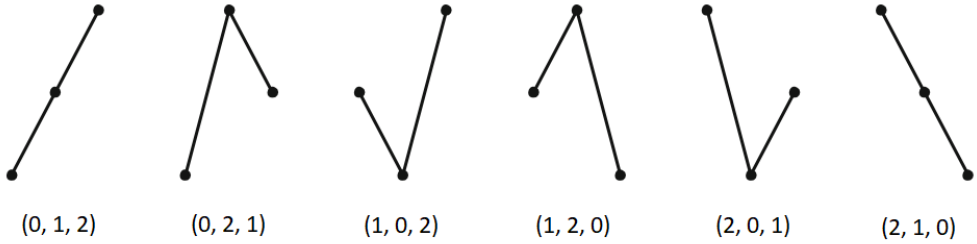

Figure 1: The six order patterns of length 3 (Bandt 2020)

Empirically, the probability of observing a particular ordinal pattern π_i in a time series can be estimated by counting how many times the pattern π_i appears, divided by the total number of ordinal patterns extracted. More precisely, if we denote by N_{π_i} the number of occurrences of pattern π_i in the series, then the empirical probability $\hat{P}(\pi_i)$ is given by:

$$\hat{P}(\pi_i) = \frac{N_{\pi_i}}{N - D + 1}$$

where $N - D + 1$ is the total number of ordinal patterns that can be extracted from the time series of length N.

From a theoretical perspective, since there are $D - 1$ successive increments ("jumps") between the D values, the probability of observing a pattern π can also be expressed as an integral over $D - 1$

variables. Assuming the increments are i.i.d. with marginal density $f(x)$, we write:

$$P(\pi_i) = \int_{\mathcal{S}_{\pi_i}} \left(\prod_{k=1}^{D-1} f(x_k) \right) dx_1 \cdots dx_{D-1}$$

Here, $\mathcal{S}_{\pi_i} \subset \mathbb{R}^{D-1}$ denotes the region of values for which the cumulative jumps reconstruct the specific ordering π_i. Note that although we integrate over $D-1$ variables, these correspond to jumps generated by D time series values. Each jump is treated as an independent realization from the distribution f.

To illustrate, let us consider some explicit examples for $D = 3$:

- Pattern $\pi = (0, 1, 2)$ (monotonically increasing):

$$P(012) = \int_0^\infty f(x_1) \int_0^\infty f(x_2)\, dx_2\, dx_1$$

- Pattern $\pi = (0, 2, 1)$ (a small drop after a rise):

$$P(021) = \int_0^\infty f(x_1) \int_{-x_1}^0 f(x_2)\, dx_2\, dx_1$$

We can also construct a more complex case, such as pattern $(0, 2, 1, 4, 3)$ for $D = 5$:

$$\begin{aligned} P(02143) = \int_0^\infty f(x_1) \int_{-x_1}^0 f(x_2) \int_{-x_2}^\infty f(x_3) \\ \int_{-x_2-x_3}^0 f(x_4)\, dx_4\, dx_3\, dx_2\, dx_1 \end{aligned}$$

This integral formulation highlights how different patterns may have distinct probabilities, depending on the properties of $f(x)$, such as symmetry, skewness, or tail behavior. In the next section, we explore analytical and numerical evaluations of these probabilities for various distributions.

It is important to highlight that the probabilities $P(\pi)$ depend solely on the shape of the probability density function $f(x)$, and not on its scale. In particular, changing the variance (i.e., stretching or compressing $f(x)$) does not affect the values of $P(\pi)$. This invariance arises because the ordinal patterns are determined by the relative ordering of the values, not by their absolute magnitudes. Or in order words, we can see also this by a change in variables in the integral.

Consequently, any distribution $f(x)$ that belongs to a location-scale family will yield the same ordinal pattern probabilities regardless of its variance. For example, a Laplace distribution with variance 2 or 10 will generate the same values of $P(\pi)$. This property considerably simplifies both theoretical analysis and numerical simulation, allowing us to fix the variance without loss of generality.

2.2 Analytic Cases

In this section, we focus solely on symmetric density functions. The first observation is:

Inverse patterns have equal probability. This follows trivially from the symmetry of the density. If $f(x)$ is symmetric (i.e., $f(x) = f(-x)$), then any pattern π and its inverse π^{-1} have the same probability, since the change of variables

$$y_k = -x_k\,, \quad k = 1, \ldots, D-1$$

in the integral for $P(\pi)$ maps the integration region $\mathcal{S}_\pi$ onto $\mathcal{S}_{\pi^{-1}}$, and $\prod f(x_k)\, dx_k$ remains invariant. Then, for example $P(1320) = P(0231)$.

Case $D = 3$. Recall that for $D = 3$ we set

$$x_1 = X_2 - X_1, \qquad x_2 = X_3 - X_2,$$

so each vector $(x_1, x_2) \in \mathbb{R}^2$ corresponds to one of the six patterns.

1. Patterns $(0, 1, 2)$ and $(2, 1, 0)$. These are the strictly ascending and descending patterns. For $(0, 1, 2)$ we require

$$X_1 < X_2 < X_3 \iff x_1 > 0,\ x_2 > 0.$$

Thus

$$P(012) = \int_0^\infty \int_0^\infty f(x_1)\, f(x_2)\, dx_2\, dx_1 = \Big(\int_0^\infty f(x)\, dx\Big)^2 = \frac{1}{4},$$

and by symmetry $P(210) = P(012) = \frac{1}{4}$.

2. Mixed pattern $(0, 2, 1)$. This pattern imposes

$$X_1 < X_3 < X_2 \iff \begin{cases} x_1 > 0, \\ x_2 < 0, \\ x_1 + x_2 > 0. \end{cases}$$

Equivalently, the integration domain is

$$\mathcal{S}_{0,2,1} = \{(x_1, x_2) : x_1 > 0,\ -x_1 < x_2 < 0\},$$

and the probability is

$$\begin{aligned}
P(0, 2, 1) &= \int_0^\infty f(x_1)\Big(\int_0^{x_1} f(u)\, du\Big)\, dx_1 \\
&= \int_0^\infty f(x_1)\big(F(x_1) - F(0)\big)\, dx_1 \\
&= \int_0^\infty f(x)\, F(x)\, dx \; - \; F(0) \int_0^\infty f(x)\, dx \\
&= \int_0^\infty F(x)\, dF(x) \; - \; F(0) \cdot \tfrac{1}{2} \\
&= \Big[\tfrac{F(x)^2}{2}\Big]_0^\infty \; - \; \tfrac{F(0)}{2} \\
&= \Big(\tfrac{1^2}{2} - \tfrac{F(0)^2}{2}\Big) - \tfrac{F(0)}{2} \quad \text{with } F(0) = \tfrac{1}{2} \text{ by symmetry} \\
&= \Big(\tfrac{1}{2} - \tfrac{(1/2)^2}{2}\Big) - \tfrac{1/2}{2} = \big(\tfrac{1}{2} - \tfrac{1}{8}\big) - \tfrac{1}{4} = \tfrac{3}{8} - \tfrac{2}{4} = \tfrac{1}{8}.
\end{aligned}$$

By the same reasoning, each of the four mixed patterns $(0, 2, 1), (1, 0, 2), (1, 2, 0), (2, 0, 1)$ has probability

$$P = \frac{1}{8}.$$

Summary for $D = 3$.

$$P(012) = P(210) = \frac{1}{4}, \quad P(021) = P(102) = P(120) = P(201) = \frac{1}{8}.$$

Case $D = 4$. If we ignore patterns related by symmetry, the following patterns have exact probabilities under any symmetric density:

$$P(0123) = P(3210) = \tfrac{1}{8}, \qquad P(0132) = P(2310) = \tfrac{1}{16}, \qquad P(0213) = P(3120) = \tfrac{1}{24},$$
$$P(0312) = P(2130) = \tfrac{1}{48}, \qquad P(1023) = P(3201) = \tfrac{1}{16}, \qquad P(3021) = P(1203) = \tfrac{1}{48}.$$

We observe that these patterns can be calculated directly using symmetry alone when the integration limits involve only adjacent jumps. In other words, exact integration is feasible when no limit in the integral requires combining two or more variables.

Table of results. The following table 1 displays the probabilities of the remaining patterns — those not covered above — computed either analytically (for uniform and Laplace distributions) or numerically (for Gaussian and q-Gaussian with $q = 1.5$):

Pattern	Uniform	Laplace	Gaussian	$q = 1.5$ q-Gaussian
(0231), (1320)	1/24	1/32	0.0355	0.0325
(0321), (1230)	1/48	1/32	0.0270	0.0300
(1032), (2301)	1/48	1/32	0.0270	0.0300
(2013), (3102)	1/24	1/32	0.0355	0.0325
(3012), (2103)	1/48	1/32	0.0270	0.0300
(2031), (1302)	1/48	1/96	0.0146	0.0116

Table 1: Pattern probabilities for $D = 4$ under various symmetric distributions. We find the same values of the gaussian column at L. Zunino et al. 2008

To validate the theoretical predictions, we performed simulations using symmetric distributions. The results are shown in Figure 2.

3 Numerical results

3.1 ORDPAT Algorithm

We introduce **ORDPAT**, a custom algorithm designed to compute the probability distribution of ordinal patterns given a time series. It is explicitly written in section 7. ORDPAT efficiently maps each data window to its corresponding permutation index through a recursive approach that avoids explicit sorting. This results in significant speed improvements, especially for large datasets.

The algorithm takes as input:

- a vector `datos` representing the time series,
- the embedding dimension D,
- and an optional delay parameter τ (defaulting to 1).

For each overlapping window of D values with delay τ, the algorithm computes the corresponding ordinal pattern and updates a histogram. The recursive subroutine `orden` maps a vector of D values to its ordinal pattern index without relying on lexicographic ordering, but instead on a more efficient, position-based encoding.

In terms of performance, we compare `ordpat` with an existing implementation known as `perm_indices` (Parlitz et al. 2012), which computes ordinal patterns via lexicographic enumeration and sorting. While `perm_indices` is slightly faster for very short series (e.g., under 1000 data points), its performance degrades rapidly with series length, as seen in Figure 3. It becomes practically unusable beyond 50,000 points, especially for $D \geq 4$.

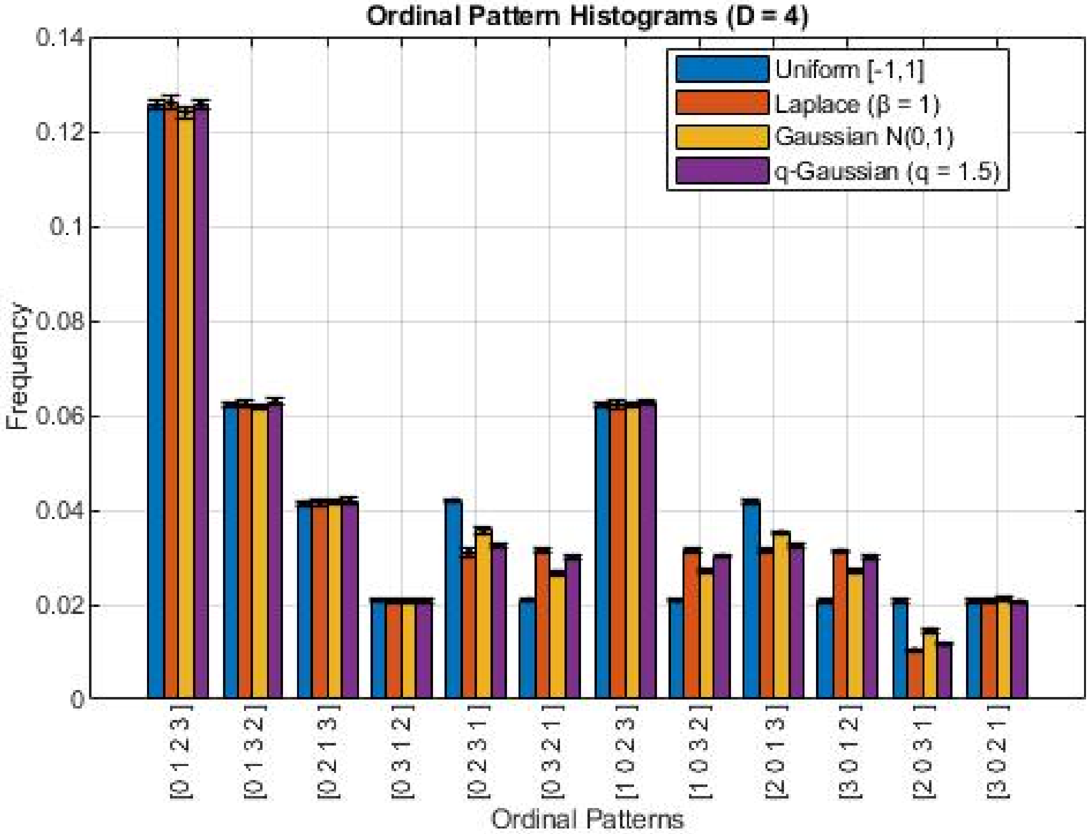

Figure 2: Empirical probabilities of ordinal patterns for $D = 4$ obtained simulation of a symmetric distribution (e.g., uniform or Laplace) with 10 iterations. The values match the analytically computed probabilities for representative patterns shown in the table 1.

In contrast, `ordpat` scales efficiently with both data length and embedding dimension, remaining stable and fast even with hundreds of thousands of points.

The following figures illustrate the runtime comparison between both algorithms:

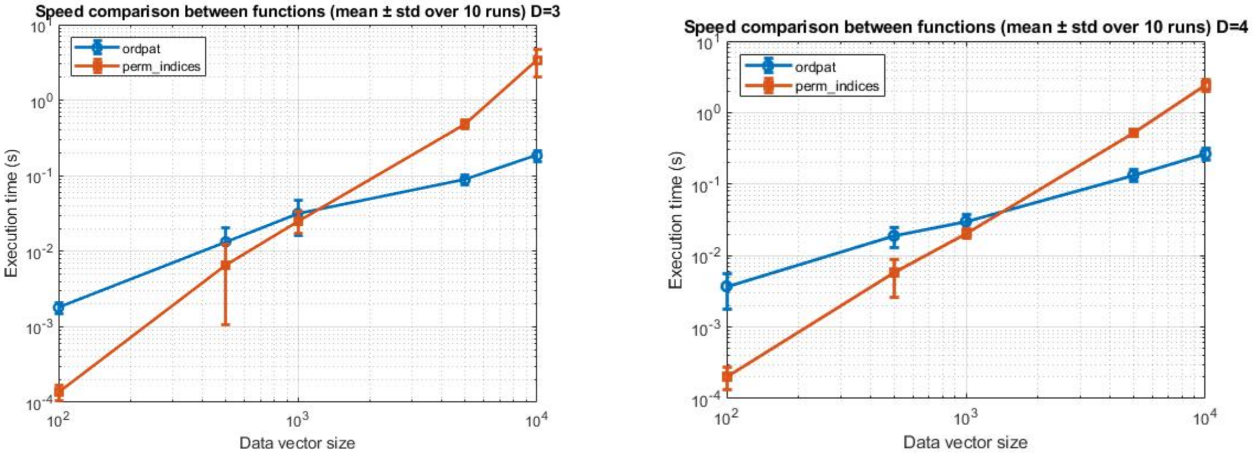

(a) Runtime comparison for $D = 3$

(b) Runtime comparison for $D = 4$

Figure 3: Execution time (in seconds) vs. series length for both `ordpat` and `perm_indices` with 10 iterations. Note that while `perm_indices` slightly outperforms for very short series, it quickly becomes inefficient.

This benchmark confirms that `ordpat` is a robust and scalable tool for estimating ordinal pattern distributions, even when D is large or the time series is long.

3.2 Validation on Synthetic Data

To validate the ability of ordinal patterns to detect properties of the underlying distribution, we begin by simulating synthetic time series composed of cumulative sums of i.i.d. random variables drawn from q-Gaussian distributions with varying values of q. A q-Gaussian distribution is a generalization of the normal (Gaussian) distribution (Tsallis 2009), defined by the probability density function:

$$p_q(x) = A_q \left[1 - (1-q)B_q x^2\right]_+^{1/(1-q)}, \tag{3.1}$$

where $[z]_+ = \max(z, 0)$ ensures the support is real-valued, and the constants A_q and B_q are normalization and scale parameters that depend on q. For $q \to 1$, the q-Gaussian converges to the standard Gaussian distribution. When $q > 1$, the distribution exhibits heavy tails, and for $q < 1$, it has compact support.

To generate i.i.d. samples from the q-Gaussian distribution, we use a generalized version of the Box-Muller transform. Specifically, we draw two independent uniform random variables $u_1, u_2 \sim \mathcal{U}(0, 1)$ and compute:

$$x = \sqrt{-2\ln_q(u_1)}\cos(2\pi u_2), \tag{3.2}$$

where $\ln_q(x)$ is the q-logarithm defined as $\ln_q(x) = \frac{x^{1-q}-1}{1-q}$. This method ensures that the resulting variable x follows a q-Gaussian distribution with zero mean and unit variance, under appropriate choice of parameters.

We fix the embedding dimension $D = 4$ and compute the relative frequency of each permutation pattern using the `ORDPAT` algorithm.

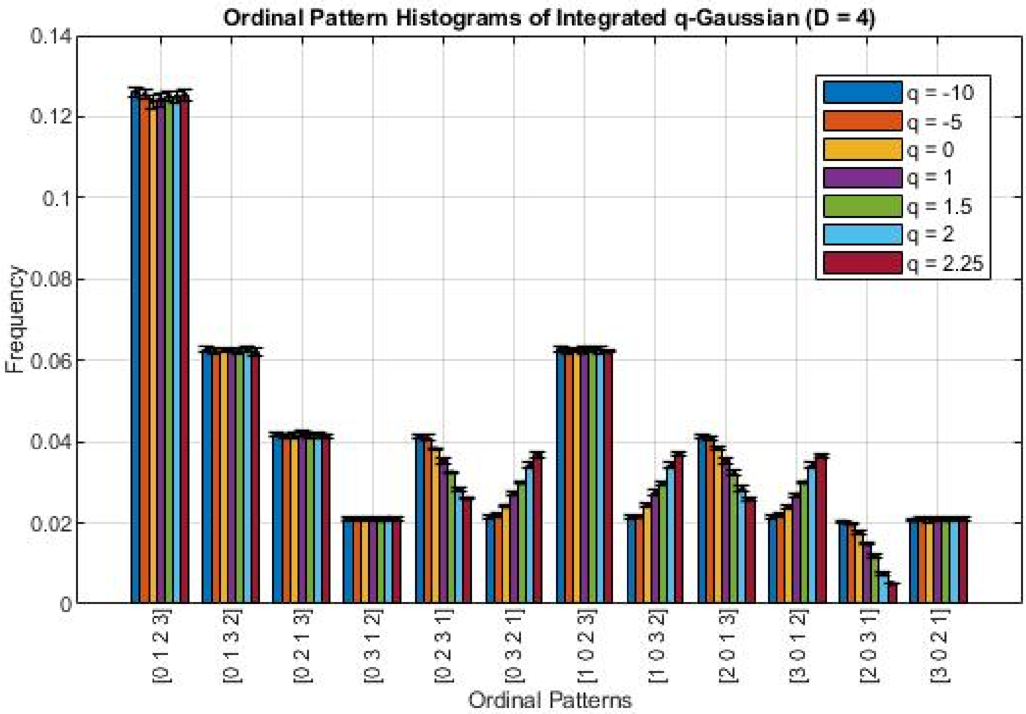

Figure 4: Histogram of permutation frequencies for $D = 4$ obtained from cumulative q-Gaussian noise with different values of q with 10 iterations.

As shown in Figure 4, the change in the tails of the distribution (controlled by the parameter q) results in a monotonic variation in the frequencies of certain ordinal patterns. In particular, we observe that patterns such as $(3, 0, 2, 1)$, $(1, 0, 3, 2)$ and $(3, 0, 1, 2)$ (Figure 5) tend to increase their probability with heavier tails (higher q). These patterns often involve large jumps between adjacent elements, suggesting that they are more likely in distributions that permit extreme values.

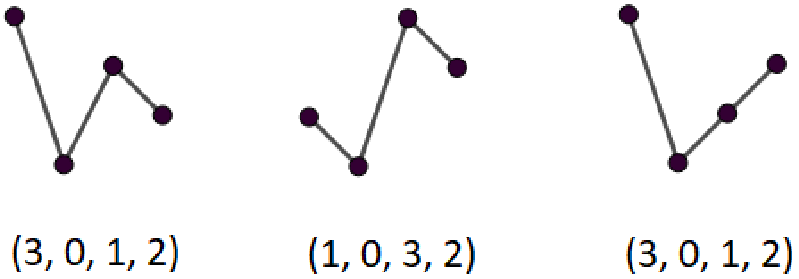

Figure 5: Patterns that increase their probability with heavier tails (higher q)

This supports the hypothesis of Luciano Zunino, Felipe Olivares, Bariviera, et al. 2017 that ordinal pattern probabilities are sensitive not just to correlation structure, but also to the shape of the marginal distribution. Furthermore, for those patterns whose probabilities were computed analytically under the assumption of symmetry, we observe in the plots that their empirical frequencies remain essentially constant across all q-Gaussian distributions. This confirms that, due to the symmetry of the patterns and of the underlying distributions, their probabilities are invariant with respect to changes in the value of q.

Entropy and Jensen–Shannon Distance. To further quantify the difference in the distributions of ordinal patterns, we compute two measures:

- *Permutation Entropy* (Bandt and Pompe 2002) $H(P) = -\sum_\pi P(\pi) \log P(\pi)$, which measures the uniformity of the pattern distribution.
- *Jensen–Shannon Distance* (Luciano Zunino, Felipe Olivares, Ribeiro, et al. 2022) between two ordinal pattern distributions P and Q, defined as:

$$\mathrm{JSD}(P, Q) = \sqrt{\frac{H(\frac{P+Q}{2}) - \frac{1}{2}H(P) - \frac{1}{2}H(Q)}{\ln 2}},$$

Figure 6 shows the behavior of the Jensen–Shannon distance when comparing the ordinal pattern distributions of a q-Gaussian with two references: a standard Gaussian distribution ($q = 1$) and a Student's t-distribution with matching tail behavior. To interpret the results properly, we introduce a baseline distance: this is the Jensen–Shannon distance computed between two independently generated realizations of the same distribution (in this case, two Gaussians with $q = 1$). This baseline accounts for the minimal expected distance arising from finite sample effects, since even when comparing two samples from the exact same distribution, randomness can lead to small discrepancies in pattern frequencies.

Importantly, we observe that the distance between the q-Gaussian and the Student's t-distribution reaches the baseline exactly at $q = 2$, confirming that their distributions are equivalent at this point. Similarly, the distance between the q-Gaussian and the standard Gaussian drops to the baseline at $q = 1$, as expected, since both distributions are identical in this case. These results confirm the

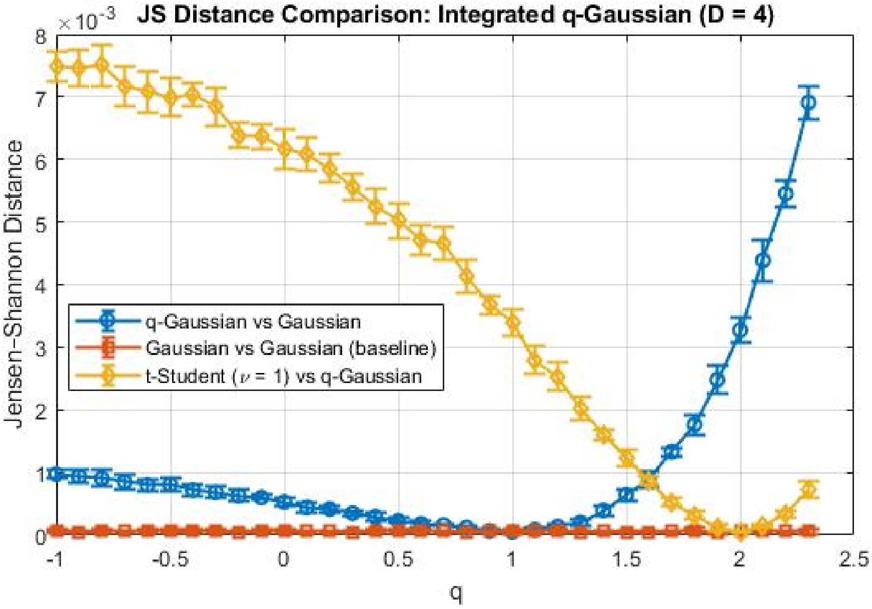

Figure 6: Jensen–Shannon distance between pattern histograms: comparison of q-Gaussian ($q = 1.5$), Gaussian ($q = 1$), and Student-t distributions with 10 iterations. Note how the distance vanishes when comparing identical distributions.

reliability of the Jensen–Shannon distance applied to ordinal pattern probabilities as a sensitive and robust tool for detecting distributional similarities and differences, especially in tail behavior.

3.3 Limitations

Despite the robustness and simplicity of the ordinal pattern framework, it is not without limitations. One notable drawback is that it can confuse two different distributions even if they exhibit completely different tail behavior at lower embedding dimensions.

For instance, using the Jensen–Shannon distance between ordinal pattern histograms, we observe that a q-Gaussian distribution with $q = 1.66$ produces a nearly indistinguishable pattern profile from that of a Laplace distribution when using embedding dimension $D = 4$. This implies that, under certain conditions, the method may fail to differentiate two fundamentally distinct distributions, effectively treating them as statistically equivalent from the ordinal perspective.

However, preliminary results suggest that this degeneracy weakens as the embedding dimension increases. At $D = 5$ and $D = 6$, differences in the tail structure become more apparent, and the ordinal pattern distributions begin to diverge. This points to a trade-off between resolution and computational cost: higher-order patterns can capture more nuanced statistical features, but at the expense of increased complexity and reduced statistical reliability due to factorial growth in the number of patterns.

These findings show that while ordinal pattern analysis is capable of detecting subtle differences between relatively similar time series, it may fail when the overall statistical structure changes drastically but happens to preserve similar local ordinal configurations. This highlights the method's sensitivity to local ordering rather than global distributional features, and calls for caution when interpreting results, especially at low embedding dimensions.

4 Asymmetry in Distributions

In this section, we explore how different centering methods affect the detection of asymmetries in skewed distributions using ordinal patterns. Specifically, we compare three preprocessing approaches

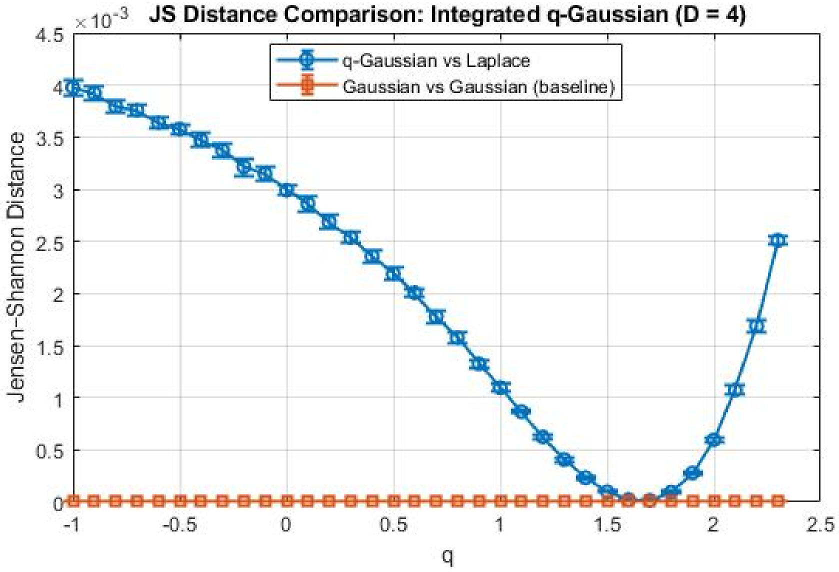

Figure 7: Comparison of ordinal pattern frequencies between q-Gaussian ($q = 1.66$) and Laplace distribution for $D = 4$ with 10 iterations. The near overlap illustrates a case of indistinguishability.

before computing ordinal probabilities: (i) using the raw data, (ii) subtracting the mean, and (iii) subtracting the median. Our goal is to determine which method best preserves the asymmetry information encoded in the ordinal structure of the data.

To illustrate this, we simulate a time series drawn from an asymmetric distribution composed of two parts: the left half follows a standard Gaussian distribution, while the right half follows a right-skewed q-Gaussian with $q = 2$. The generation process ensures that negative values come exclusively from the Gaussian component, and positive values from the q-Gaussian, by rejecting samples that fall outside the desired domain. The relative proportions of each component are adjusted according to the densities at the origin to balance their contributions.

For each centering method, we present two subfigures: on the left, a sample of the time series after preprocessing, and on the right, the corresponding histogram of ordinal pattern frequencies for embedding dimension $D = 3$. This setup allows for a clear comparison of how each method responds to symmetry and asymmetry in the data.

Raw data (no centering)

When no centering is applied, the ordinal patterns extracted from the q-Gaussian exhibit a notable bias toward ascending patterns such as $(0, 1, 2)$. This is due to the presence of heavy-tailed extreme values on the right, which inflate the local orderings and create an artificial sense of upward trend, even though the underlying distribution may not have a systematic directional behavior.

Mean-centering

Subtracting the mean leads to an opposite distortion. Since the $q = 2$ distribution has a heavy right tail, a single extreme value can greatly shift the mean upward. This results in most values being perceived as relatively small after centering, producing an artificial abundance of descending patterns like $(2, 1, 0)$. The ordinal analysis is thus heavily skewed by the instability of the mean in heavy-tailed distributions.

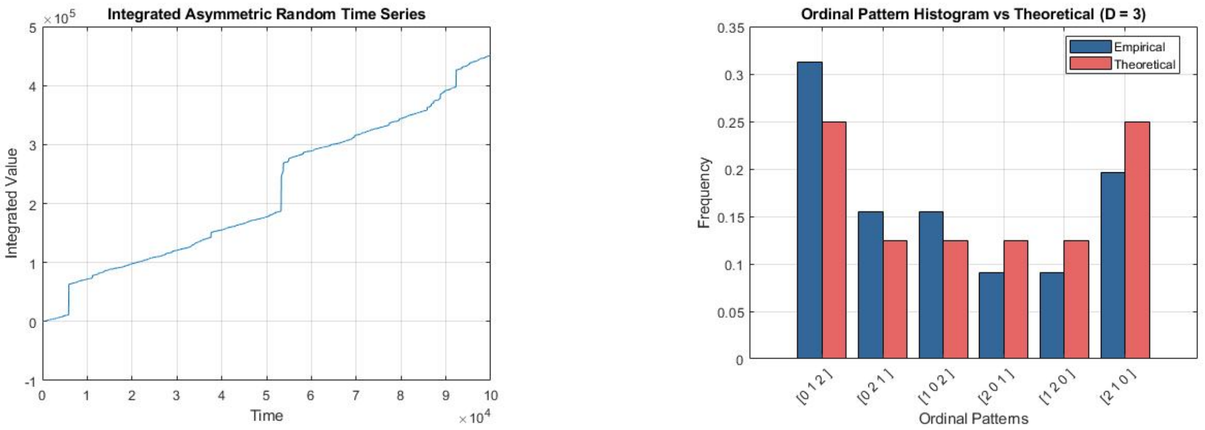

(a) Raw data: $q = 2$ Gaussian (b) Pattern histogram (D=3)

Figure 8: Effect of no centering on ordinal patterns.

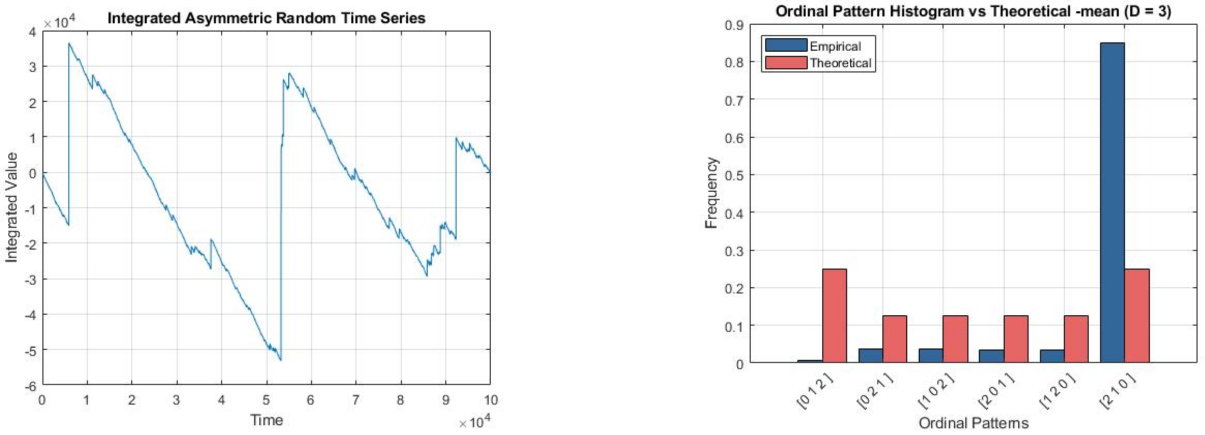

(a) Mean-centered: $q = 2$ Gaussian (b) Pattern histogram (D=3)

Figure 9: Effect of mean-centering on ordinal patterns.

Median-centering

In contrast, median-centering offers a robust alternative. Since the median is resilient to outliers, it provides a more stable central reference. When applied to the $q = 2$ series, the resulting ordinal pattern histogram reveals genuine asymmetries inherent to the distribution. For example, patterns like $(0, 2, 1)$, which reflect a sharp jump to the right, become more frequent than their mirrored counterparts. This behavior aligns with the expected influence of a heavy right tail and suggests that median-centering preserves ordinal structure more faithfully in asymmetric settings.

Conclusion

These results suggest that for skewed distributions, subtracting the median before integrating and computing ordinal patterns provides a more reliable representation of underlying asymmetries than either raw data or mean-centering. This approach enables a finer detection of subtle directional structures without being misled by extreme values or artificial centering distortions.

5 Effect of Temporal Correlation (Hurst Exponent)

This section explores how temporal correlations, quantified by the Hurst exponent H, influence ordinal pattern distributions—particularly in interaction with non-Gaussianity, encoded via the tail parameter q. While previous sections focused on i.i.d. data, here we move into temporally structured time series,

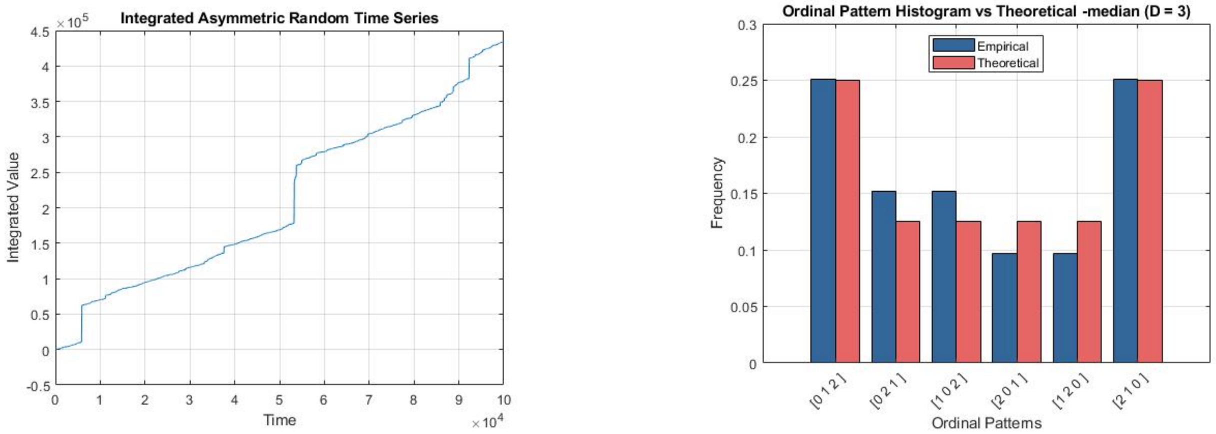

(a) Median-centered: $q = 2$ Gaussian

(b) Pattern histogram (D=3)

Figure 10: Effect of median-centering on ordinal patterns.

investigating whether ordinal analysis can capture the combined effects of memory and fat-tailedness.

5.1 Methodology for Generating q-Gaussian and fBm Data

To simulate time series with controlled temporal correlation and marginal distribution, we use a hybrid sampling technique from Carpena et al. 2020. We begin by generating fractional Brownian motion (fBm) using the wavelet-based ‘wfbm‘ function or, alternatively, via Cholesky decomposition of the covariance matrix. This yields a Gaussian process with a desired Hurst exponent $H \in (0, 1)$, where $H = 0.5$ corresponds to uncorrelated white noise, $H > 0.5$ to persistent memory, and $H < 0.5$ to antipersistence.

To introduce fat tails, we apply a rank-based transformation: first, the Gaussian fBm series is mapped to the uniform distribution using its empirical cumulative distribution function (CDF); then, the uniform values are converted into q-Gaussian-distributed samples via the inverse CDF of the target distribution.

This method enables independent control of temporal correlation and marginal shape. It is particularly well-suited to studying how both H and q jointly affect ordinal patterns.

5.2 Validation of Synthetic Data

We validate our synthetic generator by comparing both marginal and spectral properties of the simulated data. Each figure below contains two subfigures: the left shows the histogram of the data (verifying the marginal q-Gaussianity), while the right displays the power spectral density estimated via Welch’s method, confirming the expected spectral slope $\alpha = 2H - 1$ (Luciano Zunino, Felipe Olivares, Bariviera, et al. 2017) in Figures 11, 12 and 13.

However, we observe in the Figure 14 that for strongly antipersistent data ($H = 0.25$) combined with heavy tails ($q = 2$), the transformation introduces distortions. In these cases, the empirical spectrum does not fully reflect the intended correlation structure. This limitation suggests a fundamental incompatibility between strong antipersistence and long-tailed marginals when applying rank-based transformations.

5.3 Impact on Ordinal Patterns

We restrict our analysis to the region $q > 1$ and $H > 0.5$, as these conditions are typically observed in empirical time series, particularly in financial markets (as we will explore later). Moreover, these are the parameter regimes where our synthetic data generation method is most robust. To study the joint influence of q and H on ordinal patterns, we focus on a representative subset of patterns of length

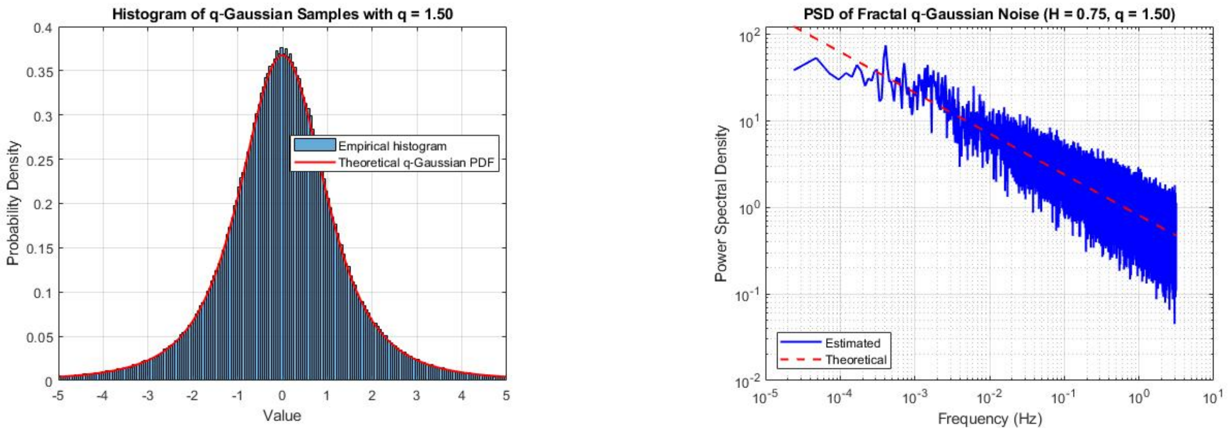

(a) Histogram: $q = 1.5$

(b) PWelch spectrum $H = 0.75$

Figure 11: Validation for heavy tails and persistent memory. $q = 1.5, H = 0.75$

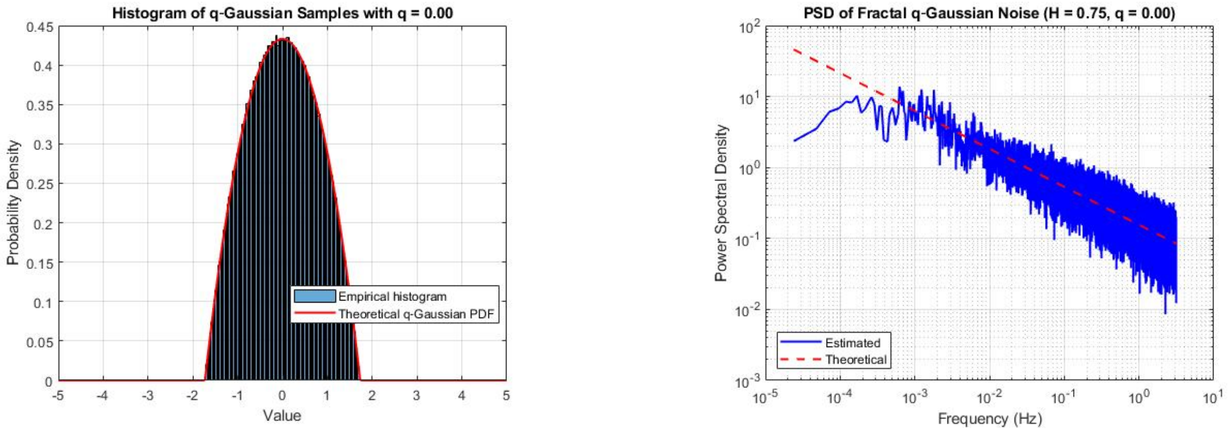

(a) Histogram: $q = 0$

(b) PWelch spectrum $H = 0.75$

Figure 12: Validation for compact support and persistent memory. $q = 0, H = 0.75$

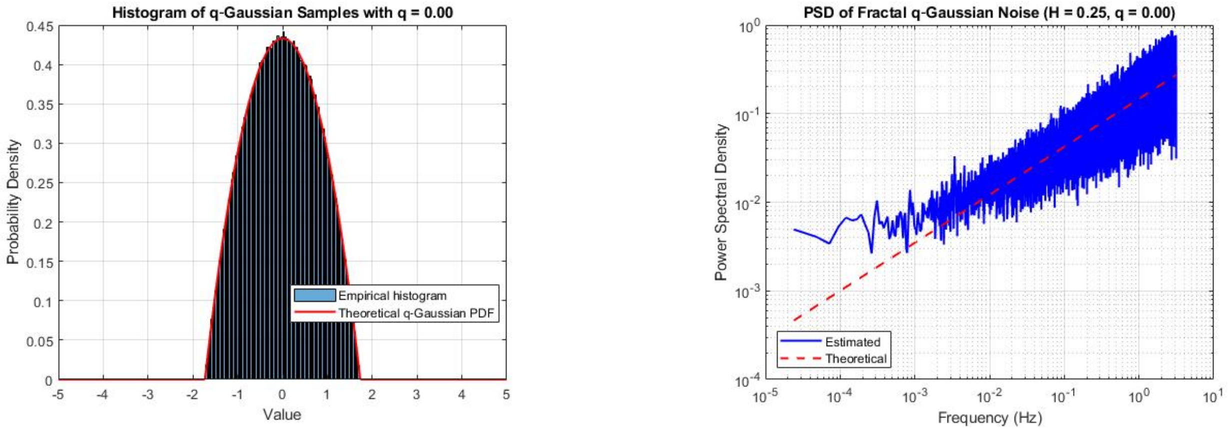

(a) Histogram: $q = 0$

(b) PWelch spectrum $H = 0.25$

Figure 13: Validation for compact support and antipersistence. $q = 0, H = 0.25$

$D = 4$. These patterns were chosen based on their distinct and illustrative behaviors.

The following figure 15 presents the evolution of the probabilities of these patterns as H increases while q is held fixed, allowing for a clear visualization of their different dynamics.

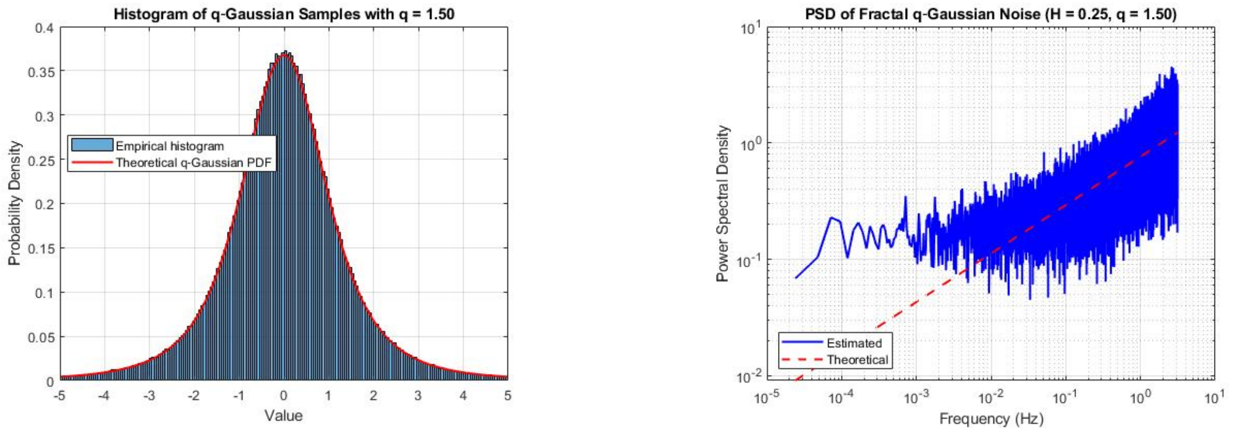

(a) Histogram: $q = 1.5$ (b) PWelch spectrum (distorted) $H = 0.25$

Figure 14: Failure of method for antipersistence with long tails. $q = 1.5, H = 0.25$

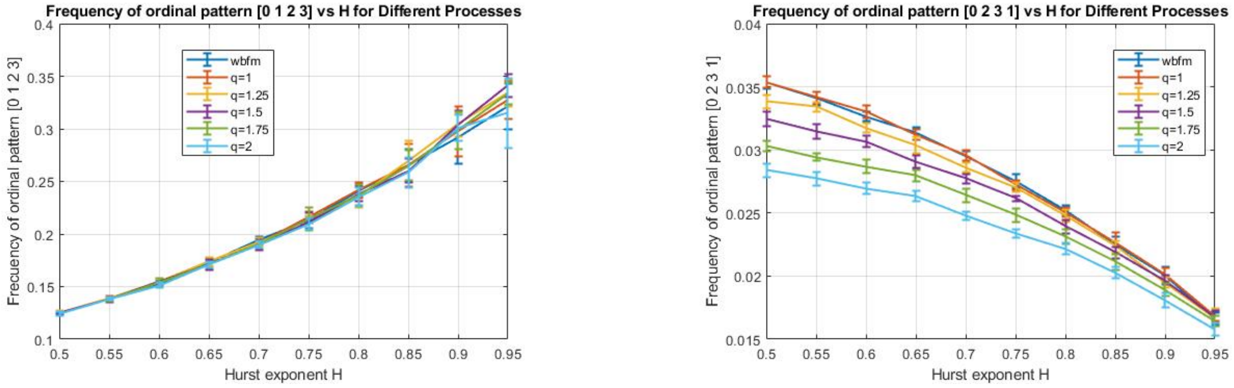

(a) Pattern 0123 (b) Pattern 0231

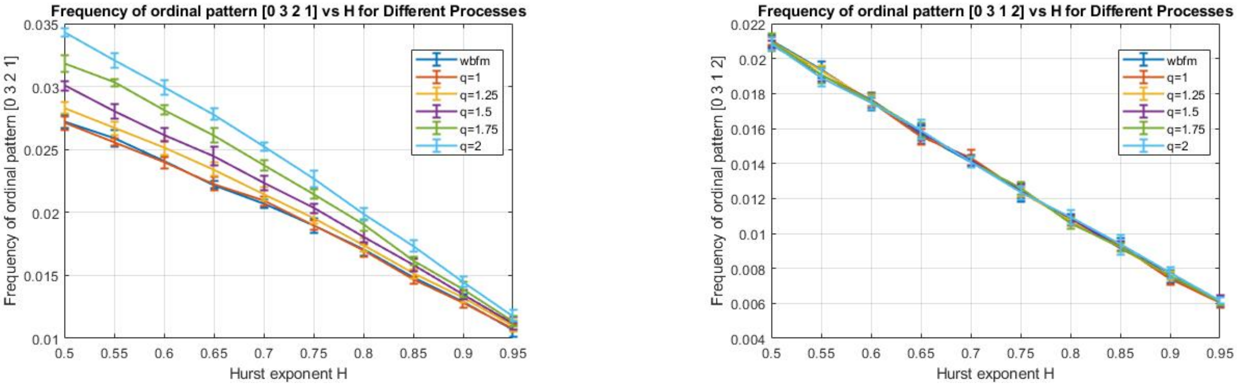

(c) Pattern 0321 (d) Pattern 0312

Figure 15: Probability evolution of specific $D = 4$ patterns as a function of H for fixed $q > 1$ with 10 iterations.

We observe that the strictly increasing pattern 0123 and the strictly decreasing pattern 0321, showing a clear indpendence of q, they have the same frequencies. However, in the cases of 0231 and 0321, although their initial probabilities differ, they respond similarly to variations in H, decreasing with memory. This reinforces the reliability of ordinal patterns as tools for detecting and characterizing temporal structure, as they are also monotonic with respect to correlation.

Additionally, these two monotonic patterns exhibit contrasting behaviors with respect to the tail parameter q: while 0231 decreases in probability as increases (indicating heavier tails), the 0321 pattern increases, highlighting their sensitivity to both temporal and distributional characteristics.

Finally, to assess whether patterns can uniquely identify a given pair (q, H), we construct a heatmap showing the Jensen-Shannon distance between a reference ordinal pattern histogram (obtained from an integrated time series with known $q = 1$ and $H = 0.5$) and others across a grid of values (Figure 16). A clear global minimum appears at the correct pair, confirming that ordinal patterns are sensitive to both fat tails and memory.

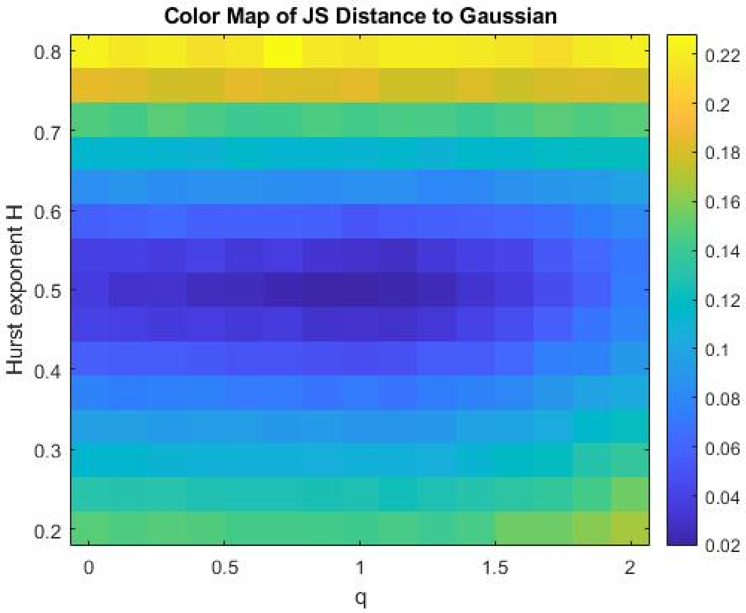

Figure 16: Jensen-Shannon distance between pattern histograms across different q, H combinations with 10 iterations.

These results suggest that ordinal patterns can jointly encode both tail heaviness and temporal correlation—provided the generation process is well-behaved—and offer a promising tool for analyzing complex time series structures.

6 Applications

The practical relevance of ordinal analysis becomes particularly evident when applied to real-world data. Among the most insightful examples are financial time series, which are known to exhibit heavy-tailed distributions and varying degrees of temporal correlation. Under the Efficient Market Hypothesis, asset returns should behave as uncorrelated Gaussian noise, closely resembling a fractional Brownian motion with Hurst exponent $H = 0.5$. Deviations from this benchmark may reveal underlying structures in the data that can be detected through ordinal patterns.

6.1 Financial Time Series

We begin by analyzing the daily returns of the NASDAQ and S&P 500 indices from 1980 to 2025. Following the methodology of Gopikrishnan et al. 1999 and Nayak, Singh, and Senapati 2021, we focus on logarithmic returns instead of raw prices, as they better capture the stochastic dynamics of financial systems. Given a time series of prices P_t, the logarithmic return at time t is defined as:

$$r_t = \log P_t - \log P_{t-1} = \log\left(\frac{P_t}{P_{t-1}}\right) \tag{6.1}$$

To isolate distributional effects from temporal correlations, we first randomize (shuffle) the return sequences and then we integrate the returns. This allows us to analyze the shape of the return distribution independently of memory effects.

We then compare the empirical ordinal pattern histograms against those generated from q-Gaussian distributions with no time correlations (Figure 17). The best match for both indices occurs around $q \approx 1.5$, consistent with the value reported for NASDAQ in Nayak, Singh, and Senapati 2021. Similarly, Gopikrishnan et al. 1999 reports a power-law exponent $\alpha = 3$ for S&P 500 returns, corresponding to $q = 5/3$, which aligns well with our estimate.

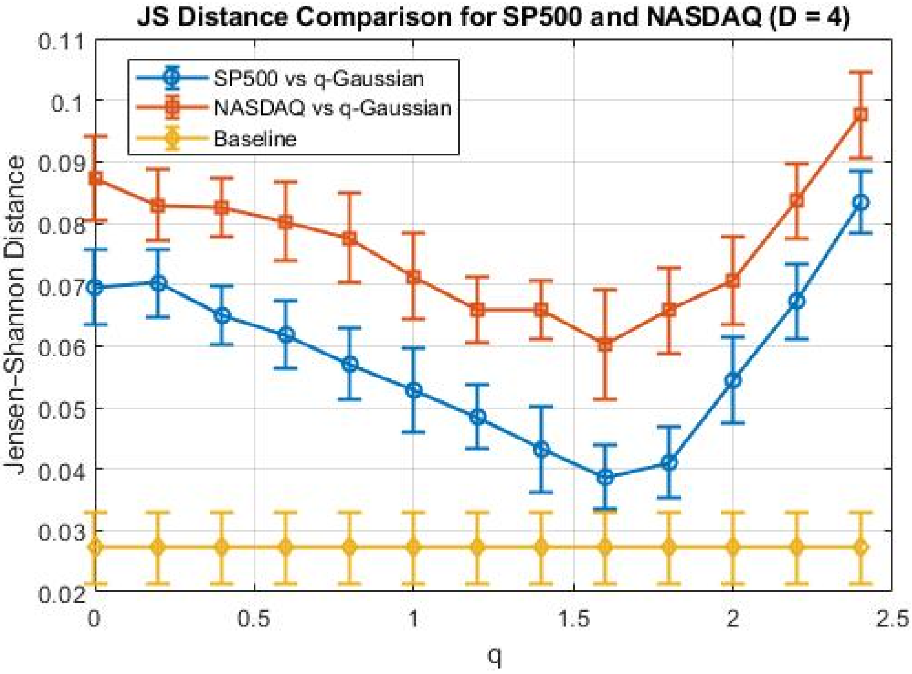

Figure 17: Best-fit q-Gaussian match for shuffled returns of NASDAQ and S&P 500 with 10 iterations. Both indices exhibit $q \approx 1.5$, confirming heavy-tailed behavior.

6.2 Time-Scale Robustness

To test whether this distributional structure persists across time resolutions, we repeat the analysis using return data at different frequencies (Figure 18). In all cases, the resulting ordinal pattern distributions continue to match those of a $q \approx 1.5$ q-Gaussian.

This robustness across scales suggests that the underlying statistical behavior of financial markets remains relatively stable and consistent with the presence of heavy tails, regardless of temporal aggregation. However, we observe that the length of the time series plays a crucial role in the analysis, as it is difficult to draw reliable conclusions from shorter datasets, such as those with only 30 minutes or 60 days of data.

6.3 Correlation Structure in Financial Markets

In addition to distributional analysis, we examine temporal dependence through the Hurst exponent. From now on, we will not shuffle the return sequences to preserve the effects from temporal correlations. By computing Jensen-Shannon distances between empirical pattern histograms and those generated from synthetic datasets with known (q, H), we construct heatmaps that identify the most likely parameter pair (Figure 19).

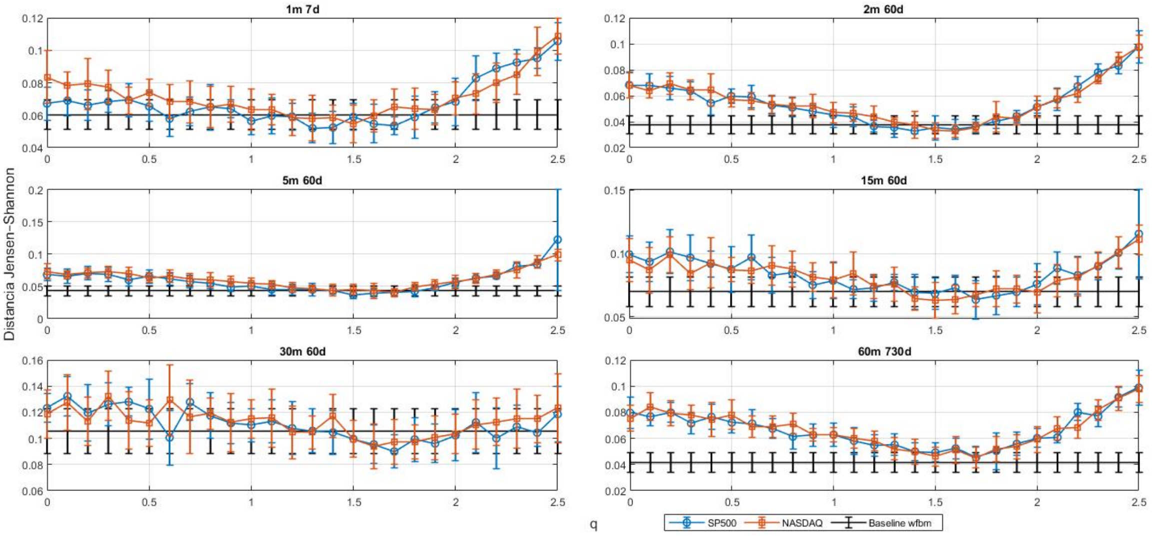

Figure 18: Best-fit q values across different time resolutions for NASDAQ and S&P 500 returns with 10 iterations. Distributional shape remains stable, with $q \approx 1.5$.

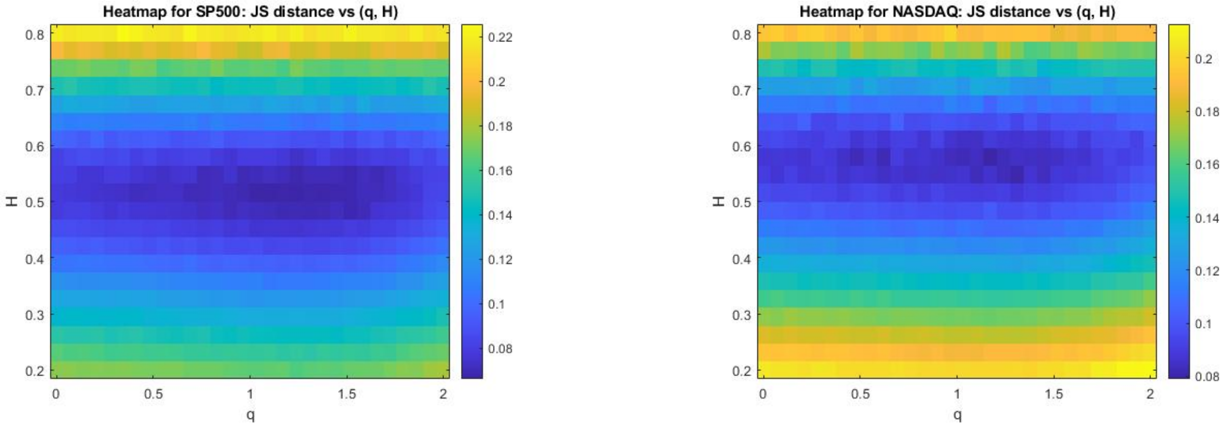

(a) S&P 500

(b) NASDAQ

Figure 19: Jensen–Shannon distance heatmaps for S&P 500 and NASDAQ returns with 10 iterations.

We observe that both markets exhibit minima at $q > 1$, with S&P 500 reaching the lowest distance near $q \approx 1.5$, and NASDAQ slightly below that value. Furthermore, we find a temporal correlation above $H > 0.5$, especially pronounced in the NASDAQ case.

Interestingly, the minimal distances reached here are higher than those found when comparing only the q-distributions. Although this may seem counterintuitive—since adding an extra degree of freedom (H) should, in principle, improve the fit—this is explained by the fact that we no longer shuffle the return sequences. As a result, the empirical data may deviate more from idealized synthetic processes due to real-world noise and spurius non-linearities.

Our estimates are consistent with previous studies Bandt 2020, which report weak persistence ($H \approx 0.5$) in major developed markets. These findings demonstrate that ordinal patterns are sensitive not only to distributional shapes but also to underlying temporal correlations.

6.4 Cross-Country Market Comparison

We now extend our analysis to global markets using data provided in Luciano Zunino, Felipe Olivares, Bariviera, et al. 2017, which includes stock indices from countries with varying levels of economic development. We again estimate effective q and H values from the ordinal pattern distributions (Figure 20). We note before that the distribution are symmetric.

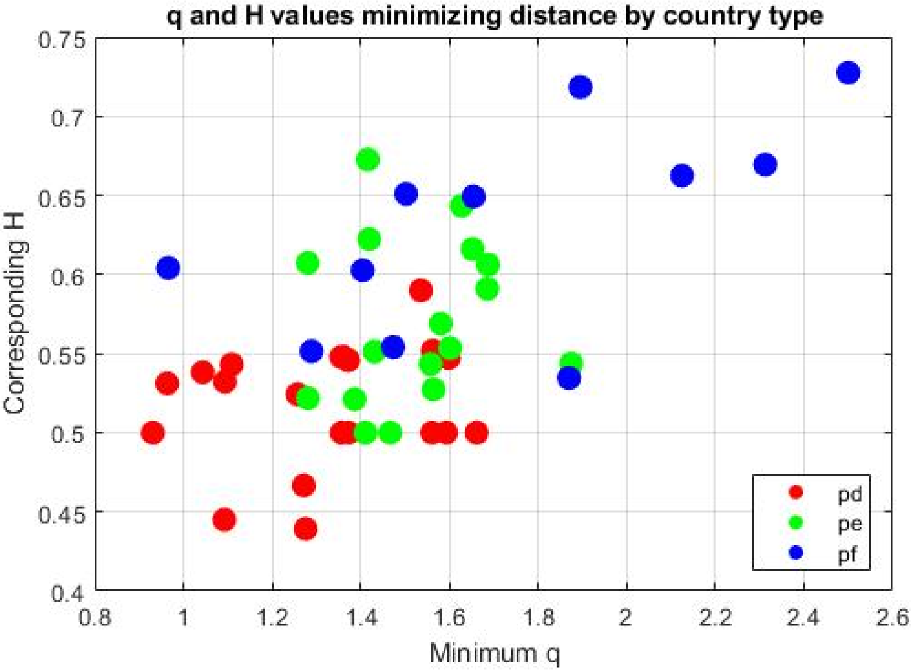

Figure 20: Estimated q and H values across countries with 10 iterations. Developed markets (red) cluster near $(q = 1, H = 0.5)$, while emerging (green) and developing markets (blue) exhibit heavier tails and stronger correlations.

Our results replicate the conclusions of Luciano Zunino, Felipe Olivares, Bariviera, et al. 2017, which found that developed markets (pd) tend to exhibit near-Gaussian behavior with low correlation ($q \approx 1$, $H \approx 0.5$), while developing (pf) and emerging markets (pe) show higher persistence and more pronounced non-Gaussianity ($q > 1$, $H > 0.5$). These observations provide strong evidence for the utility of ordinal patterns in characterizing economic maturity and market structure.

7 Conclusions

In this work, we have explored the capacity of ordinal patterns to encode meaningful information about both the underlying distribution and temporal structure of time series. We first established, through analytical integrals, that the probabilities of ordinal patterns are intrinsically linked to the shape of the probability distribution. This connection was further supported by numerical simulations for various synthetic distributions, including Gaussian, uniform, Laplace, and q-Gaussian models.

To handle the computational demands of estimating pattern probabilities efficiently, we introduced the ORDPAT algorithm, which significantly reduces runtime while preserving accuracy. This allowed us to examine the subtle ways in which ordinal patterns respond to tail heaviness and asymmetry in the underlying data. In particular, we showed that in asymmetric distributions, centering the data using the *median* rather than the mean leads to clearer and more robust pattern profiles — a methodological improvement with potential for broader use in real-world settings.

We then extended our analysis to incorporate temporal correlation via the Hurst exponent H, simulating long-ranged correlated data with prescribed q-Gaussian marginals. Ordinal patterns were shown to respond nonlinearly to changes in both q and H, with persistent processes amplifying monotonic patterns. We validated these theoretical insights against real financial data from the S&P 500 and

NASDAQ over multiple temporal scales, consistently identifying $q \approx 1.5$, in agreement with previous literature. Cross-country comparisons further revealed that developed markets cluster near Gaussian behavior, while developing markets show heavier tails and stronger correlations.

These results not only demonstrate the dual sensitivity of ordinal patterns to both distributional and dynamical features, but also highlight their *scale-robustness* and computational efficiency — making them a powerful tool for time series analysis in complex systems.

Future Directions. Building on these findings, several promising avenues for future research emerge. First, the joint estimation of q and H via ordinal patterns can be extended beyond finance to biomedical signals, such as EEG or heart rate variability, where detecting long-range dependence and non-Gaussian fluctuations is essential. Second, the proposed median-centering technique can be further generalized to non-stationary or skewed data, offering better interpretability in fields such as ecology or climate science.

Moreover, it would be interesting to explore how ordinal patterns behave under nonlinear temporal correlations, which go beyond traditional linear dependencies and could arise in chaotic or feedback-driven systems. Finally, expanding the ordinal framework to multivariate and networked time series opens up new possibilities for studying complex interactions across variables and scales.

In sum, ordinal analysis, grounded in a simple symbolic representation, proves to be a remarkably versatile tool to unveil the subtle geometry of time series data.

Acknowledgments

Acknowledge support and useful discussions:

This work was supported by the SURF@IFISC fellowship. I would like to thank my tutor Felipe Olivares for his insightful advice and for dedicating generously a lot of time to help me with this work. I would also like to thank Daniel Ruiz-Reynés and Marta Ozonas for helping me with this work so kindly and welcomingly.

ORDPAT Algorithm Implementation

Below is the MATLAB implementation of the `ordpat` algorithm used for computing ordinal pattern probabilities:

```
function v = ordpat(datos, D, tau)
    % ORDPAT calculates the empirical probability of ordinal patterns
    % from a time series ’datos’ with embedding dimension D and delay tau.
    % Output ’v’ is a vector of size D! containing the relative frequencies.

    if nargin < 3
        tau = 1;  % default delay
    end
    if nargin < 2
        error(’At least two arguments required: datos and D’);
    end

    v = zeros(1, factorial(D));  % initialize pattern count vector
    n = length(datos);
```

```
    for i = 1 : n - (D - 1) * tau
        C = datos(i : tau : i + (D - 1) * tau);  % extract window
        s = orden(C) + 1;  % compute pattern index (MATLAB is 1-based)
        v(s) = v(s) + 1;  % increment corresponding count
    end

    v = v / sum(v);  % normalize to obtain probabilities
end

function s = orden(datos)
    % Recursive function to map a vector to its permutation index.
    D = length(datos);
    if D == 1
        s = 0;
    else
        [~, idxMin] = min(datos);  % find minimum value position
        datos(idxMin) = [];  % remove the minimum
        s = orden(datos) + (idxMin - 1) * factorial(D - 1);
    end
end
```

References

Amigó, José M. and Osvaldo A. Rosso (Aug. 2023). “Ordinal methods: Concepts, applications, new developments, and challenges—In memory of Karsten Keller (1961–2022)”. In: *Chaos: An Interdisciplinary Journal of Nonlinear Science* 33.8, p. 080401. ISSN: 1054-1500. DOI: `10.1063/5.0167263`. eprint: `https://pubs.aip.org/aip/cha/article-pdf/doi/10.1063/5.0167263/18072435/080401\_1\_5.0167263.pdf`. URL: `https://doi.org/10.1063/5.0167263`.

Azami, Hamed and Javier Escudero (2016). “Amplitude-aware permutation entropy: Illustration in spike detection and signal segmentation”. In: *Computer methods and programs in biomedicine* 128, pp. 40–51.

Bandt, Christoph (2020). “Order patterns, their variation and change points in financial time series and Brownian motion”. In: *Statistical Papers* 61.4, pp. 1565–1588. DOI: `10.1007/s00362-020-01171-7`.

Bandt, Christoph and Bernd Pompe (Apr. 2002). “Permutation Entropy: A Natural Complexity Measure for Time Series”. In: *Phys. Rev. Lett.* 88 (17), p. 174102. DOI: `10.1103/PhysRevLett.88.174102`. URL: `https://link.aps.org/doi/10.1103/PhysRevLett.88.174102`.

Burgos Atencia, Rhonald, Amit Agarwal, and Dimitrie Culcer (2021). “Orbital angular momentum of Bloch electrons: equilibrium formulation, magneto-electric phenomena, and the orbital Hall effect”. In: *Communications Physics* 4.1, p. 123. DOI: `10.1038/s42005-021-00696-z`.

Carpena, Pedro et al. (Aug. 2020). “Transforming Gaussian correlations. Applications to generating long-range power-law correlated time series with arbitrary distribution”. In: *Chaos: An Interdisciplinary Journal of Nonlinear Science* 30.8, p. 083140. ISSN: 1054-1500. DOI: `10.1063/5.0013986`. eprint: `https://pubs.aip.org/aip/cha/article-pdf/doi/10.1063/5.0013986/14631905/083140\_1\_online.pdf`. URL: `https://doi.org/10.1063/5.0013986`.

Fadlallah, Bilal et al. (2013). “Weighted-permutation entropy: A complexity measure for time series incorporating amplitude information”. In: *Physical Review E—Statistical, Nonlinear, and Soft Matter Physics* 87.2, p. 022911.

Gopikrishnan, Parameswaran et al. (Nov. 1999). “Scaling of the distribution of fluctuations of financial market indices”. In: *Physical Review E* 60.5, pp. 5305–5316. ISSN: 1095-3787. DOI: `10.1103/physreve.60.5305`. URL: `http://dx.doi.org/10.1103/PhysRevE.60.5305`.

Leyva, Inmaculada et al. (May 2022). "20 years of ordinal patterns: Perspectives and challenges". In: *Europhysics Letters* 138.3, p. 31001. DOI: `10.1209/0295-5075/ac6a72`. URL: `https://dx.doi.org/10.1209/0295-5075/ac6a72`.

Nayak, Gangadhar, Amit Kumar Singh, and Dilip Senapati (2021). "Computational Modeling of Non-Gaussian Option Price Using Non-extensive Tsallis' Entropy Framework". In: *Computational Economics* 57.4, pp. 1353–1371. DOI: `10.1007/s10614-020-10015-3`.

Olivares, F., L. Zunino, and M. Zanin (Mar. 2023). "Markov-modulated model for landing flow dynamics: An ordinal analysis validation". In: *Chaos: An Interdisciplinary Journal of Nonlinear Science* 33.3, p. 033142. ISSN: 1054-1500. DOI: `10.1063/5.0134848`. eprint: `https://pubs.aip.org/aip/cha/article-pdf/doi/10.1063/5.0134848/19825472/033142\_1\_online.pdf`. URL: `https://doi.org/10.1063/5.0134848`.

Parlitz, U. et al. (2012). "Classifying cardiac biosignals using ordinal pattern statistics and symbolic dynamics". In: *Computers in Biology and Medicine* 42.3. Computing complexity in cardiovascular oscillations, pp. 319–327. ISSN: 0010-4825. DOI: `https://doi.org/10.1016/j.compbiomed.2011.03.017`. URL: `https://www.sciencedirect.com/science/article/pii/S0010482511000618`.

Tsallis, Constantino (2009). *Introduction to nonextensive statistical mechanics: approaching a complex world*. Vol. 1. 1. Springer.

Zanin, Massimiliano et al. (2012). "Permutation Entropy and Its Main Biomedical and Econophysics Applications: A Review". In: *Entropy* 14.8, pp. 1553–1577. ISSN: 1099-4300. DOI: `10.3390/e14081553`. URL: `https://www.mdpi.com/1099-4300/14/8/1553`.

Zunino, L. et al. (2008). "Permutation entropy of fractional Brownian motion and fractional Gaussian noise". In: *Physics Letters A* 372.27, pp. 4768–4774. ISSN: 0375-9601. DOI: `https://doi.org/10.1016/j.physleta.2008.05.026`. URL: `https://www.sciencedirect.com/science/article/pii/S0375960108006919`.

Zunino, Luciano (2024). "Revisiting the Characterization of Resting Brain Dynamics with the Permutation Jensen–Shannon Distance". In: *Entropy* 26.5. ISSN: 1099-4300. DOI: `10.3390/e26050432`. URL: `https://www.mdpi.com/1099-4300/26/5/432`.

Zunino, Luciano, Felipe Olivares, Aurelio F. Bariviera, et al. (2017). "A simple and fast representation space for classifying complex time series". In: *Physics Letters A* 381.11, pp. 1021–1028. ISSN: 0375-9601. DOI: `https://doi.org/10.1016/j.physleta.2017.01.047`. URL: `https://www.sciencedirect.com/science/article/pii/S0375960116316681`.

Zunino, Luciano, Felipe Olivares, Haroldo V. Ribeiro, et al. (Apr. 2022). "Permutation Jensen-Shannon distance: A versatile and fast symbolic tool for complex time-series analysis". In: *Phys. Rev. E* 105 (4), p. 045310. DOI: `10.1103/PhysRevE.105.045310`. URL: `https://link.aps.org/doi/10.1103/PhysRevE.105.045310`.

Zunino, Luciano, Xavier Porte, and Miguel C. Soriano (2024). "Identifying Ordinal Similarities at Different Temporal Scales". In: *Entropy* 26.12. ISSN: 1099-4300. DOI: `10.3390/e26121016`. URL: `https://www.mdpi.com/1099-4300/26/12/1016`.

Electrostatic Gating for Confinement Control in Magnetic Topological Insulators

Álvaro Iturbe Jabaloyes, Javier Osca Cotarelo, Llorenç Serra Crespí
Instituto de Física Interdisciplinar y Sistemas Complejos, IFISC (CSIC-UIB)
Campus Universitat de les Illes Balears, E-07122 Palma, Spain

Abstract

Magnetic Topological Insulators (MTIs) are a novel class of materials exhibiting dissipationless edge states within an insulating bulk. This work investigates the emergence and control of these edge states across different topological phases by electrostatic gating. Numerical simulations reveal distinct behaviors in each phase, including finite-size effects such as edge-state interaction, phase coexistence, and band anticrossing. These results offer insights into controlling topological features in MTIs for potential device applications.

1 Introduction

Over the last century, one of the major achievements of quantum physics has been the description of materials through band structures and Fermi surfaces in momentum space [1]. The electronic band theory of solids relies on the translational symmetry of crystals, allowing the electronic structure to be described in terms of the crystal momentum k, defined within the Brillouin Zone [2]. This framework successfully distinguishes conductors (metals) from non-conductors (insulators) based on the presence or absence of electronic band gaps.

In conductors, electrons can be easily excited within a partially filled conduction band, while insulators feature a band gap between filled valence bands and empty conduction bands. Semiconductors share a similar structure but with a smaller energy gap E_g, allowing thermal or external excitation of electrons across the gap [4].

A richer classification of electronic phases emerged with the inclusion of magnetism and superconductivity. The discovery of the Integer Quantum Hall (QH) effect in 1980 [5] was a breakpoint about the difference between metals and insulators. This phenomenon was first observed in two-dimensional electron gases confined in semiconductor quantum wells under strong magnetic fields. Electrons in the bulk undergo cyclotron motion due to the Lorentz force, while at the edges, skipping orbits form due to boundary confinement [7]. These result in unidirectional propagating edge states, known as chiral edge states, which allow for ballistic, dissipationless transport without backscattering.

Remarkably, these edge states are topologically protected and survive even in the presence of weak disorder [9]. Consequently, a two-dimensional system under strong magnetic field behaves as an insulator in the bulk but conducts along its edges through gapless states.

Later, it was discovered that such behavior can also arise without external magnetic fields, through spin-orbit coupling, especially in heavy elements like mercury and bismuth [10, 12]. This led to the prediction of the Quantum Spin Hall (QSH) effect in graphene in 2005 [11], and its experimental confirmation in HgTe quantum wells in 2007 [13]. In the QSH effect, each edge supports two counter-propagating chiral states with opposite spins. Spin-up electrons travel in one direction, while spin-down electrons move in the opposite, forming time-reversal symmetric copies of QH states.

These QSH edge states are protected by time-reversal symmetry and are not subject to backscattering as long as this symmetry is preserved [14]. Thus, QSH systems represent a new class of topological insulators where the spin degree of freedom plays a crucial role.

Another state of interest is the Quantum Anomalous Hall (QAH) effect, which mimics the QH effect but without an external magnetic field. First realized in 2013 by doping materials like Bi_2Te_3 or Sb_2Te_3 with magnetic atoms (e.g., Cr or Fe) [17], the QAH effect results from internal magnetization. While this approach may degrade material quality, more recent advances have

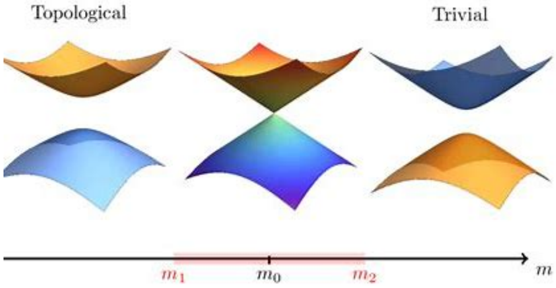

Figure 1: Difference between topological and trivial phase. The transition from the trivial to the topological phase (or vice versa) is realized when an inversion between the conduction and valence bands takes place.

demonstrated the QAH effect in MnBi_2Te_4 thin films [18]. These thin-film systems are especially interesting since their electronic behavior can be modeled effectively in two dimensions.

The materials exhibiting such behavior are known as Magnetic Topological Insulators (MTIs) [19]. These are insulating in the bulk but host topologically protected conducting states on their surface or edges. The QH state can be seen as the simplest topological phase. In this thesis, special attention is given to MTIs that realize the QAH effect via magnetic doping.

One of the most exciting aspects of topological insulators is that their existence in 2D and 3D was theoretically predicted in 2005 and 2007, respectively [11, 20], prior to experimental observation. Today, TIs represent a central topic in condensed matter physics, as recognized by the 2016 Nobel Prize in Physics for the study of topological phases in theoretical physics [21].

2 Theoretical model

2.1 Topology in Condensed Matter Physics

In condensed matter physics, *topology* refers to the study of properties of a physical system that remain invariant under continuous deformations of its parameters, such as stretching or bending, without closing the energy gap. Unlike conventional phases of matter, which are classified by local order parameters and spontaneous symmetry breaking (as described by Landau's theory), topological phases are characterized by global invariants that are robust against local perturbations [14].

A paradigmatic example is the integer quantum Hall effect, where the Hall conductance is quantized in integer multiples of e^2/h. This quantization arises from a topological invariant known as the *Chern number*, which counts the winding of the Berry curvature over the Brillouin zone. Similar ideas extend to *topological insulators*, which possess insulating bulk states and conducting surface or edge states protected by symmetries, such as time-reversal symmetry.

Mathematically, topology in condensed matter systems is often related to the mapping between the momentum-space manifold (e.g., the Brillouin zone) and a parameter space defined by the Hamiltonian. The robustness of topological invariants against disorder and perturbations makes these systems promising for applications in low-power electronics, spintronics, and topological quantum computation. The difference between topological and trivial phase is due to the inversion of the bulk energy bands, as can be seen in figure 1. For a detailed introduction to the field, see Hasan and Kane (2010) [14].

2.2 Modelization of the system

The model is based on an effective Hamiltonian that aims to describe the propagation of electrons and holes through the material. To this end, a thin 3D film is modelled as two 2D layers with a coupling term between them included in the Hamiltonian. Additionally, the model incorporates a term accounting for the interaction due to the intrinsic magnetization of the material, as well as the effect of an applied electrostatic potential. Therefore, the Hamiltonian of the system is,

$$\mathcal{H} = \left[m_0 + m_1(p_x^2 + p_y^2)\right]\lambda_x + \alpha\left[p_x\sigma_y - p_y\sigma_x\right]\lambda_z + \Delta_B\sigma_z + V_d(y)\lambda_z. \tag{2.1}$$

The parameters used in the Hamiltonian are defined as follows:

- σ, λ : Pauli matrices on spin and layer subespaces.

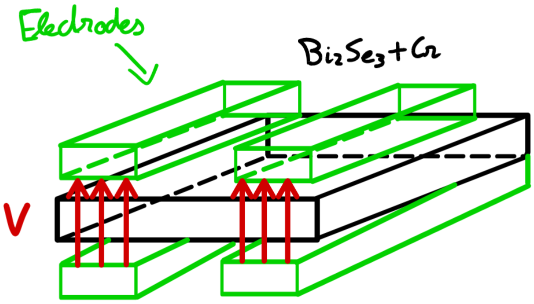

Figure 2: Proposed system. In green, two electrodes. In black, the material.

- m_0, m_1 : Parameters for interlayer coupling. $m_1^{-}1$ is an effective mass.
- p_x, p_y : Momentum operators along the x and y directions, respectively.
- α : Spin-orbit coupling.
- Δ_B : Zeeman parameter (magnetization).
- $V_d(y)$: Position-dependent electric potential.

By tuning Δ_B and $V_d(y)$, the system can be driven through different topological phases. This model describes magnetically doped topological insulators such as $Bi_2Se_3 + Cr$ and $Bi_2Te_3 + Cr$.

On the other hand, the proposed system consists of a slab of MTI material with top-bottom electrodes, allowing control of the electric potential applied to the material in specific regions of the slab, as can be seen in figure 2.

3 Results and discussion

3.1 Nomenclature and system definitions

In order to avoid confusion in the discussion of the results, we establish here the terminology that will be used throughout this work:

- **Bulk (or Extended Film):** Refers to an extended 2D bilayer system along both x and y directions. This should not be confused with the notion of a three-dimensional bulk.
- **Slab:** 2D system with a finite width L_y and infinite extension along x. We assume vacuum outside the magnetic topological insulator (MTI) boundaries.
- **Extended Film with Uniform Gating:** The gating potential is constant, $V = \text{const}$. The bulk spectrum $E(k_x, k_y)$ is obtained analytically.
- **Slab with Uniform Gating:** The gating potential is constant, $V = \text{const}$. The spectrum is computed numerically. Finite-size effects arise due to the finite width L_y.
- **Slab with Non-uniform Gating:** The gating potential depends on y, i.e., $V_d(y)$. In this case the explicit functional form of $V_d(y)$ must be specified.
- **Extended Film with Non-uniform Gating:** This case is not modeled directly. Instead, it can be studied by considering a sufficiently wide slab with non-uniform gating (large L_y), which effectively reproduces the extended limit.

3.2 Main objectives of the work

The present study focuses on three complementary goals:

1. **Confined states in extended films with non-uniform gating.** Although such systems are not modeled directly, they can be effectively studied by considering wide slabs with non-uniform gating. In the limit of large L_y, these slabs reproduce the behavior of the extended film.
2. **Confirmation of topological band theory.** By analyzing slabs under uniform gating, we confirm the expectations from band topology theory. In this case, the numerical slab spectrum provides evidence that complements the analytical bulk calculations.

3. **Interaction between edge states in slabs of finite L_y.** We aim to characterize anticrossing effects and slope deformations.

In addition, schematic sketches of all the above geometries are included in figure 3 to provide a clear visualization of the systems and the role of the gating potential.

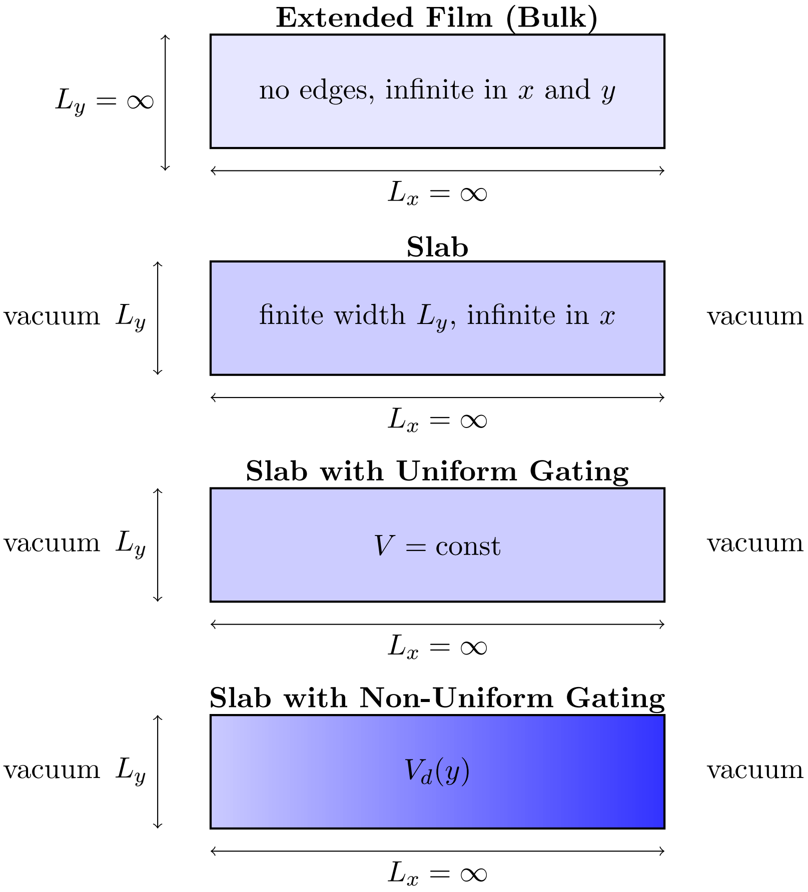

Figure 3: Schematic representations of the different systems studied in this work. From top to bottom: Extended Film (Bulk), Slab, Slab with Uniform Gating ($V = \text{const}$), and Slab with Non-Uniform Gating ($V_d(y)$). The width L_y is finite for slabs, while L_x is considered infinite. Vacuum regions are assumed outside the MTI boundaries. The blue gradient illustrates the y-dependent potential in the non-uniform slab.

3.3 Phase Diagram for the bulk

In this section, we analytically solve the equation $\det(H) = 0$ for the bulk in order to obtain the conditions that determine the phase boundaries for both $m_0 = 17$ meV and $m_0 = -17$ meV, following the approach presented by Jing Wang and Shou-Cheng Zhang in their work on *Electrically Tunable Magnetism in Magnetic Topological Insulators* [24]. Then, for a constant $V_d(y) \equiv V$ electrostatic potential the two conditions are,

1. $m_0^2 + V^2 = \Delta_B^2$,
2. $m(k) = 0$, $\Delta_B^2 + \alpha^2 k^2 = V^2$.

A detailed derivation of the conditions can be seen in Appendix A.

3.3.1 Case $m_0 > 0$

For $m_0 > 0$, we take $m_0 = 17$ meV as a characteristic value, for which we identify two distinct phases in the phase diagram: the *Quantum Anomalous Hall* (QAH) phase and the *Normal Insulator A* (NI A) phase, as can be seen in figure 4a.

In the QAH phase, the system exhibits a quantized Hall conductance $\sigma_{xy} = \pm e^2/h$ in the absence of an external magnetic field. This behavior originates from a non-zero Chern number in the band structure, which leads to the formation of chiral edge states at the sample boundaries

[22, 23]. In the band structure, these edge states manifest as characteristic "crossings" (or "X-shapes") that connect the conduction and valence bands across the bulk energy gap. The QAH effect is robust against weak disorder and perturbations that do not close the gap or alter the topological invariant.

In contrast, the NI A phase corresponds to a topologically trivial insulating state with a vanishing Chern number. In this phase, the bulk remains gapped and no protected edge states are present, which means that the band structure does not exhibit the "X-shaped" crossings characteristic of topological phases. Consequently, the system behaves as a conventional band insulator with no quantized Hall response.

The transition between the QAH and NI A phases occurs when the bulk gap closes and reopens with a change in the topological invariant, which can be tuned through model parameters such as Δ_B or V in our system, while $\hbar^2 m_1 = 0.15 \cdot 10^{-3}$ meV μm^2, $\hbar\alpha = 0.2$ meVμm.

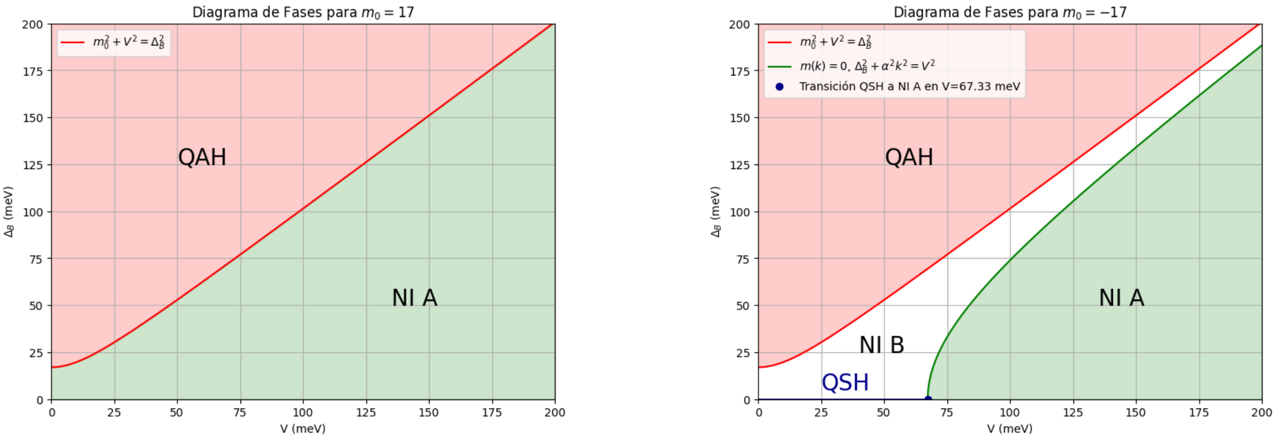

(a) $m_0 = +17$ meV. Phase diagram of a homogeneous extended film without edges.

(b) $m_0 = -17$ meV. Phase diagram of a homogeneous extended film without edges.

Figure 4: Phase diagrams of homogeneous extended films (no edges) for two opposite values of m_0: (a) $m_0 = +17$ meV and (b) $m_0 = -17$ meV.

3.3.2 Case $m_0 < 0$

For $m_0 < 0$, we take $m_0 = -17$ meV as a characteristic value, leading to the phase diagram from figure 4b revealing four distinct phases. We take also $\hbar m_1 = 0.15 \cdot 10^{-3}$ meV μm^2, $\hbar\alpha = 0.2$ meVμm, as in the previous case. As in the $m_0 = 17$ meV case, we identify a *Quantum Anomalous Hall* (QAH) phase in the same region of parameter space, characterized by a non-zero Chern number, chiral edge states, and the "X-shaped" band crossings typical of topological phases [22, 23].

In addition, an intermediate phase denoted as *Normal Insulator B* (NI B) emerges. Despite being topologically trivial (Chern number $C = 0$), the NI B phase displays edge-like states within the gap whose dispersion (slope) varies continuously with the applied electric potential V, as we will show later. These states are not protected by a topological invariant and can therefore be removed or significantly modified by perturbations that break the relevant symmetries.

Upon further increasing the electric potential, the system undergoes a transition from NI B to the NI A phase, a fully gapped trivial insulator with no in-gap edge states and no Hall response. This transition is driven by the disappearance of the residual edge-like states as the band gap evolves.

In the special case of vanishing Zeeman term ($\Delta_B = 0$ meV), only two phases appear. At low potential, the system is in a *Quantum Spin Hall* (QSH) phase [10, 11], which shares similarities with the NI B phase in its band structure (presence of gap-crossing states) but is protected by time-reversal symmetry. This symmetry ensures the robustness of the helical edge states against non-magnetic disorder. As the potential exceeds $V = 67.33$ meV, the QSH phase transitions into the trivial NI A phase via a gap-closing and reopening process that changes the topological invariant from $\mathbb{Z}_2 = 1$ to $\mathbb{Z}_2 = 0$.

3.4 Slab with uniform gating

In this section, we apply a uniform electrostatic potential across the slab of width L_y. For large L_y this corresponds to the homogeneous system, following the phase diagrams shown in 4a and 4b.

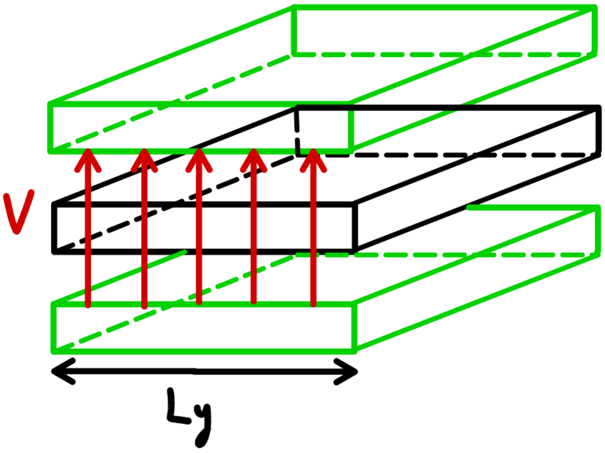

Figure 5: Slab (in black) with uniform gating using electrodes (in green).

A sketch of the system can be seen in figure 5. To analyze the phase behavior of the system, we consider three distinct cases.

We first consider the case $m_0 > 0$ with $\Delta_B > m_0$, in order to analyze the transition from the QAH to the NI A phase. Specifically, for $m_0 = 17$ meV, $\Delta_B = 20$ meV, and slab width $L_y = 0.75\,\mu$m, we observe a direct phase transition from the QAH phase to the NI A phase as the uniform electrostatic potential is increased. The QAH phase is characterized by a non-zero Chern number and the presence of chiral edge states, whereas in the NI A phase the system becomes a trivial insulator with no in-gap states. This behavior is consistent with the predictions of the phase diagram in Fig. 4a.

We next analyze the case $m_0 < 0$, considering two different values of Δ_B. First, for $\Delta_B = 20$ meV, $m_0 = -17$ meV, and $L_y = 0.75\,\mu$m, the system undergoes a sequence of phase transitions as the uniform electrostatic potential increases: from the QAH phase to the NI B phase, and finally to the NI A phase. The NI B phase is characterized by edge-like states forming "X-shaped" crossings within the gap, whose slope evolves with the applied potential, while the separation between the bulk states also changes. Upon further increasing the potential, these "X-shaped" features gradually vanish, and the system enters the NI A phase, where no in-gap edge states are present. This sequence of transitions is consistent with the phase diagram in Fig. 4b, and can be clearly observed in Figs. 6.

Second, for $\Delta_B = 0$ meV with the same parameters $m_0 = -17$ meV and $L_y = 0.75\,\mu$m, we focus on the transition from the QSH to the NI A phase. As shown in Figs. 7 and 8, the system initially hosts time-reversal protected helical edge states, which are doubly degenerate and localized in pairs along the sample boundaries. When the applied potential exceeds the critical value $V = 67.33$ V, the Dirac cone in the band structure disappears and the system becomes a trivial insulator (NI A phase). This behavior is in full agreement with the phase diagram.

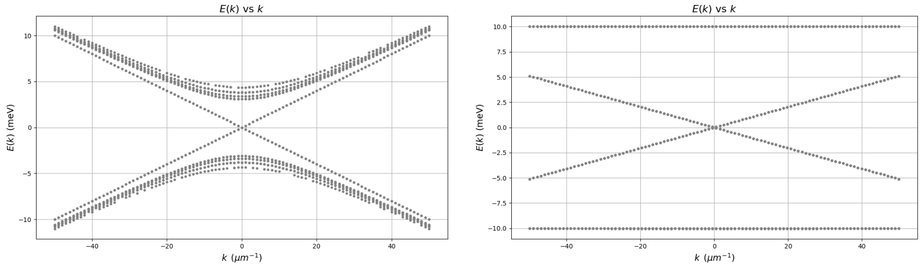

(a) $V = 0$ meV **(b)** $V = 25$ meV

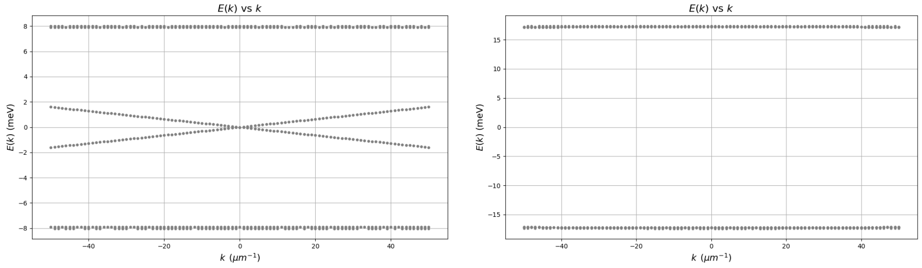

(c) $V = 50$ meV **(d)** $V = 100$ meV

Figure 6: Evolution of the band structure for increasing values of the uniform applied potential V. Case $m_0 = -17$ meV, $\Delta_B = 20$ meV.

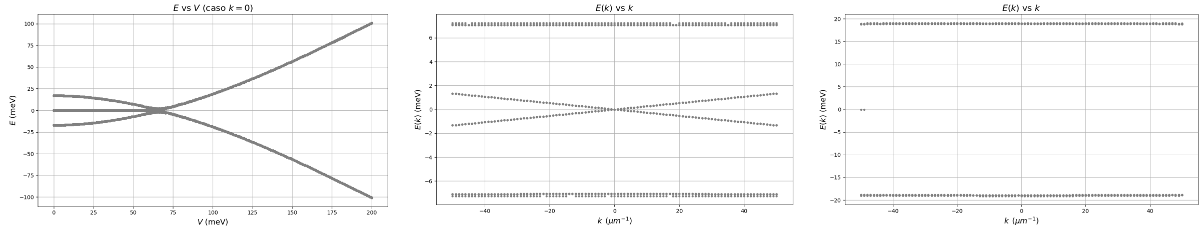

(a) Energy gap closing for $k = 0$ due to the increase of V **(b)** $V = 50$ meV **(c)** $V = 100$ meV

Figure 7: Energy gap closing for $k = 0$ due to the increase of V and evolution of the band structure for increasing values of the uniform applied potential V. Case $m_0 = -17$ meV, $\Delta_B = 0$ meV.

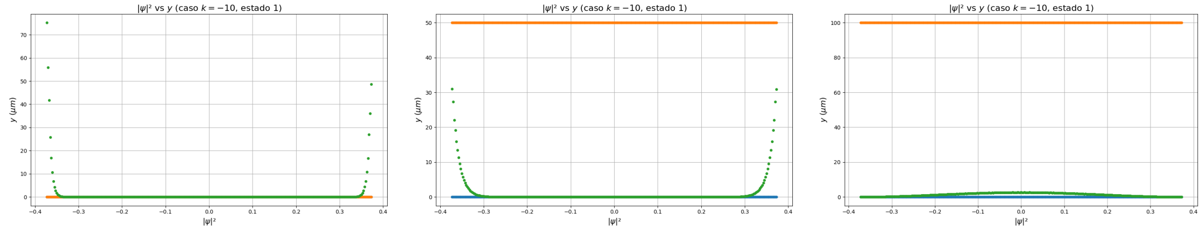

(a) State 1 for $V = 0$ meV **(b)** State 1 for $V = 50$ meV **(c)** State 1 for $V = 100$ meV

Figure 8: Distributions of probability density along y for selected states. Case $m_0 = -17$ meV, $\Delta_B = 0$ meV.

3.5 Dependence of the Dirac Cone Slope on the Applied Potential in the NI B Phase for slab with uniform gating

In this section, we aim to study the relationship between the slope of the Dirac cone and the bulk energy bands. Since the Dirac cone corresponding to the edge states is formed from the bulk energy bands that close and give rise to the characteristic cross-shaped form in the two-dimensional projections, the slope of the cone will be related to the shape of the bulk energy bands. Therefore, we expect to see that if the shape of these bands changes upon applying an electrostatic potential, the slope will consequently change as well. The same applies both in the case of the slab with uniform gating and in the case of the slab with non-uniform gating.

Specifically, in the *Normal Insulator B* (NI B) and *Quantun Spin Hall* phases, we have seen a change in the slope of Dirac cones when we change the applied electrostatic potential, while in the *Quantum Anomalous Hall* (QAH) this change is very slow or not appreciable. This has sense since NI B and QSH are essentially the same phase because the only difference is the time reversal symmetry, since the QAH is very different from them. So the slope of the Dirac cones in NI B should be directly related to the energy separation between the bulk valence and conduction bands. This separation is sensitive to the application of an external electrostatic potential, which modifies the dispersion relations by altering the effective band gap.

Our analysis shows that, as the electrostatic potential V approaches the critical value V_c—marking the transition between the NI B and *Normal Insulator A* (NI A) phases—the slope of the Dirac cone changes in a non-linear fashion. This behavior can be quantitatively described through the analytical expression derived in Appendix B, which is obtained by projecting the Hamiltonian spectrum along $k_y = 0$ and evaluating the smallest positive eigenenergy. The resulting slope depends explicitly on V, Δ_B, m_0, m_1, and α, revealing a clear tunability of the band structure via electrostatic gating.

In figure 9, it can be observed the evolution of the band structure for increasing values of the applied electrostatic potential, what leads to the change of the slope in the Dirac cone when edge states are formed.

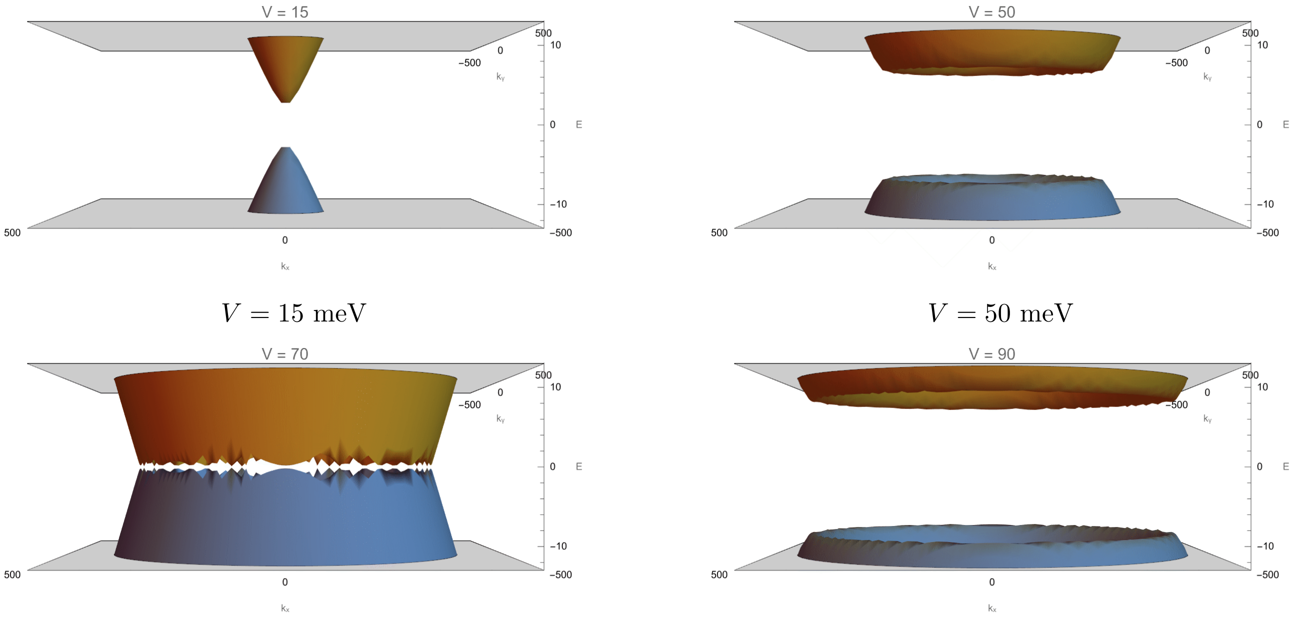

$V = 15$ meV

$V = 50$ meV

$V = 70$ meV

$V = 90$ meV

Figure 9: Evolution of the band structure for increasing values of the applied potential V in the NI B phase. Here we represent the band energies (eigenvalues) of the Hamiltonian for the slab with uniform gating ($m_0 = -17$ meV, $m_1 = 0.15 \cdot 10^{-3}$ meV, $\alpha = 0.2$, $\Delta_B = 20$ meV, $V \in [0, 100]$ meV).

Using the substitutions $k_y = 0$, $k_x \to k$, $\Delta_B = 20$ meV, $\hbar\alpha = 0.2$ meV μm, $\hbar^2 m_1 = 0.15 \cdot 10^{-3}$ meV μm^2 and $m_0 = -17$ meV in the analytical expression derived in Appendix B, the slope reduces to the following compact form for this case,

$$m(V) = 0.00297044\sqrt{4933.33 + V^2 - 2\sqrt{4533.33\,V^2 + 400\,(1.26218 \times 10^{-29} + V^2)}}.$$

Figure 10 illustrates this dependence of the Dirac cone slope on the applied electrostatic potential. The plotted curve in the interval $V \in [0, 200]$ (vertical axis limited to $[0, 1]$) shows a non-linear behaviour with a minimum near $V \approx 70.24$ for these parameters. Physically, this minimum corresponds to the point where the positive-band energy approaches zero at the critical momentum and the effective slope of the linearised dispersion vanishes; for larger V the slope increases again. This behaviour exemplifies how electrostatic gating provides a direct handle on the band dispersion in the NI B phase through its influence on the valence–conduction band separation. The detailed derivation and intermediate algebraic steps are provided in Appendix B.

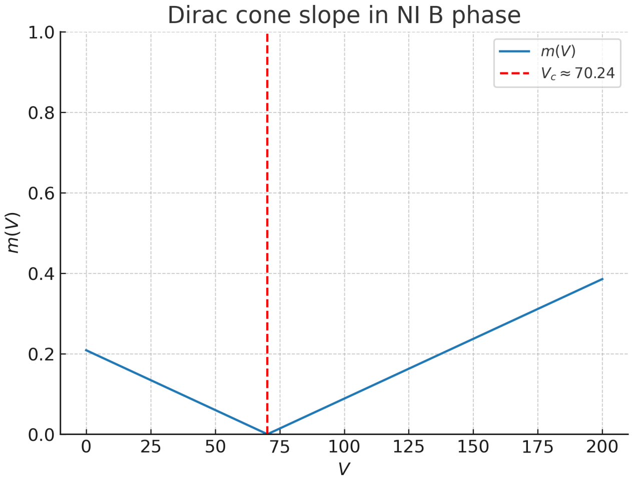

Figure 10: Parameterised Dirac cone slope $m(V)$ as a function of the applied electrostatic potential V for the chosen parameters $M_z = 20$, $m_0 = -17$ meV, $\hbar^2 m_1 = 0.15 \cdot 10^{-3}$ meV μm^2 and $\hbar\alpha = 0.2$ meV μm. The vertical axis is restricted to the range $[0, 1]$ for clarity.

3.6 Non uniform gating: symmetric potential barriers along y

The aim of this section is to characterize the behavior of the system when a non-uniform electrostatic potential is applied. This potential, $V_d(y)$, is introduced symmetrically at a certain distance from the center of the box, creating three distinct regions with different phase behaviors, while also attempting to induce confinement of the edge states through electrostatic gating. Specifically, we obtain a central region of length L_y where no electrostatic potential is applied, flanked by two outer regions that are separated from the central one by the potential barriers. Therefore, $V_d(y)$ is a function that takes the value zero in the central region and increases until reaching its maximum in the lateral regions.

We adopt a compact notation for the different phases observed in the phase diagrams:

- A: *Normal Insulator A* (NI A)
- B: *Normal Insulator B* (NI B)
- S: *Quantum Spin Hall* (QSH)
- H: *Quantum Anomalous Hall* (QAH)
- +: *Case* $m_0 = 17$ *meV*
- -: *Case* $m_0 = -17$ *meV*

For example, `ASA-` denotes a configuration where the central region is in phase S, while both sides are in phase A along y due to the effect of the potential barriers, and $-$ indicates the case $m_0 = -17$ meV. Similarly, $+$ corresponds to $m_0 = 17$ meV, as can be seen in figure 11.

Figure 11: Example schematic for notation `ASA`: each box represents a spatial region along y, with letters indicating the phase in the left, middle, and right segments, respectively. The signs ± specify the value of m_0.

We will maintain $\hbar^2 m_1 = 0.15 \cdot 10^{-3}$ meV μm^2 and $\hbar\alpha = 0.2$ meV μm for the rest of the section.

3.6.1 Abrupt potential barriers (smoothing parameter 0)

In this section we analyze the case of abrupt potential barriers. The potential displays a sharp discontinuity between the central and lateral regions and reaches its maximum value abruptly at the boundaries. This modification of the potential profile changes the coexistence regions and therefore leads to qualitatively different edge-state phenomenology compared with the smooth-barrier case that we will see later. Below we describe the main features found for positive and negative m_0 and for several central-region lengths L_y, referring to the corresponding band-structure

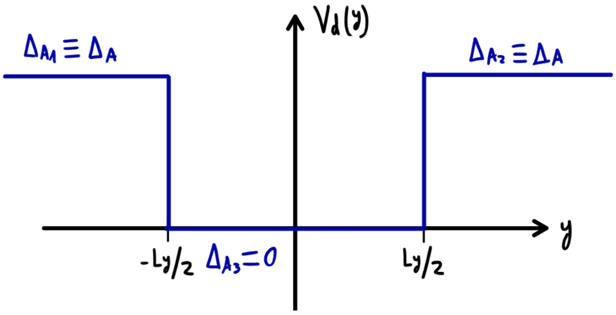

Figure 12: Potential profile for the abrupt case.

and probability-density panels. To shorten repeated expressions and avoid subscript errors we define for the non-uniform potential $V_d(y)$,

$$\Delta_A \equiv \Delta_{A_1} = \Delta_{A_2}, \qquad \Delta_{A_3} = 0,$$

where $\Delta_A \equiv \Delta_{A_1} = \Delta_{A_2}$ refers to the maximum values of the potential while $\Delta_{A_3} = 0$ meV refers to the central region of length L_y. The form of the abrupt potential profile can be seen in figure 12. Throughout the text and in figure captions we write e.g. ‘$\Delta_A = 25$ meV‘ to mean ‘$\Delta_{A_1} = \Delta_{A_2} = 25$ meV, $\Delta_{A_3} = 0$‘.

For $m_0 > 0$ we focus on the coexistence between the `H` and `A` phases. For the parameters $\Delta_B = 20$ meV, $m_0 = +17$ meV and $L_y = 0.75\,\mu$m, the system evolves from the `HHH+` phase (case $\Delta_A = 0$ meV) into the `AHA+` phase (case $\Delta_A = 50, 100$ meV) as the barrier height is increased. In the `AHA+` regime both the slope of the "H" branches and the separation between bulk bands vary only slowly with the barrier height, reflecting the limited impact of the electrostatic profile on the bulk spectrum. This behavior is illustrated in Figs. 13 and 14.

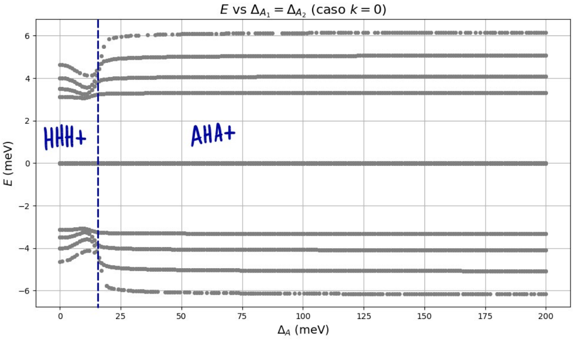

(a) Energy gap closing at $k = 0$ as Δ_A increases

Figure 13: Gap closure at $k = 0$ as Δ_A increases (i.e. $\Delta_{A_1} = \Delta_{A_2}$ while $\Delta_{A_3} = 0$). Case $m_0 = +17$ meV, $\Delta_B = 20$ meV, abrupt potential barriers.

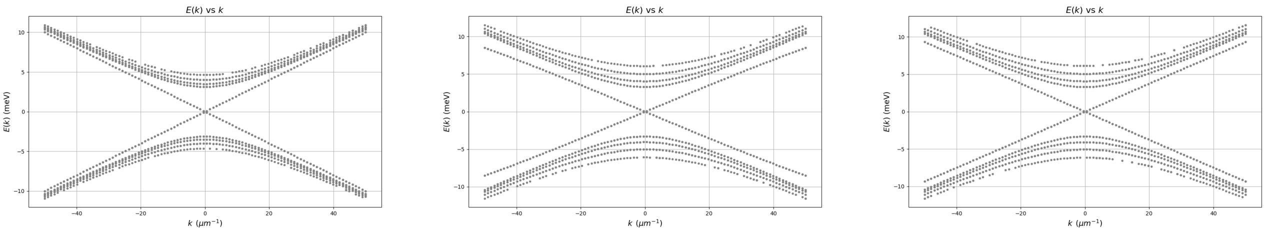

(a) $\Delta_A = 0$ meV **(b)** $\Delta_A = 50$ meV **(c)** $\Delta_A = 100$ meV

Figure 14: Evolution of the band structure for increasing Δ_A (with $\Delta_{A_3} = 0$). Case $m_0 = +17$ meV, $\Delta_B = 20$ meV, abrupt potential barriers.

We now turn to $m_0 < 0$. We first discuss the family of results obtained for $\Delta_B = 20$ meV and $m_o = -17$ meV, comparing them with the smooth-barrier case and exploring the effect of reducing the central-region length L_y (stronger hybridization between central and lateral regions is expected for smaller L_y).

For $\Delta_B = 20$ meV, $m_0 = -17$ meV and $L_y = 0.75\,\mu$m the system starts in the `HHH-` phase ($\Delta_A = 0$ meV). Increasing the barrier height drives a transition to `BHB-` ($\Delta_A = 25, 50$ meV), where we identify eight states localized at the slab–vacuum boundaries (such as the two first states from figure 16) and four states localized at the potential barriers (such as the three other states from figure 16). In this sequence the slope of the “B” branches varies with the potential due to the change of the Dirac cone as we explained before, while the “H” branches remain essentially unchanged. Further increase of the barrier height leads to an `AHA-` phase ($\Delta_A = 100, 500$ meV) with four states localized at the barriers (corresponding to `H`-type states). These features are displayed in Figs. 15, 16 and 17.

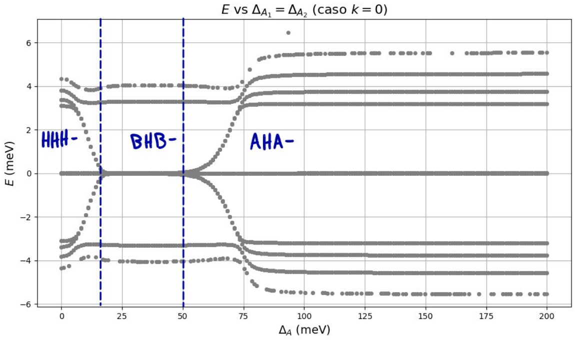

Figure 15: Energy gap closing at $k = 0$ as Δ_A increases (with $\Delta_{A_3} = 0$). Case $m_0 = -17$ meV, $\Delta_B = 20$ meV, abrupt potential barriers, $L_y = 0.75$ μm.

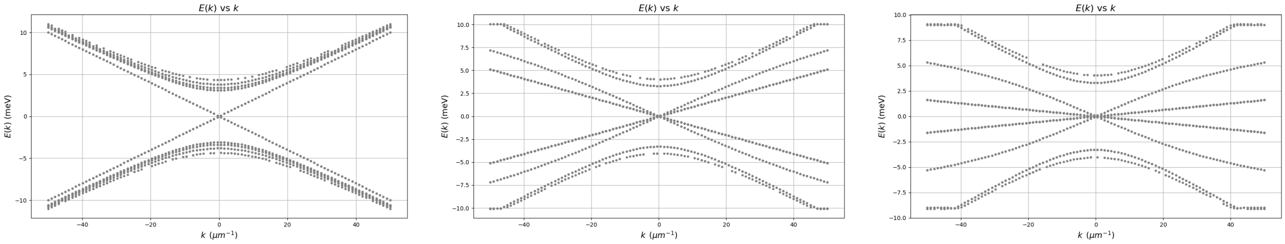

$\Delta_A = 0$ meV $\Delta_A = 25$ meV $\Delta_A = 50$ meV

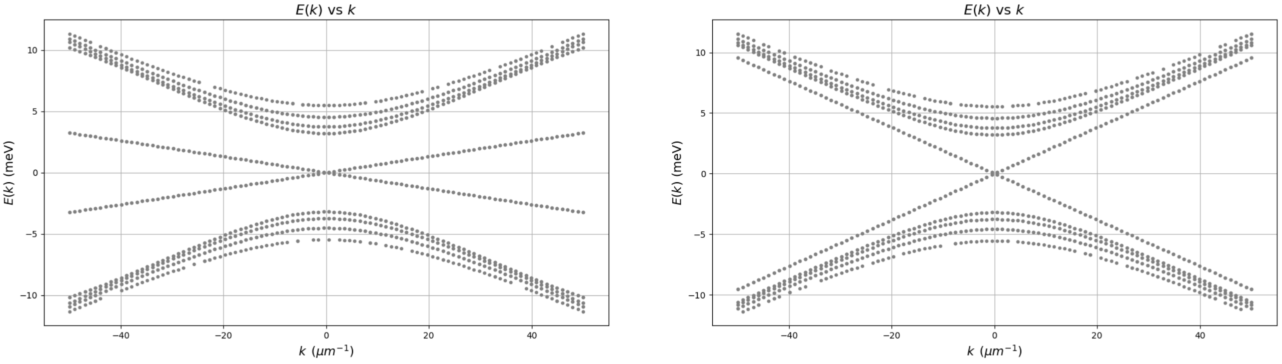

$\Delta_A = 100$ meV $\Delta_A = 500$ meV

Figure 16: Evolution of the band structure for increasing Δ_A (with $\Delta_{A_3} = 0$). Case $m_0 = -17$ meV, $\Delta_B = 20$ meV, abrupt potential barriers, $L_y = 0.75$ μm.

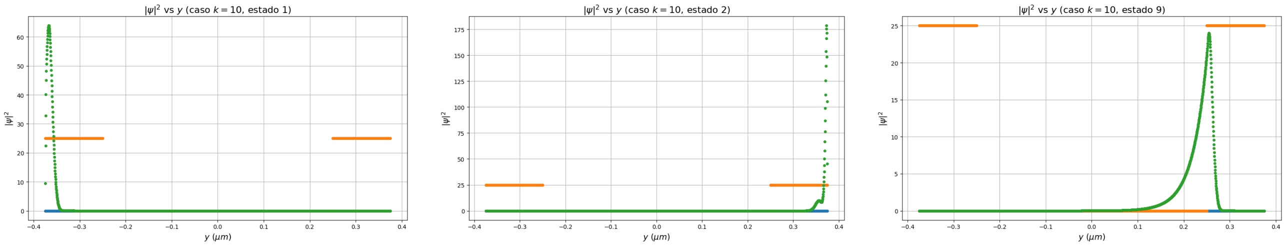

State 1, $\Delta_A = 25$ meV

State 2, $\Delta_A = 25$ meV

State 9, $\Delta_A = 25$ meV

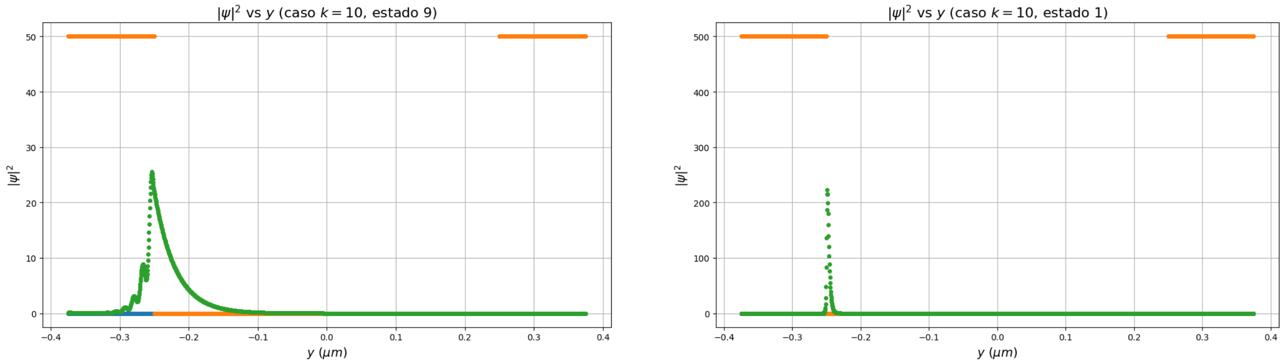

State 9, $\Delta_A = 50$ meV

State 1, $\Delta_A = 500$ meV

Figure 17: Probability-density distributions along y for selected states under the non-uniform potential (Δ_A, with $\Delta_{A_3} = 0$). Case $m_0 = -17$ meV, $\Delta_B = 20$ meV, abrupt potential barriers, $L_y = 0.75$ μm.

Reducing the central-box length to $L_y = 0.60\,\mu$m enhances interaction effects between states. Starting again from `HHH-` ($\Delta_A = 0$ meV) and increasing the barrier height we reach `BHB-` ($\Delta_A = 25, 50$ meV), with eight states pinned at the box edges. Of the remaining four states, two are localized at the potential barriers while two occupy intermediate positions; this intermediate localization is likely a consequence of hybridization between box-edge and barrier-edge states (notably visible at $\Delta_A = 25$ meV). At $\Delta_A = 50$ meV clear anticrossings occur: the spectrum displays eight box-edge states and four states localized between barriers and box edges. With further increase of the barrier height the system evolves into the `AHA-` phase ($\Delta_A = 100$ meV). See Figs. 18, 19 and 20.

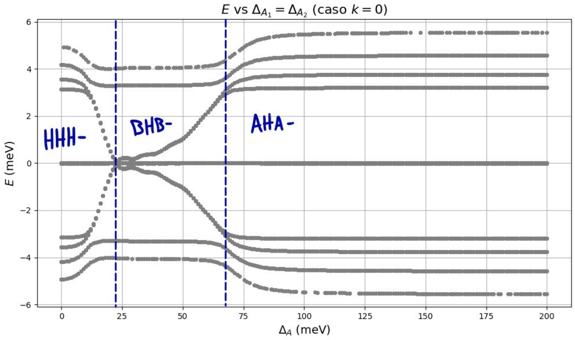

Figure 18: Energy gap closing at $k = 0$ as Δ_A increases (with $\Delta_{A_3} = 0$). Case $m_0 = -17$ meV, $\Delta_B = 20$ meV, abrupt potential barriers, $L_y = 0.60$ μm.

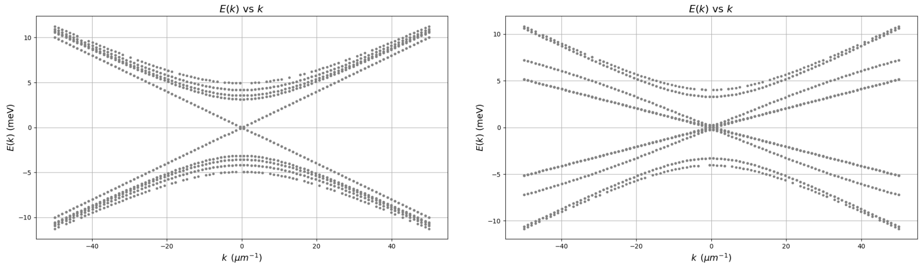

(a) $\Delta_A = 0$ meV **(b)** $\Delta_A = 25$ meV

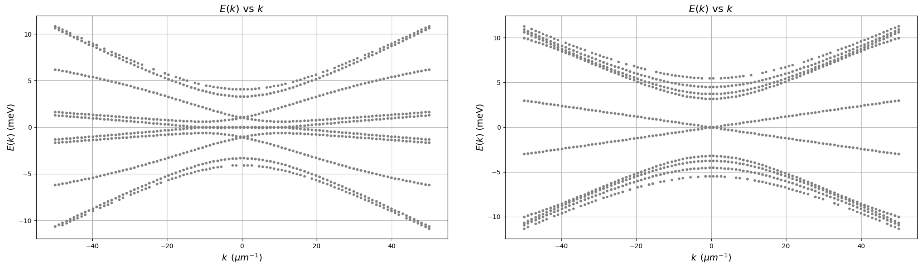

(c) $\Delta_A = 50$ meV **(d)** $\Delta_A = 100$ meV

Figure 19: Evolution of the band structure for increasing Δ_A (with $\Delta_{A_3} = 0$). Case $m_0 = -17$ meV, $\Delta_B = 20$ meV, abrupt potential barriers, $L_y = 0.60$ μm.

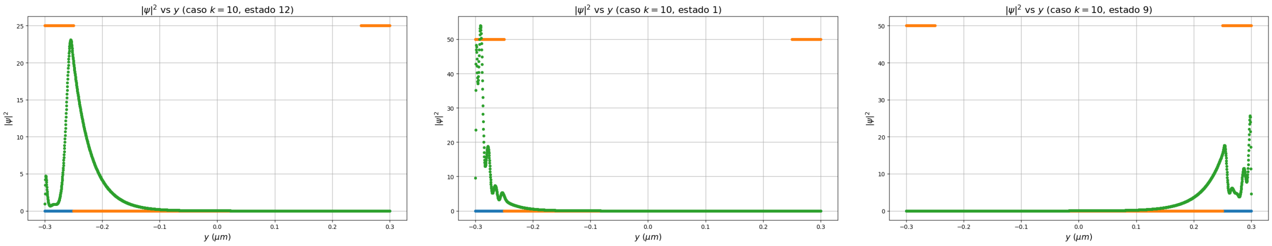

(a) State 12, $\Delta_A = 25$ meV **(b)** State 1, $\Delta_A = 50$ meV **(c)** State 9, $\Delta_A = 50$ meV

Figure 20: Probability-density distributions along y for selected states under the non-uniform potential (Δ_A, with $\Delta_{A_3} = 0$). Case $m_0 = -17$ meV, $\Delta_B = 20$ meV, abrupt potential barriers, $L_y = 0.60$ μm.

For $L_y = 0.56\,\mu$m hybridization and anticrossing effects become even more pronounced. From the initial `HHH-` configuration ($\Delta_A = 0$ meV) the system transitions to `BHB-` already at $\Delta_A = 25$ meV, with a clear anticrossing pattern: the spectrum can be decomposed into four box-edge states, four barrier-edge states and four hybridized (intermediate) states (such as the first state from figure 21). The same qualitative configuration persists at $\Delta_A = 50$ meV. At sufficiently large barrier height (for instance $\Delta_A = 100$ meV) the system reaches the `AHA-` phase. Corresponding band structures and representative state localizations are shown in Figs. 21, 22 and 23.

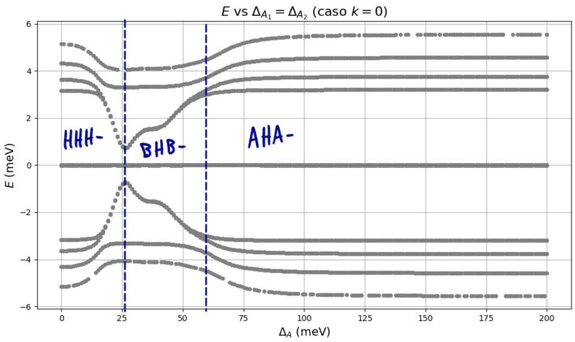

Figure 21: Gap closure at $k = 0$ as Δ_A increases (with $\Delta_{A_3} = 0$). Case $m_0 = -17$ meV, $\Delta_B = 20$ meV, abrupt potential barriers, $L_y = 0.56$ μm.

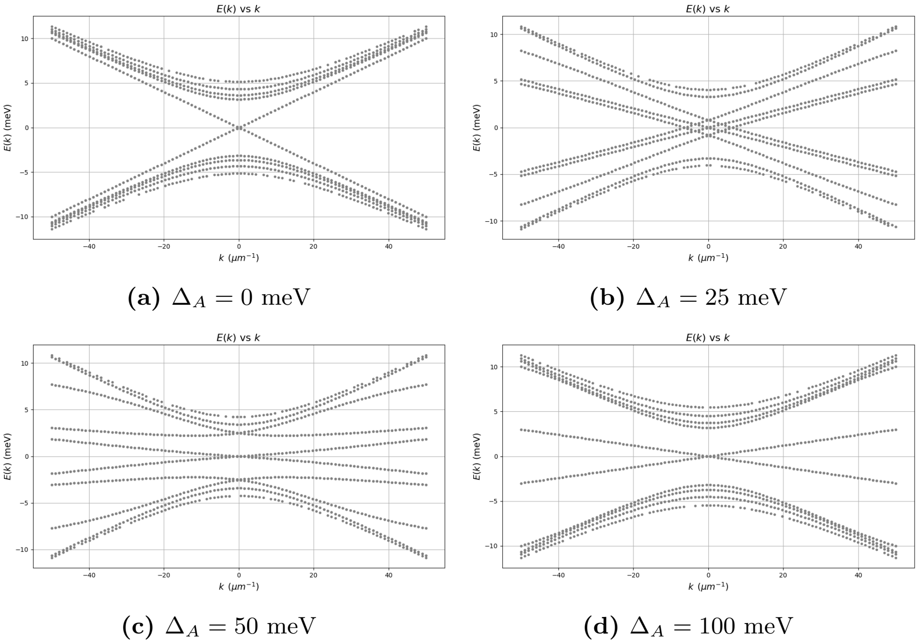

(a) $\Delta_A = 0$ meV **(b)** $\Delta_A = 25$ meV

(c) $\Delta_A = 50$ meV **(d)** $\Delta_A = 100$ meV

Figure 22: Evolution of the band structure for increasing Δ_A (with $\Delta_{A_3} = 0$). Case $m_0 = -17$ meV, $\Delta_B = 20$ meV, abrupt potential barriers, $L_y = 0.56\ \mu$m.

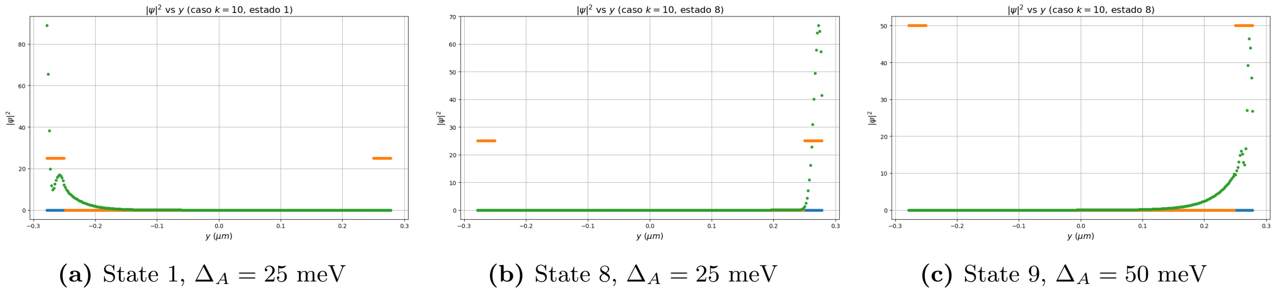

(a) State 1, $\Delta_A = 25$ meV **(b)** State 8, $\Delta_A = 25$ meV **(c)** State 9, $\Delta_A = 50$ meV

Figure 23: Probability-density distributions along y for selected states under the non-uniform potential (Δ_A, with $\Delta_{A_3} = 0$). Case $m_0 = -17$ meV, $\Delta_B = 20$ meV, abrupt potential barriers, $L_y = 0.56\ \mu$m.

For $L_y = 0.52\,\mu$m we again observe the same sequence: from `HHH-` to `BHB-` already at moderate barrier height. At $\Delta_A = 25$ meV there are four states at the box edge; at $\Delta_A = 50$ meV one of the "B" branches displays a very small slope and the bulk bands develop noticeable curvature. We also detect four intermediate (hybridized) states between box and barrier edges in addition to four box-edge states. At $\Delta_A = 100$ meV the system enters the `AHA-` regime. See Figs. 24, 25 and 26 for details.

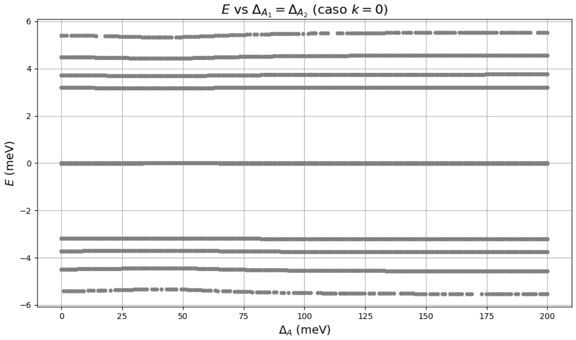

Figure 24: Energy-gap behaviour at $k = 0$ as Δ_A increases (with $\Delta_{A_3} = 0$). Case $m_0 = -17$ meV, $\Delta_B = 20$ meV, abrupt potential barriers, $L_y = 0.52\ \mu$m.

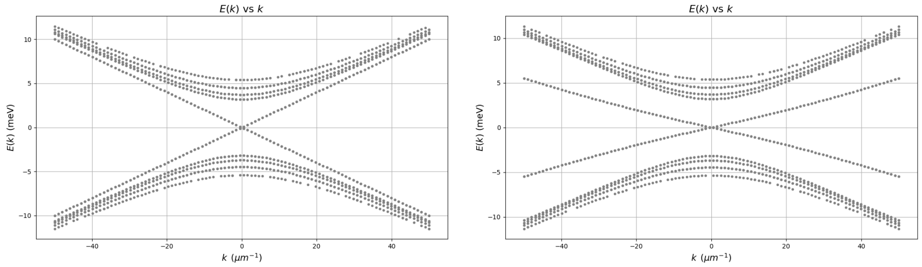

(a) $\Delta_A = 0$ meV **(b)** $\Delta_A = 25$ meV

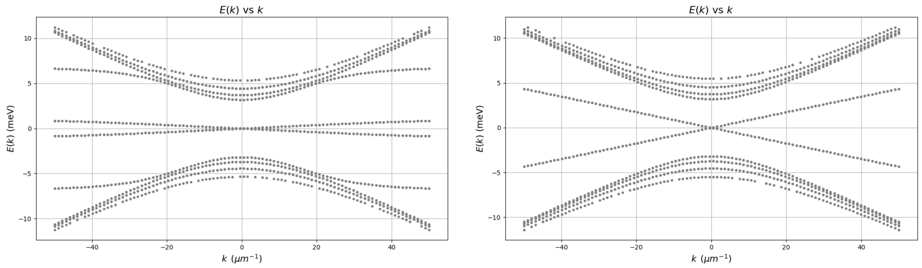

(c) $\Delta_A = 50$ meV **(d)** $\Delta_A = 100$ meV

Figure 25: Evolution of the band structure for increasing Δ_A (with $\Delta_{A_3} = 0$). Case $m_0 = -17$ meV, $\Delta_B = 20$ meV, abrupt potential barriers, $L_y = 0.52$ μm.

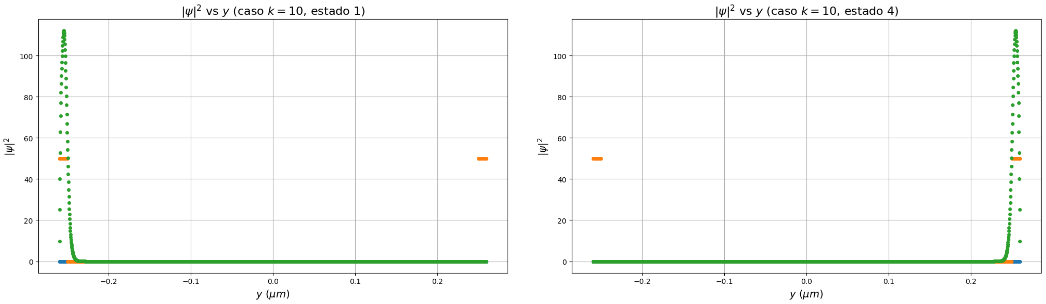

(a) State 1, $\Delta_A = 50$ meV. **(b)** State 4, $\Delta_A = 50$ meV.

Figure 26: Probability-density distributions along y for selected states under the non-uniform potential (Δ_A, with $\Delta_{A_3} = 0$). Case $m_0 = -17$ meV, $\Delta_B = 20$ meV, abrupt potential barriers, $L_y = 0.52$ μm.

Finally, we consider the quantum-spin-Hall (QSH) region obtained for $\Delta_B = 0$ meV and $m_0 < 0$. In our implementation we introduced a parameter `RIC` that switches the Rashba-like term $\alpha\,[p_x\sigma_y - p_y\sigma_x]\,\lambda_z$ on (`RIC`=1.0) or off (`RIC`=0.0). Keeping `RIC`=1.0 reproduces the same Hamiltonian used above, while `RIC`=0.0 may remove more components than intended and thus produce an anomalous phenomenology.

When $\Delta_B = 0$ meV, $m_0 = -17$ meV, $L_y = 0.75$ μm and `RIC`=0.0 the phenomenology appears unusual (possibly because some spin–orbit terms were effectively suppressed); representative band and state panels are shown in Figs. 27, 28 and 29.

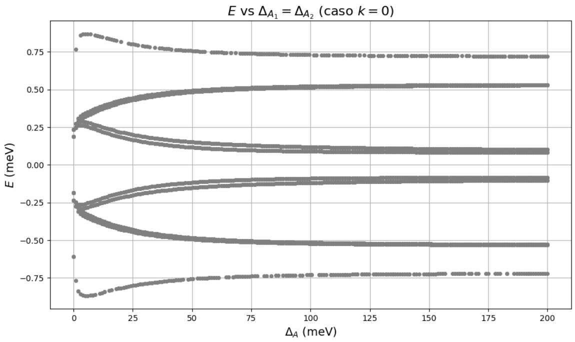

Figure 27: Energy gap closing at $k = 0$ as Δ_A increases (with $\Delta_{A_3} = 0$). Case $m_0 = -17$ meV, $\Delta_B = 0$ meV, abrupt potential barriers, $L_y = 0.75\ \mu$m, `RIC`=0.0.

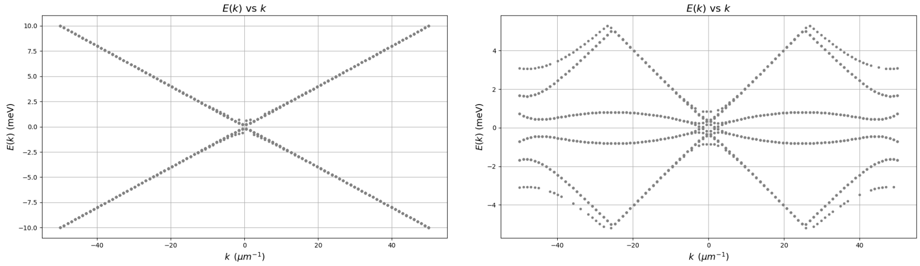

(a) $\Delta_A = 0$ meV **(b)** $\Delta_A = 10$ meV

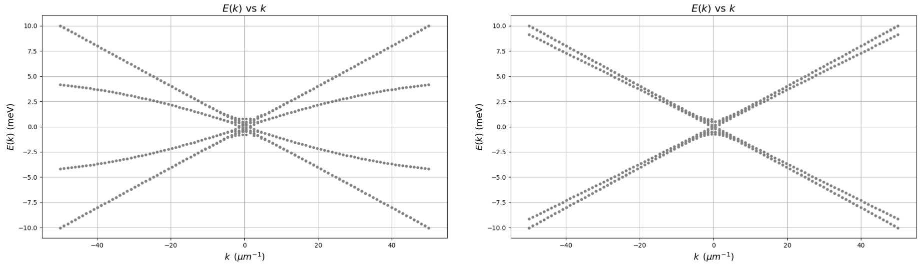

(c) $\Delta_A = 25$ meV **(d)** $\Delta_A = 100$ meV

Figure 28: Evolution of the band structure for increasing Δ_A (with $\Delta_{A_3} = 0$). Case $m_0 = -17$ meV, $\Delta_B = 0$ meV, abrupt potential barriers, $L_y = 0.75\ \mu$m, `RIC`=0.0.

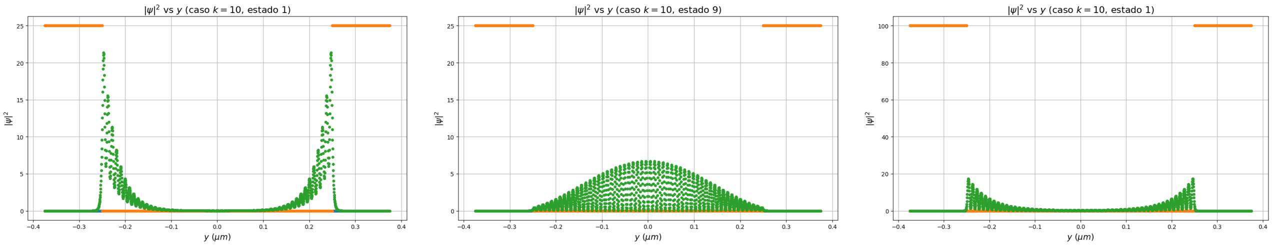

(a) State 1, $\Delta_A = 25$ meV **(b)** State 9, $\Delta_A = 25$ meV **(c)** State 1, $\Delta_A = 100$ meV

Figure 29: Probability-density distributions along y for selected states under the non-uniform potential (Δ_A, with $\Delta_{A_3} = 0$). Case $m_0 = -17$ meV, $\Delta_B = 0$ meV, abrupt potential barriers, $L_y = 0.75\ \mu$m, `RIC`=0.0.

When $\Delta_B = 0$ meV, $m_0 = -17$ meV, $L_y = 0.75\ \mu$m and `RIC`=1.0 the system shows the expected QSH-like phenomenology. The system initially resides in a phase we label `SSS-` ($\Delta_A = 0$ meV); states appear in pairs localized at the box boundaries (eight states in total). As the barrier height increases (for example at $\Delta_A = 25$ meV) the slope of the "S" branches decreases and the spectrum develops paired states peaking between barriers and box edges as well as paired states with two peaks. At $\Delta_A = 50$ meV the "S"-branch slope is further reduced and bulk-band separations change noticeably. When the barrier height exceeds the critical potential $V_c \approx 67.33$ meV, the system undergoes a transition to an `ASA-` configuration; at $\Delta_A = 100$ meV the `ASA-` phase is characterized by eight paired states at the barrier edges associated to the central S region. These features are illustrated in Figs. 30, 31 and 32.

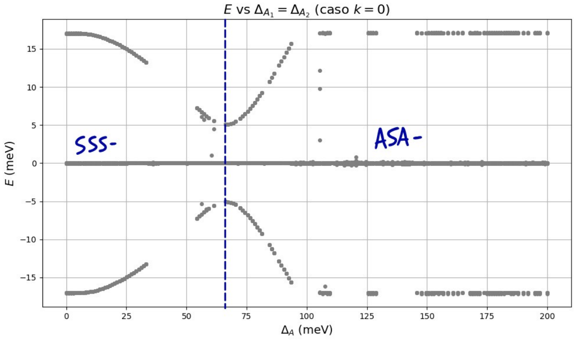

Figure 30: Energy gap closing at $k = 0$ as Δ_A increases (with $\Delta_{A_3} = 0$). Case $m_0 = -17$ meV, $\Delta_B = 0$ meV, abrupt potential barriers, $L_y = 0.75$ μm, `RIC`=1.0.

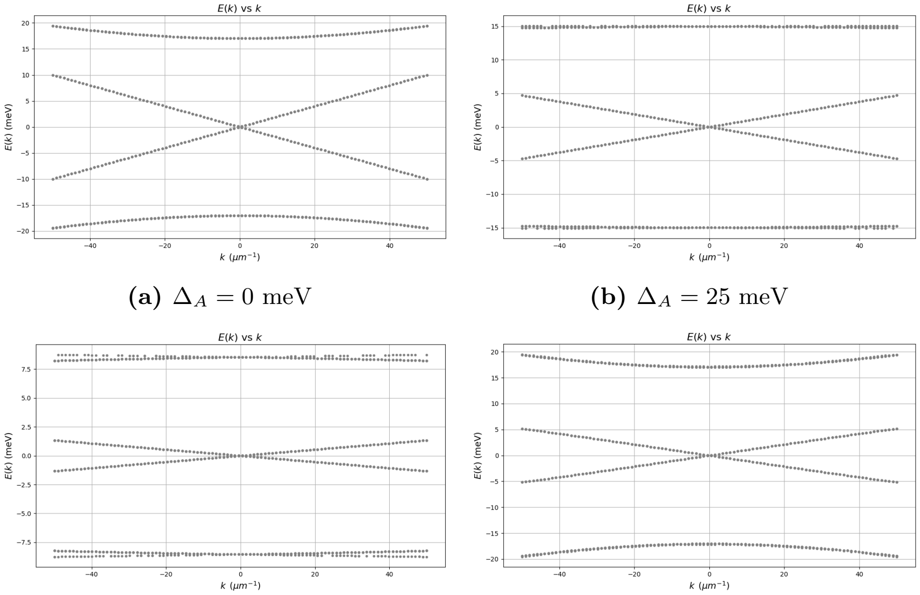

(a) $\Delta_A = 0$ meV

(b) $\Delta_A = 25$ meV

(c) $\Delta_A = 50$ meV

(d) $\Delta_A = 100$ meV

Figure 31: Evolution of the band structure for increasing Δ_A (with $\Delta_{A_3} = 0$). Case $m_0 = -17$ meV, $\Delta_B = 0$ meV, abrupt potential barriers, $L_y = 0.75$ μm, `RIC`=1.0.

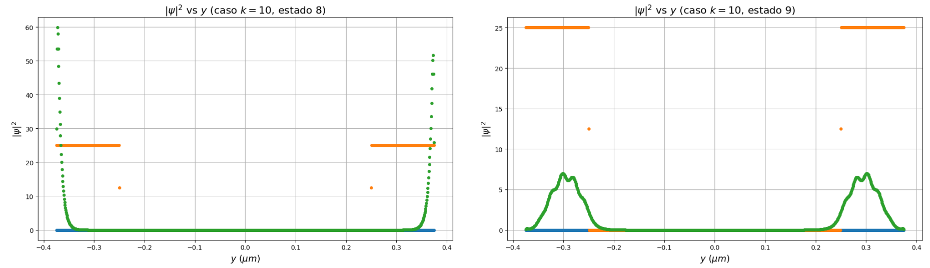

(a) State 8, $\Delta_A = 25$ meV **(b)** State 9, $\Delta_A = 25$ meV

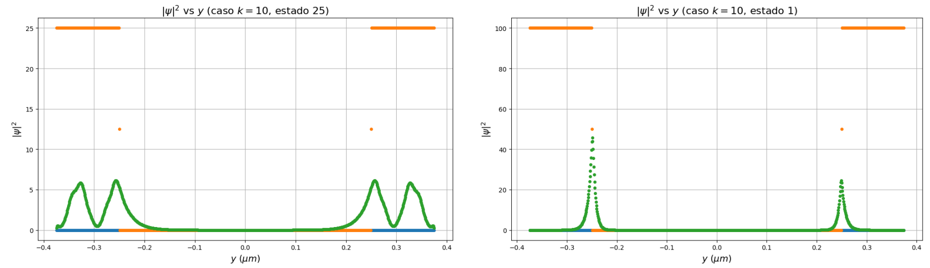

(c) State 25, $\Delta_A = 25$ meV **(d)** State 1, $\Delta_A = 100$ meV

Figure 32: Probability-density distributions along y for selected states under the non-uniform potential (Δ_A, with $\Delta_{A_3} = 0$). Case $m_0 = -17$ meV, $\Delta_B = 0$ meV, abrupt potential barriers, $L_y = 0.75$ meV, `RIC`=1.0.

We also explored the effect of increasing the box length to $L_y = 1.5\,\mu$m with `RIC`=1.0 in order to mitigate finite-size effects and better characterize transitions between QSH and NI A phases. For this larger box we performed sweeps in Δ_B at fixed $\Delta_A = 25$ meV and observed that a small sweep of Δ_B between 0 and 1 meV does not produce a clear transition at $k = 0$. A larger sweep in Δ_B (0 to 30 meV) was used to track band closures at $k = 0$ for the `SSS-` to `ASA-` transition. With $\Delta_B = 0$ meV we observe eight paired edge states at the box boundaries; states above these (starting around state 9) are bulk-like and confined by the barriers, and they appear in pairs. When Δ_B is increased to 0.1 meV (close to the B boundary) these bulk-confined states cease to appear in pairs and become single; the same behavior is observed for $\Delta_B = 1$ meV. The gap and band-structure sweeps and selected state profiles are presented in Figs. 33, 34 and 35.

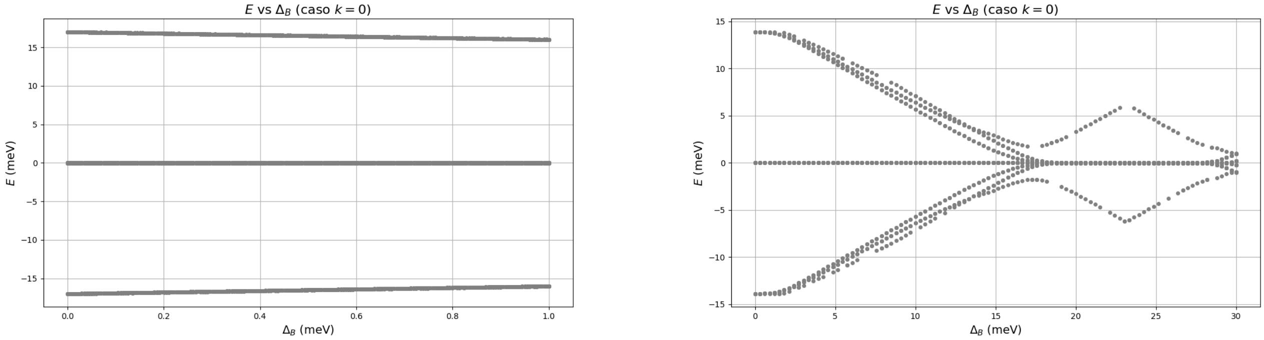

(a) Energy gap behaviour for $k = 0$ as Δ_B varies between 0 and 1 (no clear closing observed)

(b) Energy gap closing for $k = 0$ as Δ_B varies between 0 and 30 (closure relevant for `SSS-`$\rightarrow$`ASA-`)

Figure 33: Energy-gap evolution at $k = 0$ as Δ_B varies. Case $m_0 = -17$ meV, abrupt potential barriers, $L_y = 1.5$ μm, `RIC`=1.0.

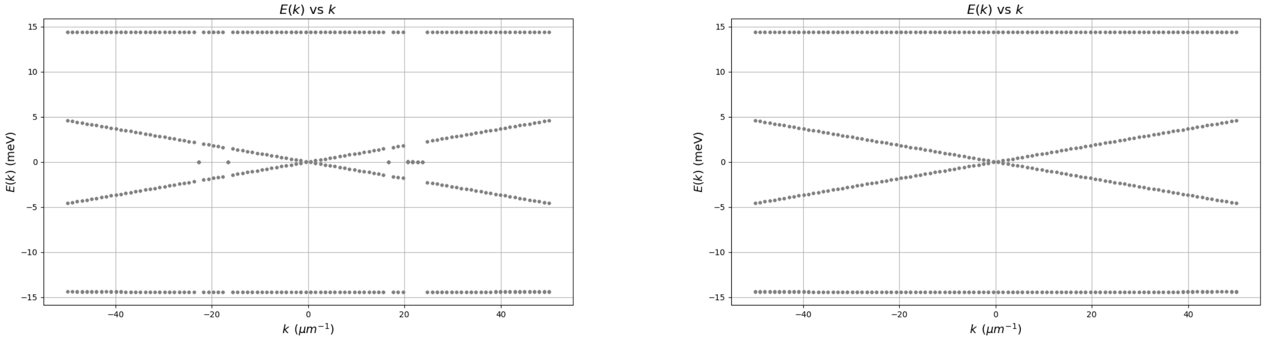

(a) $\Delta_A = 25$ meV, $\Delta_B = 0$ **(b)** $\Delta_A = 25$ meV, $\Delta_B = 0.1$ meV

Figure 34: Band-structure evolution for fixed $\Delta_A = 25$ meV (with $\Delta_{A_3} = 0$) as Δ_B increases. Case $m_0 = -17$ meV, abrupt potential barriers, $L_y = 1.5$ μm, `RIC`=1.0.

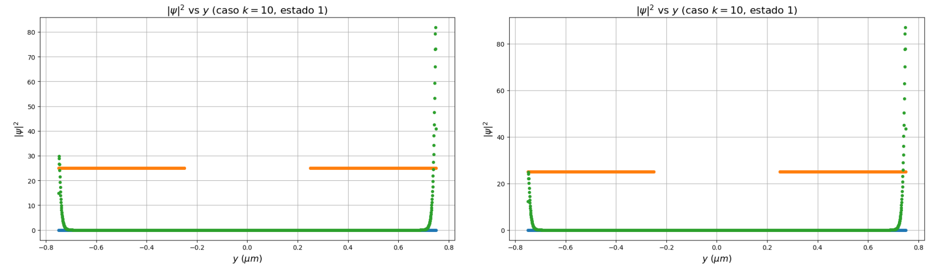

(a) State 1, $\Delta_B = 0$, $\Delta_A = 25$ meV **(b)** State 1, $\Delta_B = 0.1$ meV, $\Delta_A = 25$ meV

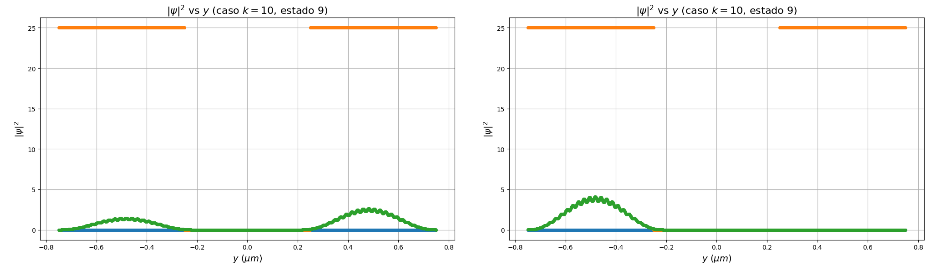

(c) State 9, $\Delta_B = 0$, $\Delta_A = 25$ meV **(d)** State 9, $\Delta_B = 0.1$ meV, $\Delta_A = 100$ meV

Figure 35: Probability-density distributions along y for selected states under different values of Δ_B. Case $m_0 = -17$ meV, variable $\Delta_A = 25$, abrupt potential barriers, $L_y = 1.5$ μm, `RIC`=1.0.

3.6.2 Smoothing parameter 0.0125 μm

In this subsection we study the formation of edge states when the applied potential barriers are smooth (smoothing parameter = 0.0125 μm). In this configuration the potential reaches its maximum (which we denote as before Δ_A) at the lateral boundaries and decays smoothly toward zero ($\Delta_{A_3} = 0$) in the central region, which produces coexistence regions between central and lateral domains. In figure 40 can be seen the shape of the smooth potential. The principal difference with the abrupt-barrier case appears in the edge-state spectrum: smooth barriers may support in-gap edge states inside the coexistence region, while abrupt barriers typically do not.

We first consider $m_0 > 0$ with $\Delta_B > m_0$ to analyze how different barrier heights in the central and lateral regions favor the coexistence of distinct phases. For $\Delta_B = 20$ meV, $m_0 = +17$ meV and $L_y = 0.75\,\mu$m, the system evolves from the `HHH+` phase ($\Delta_A = 0$ meV) into the `AHA+` phase ($\Delta_A = 50, 100$ meV) as the smooth potential increases. At the transition point the slope of the "H" branches and the bulk bands change; once inside the `AHA+` regime the bulk spectrum becomes essentially insensitive to further increases of the potential height. This behaviour is shown in Fig. 36.

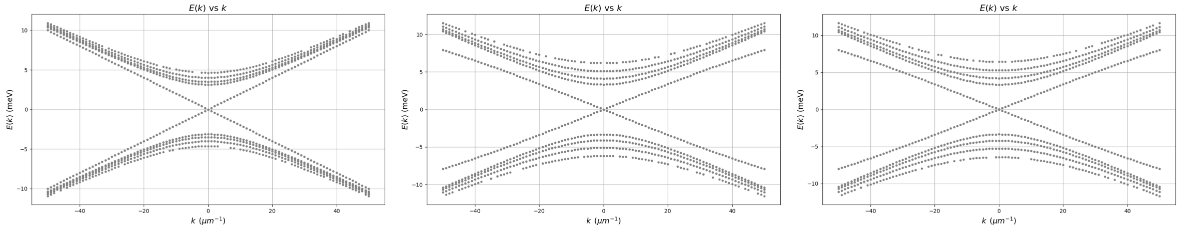

(a) $\Delta_A = 0$ meV **(b)** $\Delta_A = 50$ meV **(c)** $\Delta_A = 100$ meV

Figure 36: Evolution of the bulk band structure as a function of the non-uniform electrostatic potential expressed as Δ_A (with $\Delta_{A_3} = 0$). Parameters: $m_0 = +17$ meV, $\Delta_B = 20$ meV, smooth potential barriers.

Next we consider $m_0 > 0$ with Δ_B extremely small to probe coexistence within the `A` family. For $\Delta_B = 0.001$ meV, $m_0 = +17$ meV and $L_y = 0.75\,\mu$m the system remains in the `AAA+` phase irrespective of the barrier height; representative band structures for $\Delta_A = 0$ meV and $\Delta_A = 100$ meV are shown in Fig. 37.

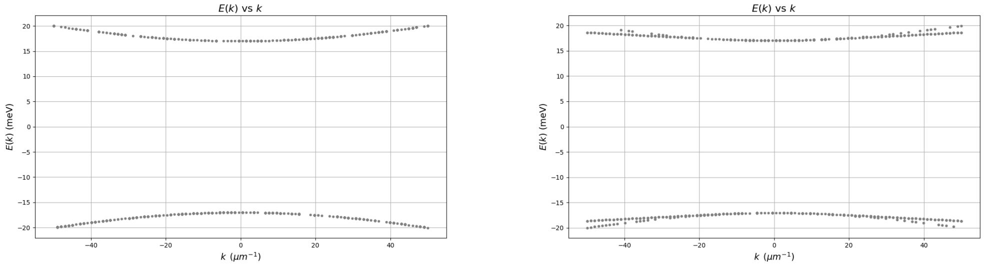

(a) $\Delta_A = 0$ meV **(b)** $\Delta_A = 100$ meV

Figure 37: Bulk band structure for $\Delta_B = 0.001$ meV, $m_0 = +17$ meV and smooth potential barriers. The system remains in the `AAA+` phase for both (a) $\Delta_A = 0$ meV and (b) $\Delta_A = 100$ meV.

We now turn to $m_0 < 0$ with $\Delta_B = 20$ meV and $L_y = 0.75\,\mu$m to study the sequence of transitions produced by the smooth potential and the coexistence of `A`, `H` and `B` phases. As Δ_A increases the system moves from `HHH-` ($\Delta_A = 0$ meV) to `BHB-` ($\Delta_A = 50$ meV): the "H" branches retain an approximately constant slope while the "B" branches gradually change with the potential. In the `BHB-` regime (for example at $\Delta_A = 50$ meV) we observe eight states associated with phase `B` localized near the slab boundaries and four states associated with phase `H` localized near the potential barriers. Further increase of Δ_A drives the system into an `AHA-` configuration ($\Delta_A = 200$ meV) where anticrossings appear; barrier-localized states in this regime are influenced by finite-size hybridization, as evidenced by band anticrossings and also the influence of the smooth potential. The gap closing and selected band/state panels are shown in Figs. 38, 39 and 40.

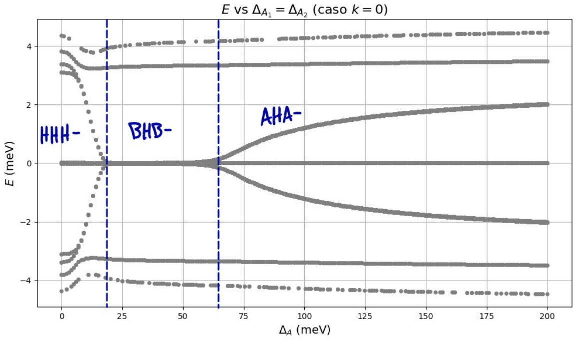

Figure 38: Energy-gap closing at $k = 0$ as Δ_A increases (with $\Delta_{A_3} = 0$). Case $m_0 = -17$ meV, $\Delta_B = 20$ meV, smooth potential barriers.

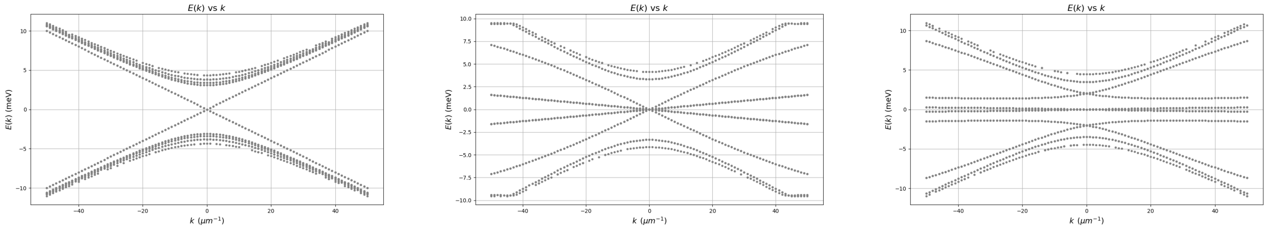

(a) $\Delta_A = 0$ meV **(b)** $\Delta_A = 50$ meV **(c)** $\Delta_A = 200$ meV

Figure 39: Evolution of the band structure for increasing Δ_A (with $\Delta_{A_3} = 0$). Case $m_0 = -17$ meV, $\Delta_B = 20$ meV, smooth potential barriers.

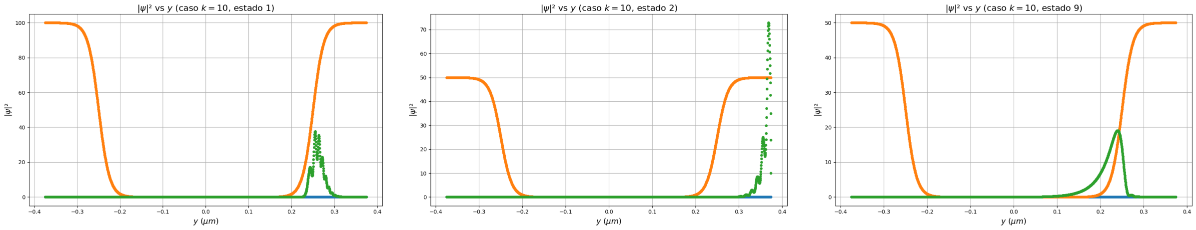

(a) State 1, $\Delta_A = 10$ meV **(b)** State 2, $\Delta_A = 50$ meV **(c)** State 9, $\Delta_A = 50$ meV

Figure 40: Probability-density distributions along y for selected states under smooth potential barriers. Case $m_0 = -17$ meV, $\Delta_B = 20$ meV.

4 Conclusions

The present study suggests that electrostatic gates can be effectively employed to induce confinement in the system, providing a versatile and tunable mechanism to manipulate its electronic properties. By carefully adjusting the electrostatic potential, we can drive phase transitions between the *Normal Insulator B* (NI B), *Normal Insulator A* (NI A), *Quantum Anomalous Hall* (QAH), and *Quantum Spin Hall* (QSH) phases, thus enabling precise control over the system's topological behavior.

In particular, for the NI B phase, the slope of the Dirac cones exhibits a systematic dependence on the applied electrostatic potential both in the case of slab with uniform gating as in non uniform gating, offering an additional pathway to engineer the band structure and its dispersion relations, while in the other phases this behavior is not so significant. In non uniform gating configurations, distinct topological phases can coexist within the same device. Owing to finite-size effects, these phases may interact, giving rise to phenomena such as anticrossing or hybridization between edge states when the characteristic dimensions are reduced. The use of abrupt or smooth potential barriers has different effects on these phenomena. These findings highlight the potential of electrostatic engineering as a robust approach for tailoring both bulk and edge properties in topological systems.

On the other hand, it has been observed that in the cases of the NI B and QSH phases, the edge states remain confined to the potential boundaries, whereas the edge states corresponding to QAH tend to move towards the boundaries of the box, which seems to indicate that they are not affected by the application of the potential.

Suggestions for future researches: a) role of asymmetric potential gatings, b) edge gating and superconductivity (chiral Majorana modes). Ultimately, these advances may pave the way toward novel device architectures that harness the interplay of confinement, topology, and superconductivity for next-generation quantum technologies.

Acknowledgments

This work was supported by the SURF@IFISC fellowship, which provided both the opportunity and the resources to carry out this research. I would like to express my deepest gratitude to Javier Osca and Llorenç Serra for their invaluable supervision, guidance, and patience throughout the entire month of July. Their expertise and constructive feedback have greatly enriched this work and my understanding of the subject. I am also grateful to Daniel Ruiz and Manuel Matias for coordinating the SURF@IFISC fellowship program and for providing the framework that made this project possible.

Appendix

A Analytical determination of phase boundaries

We consider the effective Hamiltonian

$$\mathcal{H} = \left[m_0 + m_1(k_x^2 + k_y^2)\right]\lambda_x + \alpha\big(k_x\sigma_y - k_y\sigma_x\big)\lambda_z + \Delta_B\,\sigma_z + V\,\lambda_z, \tag{A.1}$$

where from now on the electrostatic potential is assumed uniform, $V_d(y) = V$. To determine the phase boundaries we solve the condition

$$\det \mathcal{H}(\mathbf{k}) = 0, \tag{A.2}$$

following the approach of Wang and Zhang [24].

A.1 Block structure and reduction to a 2×2 problem

Working in the λ_z basis ($\lambda_z = \mathrm{diag}(1, -1)$, λ_x off-diagonal), the Hamiltonian can be written in 2×2 block form (each block acts on spin space):

$$\mathcal{H}(\mathbf{k}) = \begin{pmatrix} D(\mathbf{k}) + \Delta_B\sigma_z & m(\mathbf{k})\,\mathbb{I}_2 \\ m(\mathbf{k})\,\mathbb{I}_2 & -D(\mathbf{k}) + \Delta_B\sigma_z \end{pmatrix}, \tag{A.3}$$

where we defined

$$m(\mathbf{k}) \equiv m_0 + m_1 k^2, \qquad k^2 \equiv k_x^2 + k_y^2, \tag{A.4}$$

and

$$D(\mathbf{k}) \equiv V\,\mathbb{I}_2 + \alpha\big(k_x\sigma_y - k_y\sigma_x\big). \tag{A.5}$$

For this block matrix, with the off-diagonal blocks proportional to the 2×2 identity, the determinant condition reduces to

$$\det\Big[(D + \Delta_B\sigma_z)(-D + \Delta_B\sigma_z) - m(\mathbf{k})^2\mathbb{I}_2\Big] = 0. \tag{A.6}$$

A.2 Explicit scalar equation

Using Pauli matrix identities, $\sigma_i\sigma_j = \delta_{ij}\mathbb{I} + i\epsilon_{ijk}\sigma_k$, and $(k_x\sigma_y - k_y\sigma_x)^2 = k^2\mathbb{I}$, the determinant condition becomes a scalar equation for k^2:

$$\Big(\Delta_B^2 - m(\mathbf{k})^2 - V^2 - \alpha^2 k^2\Big)^2 - 4\alpha^2 k^2\big(V^2 - \Delta_B^2\big) = 0. \tag{A.7}$$

For given parameters $(m_0, m_1, \alpha, \Delta_B, V)$, real non-negative solutions $k^2 \geq 0$ of Eq. (A.7) indicate bulk gap closings and hence phase boundaries.

A.3 Γ-point ($k = 0$) boundaries

Setting $k = 0$ in Eq. (A.7) yields

$$\big(\Delta_B^2 - m_0^2 - V^2\big)^2 = 0 \quad\Longrightarrow\quad \boxed{\Delta_B^2 = m_0^2 + V^2}. \tag{A.8}$$

This closed-form relation links the Zeeman term Δ_B, the uniform potential V, and the mass parameter m_0. It describes topological transitions at the Brillouin-zone center.

A.4 Finite-k band closings

Because $m(\mathbf{k}) = m_0 + m_1 k^2$, Eq. (A.7) becomes a quartic equation in $x \equiv k^2$:

$$\left[\Delta_B^2 - (m_0 + m_1 x)^2 - V^2 - \alpha^2 x\right]^2 - 4\alpha^2 x\big(V^2 - \Delta_B^2\big) = 0. \tag{A.9}$$

Real, non-negative roots $x \geq 0$ correspond to finite-momentum gap closings (ring- or off-Γ transitions), giving additional phase boundaries beyond the Γ-point condition.

A.5 Application to $m_0 = 17$ and $m_0 = -17$

- The Γ-point condition $\Delta_B^2 = m_0^2 + V^2$ provides a quick estimate of the first transition.
- If $\Delta_B^2 < V^2$ or the quartic has positive x solutions, the gap closing occurs at finite k.
- For $m_0 = 17$ and $m_0 = -17$, Eq. (A.7) applies in both cases; differences arise from how the quartic roots satisfy the condition as V and Δ_B vary.

A.6 Remarks

1. Eq. (A.7) is the working analytic condition for phase boundaries in the uniform potential case.
2. Phase diagrams are usually obtained by: (i) evaluating the Γ-point condition analytically, and (ii) solving the quartic in $x = k^2$ numerically to find finite-k closings.
3. This methodology follows Wang and Zhang [24] for related models of tunable magnetism in magnetic topological insulators.

B Detailed Derivation of the Dirac Cone Slope Dependence

We start from the eigenvalues of the Hamiltonian, given by:

$$
\begin{aligned}
E = \Big\{ & -\sqrt{(m_0 + (k_x^2 + k_y^2)m_1)^2 + M_z^2 + V^2 + (k_x^2 + k_y^2)\alpha^2} \\
& \quad - 2\sqrt{M_z^2\left[(m_0 + (k_x^2 + k_y^2)m_1)^2 + V^2\right] + (k_x^2 + k_y^2)V^2\alpha^2}, \\
& \sqrt{(m_0 + (k_x^2 + k_y^2)m_1)^2 + M_z^2 + V^2 + (k_x^2 + k_y^2)\alpha^2} \\
& \quad - 2\sqrt{M_z^2\left[(m_0 + (k_x^2 + k_y^2)m_1)^2 + V^2\right] + (k_x^2 + k_y^2)V^2\alpha^2}, \\
& -\sqrt{(m_0 + (k_x^2 + k_y^2)m_1)^2 + M_z^2 + V^2 + (k_x^2 + k_y^2)\alpha^2} \\
& \quad + 2\sqrt{M_z^2\left[(m_0 + (k_x^2 + k_y^2)m_1)^2 + V^2\right] + (k_x^2 + k_y^2)V^2\alpha^2}, \\
& \sqrt{(m_0 + (k_x^2 + k_y^2)m_1)^2 + M_z^2 + V^2 + (k_x^2 + k_y^2)\alpha^2} \\
& \quad + 2\sqrt{M_z^2\left[(m_0 + (k_x^2 + k_y^2)m_1)^2 + V^2\right] + (k_x^2 + k_y^2)V^2\alpha^2} \Big\}.
\end{aligned}
\tag{B.1}
$$

The critical potential V_c separating the NI B and NI A phases is obtained from the boundary condition:

$$V_c = \sqrt{M_z^2 - \frac{m_0}{m_1}\alpha^2}. \tag{B.2}$$

Fixing $k_y = 0$, the momentum k_x at the transition satisfies:

$$k = \sqrt{\frac{V^2 - M_z^2}{\alpha^2}}. \tag{B.3}$$

We define the smallest positive eigenenergy along $k_y = 0$ as:

$$E_q(k_x) = \sqrt{(m_0 + k_x^2 m_1)^2 + M_z^2 + V^2 + k_x^2\alpha^2 - 2\sqrt{M_z^2\left[(m_0 + k_x^2 m_1)^2 + V^2\right] + k_x^2 V^2\alpha^2}}. \tag{B.4}$$

The slope m of the Dirac cone is then defined as:

$$m = \frac{E_q(k_x)}{k_x}. \tag{B.5}$$

Substituting k_x from the critical momentum condition and simplifying, we obtain the explicit dependence of the slope on the applied potential:

$$m(V) = \frac{\sqrt{2V^2 - 2\sqrt{V^4 + M_z^2\left[m_0 + \frac{m_1(-M_z^2+V^2)}{\alpha^2}\right]^2} + \left[m_0 + \frac{m_1(-M_z^2+V^2)}{\alpha^2}\right]^2}}{\sqrt{\frac{-M_z^2+V^2}{\alpha^2}}}. \tag{B.6}$$

This analytical expression quantitatively captures the non-linear variation of the Dirac cone slope with the electrostatic potential, explicitly showing its dependence on the system parameters M_z, m_0, m_1, and α.

References

[1] N. W. Ashcroft and N. D. Mermin, *Solid State Physics*, Holt, Rinehart and Winston (1976).

[2] C. Kittel, *Introduction to Solid State Physics*, Wiley (2004).

[3] J. M. Ziman, *Principles of the Theory of Solids*, Cambridge University Press (1972).

[4] P. Y. Yu and M. Cardona, *Fundamentals of Semiconductors*, Springer (2010).

[5] K. v. Klitzing, G. Dorda, and M. Pepper, *New method for high-accuracy determination of the fine-structure constant based on quantized Hall resistance*, Phys. Rev. Lett. **45**, 494 (1980).

[6] D. C. Tsui, H. L. Stormer, and A. C. Gossard, *Two-dimensional magnetotransport in the extreme quantum limit*, Phys. Rev. Lett. **48**, 1559 (1982).

[7] B. I. Halperin, *Quantized Hall conductance, current-carrying edge states, and the existence of extended states in a two-dimensional disordered potential*, Phys. Rev. B **25**, 2185 (1982).

[8] R. B. Laughlin, *Quantized Hall conductivity in two dimensions*, Phys. Rev. B **23**, 5632 (1981).

[9] D. J. Thouless, M. Kohmoto, M. P. Nightingale, and M. den Nijs, *Quantized Hall conductance in a two-dimensional periodic potential*, Phys. Rev. Lett. **49**, 405 (1982).

[10] C. L. Kane and E. J. Mele, $\mathbb{Z}_2$ *topological order and the quantum spin Hall effect*, Phys. Rev. Lett. **95**, 146802 (2005).

[11] C. L. Kane and E. J. Mele, *Quantum spin Hall effect in graphene*, Phys. Rev. Lett. **95**, 226801 (2005).

[12] B. A. Bernevig, T. L. Hughes, and S.-C. Zhang, *Quantum spin Hall effect and topological phase transition in HgTe quantum wells*, Science **314**, 1757 (2006).

[13] M. König *et al.*, *Quantum spin Hall insulator state in HgTe quantum wells*, Science **318**, 766 (2007).

[14] M. Z. Hasan and C. L. Kane, *Colloquium: Topological insulators*, Rev. Mod. Phys. **82**, 3045 (2010).

[15] X.-L. Qi and S.-C. Zhang, *Topological insulators and superconductors*, Rev. Mod. Phys. **83**, 1057 (2011).

[16] R. Yu *et al.*, *Quantized anomalous Hall effect in magnetic topological insulators*, Science **329**, 61 (2010).

[17] C.-Z. Chang *et al.*, *Experimental observation of the quantum anomalous Hall effect in a magnetic topological insulator*, Science **340**, 167 (2013).

[18] Y. Deng *et al.*, *Quantum anomalous Hall effect in intrinsic magnetic topological insulator* $MnBi_2Te_4$, Science **367**, 895 (2020).

[19] Y. Tokura, K. Yasuda, and A. Tsukazaki, *Magnetic topological insulators*, Nature Rev. Phys. **1**, 126 (2019).

[20] L. Fu, C. L. Kane, and E. J. Mele, *Topological insulators in three dimensions*, Phys. Rev. Lett. **98**, 106803 (2007).

[21] Nobel Prize in Physics 2016, *Scientific background: Topological phase transitions and topological phases of matter*, The Royal Swedish Academy of Sciences (2016).

[22] F. D. M. Haldane, *Model for a Quantum Hall Effect without Landau Levels: Condensed-Matter Realization of the "Parity Anomaly"*, Phys. Rev. Lett. **61**, 2015 (1988).

[23] X.-L. Qi, Y.-S. Wu, and S.-C. Zhang, *Topological quantization of the spin Hall effect in two-dimensional paramagnetic semiconductors*, Phys. Rev. B **74**, 085308 (2006).

[24] J. Wang, B. Lian, H. Zhang, and S.-C. Zhang, *Electrically Tunable Magnetism in Magnetic Topological Insulators*, Phys. Rev. Lett. **115**, 036805 (2015).

Spatiotemporal dynamics of vegetation patterns

Miguel Cerdán Ortuño, Daniel Ruiz-Reynés and Damià Gomila
Instituto de Física Interdisciplinar y Sistemas Complejos, IFISC (CSIC-UIB)
Campus Universitat de les Illes Balears, E-07122 Palma de Mallorca, Spain

Abstract

It has been observed that the vegetation of an ecosystem exhibits intermediate heterogeneous states between the homogeneous occupation of a meadow and its complete depopulation. These patterns naturally arise as a result of the influence of environmental conditions on the plants and the interactions of the individuals with their adjacent neighbours. Identifying these inhomogeneities and the conditions under which they occur is key to assessing vegetation health, enabling us to identify risk factors for the ecosystem. Spatial heterogeneities have been observed both in drylands and underseas, with this work focusing on *Posidonia oceanica* in the Mediterranean Sea. The aim of this study is to build upon the work developed by Moreno-Spiegelberg et al. and analyse the influence of long-range spatial interactions in a previously studied model that did not account for the diffusion mechanism.

1 Introduction

1.1 Spatiotemporal dynamics in plant population

When the conditions in an ecosystem are extremely favourable for the growth of a particular plant species, it will spread across the entire area until it homogeneously covers the surface. However, if these conditions are affected by new stress factors that compromise the health of the vegetation, the meadow does not necessarily evolve directly toward a complete depopulation. Instead, it is common to observe intermediate states of heterogeneous density that can enhance ecosystem resilience [1].

Environmental conditions such as temperature, nutrient availability, or soil composition, among others, can generate spatial heterogeneity, but these effects will not exhibit a typical length scale nor represent a mechanism of resilience. On the contrary, spatial interactions, such as those mediated by diffusion mechanisms, lead to observable inhomogeneous structures with a typical length scale and higher tolerance to environmental stressors.

Spatial self-organization enables complex systems to exhibit multistability of coexistence states. Therefore, the formation of patterns can aid ecosystems in avoiding tipping points, thereby enhancing resilience. Perturbations can be confined to a particular state of the system, preventing the disturbance from propagating throughout the system. Spatial patterns damp the effects of external changes, reducing catastrophic transitions and promoting more gradual responses [2]. Although these patterns have been extensively studied in terrestrial ecosystems, such as spiral vegetation patterns in Chilean high-altitude wetlands [3] or fairy circles in the grassy deserts of Namibia [4] and Australia [5], recent studies have expanded the research to marine environments, as is the case of *Posidonia oceanica*.

P. oceanica is the dominant endemic seagrass in the Mediterranean Sea, being a crucial hot spot of biodiversity [6]. Furthermore, it stabilizes the sediment, protects the coastline from erosion, and captures large amounts of CO_2, releasing O_2 in the process, which is vital for marine biodiversity [6]. Nevertheless, the anthropogenic pressure on the Mediterranean coastal zone has resulted in a rise of stressors, which have harmed the vegetation's health and gradually reduced the population of *P. oceanica* over the years [6]. Therefore, monitoring the behaviour of this species is crucial to safeguard the Mediterranean ecosystem. Previous studies have developed models explaining various phenomena observed in *P. oceanica*, such as the formation of fairy circles [7], the toxic effect of sulfide [8], and excitability mechanisms that enhance local vegetation resilience [1]. The aim of this work is to extend the model developed by Moreno-Spiegelberg et al. [1] by introducing a diffusive term to quantify long-range spatial interactions. In addition to reproducing the behaviours already analysed in the previous model, such as bistability and temporal oscillations, this study will investigate the conditions under which static Turing patterns can emerge.

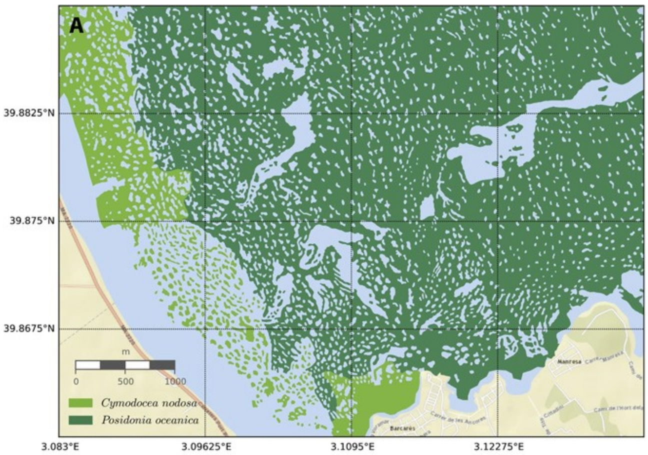

Figure 1: Vegetation patterns of *P. oceanica* and *C. nodosa* in a seagrass meadow in Pollença bay (Mallorca Island, Western Mediterranean). Side-scan image from LIFE Posidonia [7].

1.2 Theory of bifurcations

Complex systems can exhibit multiple distinct behaviours, displaying one or another depending on the state of the system, which is determined by the values of the system parameters. That is why the concept of bifurcation is key. A bifurcation is defined as a sudden and abrupt change (though not mathematically discontinuous) in the behaviour of a system [9]. To determine the total number of possible behaviours exhibited by the model, as well as their nature, it is necessary to carry out a thorough analysis to identify all the bifurcations present in the system. When the entire dynamics of a system are governed by only one parameter, the bifurcation is characterized by a specific value called the critical point. Otherwise, if the system depends on several parameters, as is the case in this work, each bifurcation of the model is characterized by a certain relation between the different parameters.

In order to understand the types of bifurcations, the concept of fixed point must be introduced. Let $f(x, y, t)$ be a function that describes the temporal evolution of a field defined over a given surface. A fixed point (x^*, y^*, t^*) of $f(x, y, t)$ is defined by the condition $f(x^*, y^*, t^*) = 0$. The location of the fixed points is a fundamental aspect of a dynamic system because nonlinear systems are usually studied by analysing small perturbations around these points. The fixed points are mainly classified as stable or unstable according to whether flow lines of the phase diagram converge or diverge at the fixed point, respectively. The nature of a fixed point can be known by the eigenvalues of the resulting Jacobian after the linearization around small perturbations.

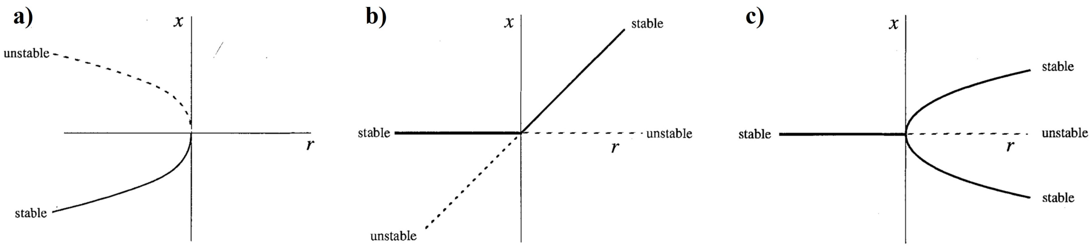

Figure 2: Bifurcations diagrams for the three principal families, in solid line the stable fixed points and in dashed line the unstable fixed points. a) Saddle-node bifurcation. b) Transcritical bifurcation. c) Supercritical pitchfork bifurcation. Picture adapted from [10].

The three main families of bifurcations are the saddle-node, the pitchfork, and the transcritical bifurcation [10]. However, this work also involves Hopf and Turing bifurcations. The saddle-node bifurcation is the basic mechanism by which fixed points are created and destroyed in pairs [10]. The pitchfork bifurcation, common in systems that have symmetry, is defined by both the change of stability of a fixed point and the creation of two new symmetric fixed points [10]. It can be supercritical (if the new fixed points are stable) or subcritical (unstable). On the other hand, if a limit cycle, a closed and periodic orbit in the phase diagram [9], emerges from the stable equilibrium point, the system undergoes a supercritical Hopf bifurcation. At this point, the system begins to oscillate periodically with time. Mathematically, Hopf bifurcation is a consequence of the change of sign from negative to positive of the real part of a complex eigenvalue of the system [10]. The transcritical bifurcation is characterized by the collision of two fixed points, exchanging their stabilities [10].

In addition, we will focus on the Turing bifurcation of the model. In reaction-diffusion models, where the substances spread across the system via a diffusion mechanism, static spatially extended patterns can appear independently of the previous state as a consequence of the self-regulating nature of the complex system [11, 12]. These heterogeneous distributions of the species are called Turing patterns. The main objective of this work is to determine the conditions under which these patterns can emerge, obtaining relationships between the parameters of the system that will characterize the Turing bifurcation.

2 Theoretical model

The theoretical model used to explain the growth and death of a plant located at a certain point of the meadow combines the effect of the feedback of contiguous vegetation and the toxin accumulation. The interaction among different individuals within the meadow can be negative, for example if they are competing for resources, or positive, as in cases where the plants cluster together to withstand external phenomena like intense marine currents. In addition, we take into account the effect of sulfides on the environment. The presence of this toxic substance is inevitable because this molecule is a byproduct of the metabolism of the *P. oceanica* [1]. There is evidence of sulfide as a mediator of spatial interactions leading to seagrass self-organization as a result of the negative allelopathic relation established between different parts of the meadow [1]. The model is constituted by a system of two partial differential equations that describes the evolution of two fields: the density of the plant population $P(x, y, t)$ and the concentration of toxins in the sediment $T(x, y, t)$ [1]

$$\partial_t P = (-\omega + \alpha P - P^2 - T)P + \nabla^2 P \tag{2.1a}$$

$$\tau \partial_t T = P - T + D_T \nabla^2 T \tag{2.1b}$$

Here, the parameters (ω, α, τ, D_T) are defined as follows: ω is the net mortality rate. It represents the balance between growth and mortality in the absence of other plants or toxins and is influenced by environmental factors. α is the ratio between positive and negative feedback, evaluating the plant's growth enhancement in response to increased local density. τ is the timescale for toxin accumulation and decay, reflecting the relative speed at which toxins are produced by plants and removed from the environment as compared to the plant growth timescale. Lastly, D_T is the ratio between the diffusion coefficient of the toxin and the diffusion coefficient of the plant. These coefficients can be related to experimental data reversing the previous normalization detailed in the *SI Appendix* of reference [1]. On the other hand, ∇^2 is the Laplacian operator that describes the spatial diffusion of both plant density and toxin concentration in sediment.

Eqs. 2.1 can be compacted with the following vector form

$$\partial_t \begin{pmatrix} P \\ T \end{pmatrix} = J \begin{pmatrix} P \\ T \end{pmatrix} \tag{2.2}$$

characterized by the Jacobian

$$J = \begin{pmatrix} -\omega + \alpha P - P^2 + \nabla^2 & -P \\ 1/\tau & (-1 + D_T \nabla^2)/\tau \end{pmatrix} \tag{2.3}$$

3 Linear stability analysis

3.1 Homogeneous steady states

In this section, we derive the homogeneous steady states of the model described by Eqs. 2.1. Hence, we impose that temporal and spatial derivatives of Eqs. 2.1 are zero. Solving the resulting conditions, we reach three fixed points (P^*): the trivial bare state $P_0 = 0$ and the populated states $P_\pm$, given by

$$P_\pm = \frac{(\alpha - 1)}{2} \pm \sqrt{\frac{(\alpha - 1)^2}{4} - \omega} \tag{3.1}$$

It should be noted that, as the density of plant population must be a real value, Eqs. 3.1 are only valid under the condition $\frac{(\alpha-1)^2}{4} \geq \omega$, marking a saddle-node bifurcation as we will describe in the following sections. In addition, it is important to mention that for homogeneous steady states, both fields exhibit the same behaviour

$$P^* = T^* \tag{3.2}$$

As we can expect, for the stable fixed point P_+ (see Fig. 3a) the plant population is high where the mortality is negative and positive feedback is elevated. Also, it can be seen that, when the mortality is positive or nearly zero, a minimum vegetation density to cross a threshold is needed for the plant growth. The bifurcation diagram (see Fig. 3b) shows how the saddle-node bifurcation marks the limit of a region of bistability, where the solutions P_+ and P_0 coexist as stable fixed points. Thus, the system can evolve into either of the two depending on the initial state. However, it should be pointed out that, although the bifurcation diagram Fig. 3b is useful because it allows us to easily understand the bistable nature of the system, it is a simplified version because it is plotted imposing $\tau = 0$, modelling a situation with direct negative feedback. Therefore, it does not take into account other behaviours, such as temporal oscillations or spatial patterns, which can affect the stability of the homogeneous solutions.

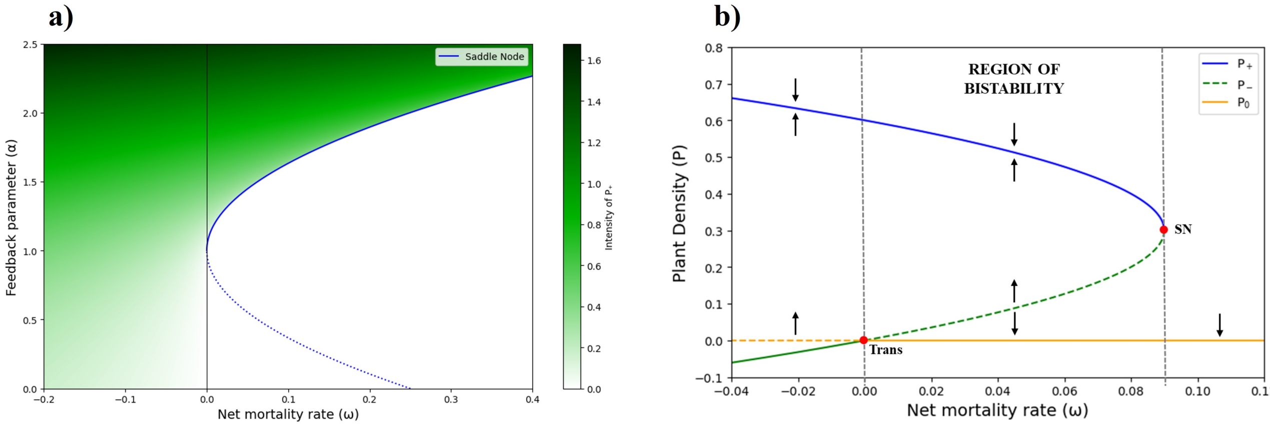

Figure 3: a) Heat map of the intensity of the stable fixed point P_+ in the phase diagram in the (ω, α) plane. The intensity of the plant density is painted in the scale from white (bare) to dark green (populated) and the red line represents the saddle-node bifurcation. b) Bifurcation diagram of Eqs. 2.1. Only solutions of the system without space (temporal system) are shown for $\alpha = 1.6$ and $\tau = 0$, corresponding to the case of a system with direct negative feedback. Solid (dashed) lines represent stable (unstable) solutions. Labelled dots indicate bifurcation points for saddle-node (**SN**) and transcritical (**Trans**) bifurcations, delimiting the region of bistability, where both P_+ and P_0 coexist as stable solutions. The arrows indicate the flow lines of the diagram, showing toward which fixed point the system would evolve from a given state.

3.2 Linearization and temporal evolution

In order to understand the dynamics of the systems, we analyse the behaviour of the fields via linearization around the steady states. That is, we study small perturbations (P_p, T_p) with the form $X_p \propto e^{-i(q_x x + q_y y)}$ around the fixed points (P^*, T^*). Hence, if we introduce the expressions $P(t) = P^* + P_p(t)$ and $T(t) = T^* + T_p(t)$ in Eq. 2.2 and then neglecting higher-order perturbing terms $\mathcal{O}(P_p^2, T_p^2, P_p T_p, \dots)$, the Jacobian that describes the evolution of the perturbations around the bare solution S_0 is

$$J_{S_0} = \begin{pmatrix} -\omega - q^2 & 0 \\ 1/\tau & -(1 + q^2 D_T)/\tau \end{pmatrix} \tag{3.3}$$

where $q^2 = q_x^2 + q_y^2$. For the nontrivial steady states $S_\pm$, the Jacobian is

$$J_{S_\pm} = \begin{pmatrix} (\alpha P_\pm - P_\pm^2) - q^2 & -P_\pm \\ 1/\tau & -(1 + q^2 D_T)/\tau \end{pmatrix} \tag{3.4}$$

3.3 Local bifurcation analysis

3.3.1 Eigenvalues of the system

In order to study the stability of the homogeneous steady states, we must diagonalize the Jacobians and evaluate the resulting eigenvalues. We focus the study on the populated $P_\pm$ solution; thus, the eigenvalues of the Jacobian described by the Eq. 3.4 satisfy the condition:

$$\lambda^2 - \lambda\left[(-q^2 + \alpha P_\pm - 2P_\pm^2) - (1 + q^2 D_T)/\tau\right] - \left[(1 + q^2 D_T)/\tau \cdot (-q^2 + \alpha P_\pm - 2P_\pm^2) - P_\pm/\tau\right] = 0 \tag{3.5}$$

The expression can be simplified by defining the functions

$$\xi = -q^2 + \alpha P_\pm - 2P_\pm^2 \tag{3.6a}$$

$$\zeta = -(1 + q^2 D_T)/\tau \tag{3.6b}$$

so Eq. 3.5 is rewritten as

$$\lambda^2 - \lambda(\xi + \zeta) + (\xi \cdot \zeta + P_\pm/\tau) = 0 \tag{3.7}$$

Solving the quadratic equation, the eigenvalues are

$$\lambda_\pm = \frac{\xi + \zeta}{2} \pm \sqrt{\frac{(\xi + \zeta)^2}{4} - (\xi \cdot \zeta + P_\pm/\tau)} \tag{3.8}$$

3.3.2 Bifurcations

Analysing the dispersion relation, we found the appearance conditions for several bifurcations. As we mentioned before, the plant density must be a real value, so a saddle-node bifurcation appears when

$$\omega_{SN} = \frac{(\alpha - 1)^2}{4} \tag{3.9}$$

The bifurcation is of the type saddle-node because, at this point, the solutions P_+ and P_- become equal due to the root term vanishes and both fixed points are annihilated, as $P_\pm$ do not exist for further values of mortality ω.

On the other hand, a Hopf bifurcation is found by imposing $\mathrm{Re}(\lambda_\pm) = 0$ (with $\mathrm{Im}(\lambda_\pm) \neq 0$). If we look at the quadratic expression of Eq. 3.7, with form $\lambda^2 + B\lambda + C = 0$, the condition is equivalent to impose $B = 0$. That is

$$\xi + \zeta = 0 \tag{3.10}$$

Introducing the definitions of the functions and organizing the terms, the condition of the Hopf Bifurcation for the mode q is

$$(-q^2 + \alpha P_+ - 2P_+^2) - (1 + q^2 D_T)/\tau = 0 \tag{3.11}$$

which is only valid for P_+ solution. For the case $q = 0$, the condition is simplified as

$$\alpha P_+ - 2P_+^2 - \tau^{-1} = 0 \tag{3.12}$$

bringing back the results of previous works [1].

Lastly, the Turing bifurcation is defined by a certain value q_c characterized by the conditions $\left.\frac{\mathrm{d}\lambda}{\mathrm{d}q}\right|_{q_c} = 0$ and $\lambda(q_c) = 0$ (see Fig. 4). In terms of the quadratic expression of Eq. 3.7, these conditions are equivalent to $\left.\frac{\mathrm{d}C}{\mathrm{d}q}\right|_{q_c} = 0$. Applying this relation, q_c is defined by

$$q_c^2 = \left(\alpha P_+ - 2P_+^2 - \frac{1}{D_T}\right) \tag{3.13}$$

In order to write the expression as a function of α, we introduce the Eq. 3.13 in the quadratic expression, reaching the condition of $C(q_c) = 0$. Ordering the terms, this condition is written as

$$\alpha = 2P_\pm + \frac{1}{P_\pm D_T}\left(-1 + \sqrt{4P_\pm D_T}\right) \tag{3.14}$$

It should be noted that, as q_c must be real, $q_c^2 > 0$ must also be satisfied. Thus, if we combine Eq. 3.13 and Eq. 3.14 under this condition, the Turing patterns only appear if the following condition also occurs

$$D_T > \frac{1}{P_\pm} \tag{3.15}$$

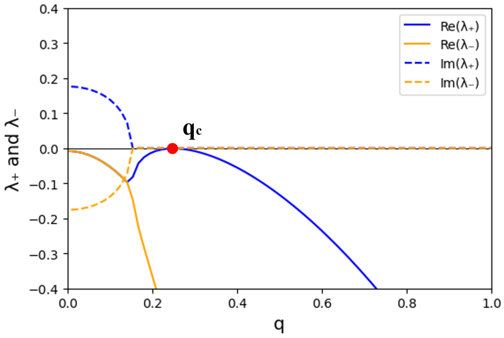

Figure 4: Eigenvalues of the Jacobian $J_{S_\pm}$ calculated with the dispersion relation Eq. 3.8 for a constituent point of the Turing bifurcation. The red dot marks the q_c.

This expression implies that there must be a minimum value of the coefficient D_T for the pattern to form, but as the population $P_\pm$ increases, this minimum value becomes less restrictive. For regions with small values of $P_\pm$, the diffusion coefficient of the toxin must be much larger than the one for plant density, due to D_T being normalized as $D_T = \frac{D_{Toxin}}{D_{Plant}}$.

3.3.3 Codimension-n bifurcations

The point where Hopf and saddle-node bifurcations collide in the (ω, α) plane is called the Takens-Bogdanov codimension-2 bifurcation. It is determined by imposing both conditions, or equivalently, by substituting Eq. 3.9 into Eq. 3.11, which yields the expression

$$\frac{1}{\tau} = \frac{\frac{\alpha+1}{2} - q^2}{1 + q^2 D_T} \tag{3.16}$$

for the mode q of perturbation. Simplifying for the mode $q = 0$, the point is at the values $(\omega, \alpha) = (\tau^{-2}, 2\tau^{-1} + 1)$. Furthermore, a Takens-Bogdanov-Turing codimension-3 bifurcation is found if we introduce Eq. 3.9 into Eq. 3.14. This point shows up at $(\omega, \alpha, D_T) = (\tau^{-2}, 2\tau^{-1} + 1, \tau)$.

In what follows, except for the last section of results, we use a value of $\tau = 6.25$ (see Fig. 5.a), which corresponds to the dynamics observed in real meadows [1]. For illustrative purposes, we use parameter values that simplify the analysis. Therefore, a value of $D_T = 50$ is used, although it is possibly slightly overestimated.

For the last section, focused on the dynamics near the Takens-Bogdanov-Turing codimension-3 bifurcation, we use a value of $\tau = 20$ (see Fig. 5.b) in order to increase the space between the different bifurcations and achieve distinguishable regions, despite the value being far from a realistic physical condition.

4 Results and discussion

4.1 Numerical methods and initial conditions

For all the spatiotemporal simulations performed, the calculations were run using the pseudo-spectral method described by Montagne et al. [13]. The simulations were carried out using two different types of initial conditions: the homogeneous stable solution P_+ and a Gaussian function. Using P_+ as the initial condition, we examined the stability of this solution under certain system conditions, verifying whether it remains stable, with the system persisting in the same state, or becomes unstable, thereby exhibiting new behaviours. From an ecological perspective, this initial condition can be understood as a populated meadow whose environment has moved to the state described by the new system parameters. Consequently, the vegetation will evolve to adapt to this new state, this last stage being what is observed in the simulation.

On the other hand, the Gaussian function generates a sharp population spike that is highly concentrated at the centre of the simulated surface. This can be interpreted as bare soil where a small patch of *P. oceanica* has been planted with the aim of repopulating a specific region. In this way, we can analyse how such a cultivation would evolve, providing insight into which regions would be more favourable for this hypothetical repopulation. Regardless of the initial conditions, a background noise of $P_{Noise} = 0.001$ was introduced to more accurately reproduce the real environment and observe how unstable states evolve.

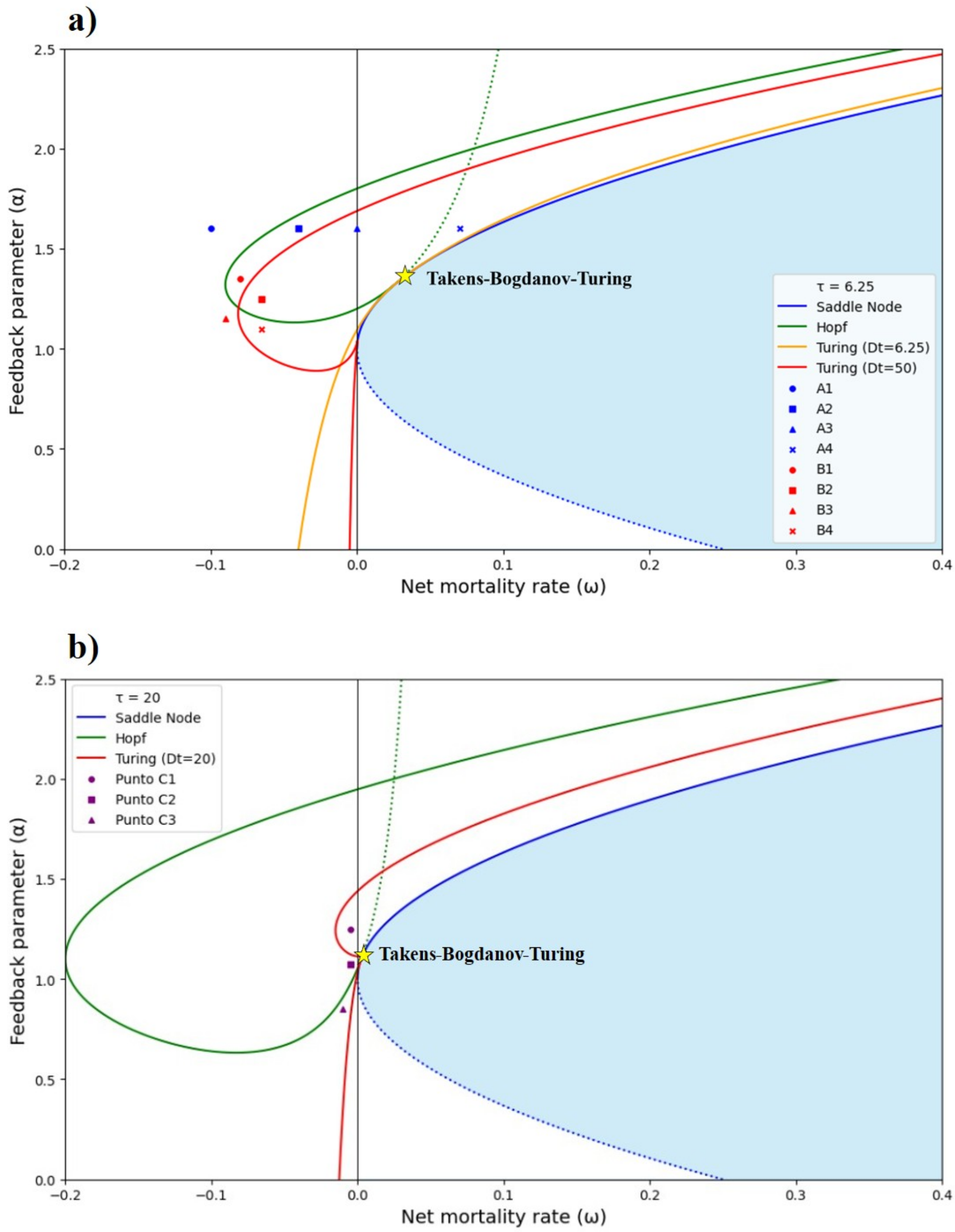

Figure 5: Phase diagrams in the (ω, α) plane for: a) $\tau = 6.25$ and b) $\tau = 20$. Saddle-node bifurcation (blue line), Hopf bifurcation (green line) and several Turing bifurcations are represented. Painted in light blue the zone limited by the saddle-node, where there is no solution for the plant density. The dotted line represents the bifurcation for the P_- in the case of the Hopf, and the negative solution in the case of the saddle-node. In addition, the points simulated are represented in two groups different groups, with which the discussion of results will be organized. Lastly, the Takens-Bogdanov-Turing codimension-3 bifurcation is represented with a yellow star.

4.2 Effect of rising mortality under constant feedback

In this section, we carried out a set of simulations over a range of mortality values, considering ω as the main control parameter while keeping the remaining parameters fixed at values of $(\alpha, D_T, \tau) = (1.6, 50, 6.25)$. The points selected for this analysis correspond to the so-called group A, which can be observed in the phase diagram Fig. 5.a.

For point A1 defined by $\omega = -0.1$ (see Fig. 6), it was observed that the homogeneous steady solution is stable and the system converges to P_+ regardless of the initial condition. This final state is a result of the dispersion relation and the value of the eigenvalues, whose real part is negative for all modes of perturbation q ($\text{Re}\{\lambda_\pm(q)\} < 0 \quad \forall q$), hence the disturbances are suppressed with time and the system remains in the fixed point. The simulation with the Gaussian functions exhibits a short transient stage where the initial spike grows and eventually extends over the entire surface (see Fig. 7).

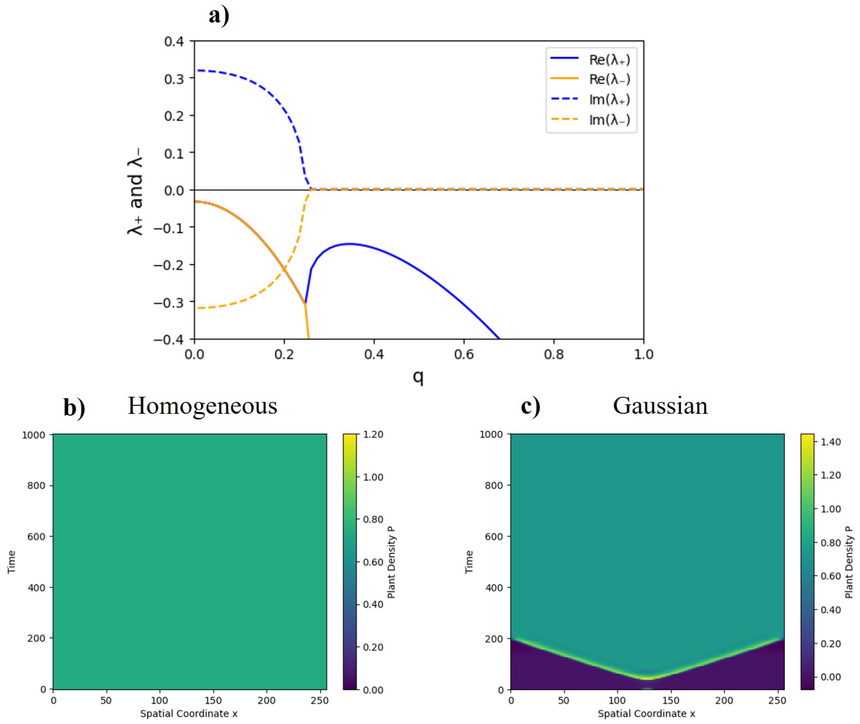

Figure 6: Results of the simulations performed at the point A1 $(\omega, \alpha, D_T) = (-0.1, 1.6, 50)$ with $\tau = 6.25$. a) Eigenvalues of the Jacobian $J_{S_\pm}$ calculated with the dispersion relation Eq. 3.8. b) and c) Spatiotemporal evolution of the pattern at half height $(y = 128)$ for homogeneous steady solution P_+ and Gaussian function as initial conditions, respectively.

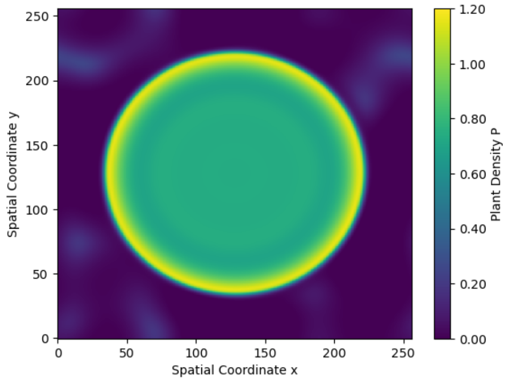

Figure 7: Transient state of the initial spike generated with the Gaussian function propagating across the surface before covering the entire area.

For point A2 defined by $\omega = -0.04$ (see Fig. 8), the system initially adopts a homogeneous density in space, which slowly starts exhibiting the characteristic periodic temporal oscillations of a system that has undergone a Hopf bifurcation. This behaviour is expected looking at the dispersion relation, where we can see that all the active modes $(\mathrm{Re}\{\lambda_\pm(q)\} > 0)$ are complex eigenvalues, causing the imaginary part to generate the temporal oscillations. However, after a certain time, the oscillations are damped and a negative hexagon pattern begins to form (see Fig. 9.a), creating depopulated gaps. Although the final state of the Gaussian simulation is not exactly the same pattern, the system was slowly evolving toward the final state observed with the homogeneous initial condition. The formation of this pattern may be due to the subcritical nature of the Turing bifurcation.

Point A3, defined by $\omega = 0$ (see Fig. 10), is the first one to exhibit different final states according to their initial condition. When P_+ is used as initial condition, the behaviour is similar to the point A2, omitting the temporal oscillations and emerging directly the same negative hexagon pattern shown by A2 (see Fig. 9.b). The only difference between the two patterns is the size of the gaps, which are wider for A3 than for A2, probably a result of its higher mortality. The straightforward formation of these patterns reinforces the idea that the modes responsible for the Turing patterns ($\mathrm{Re}\{\lambda_\pm(q)\} > 0$ and $\mathrm{Im}\{\lambda_\pm(q)\} = 0$) govern the system's dynamics, since in A3 no spatial oscillations are observed despite being predicted by the dispersion relation. On the other hand, the simulation performed with the Gaussian function quickly converges to the bare state, which is a stable fixed point at this mortality. The spike of population is not resilient enough and the plant density tends toward zero indefinitely. Although this is not the behaviour predicted by the dispersion relation, it should be recalled that the model was derived under the assumption of small perturbations around the fixed point, which is $P_+ = 0.6$ for A3. Therefore, the predictions may fail if the initial condition differs significantly from this state, as is the case here.

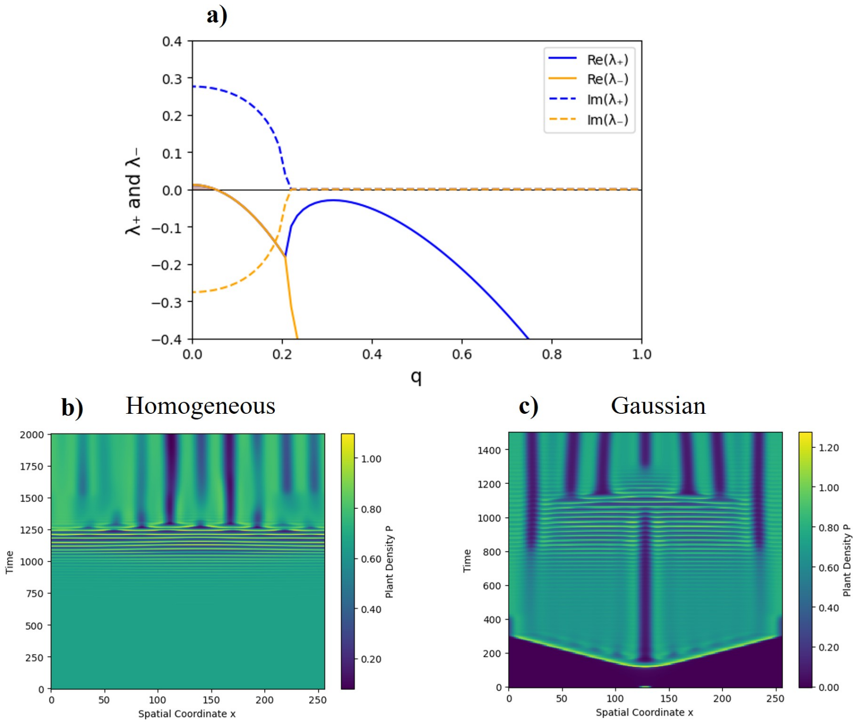

Figure 8: Results of the simulations performed at the point A2 $(\omega, \alpha, D_T) = (-0.04, 1.6, 50)$ with $\tau = 6.25$. a) Eigenvalues of the Jacobian $J_{S_\pm}$ calculated with the dispersion relation Eq. 3.8. b) and c) Spatiotemporal evolution of the pattern at half height ($y = 128$) for homogeneous steady solution P_+ and Gaussian function as initial conditions, respectively.

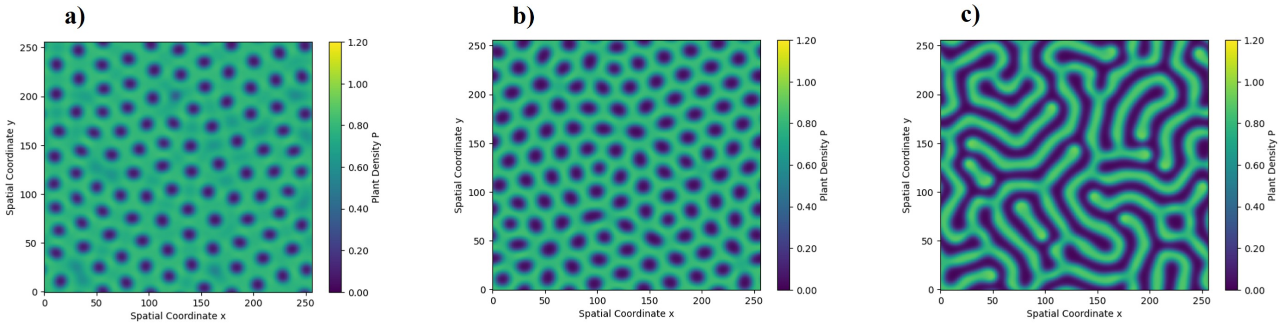

Figure 9: Spatial patterns of the final state exhibited by the spatiotemporal simulations of the group A points. a) and b) Negative hexagon patterns for points A2 ($\omega = -0.04$) and A3 ($\omega = 0$), respectively. c) Complex Turing pattern of point A4 ($\omega = 0.07$).

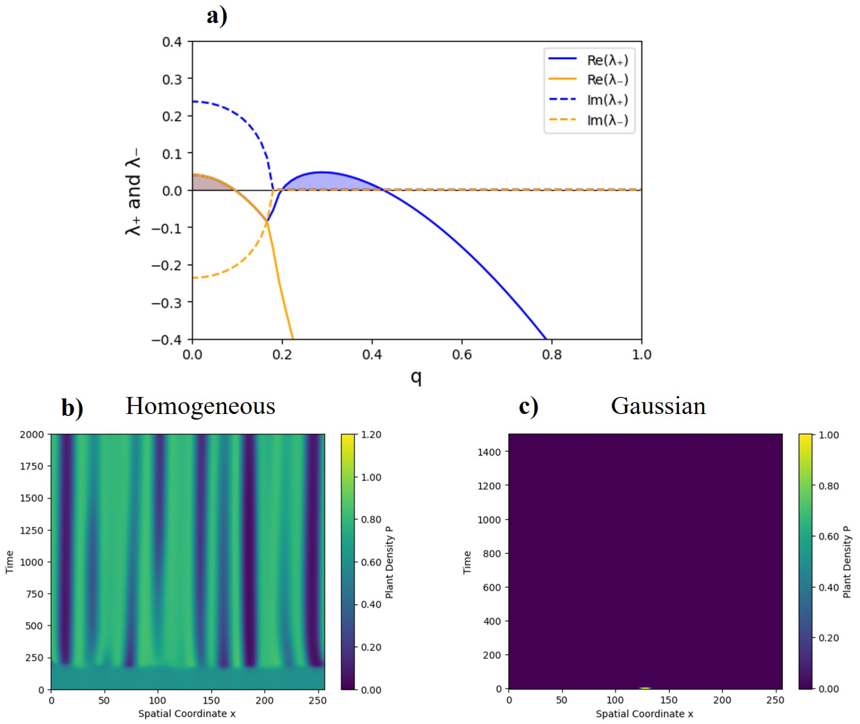

Figure 10: Results of the simulations performed at the point A3 $(\omega, \alpha, D_T) = (0, 1.6, 50)$ with $\tau = 6.25$. a) Eigenvalues of the Jacobian $J_{S_\pm}$ calculated with the dispersion relation Eq. 3.8. b) and c) Spatiotemporal evolution of the pattern at half height ($y = 128$) for homogeneous steady solution P_+ and Gaussian function as initial conditions, respectively.

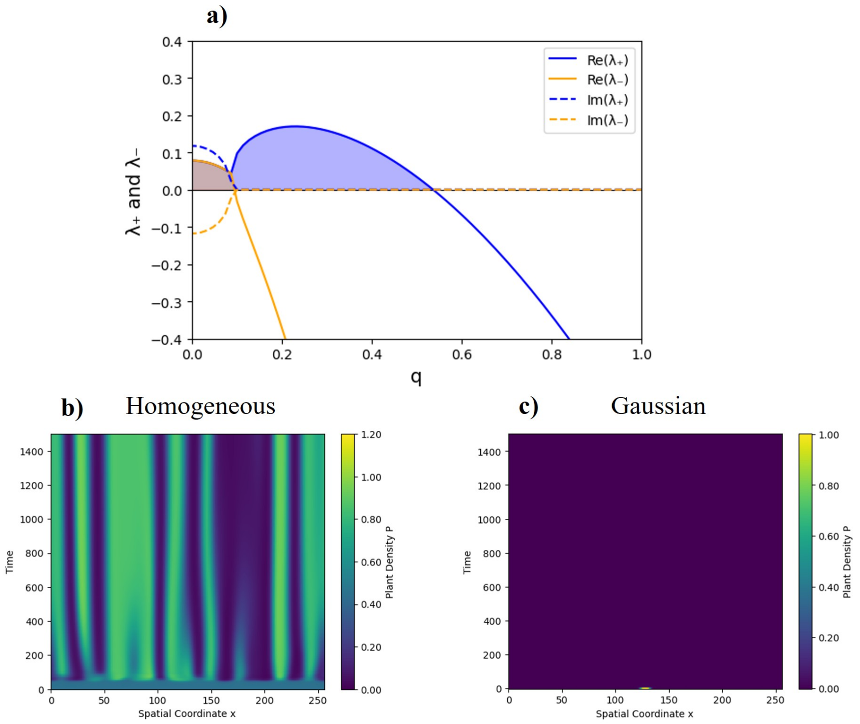

Figure 11: Results of the simulations performed at the point A4 $(\omega, \alpha, D_T) = (0.07, 1.6, 50)$ with $\tau = 6.25$. a) Eigenvalues of the Jacobian $J_{S_\pm}$ calculated with the dispersion relation Eq. 3.8. b) and c) Spatiotemporal evolution of the pattern at half height ($y = 128$) for homogeneous steady solution P_+ and Gaussian function as initial conditions, respectively.

Lastly, point A4 ($\omega = 0.07$) can be interpreted as an extreme case of point A3. Once again, the simulation with the Gaussian initial condition converges to the bare state (see Fig. 11). On the other hand, when P_+ is used as the initial condition, the direct formation of the Turing pattern is observed, without oscillations. Although the resulting pattern appears very different from those observed previously (see Fig. 9.c), it is likely that the new structures are an evolution of the negative hexagonal pattern. Since mortality is higher than in cases A2 and A3, the gaps are expected to widen further. Being slightly irregular, they expand more in some directions than in others, which may cause two gaps to grow sufficiently in a given direction to collide and generate the irregular stripes between vegetated and bare regions observed in the final pattern.

4.3 Analysis of the Hopf-Turing transition zone

In this section, we analyse four points near the intersection of the Hopf and Turing bifurcations. The points selected for this analysis correspond to the so-called group B, which can be observed in the phase diagram Fig. 5.a.

In the case of point B1 (see Fig. 12), characterized by the parameters $(\omega, \alpha) = (-0.08, 1.35)$, we observe that the behaviour differs slightly depending on the initial condition. The dispersion relation indicates that soft temporal oscillations should occur, a phenomenon observed in both cases. However, only the simulation with the Gaussian function exhibits the same spatial pattern previously observed in the points of group A, since in the case of P_+ as the initial condition the oscillations occur with a spatially homogeneous population. It should be noted that, unlike the cases simulated in group A, here the negative hexagonal pattern also oscillates in a moderate way. This phenomenon may indicate that the Turing pattern modes are not strong enough to displace the other system dynamics. Furthermore, the different final states according to the initial condition may indicate again that the Turing bifurcation is subcritical. The perturbation generated by the noise in the first case is insufficient to drive the system toward pattern formation, a situation that does occur with the Gaussian function, a state far from the equilibrium.

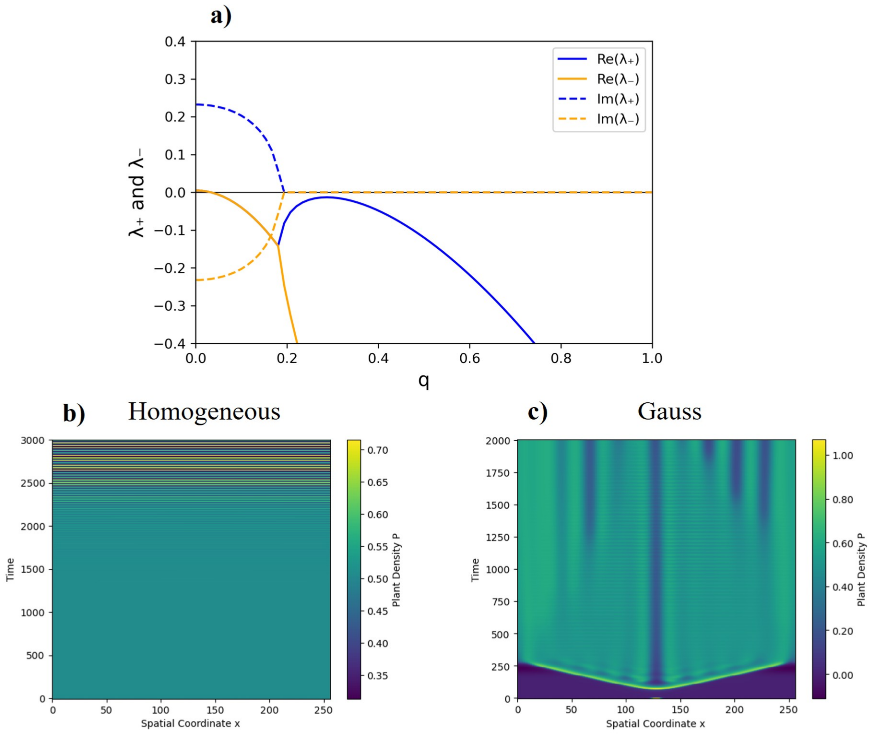

Figure 12: Results of the simulations performed at the point B1 $(\omega, \alpha, D_T) = (-0.08, 1.35, 50)$ with $\tau = 6.25$. a) Eigenvalues of the Jacobian $J_{S_\pm}$ calculated with the dispersion relation Eq. 3.8. b) and c) Spatiotemporal evolution of the pattern at half height ($y = 128$) for homogeneous steady solution P_+ and Gaussian function as initial conditions, respectively.

Both simulations at point B2 (see Fig. 14), defined by $(\omega, \alpha) = (-0.065, 1.25)$, exhibit the negative hexagon pattern as the final state. In this case, the Turing pattern dominates the system, and no significant temporal oscillations are observed in either simulation. As expected, since it has no active unstable modes, point B3 (see Fig. 15), defined by $(\omega, \alpha) = (-0.09, 1.15)$, is similar to point A1 and it converges to the homogeneous stable solution regardless of the initial condition.

Finally, point B4 (see Fig. 16), defined by $(\omega, \alpha) = (-0.065, 1.1)$, is the only one of the simulated points in this study that exhibits active Turing pattern modes without being within the oscillatory regime delimited by the Hopf bifurcation. Since the conditions are slightly more adverse than for point B2, due to the lower feedback, both simulations of this point exhibit an intermediate state between the negative hexagon pattern and the one that emerged in simulation A4 (see Fig. 13), providing further evidence that the latter is a natural and continuous evolution of the former.

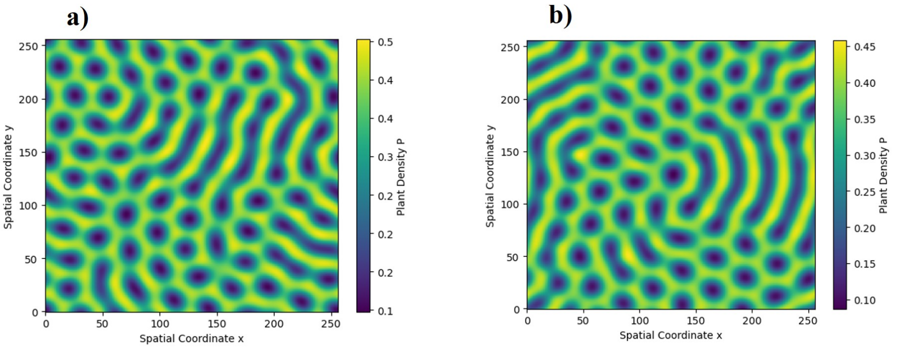

Figure 13: Spatial Turing patterns of the final state exhibited by the spatiotemporal simulations of the point B4 for different initial condition. a) Homogeneous steady solution P_+. b) Gaussian function.

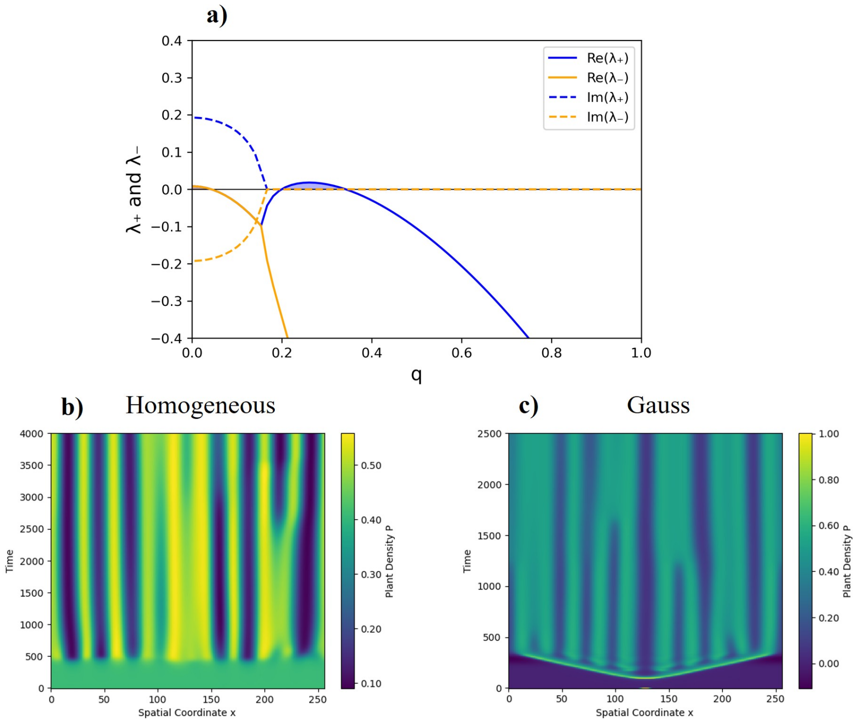

Figure 14: Results of the simulations performed at the point B2 $(\omega, \alpha, D_T) = (-0.065, 1.25, 50)$ with $\tau = 6.25$. a) Eigenvalues of the Jacobian $J_{S_\pm}$ calculated with the dispersion relation Eq. 3.8. b) and c) Spatiotemporal evolution of the pattern at half height $(y = 128)$ for homogeneous steady solution P_+ and Gaussian function as initial conditions, respectively.

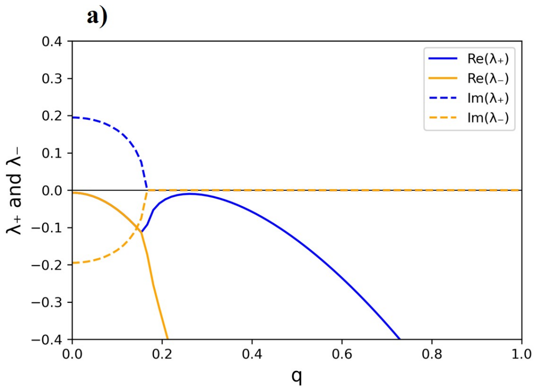

b) Homogeneous

c) Gauss

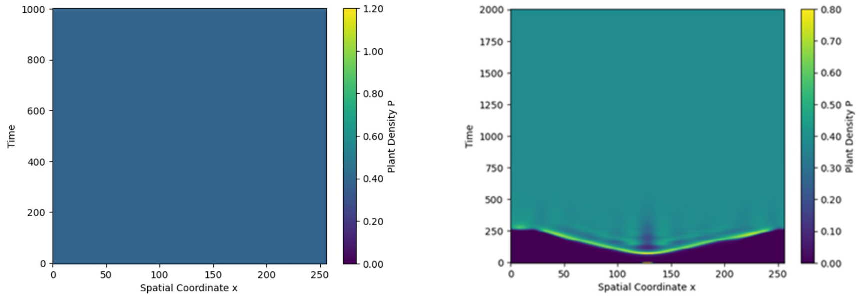

Figure 15: Results of the simulations performed at the point B3 $(\omega, \alpha, D_T) = (-0.09, 1.15, 50)$ with $\tau = 6.25$. a) Eigenvalues of the Jacobian $J_{S_\pm}$ calculated with the dispersion relation Eq. 3.8. b) and c) Spatiotemporal evolution of the pattern at half height $(y = 128)$ for homogeneous steady solution P_+ and Gaussian function as initial conditions, respectively.

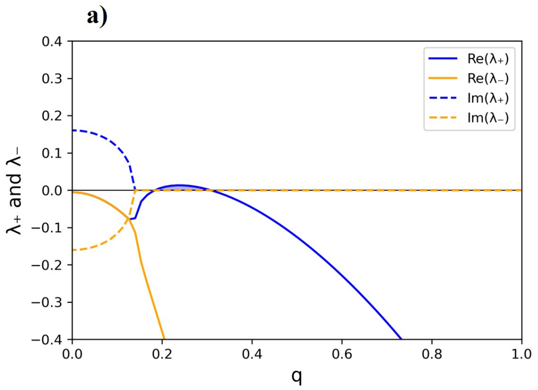

b) Homogeneous

c) Gauss

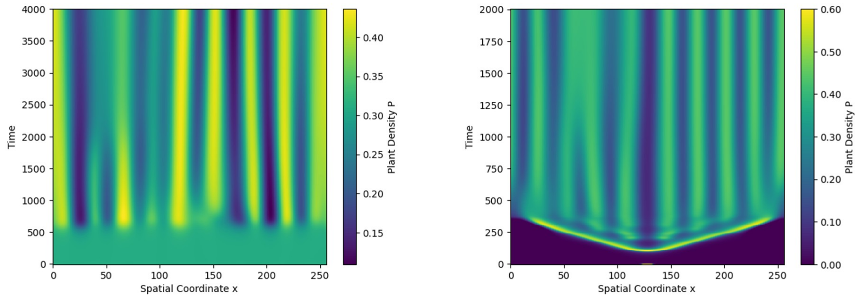

Figure 16: Results of the simulations performed at the point B4 $(\omega, \alpha, D_T) = (-0.065, 1.1, 50)$ with $\tau = 6.25$. a) Eigenvalues of the Jacobian $J_{S_\pm}$ calculated with the dispersion relation Eq. 3.8. b) and c) Spatiotemporal evolution of the pattern at half height $(y = 128)$ for homogeneous steady solution P_+ and Gaussian function as initial conditions, respectively.

4.4 Dynamics around Takens-Bogdanov-Turing codimension-3 bifurcation

In this section, we briefly study the dynamics of three points near the Takens-Bogdanov-Turing codimension-3 bifurcation for the case $\tau = 20$. The simulations carried out for this section are performed with the homogeneous steady state as the initial condition. The points selected for this analysis correspond to the so-called group C, which can be observed in the phase diagram Fig. 5.b. The simulations carried out for this section are performed with the homogeneous steady state as the initial condition.

First, it should be noted that, under the condition $D_T = \tau = 20$, the imaginary part of the eigenvalues is constant and independent of perturbation mode ($\text{Im}\{\lambda_\pm(q)\} = cte$). This is manifested in the dispersion relations (see Fig. 17). The point C3 $(\omega, \alpha) = (-0.01, 0.85)$, as it has no active modes, remains in the populated stable solution P_+ over time, as was observed for cases A1 or B3. Hence, the dynamics at this point are not addressed in detail.

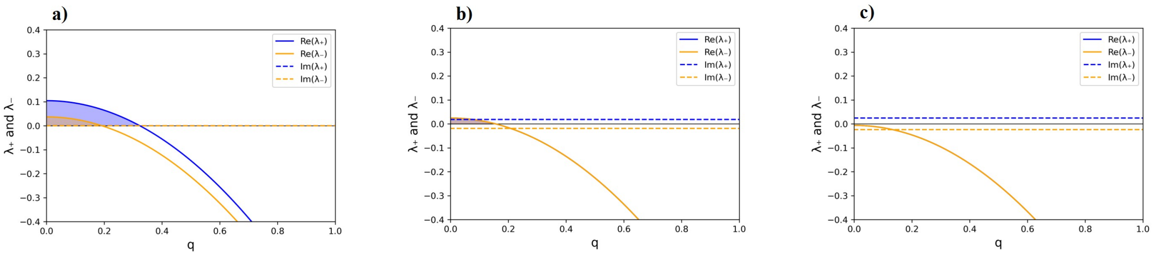

Figure 17: Dispersion relation for the points of group C simulated. a) Point C1 defined by $(\omega, \alpha) = (-0.005, 1.25)$. b) Point C2 defined by $(\omega, \alpha) = (-0.005, 1.075)$. c) Point C3 defined by $(\omega, \alpha) = (-0.01, 0.85)$.

On the other hand, the spatiotemporal evolutions for points C1 $(\omega, \alpha) = (-0.005, 1.25)$ and C2 $(\omega, \alpha) = (-0.01, 0.85)$ are presented in Fig. 18. Both plots exhibit oscillations. However, the fact that they are not completely horizontal indicates that these are not oscillations of a homogeneous population, as was observed in previous sections. In this case, the oscillations correspond to the formation and annihilation of vegetation pulses. The pulses of vegetation emerge as a result of the excitable nature of the system. The population remains at low density levels until, at a certain point, the system is excited and a pulse is generated. This pulse propagates across the space until it collides with another pulse, resulting in mutual annihilation. The conditions of C1 generate a pair of two isolated travelling waves that propagate until they collide, maintaining the system in a relatively symmetric state (see Fig. 19.a). On the other hand, under C2 parameters, the system acquires a high level of complexity, not only due to the number of pulses but also because of their shapes. However, it is worth noting that, in all cases, the origin of the pulses remains fixed at the same location. Hence, the symmetric pattern observed in the spatiotemporal diagrams of Fig. 18.

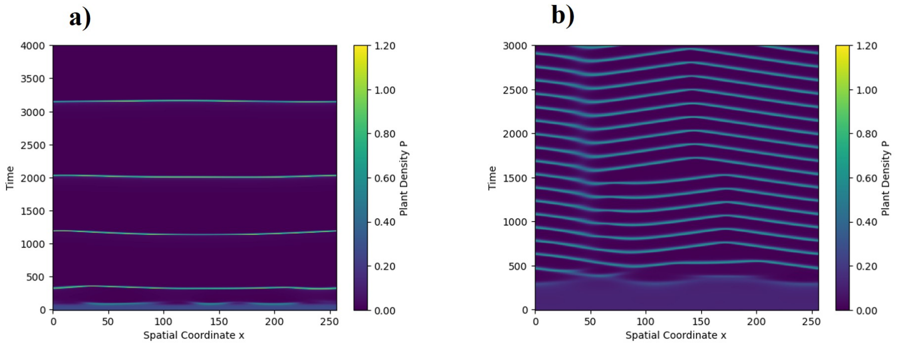

Figure 18: Spatiotemporal evolution of the pattern at half height ($y = 128$) for: a) Point C1 defined by $(\omega, \alpha) = (-0.005, 1.25)$ and b) Point C2 defined by $(\omega, \alpha) = (-0.005, 1.075)$.

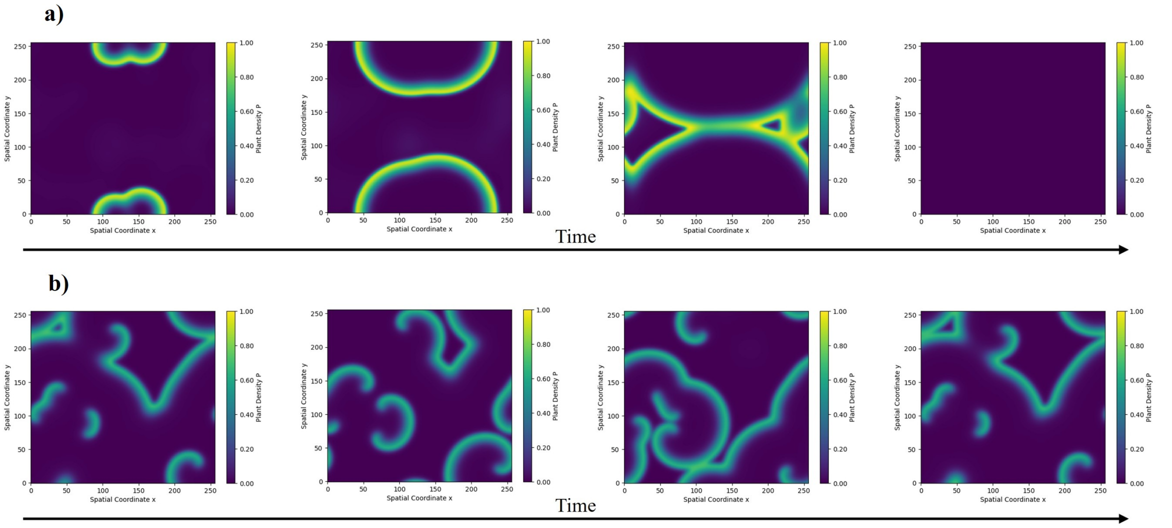

Figure 19: Temporal evolution of the pulses emerged in the numerical simulation for: a) Point C1 defined by $(\omega, \alpha) = (-0.005, 1.25)$ and b) Point C2 defined by $(\omega, \alpha) = (-0.005, 1.075)$.

5 Conclusions

First, the theoretical results, which consist of introducing the diffusion mechanism into the mathematical model that describes the evolution of a *P. oceanica* meadow, have shown that Turing patterns may emerge given appropriate conditions. The expression that delimits the Turing bifurcation was derived analytically in terms of the parameters of the system, along with the relations that define Takens-Bogdanov-Turing codimension-3 bifurcation.

Spatiotemporal simulations have allowed us to observe the trends previously predicted by the model's phase diagram. The predominant Turing pattern is a negative hexagon pattern featuring spaced gaps. In addition, more complex structures have been developed as an evolution of the negative hexagon pattern under more stressful conditions, manifesting as elongated structures with non-trivial geometries.

The appearance of patterns in regions where only spatial oscillations would be expected may indicate that the Turing bifurcation is subcritical. However, further work, including a stability analysis, would be necessary to verify this hypothesis.

Finally, the dynamics near the Takens-Bogdanov-Turing codimension-3 bifurcation reveal that the system exhibits an excitable behaviour due to the formation of pulses of vegetation.

Acknowledgments

Firstly, I would like to thank my tutors Daniel and Damià for their support, guidance, and patience throughout the project, providing me with the confidence to carry out the work. I would also like to thank all the members of the IFISC team that make this fellowship possible, which has been an extremely rewarding experience. Finally, a special acknowledgment to my colleagues of the fellowship, who have made this month as beautiful as the moon.

This work was supported by the SURF@IFISC fellowship.

References

[1] P. Moreno-Spiegelberg, M. Rietkerk, and D. Gomila, "How spatiotemporal dynamics can enhance ecosystem resilience," *Proc. Natl. Acad. Sci. U.S.A.*, vol. 122, no. 11, article e2412522122, 2025. DOI: https://doi.org/10.1073/pnas.2412522122.

[2] M. Rietkerk *et al.*, "Evasion of tipping in complex systems through spatial pattern formation," *Science*, vol. 374, article eabj0359, 2021. DOI: https://doi.org/10.1126/science.abj0359.

[3] C. Fernandez-Oto, D. Escaff, and J. Cisternas, "Spiral vegetation patterns in high-altitude wetlands," *Ecological Complexity*, vol. 37, pp. 38–46, 2019. DOI: https://doi.org/10.1016/j.ecocom.2018.12.003.

[4] M. D. Cramer and N. N. Barger, “Are Namibian ‘Fairy Circles’ the consequence of self-organizing spatial vegetation patterning?,” *PLOS ONE*, vol. 8, no. 8, pp. 1–12, 2013. DOI: https://doi.org/10.1371/journal.pone.0070876.

[5] S. Getzin *et al.*, “Discovery of fairy circles in Australia supports self-organization theory,” *Proc. Natl. Acad. Sci. U.S.A.*, vol. 113, no. 13, pp. 3551–3556, 2016. DOI: https://doi.org/10.1073/pnas.1522130113.

[6] N. Marbà, E. Díaz-Almela, and C. M. Duarte, *Mediterranean seagrass (Posidonia oceanica) loss between 1842 and 2009*, *Biological Conservation*, vol. 176, pp. 183–190, 2014. DOI: https://doi.org/10.1016/j.biocon.2014.05.024.

[7] D. Ruiz-Reynés *et al.*, “Fairy circle landscapes under the sea,” *Science Advances*, vol. 3, no. 8, article e1603262, 2017. DOI: https://doi.org/10.1126/sciadv.1603262.

[8] D. Ruiz-Reynés *et al.*, “Self-organized sulfide-driven traveling pulses shape seagrass meadows,” *Proc. Natl. Acad. Sci. U.S.A.*, vol. 120, no. 3, article e2216024120, 2023. DOI: https://doi.org/10.1073/pnas.2216024120.

[9] P. Fieguth, *An Introduction to Complex Systems.* Springer, 2017.

[10] S. H. Strogatz, *Nonlinear Dynamics and Chaos: With Applications to Physics, Biology, Chemistry, and Engineering.* CRC Press, 2018. ISBN: 9780429961113.

[11] S. Kondo and T. Miura, “Reaction-diffusion model as a framework for understanding biological pattern formation,” *Science*, vol. 329, no. 5999, pp. 1616–1620, 2010. DOI: https://doi.org/10.1126/science.1179047.

[12] A. M. Turing, “The chemical basis of morphogenesis,” *Phil. Trans. R. Soc. Lond. B*, vol. 237, pp. 37–72, 1952. DOI: https://doi.org/10.1098/rstb.1952.0012.

[13] R. Montagne, E. Hernández-García, A. Amengual, and M. San Miguel, “Wound-up phase turbulence in the complex Ginzburg–Landau equation,” *Phys. Rev. E*, vol. 56, pp. 151–167, 1997. DOI: https://doi.org/10.1103/PhysRevE.56.151.

The Role of Temporal Feedback Modulation in Single-Node Delay Reservoirs

Pau Rocabert, Silvia Ortín
Instituto de Física Interdisciplinar y Sistemas Complejos, IFISC (CSIC-UIB)
Campus Universitat de les Illes Balears, E-07122 Palma de Mallorca, Spain

Abstract

Reservoir computing (RC) is a machine learning framework that harnesses the high-dimensional dynamics of nonlinear systems for efficient time-series processing and prediction. While conventional RC relies on large recurrent networks with many neurons, equivalent functionality can be achieved with a single nonlinear node subject to delayed feedback. In this work, we investigate the impact of introducing variability in the feedback, implemented both through temporal modulation of the nonlinear term in the node dynamics and by direct modulation of the feedback signal, using values drawn from uniform and Gaussian distributions. We find that such nonlinear modulation enhances reservoir performance by enriching the effective internal connectivity, with Gaussian sampling consistently outperforming uniform sampling. These results could provide new insights and practical guidelines for the design of delay-based reservoir computing systems.

1 Introduction

Machine learning techniques have recently had a profound impact on data-driven research, high-technology industries, and a wide range of scientific and non-scientific domains. Among these approaches, deep neural networks (DNNs) have become one of the most widely adopted models, achieving remarkable success across multiple tasks. However, DNNs are computationally demanding, requiring a large number of operations to be performed within a short time window. By contrast, the human brain is capable of solving complex tasks almost instantaneously with minimal energy cost. This contrast has motivated the development of energy-efficient machine learning models inspired by neural computation in biological systems [1].

In biological systems, assemblies of recurrently coupled and mutually interacting neurons exhibit rich temporal dynamics that enable the efficient encoding of temporal relations [2]. Similarly, recurrent neural networks (RNNs) are capable of learning to mimic target systems with, in principle, arbitrary accuracy [3]. Nevertheless, training RNNs is notoriously difficult due to problems such as vanishing gradients [1] and bifurcations in the network dynamics, which can hinder convergence during training [4].

To address these challenges in RNNs, alternative models, such as Echo State Networks (ESNs) and Liquid State Machines (LSMs), have been introduced. In ESNs, only the connections between the recurrent network and the output layer are adapted during training, while the internal reservoir connections and the input-to-reservoir connections remain fixed and are initialized randomly [3]. This mechanism resembles the model of sensorimotor sequence learning proposed by [5], where the prefrontal cortex is represented as a recurrent network with fixed internal connections, and neural plasticity is used to associate recurrent activity states with appropriate responses in the output layer, analogous to the caudate or striatum in biological systems [5].

The concept of reservoir computing (RC) provides a unifying framework that includes both Echo State Networks and Liquid State Machines, offering an efficient architecture for processing temporal information. Traditional reservoir computing has a typical architecture constituted around three distinct components: an input layer, which injects the input data into the system; a recurrent reservoir matrix, which connects the nodes of the reservoir with fixed random weights; and an output layer, where the readout is computed (See section 2.1 and Fig. 1). The core principle is to transform the input signal through a nonlinear, high-dimensional dynamical system—the reservoir—whose states are then projected onto the output via a simple linear readout layer. This design enables highly efficient training, since only the linear output weights need to be optimized, typically using inexpensive methods such as linear or ridge regression. Importantly, the nonlinear dynamics of the reservoir expand the representational capacity of the system, allowing the linear readout to solve classification or regression tasks that would otherwise be intractable for purely linear models when confronted with nonlinear input data [6].

More generally, reservoir computing can be defined as any system that satisfies a set of key properties. First, it should exhibit *reproducibility*, meaning that similar inputs should lead to similar outputs, allowing the model to generalize from the training data. Second, it should display *pointwise separability*, i.e., the ability to distinguish between different kinds of inputs [4]. Third, the system should produce the same output sequence for a given input sequence regardless of the reservoir's initial conditions. This requires the presence of fading memory, where recent inputs are prioritized while the influence of distant past inputs decays. This property is commonly referred to as the *Echo State Property* [7]. It is quantified by conditional Lyapunov exponents λ, which measure the rate at which two reservoir trajectories with different initial states but driven by the same input converge to one another [8]. Notably, reservoir performance is often maximized when the system operates near the so-called "edge of chaos," i.e, when $\lambda \approx 0$.

Therefore, any system that exhibits these properties can, in principle, be used as a reservoir. This generality has motivated the development of a wide range of *in-materia* implementations of reservoir computing, which exploit the intrinsic temporal dynamics of physical systems to provide advantages over software-based realizations, particularly in terms of low power consumption and high processing speed. Examples include electronic, optoelectronic, photonic, spintronic, mechanical, biological, and even quantum systems [1].

Despite their promise, such physical reservoirs often face challenges in terms of scalability, particularly when attempting to increase the number of physical nodes. To overcome this limitation, it has been shown that reservoir computing can be efficiently implemented using a single nonlinear neuron—or, more generally, a single nonlinear dynamical element—subject to delayed feedback. This approach is attractive because it requires only two components: a nonlinear node and a delay loop. Single-node reservoir computing has been implemented in optics and optoelectronics, where a semiconductor laser is subject to external optical feedback, creating the delayed dynamics required for single-node reservoir computing [9].

Time-delay reservoirs can be regarded as conventional reservoirs implemented through time multiplexing, where each virtual neuron corresponds to the state of the reservoir within a specific time interval. The input signal is sequentially fed into the nonlinear node, with each input value temporally masked before being injected into the reservoir [10] (see Section 2.2.1). In this formulation, the feedback term plays a key role in defining the effective interconnections between virtual neurons. Modulating this feedback term is therefore analogous to modifying the connection weights between neurons in a standard recurrent network. Typically, the feedback strength is kept constant, implying that all virtual neuron interconnections share the same weight. In this work, we investigate the impact of introducing a temporal modulation of the feedback, thereby inducing variability in the effective connection weights between neurons.

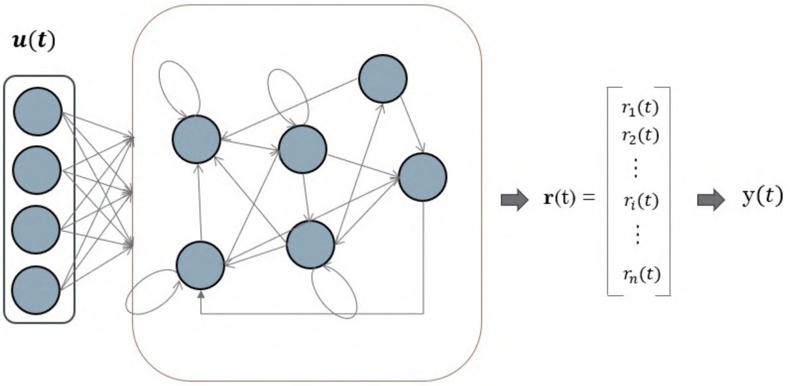

Figure 1: Traditional Reservoir Computing architecture.

2 Theoretical model

2.1 Echo State Network Model

The Echo State Network (ESN) is a widely used reservoir architecture based on recurrent neural networks and serves as a theoretical foundation for time-delayed reservoir computing. Let $n \in \mathbb{Z}^+$ denote the time step, and let $r_i(n)$ represent the state of the i-th node at time n in a reservoir of dimension D. The reservoir state evolves according to

$$r_i(n) = \phi\left(\beta \sum_{j=1}^{D} W_{ij} r_j(n-1) + \gamma \sum_{j=1}^{N} W_{ij}^{\text{in}} u_j(n)\right), \tag{2.1}$$

$$o_j(n) = \sum_{i=1}^{D} W_{ij}^{\text{out}} r_i(n), \tag{2.2}$$

where ϕ is a nonlinear activation function, W_{ij} are the recurrent connection weights between reservoir nodes, W_{ij}^{in} are the input weights, and $\mathbf{u}(n) = [u_1(n), \ldots, u_N(n)]^\top$ is the N-dimensional input vector at time n. The reservoir state is $\mathbf{r}(n) = [r_1(n), \ldots, r_D(n)]^\top$, and the output is $\mathbf{o}(n) = [o_1(n), \ldots, o_M(n)]^\top$, computed using the readout weights W_{ij}^{out}. The matrices W_{ij} and W_{ij}^{in} are randomly initialized from a uniform distribution over $[-a, a]$ where a is fixed according to the spectral radius of the reservoir matrix, while the readout weights W_{ij}^{out} are optimized via linear regression, minimizing the following loss function

$$\mathcal{L} = \sum_{n} \|\mathbf{y}(n) - \mathbf{o}(n)\|^2 + \alpha \|\mathbf{W}^{\text{out}}\|^2 \tag{2.3}$$

using the Moore–Penrose pseudoinverse [7, 11].

2.2 Single non-linear node reservoir computing

As stated in Section 1, one of the main advantages of reservoir computing is its suitability for implementation in analog physical systems, which avoids the need to interconnect large numbers of discrete neurons. In optoelectronics, for instance, a reservoir can be realized using a single nonlinear node with delayed feedback. The evolution of this nonlinear node with delay can be written in general as:

$$\dot{x}(t) = f(x(t), x(t-\tau) + \gamma J(t)), \tag{2.4}$$

where $f(x)$ is a nonlinear function, τ is the delay time, $J(t)$ is the masked input, and γ is a modulation factor [10].

In this work, we focus on modeling an optoelectronic device governed by Ikeda dynamics. In this case, the reservoir evolution is described by

$$\dot{x}(t) = -x(t) + \eta \sin(x(t-\tau) + \gamma J(t)), \tag{2.5}$$

where η is a nonlinear modulation factor. Notice that η indirectly controls the strength of the feedback. The parameters η and γ are chosen such that the reservoir exhibits the desired dynamical regime, as discussed in Section 1, and are optimized for the target task. The optimal configuration is determined by scanning the parameter space.

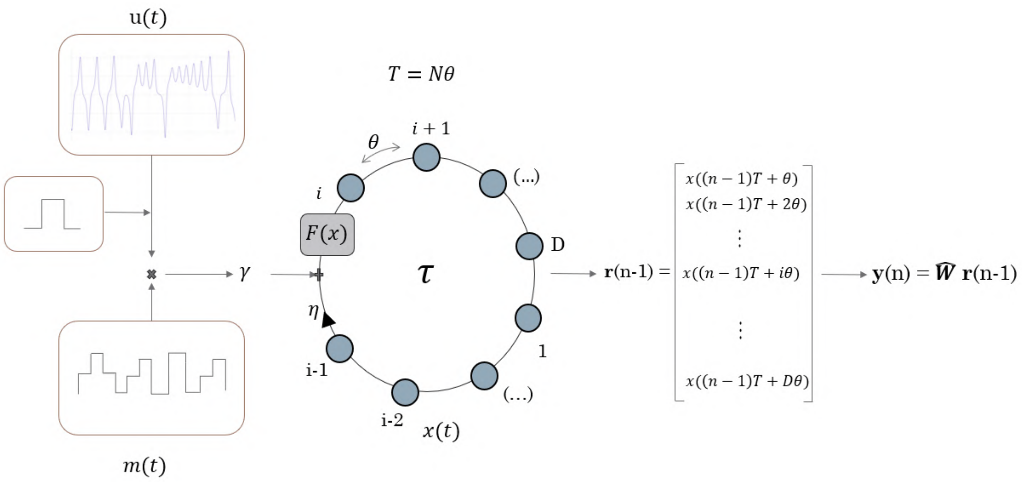

Figure 2: Time multiplexing scheme of a time delay reservoir.

2.2.1 Time multiplexing

A nonlinear node governed by Eq. (2.4) can reproduce the behavior of an Echo State Network (ESN) reservoir through time multiplexing (Fig. 2). Instead of using D distinct spatial nodes, we define D *virtual nodes* as

$$r_i(n) = x(t), \quad nT + i\theta \leq t < nT + (i+1)\theta, 0 < i \leq D \tag{2.6}$$

where $x(t)$ is the state of the non-linear single-node, θ is the duration of a virtual node and $T = D\theta$ is the total duration of the reservoir state at time step n. We consider that the nonlinear node is driven by either a continuous N-dimensional input $\mathbf{u}(t)$ or a discrete N-dimensional input $\mathbf{u}(n)$. For each discrete time step n, the input $\mathbf{u}(n)$ is held constant over an interval of duration T, defining the piecewise constant function $\mathbf{I}(t) = \mathbf{u}(n), \quad nT \leq t < (n+1)T$. This function $\mathbf{I}(t)$ is modulated by a masking function $\mathbf{M}(t)$, where

$$M_j(t) = W^{\text{in}}_{ij}, \quad nT + i\theta \leq t < nT + (i+1)\theta, \qquad M_j(t) = M_j(t+T) \tag{2.7}$$

Introducing the masked input $J(t) = \sum_{j=1}^{N} M_j(t) I_j(t)$ in Eq. (2.4) is analogous to introducing the term $\sum_{j=1}^{N} W^{\text{in}}_{ij} u_j(n)$ in Eq. (2.1). On the other hand, the recurrent connections between neurons given by $\sum_{j=1}^{D} W_{ij} r_j(n-1)$ in Eq. (2.1) are implemented in a single nonlinear node reservoir through both the delayed feedback term $x(t-\tau)$ and the intrinsic dynamics of the system. The contribution of the delayed feedback can be understood as follows. Define $\alpha = \frac{\tau - T}{\theta}$ and $t = nT + \hat{t}, \quad 0 \leq \hat{t} < T$. Then

$$x(t-\tau) = x((n-1)T + \hat{t} - \alpha\theta) = x((n-2)T + \hat{t} - (\alpha - D)\theta).$$

Using the definition of virtual nodes in Eq. (2.6), the feedback term can be expressed as contributions from previous virtual nodes [10]:

$$x(t-\tau) = \begin{cases} r_{i-\alpha}(n-1), & \alpha \leq i < D, \\ r_{D+i-\alpha}(n-2), & 0 \leq i < \alpha, \end{cases} \qquad nT + i\theta \leq t < nT + (i+1)\theta. \tag{2.8}$$

The effective connections between neurons due to the system's inherent dynamics can be understood as the dependence of the current state on previous states, caused by the finite response time of the physical system. For the Ikeda dynamics of Eq. (2.5), this dependence can be approximated as

$$r_i(n) = \Omega_i \, r_1(n-1) + \sum_{j=1}^{i} \Delta_{ij} \, \eta \, \sin\!\big(r_j(n-1) + W^{\text{in}}_j u(n)\big) \, , \tag{2.9}$$

where $\Omega_i = e^{-i\theta}$ and $\Delta_{ij} = (1 - e^{-\theta})e^{-(i-j)\theta}$ [10]. Notice that this contribution becomes less significant for large values of θ.

Finally, the output is computed in an analogous way to ESN with equation Eq. (2.2):

$$o_j(n) = \sum_{i=1}^{D} W^{\text{out}}_{ij} x((n-1)T + i\theta) \tag{2.10}$$

The output weights are determined as in the ESN case, with a simple linear regression or a ridge regression.

2.2.2 Multiple Feedbacks

To increase the connectivity between the virtual nodes of the reservoir through feedback, additional delay lines can be introduced, leading to the following dynamics:

$$\dot{x}(t) = -x(t) + \sin(\beta_1 x(t-\tau_1) + \beta_2 x(t-\tau_2) + \gamma J(t))\,, \tag{2.11}$$

where β_1 and β_2 are the modulation factors associated with the two feedback delays τ_1 and τ_2. If the ratio $\frac{\tau_2}{\tau_1}$ is rational, i.e., $\frac{\tau_2}{\tau_1} \in \mathbb{Q}$, the system exhibits a resonance at some time t_R, corresponding to a periodic overlap between the two delays. This resonance has been reported to degrade performance in tasks such as NARMA-10 [12]. To avoid such resonances, the relation between delays is chosen to be irrational, for instance by setting $\tau_2 \approx \sqrt{2}\,\tau_1$.

2.3 Feedback modulation

In the Echo State Network reservoir, the recurrent connections W_{ij} in Eq. (2.1) differ for each pair of nodes. In analogy, in this work we substitute the constant feedback strength parameters—η in Eq. (2.5) and β_k ($k \in \{1,2\}$) in Eq. (2.11)—with time-dependent modulation functions, $\eta(t)$ and $\beta_k(t)$, defined as

$$\eta(t) = W_{i,j}, \quad nT + i\theta \le t < nT + (i+1)\theta, \tag{2.12}$$

$$\beta_k(t) = W_{i,j_k}, \quad nT + i\theta \le t < nT + (i+1)\theta, \tag{2.13}$$

with periodicity $\eta(t) = \eta(t+T)$ and $\beta_k(t) = \beta_k(t+T)$. According to Eq. (2.6), the index j is determined by $j = i - \alpha, \quad \alpha \le i < D$ and $j = D + i - \alpha, \quad 0 \le i < \alpha.$. As in the ESN case, the reservoir weights W_{ij} are generated randomly. Thus, the equations Eq. (2.5) and Eq. (2.11) become respectively:

$$\dot{x}(t) = -x(t) + \eta(t)\sin(x(t-\tau) + \gamma J(t)) \tag{2.14}$$

$$\dot{x}(t) = -x(t) + \sin(\beta_1(t)x(t-\tau_1) + \beta_2(t)x(t-\tau_1) + \gamma J(t)) \tag{2.15}$$

The main objective of this work is to investigate the impact of such temporal modulation on reservoir performance. As pointed out by [7], in ESN the randomness of the connection weights W_{ij} of equation Eq. (2.1) varies the response of each node to the input signal and therefore enhances the degree of linear independence of each RC state $\mathbf{r}(n)$. Thus, it is expected that the temporal modulation in $\eta(t)$ and $\beta(t)$ respectively in equation Eq. (2.14) and Eq. (2.15) increase the linear independence of the RC states.

3 Results and discussion

3.1 Tasks

To investigate the impact of temporal modulation on the parameters $\eta(t)$ and $\beta_k(t)$ in Eqs. (2.14) and (2.15), we generate the connection weights W_{ij} from different probability distributions. Specifically, W_{ij} is drawn from either a normal distribution, $\mathcal{N}(\eta_0, \sigma)$ and $\mathcal{N}(\beta_0, \sigma)$ respectively, or a uniform distribution, $\mathcal{U}(\eta_0 - \Delta,\, \eta_0 + \Delta)$ and $\mathcal{U}(\beta_0 - \Delta,\, \beta_0 + \Delta)$ respectively, with varying values of σ and Δ. The parameters η_0 and β_0 correspond to the optimal values that minimize the root-mean-square error (RMSE) in the one–step–ahead prediction task described in Sec. 3.1.1 when η and β_k are kept constant, i.e, the reservoir follows equations Eq. (2.5) and Eq. (2.11) respectively. For each choice of σ and Δ, we evaluate the reservoir performance on the tasks outlined in the subsequent sections with 15 different experiments.

All simulations are performed with a reservoir of $D = 250$ neurons. Equations Eq. (2.14) and Eq. (2.15) are integrated using Euler's method with an integration step $\Delta t = 0.1$. The neuron width is set to $\theta = 7.0\Delta t$, which provides a balance between connections due to inherent dynamics and those due to feedback. The reservoir is trained to minimize the loss function Eq. (2.3) with $\alpha = 0$, as this value has been found to optimize performance. In the one delay $\tau = T$ where $T = D\theta$ while in the two delay system $\tau_1 = T$ and $\tau_2 = T + 170\Delta t$, therefore $\frac{\tau_2}{\tau_1} \approx \sqrt{2}$.

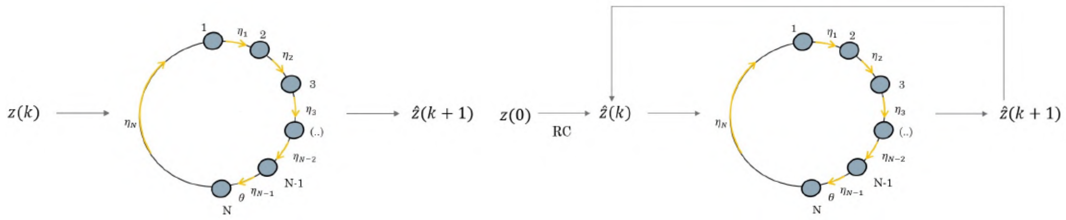

Figure 3: Left: Next step prediction scheme. $z(t)$ stands for real time series values and $\hat{z}(t)$ stands for predicted time series values. Right: Autonomous dynamics reconstruction.

3.1.1 One step ahead Prediction

Once the reservoir has been trained with the first N_{train} points of a given time series, its performance is first evaluated by predicting the next N_{test} points using a one-step-ahead prediction scheme. Specifically, at each time step n, the true value of the time series $\mathbf{y}(n-1)$ is used to compute the D reservoir states $r_i(n-1)$, defined in Eq. (2.6), by evolving the reservoir according to Eq. (2.14) or Eq. (2.15). The predicted output $\mathbf{o}(n)$ is then obtained from the readout equation (Eq. (2.10)) Fig. 3.

After computing $\mathbf{o}(n)$ for all $n = N_{\text{train}} + 1, \ldots, N_{\text{train}} + N_{\text{test}}$, the root mean squared error (RMSE) is evaluated as

$$\text{RMSE} = \sqrt{\frac{1}{N_{\text{test}}} \sum_{n=1}^{N_{\text{test}}} \|\mathbf{o}(n + N_{\text{train}}) - \mathbf{y}(n + N_{\text{train}})\|^2}. \tag{3.1}$$

For comparison across different datasets and tasks, we also compute the normalized root mean squared error (NRMSE), defined as

$$\text{NRMSE} = \frac{\text{RMSE}}{\sigma_{\mathbf{y}}}, \tag{3.2}$$

where $\sigma_{\mathbf{y}}$ is the standard deviation of the target time series $\mathbf{y}(n)$ in the test set.

3.1.2 Autonomous Reconstruction

The second task used to evaluate the performance of the reservoir is the autonomous prediction of a time series $\mathbf{u}(t)$, i.e., the output of the reservoir $\mathbf{o}(n-1)$ is fed back as the input for the prediction of $\mathbf{o}(n)$, Fig. 3. Explicitly, for a single delay, the evolution of the reservoir during autonomous reconstruction can be written as:

$$\dot{x}(t) = -x(t) + \eta(t) \sin\Big(x(t-\tau) + \gamma \sum_{j=1}^{N} M_j(t) \sum_{i=1}^{D} W_{ij}^{\text{out}} x((n-1)T + i\theta)\Big), \quad nT \le t < (n+1)T \tag{3.3}$$

The reservoir output computed via Eq. (2.10) provides the predicted value of $\mathbf{u}(t)$ for $t > 0$. However, due to the chaotic amplification of errors, the prediction eventually breaks down [13]. We define the time τ_ϵ as the time at the moment when the RMSE of the last K autonomous predictions $\hat{\mathbf{o}}(i)$ $(i = n - (K-1), \ldots, n-1, n)$ reaches a threshold ϵ:

$$\sqrt{\sum_{i=0}^{K-1} \|\hat{\mathbf{o}}(n-i) - \mathbf{y}(n-i)\|^2} \ge \epsilon. \tag{3.4}$$

Additionally, we compute the RMSE for all predictions up to $n(\tau_\epsilon)$:

$$\text{RMSE} = \sqrt{\sum_{i=0}^{n(\tau_\epsilon)} \|\hat{\mathbf{o}}(i) - \mathbf{y}(i)\|^2}. \tag{3.5}$$

To normalize results across different systems, we express $\tau_\epsilon = n_\epsilon \Delta t \Lambda_1$, where Δt is the time step of the original time series $\mathbf{u}(t)$ and Λ_1 is the largest Lyapunov exponent. This follows from $\|\delta \mathbf{u}^T\| \approx e^{\Lambda_1 t} \|\delta \mathbf{u}^0\|$.

To compute the Lyapunov exponents for a system defined by $\dot{\mathbf{z}} = \mathbf{F}(\mathbf{z})$, we evolve an initial perturbation $\delta\mathbf{u}(0) = \mathbb{1}$ according to $\frac{d}{dt}\,\delta\mathbf{u}(t) = \mathcal{D}\mathbf{F}\,\delta\mathbf{u}(t)$ where $\mathcal{D}\mathbf{F}$ is the Jacobian of $\mathbf{F}$. The variational equation is integrated for a time T, after which $\delta\mathbf{u}(t)$ is orthonormalized using the Gram–Schmidt procedure. This process is repeated N times. The Lyapunov exponents are then computed as

$$\lambda_j = \frac{1}{TN}\sum_{k=1}^{N} \|\delta u_j(Tk)\|.$$

For sufficiently large N, the values λ_j converge to the true Lyapunov exponents [14].
For the Mackey–Glass system, the delayed differential equation is converted into an ordinary differential equation using the Galerkin approximation, as described in [15].

3.2 Narma-10 system

The NARMA-10 time series is the first forecasting benchmark employed to evaluate the effect of feedback time modulation in delay-based reservoirs. The system is defined by the recursive map:

$$y_{k+1} = 0.3y_k + 0.05y_k \sum_{i=0}^{9} y_{k-i} + 1.5u_k u_{k-9} + 0.1, \tag{3.6}$$

where u_k is sampled from a uniform distribution $\mathcal{U}(0, 0.5)$. A total of $N = 6000$ points were generated and partitioned into training ($N_{\text{train}} = 4000$), validation ($N_{\text{validation}} = 1000$), and test ($N_{\text{test}} = 1000$) sets.

NARMA-10 is widely used as a benchmark in reservoir computing because it combines strong nonlinearity with long-range temporal dependencies, making accurate prediction particularly challenging and an indicator of the nonlinear memory of the reservoir [16]. Its dependence on both past outputs and delayed inputs requires the reservoir to simultaneously capture nonlinear dynamics and maintain memory over multiple time steps.

Hyperparameter optimization The reservoir hyperparameters γ, η_0, and β_0 were tuned by exploring the parameter space to minimize the root-mean-square error (RMSE) in the one-step-ahead prediction on the validation set. Figure 4 reports the RMSE values obtained across the explored parameter ranges. The optimal parameters selected were $(\eta_0, \gamma) = (0.50, 1.35)$ for the single-delay reservoir (Eq.(2.14)) and $(\beta_0, \gamma) = (0.70, 1.01)$ for the two-delay reservoir (Eq.(2.15)).

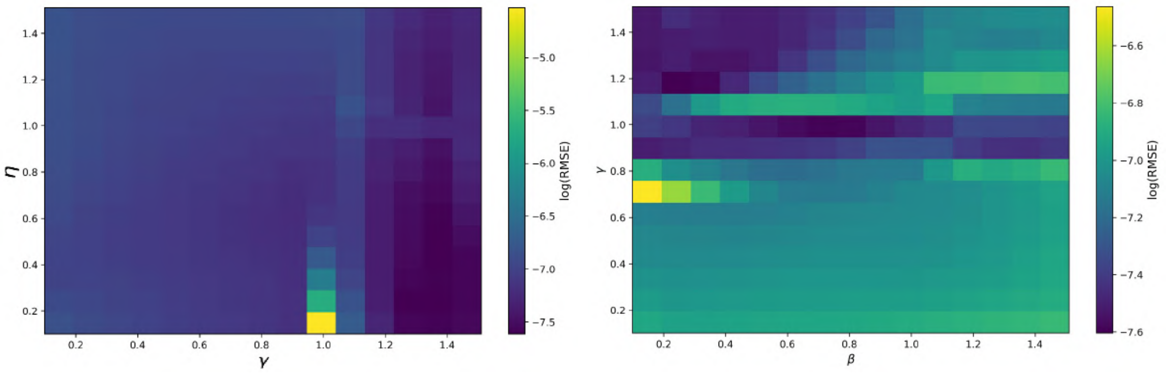

Figure 4: One-step-ahead prediction RMSE of NARMA-10 time series across the parameter spaces of time-delayed reservoirs. Left: RMSE in the (η, γ) parameter space for the single-delay reservoir (Eq. (2.14)). Right: RMSE in the (β, γ) parameter space for the two-delay reservoir (Eq. (2.15)).

Results Figure 5 presents the one-step-ahead prediction RNMSE for the single-delay and two-delay reservoirs when $\eta(t)$ and $\beta_k(t)$ are drawn from either normal or uniform distributions. Increasing the standard deviation of the temporal modulation of $\eta(t)$ consistently reduced the expected RNMSE, indicating improved reservoir performance regardless of the distribution.

In the single-delay reservoir, the expected RNMSE decreased by $(4.6 \pm 3.2)\%$ when $\eta(t)$ was drawn from a normal distribution with $\sigma = 0.5$, and by $(2.7 \pm 4.3)\%$ when drawn from a uniform distribution, relative to the RNMSE at the optimal static value. Consistent with previous findings [12], the two-delay reservoir achieved lower RNMSE values overall compared to the single-delay reservoir. In contrast, temporal modulation of $\beta(t)$ in the two-delay reservoir did not yield a systematic reduction in the expected RNMSE. However, the substantial variability observed across trials indicates that, in certain cases, $\beta(t)$ modulation improved performance. For example, in the single-delay reservoir, the minimum RNMSE achieved was $8.76 \cdot 10^{-2}$ for $\eta(t)$ drawn from a normal distribution, $8.64 \cdot 10^{-2}$ for a uniform distribution, $8.85 \cdot 10^{-2}$ for $\beta(t)$ drawn from a normal distribution, and $8.86 \cdot 10^{-2}$ for $\beta(t)$ drawn from a uniform distribution.

A plausible explanation for the differing impact of feedback time modulation between single-delay and two-delay reservoirs lies in the geometry of their respective parameter spaces. As shown in Fig. 4, the error surface of the single-delay reservoir is relatively flat around the chosen optimum, indicating that small perturbations of the parameters have a limited effect on performance. In contrast, the optimum for the two-delay reservoir lies in a sharper region of the parameter space, where small changes can more easily degrade performance. This difference in landscape geometry may underlie the stronger sensitivity of the two-delay reservoir to temporal modulation. A more rigorous analysis, would be required to substantiate this hypothesis.

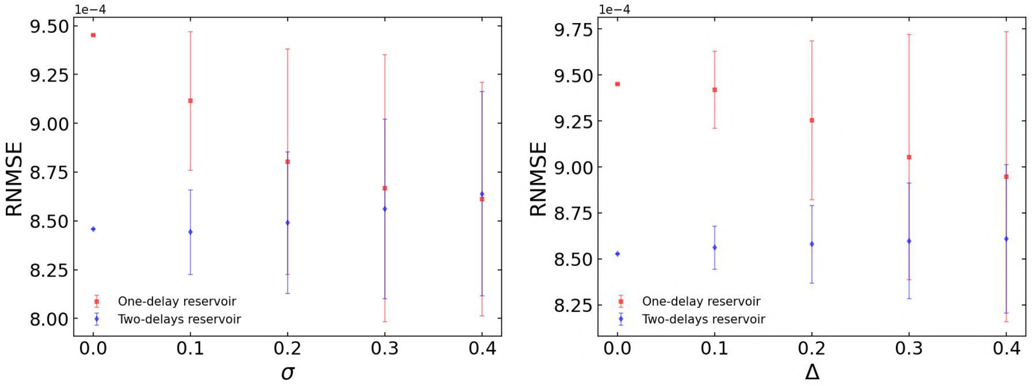

Figure 5: Normalized root mean square error (NRMSE) for the one-step-ahead prediction of the NARMA-10 time series under different values of σ and Δ. Left: $\eta(t)$ and $\beta(t)$ are drawn independently from Gaussian distributions, $\mathcal{N}(\eta_0, \sigma)$ and $\mathcal{N}(\beta_0, \sigma)$, respectively. Right: $\eta(t)$ and $\beta(t)$ are drawn independently from uniform distributions, $\mathcal{U}(\eta_0 - \Delta, \eta_0 + \Delta)$ and $\mathcal{U}(\beta_0 - \Delta, \beta_0 + \Delta)$, respectively.

3.3 Mackey-Glass-17 system

The second time series analyzed to assess the impact of feedback modulation in time-delayed reservoir computing is generated by the Mackey–Glass chaotic system, governed by the delayed differential equation

$$\dot{z}(t) = \frac{a, z(t-\tau)}{1 + z^n(t-\tau)} - bz(t), \tag{3.7}$$

where $a = 0.2$, $b = 0.1$, $n = 10$, and $\tau = 17$. The Mackey–Glass equation (Eq. (3.7)) was originally introduced by Mackey and Glass in the context of modeling white blood cell production, providing an early example of how delayed feedback can lead to complex, nonlinear dynamics in physiological control systems [17]. A well-known property of this system is that the information dimension of the attractor increases with the delay τ, reflecting the emergence of higher-dimensional dynamics. Under the chosen parameters, the system evolves in a mildly chaotic regime [18]. The larger lyapunov exponent computed following the method described in [15] is $\Lambda_1 \approx 0.0059$. The time series is generated by integrating Eq. (3.7) for $N = 6000$ points with a time step $dt = 1$ using Runge-Kutta 4. The first 18 initial points $\tau \leq t < 0$ are set to a fixed value $z(t) = z_0$ with $z_0 = 0.5$. The series is then normalized as

$$\hat{z}(t) = \frac{z(t) - \langle z(t) \rangle}{\sigma_z(t)} \tag{3.8}$$

To increase the robustness of the trained reservoir, noise is added to the temporal series. Specifically, white noise is added as follows $\hat{z}_\varepsilon(t) = \hat{z}(t) + \alpha\varepsilon(t)$ where ε is sampled from a standard normal distribution and α is set to $1.0 \cdot 10^{-6}$. Finally, the temporal series is then divided into a training set with $N_{\text{train}} = 4000$ points, a validation set with $N_{\text{validation}} = 1000$ points, and a test set with

$N_{\text{test}} = 1000$ points.

Hyperparameter optimization As described in Sec. 3.1, the hyperparameters γ, η_0, and β_0 are determined through exploration of the parameter space. Specifically, η_0 and β_0 are chosen to minimize the RMSE in the one-step-ahead prediction on the validation set while also ensuring reproduction of the Mackey-Glass chaotic dynamics for at least approximately one Lyapunov time $\tau_1 \sim 1/\Lambda_1$. Figure 6 shows the RMSE across the explored parameter spaces. The selected points are $(\eta_0, \gamma) = (0.850, 0.714)$ for Eq. (2.14) and $(\beta_0, \gamma) = (0.51, 1.25)$ for Eq. (2.15). Notice that in Figure 6, there are regions of the parameter space where the RMSE is significantly larger. These regions can be related to cases where the reservoir dynamics do not converge to a fixed point, where the performance of the reservoir decreases [10, 7].

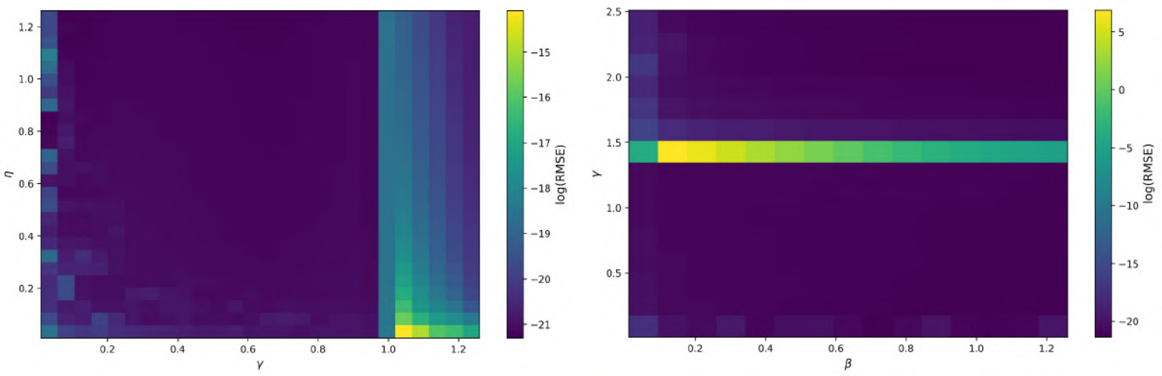

Figure 6: One-step-ahead prediction RMSE of Mackey-Glass time-series across the parameter spaces of time-delayed reservoirs. Left: RMSE in the (η, γ) parameter space for the single-delay reservoir (Eq. (2.14)). Right: RMSE in the (β, γ) parameter space for the two-delay reservoir (Eq. (2.15)).

Results The overall results of the one-step-ahead prediction and autonomous reconstruction tasks for the single-delay reservoir (Eq. (2.14)) with $\eta(t) \sim \mathcal{N}(\eta_0, \sigma)$ and $\eta(t) \sim \mathcal{U}(\eta_0 - \Delta, \eta_0 + \Delta)$ are presented in Figures 7 and 8. In both cases, for the single delayed reservoir, increasing the variability of $\eta(t)$—and hence the variability in neuron interconnections—improves performance in the one-step-ahead prediction task as well as in autonomous reconstruction.

For the Gaussian modulation (Fig. 7), the single-delay reservoir shows a monotonic decrease in the expected RNMSE of one-step-ahead prediction as the standard deviation σ increases, with the largest improvement of $(1.59 \pm 0.22)\%$ reached at $\sigma = 0.5$. In contrast, the two-delay reservoir—which already achieves a lower optimal RNMSE than the single-delay case—only shows improvement for $\sigma = 0.10$, with a smaller gain of $(0.75 \pm 0.18)\%$. The middle and right panels further indicate that, in the single-delay reservoir, increasing σ reduces the RNMSE of autonomous prediction (before divergence) and extends the divergence time τ_ϵ, pointing to enhanced accuracy and robustness. On average, τ_ϵ increases by $(41 \pm 51)\%$, while the expected RNMSE for $\sigma = 0.3$ decreases by $(19.8 \pm 7.9)\%$ compared to the optimal static case. By contrast, for the two-delay reservoir, Gaussian modulation of the feedback coefficients β_k does not yield a clear performance improvement. The expected RNMSE for one-step-ahead prediction decreases only at $\sigma = 0.1$, after which it remains essentially at the level of the optimal point. For autonomous prediction, the RNMSE before divergence increases slightly up to $\sigma = 0.2$, and then decreases, outperforming the optimal point. Finally, although the divergence time of the optimal point remains larger than the expected divergence time for all σ, the expected divergence time still shows an increasing trend for the first three σ values with $\sigma > 0.0$.

For the uniform modulation (Fig. 8), the left panel shows that in the single-delay reservoir, the RMSE in one-step-ahead prediction decreases with Δ, but only for $\Delta < 2$. In the two-delay reservoir, a similar improvement is observed, though limited to $\Delta \leq 0.3$. The performance gain at $\Delta = 0.1$ is $(0.75 \pm 0.76)\%$ for the single-delay case and $(1.11 \pm 0.18)\%$ for the two-delay case. The middle and right panels reveal a consistent trend: in the single-delay reservoir, both the RMSE of autonomous prediction decreases and the divergence time τ_ϵ increases with Δ, but only up to $\Delta = 0.3$, beyond which performance deteriorates. At this point, the expected number of steps before divergence increases by $(38 \pm 51)\%$, while the RNMSE before divergence decreases by $(15 \pm 11)\%$. In the two-delay reservoir, a reduction in expected RMSE is also observed for $\Delta \geq 0.2$, corresponding to a $(3.2 \pm 7.0)\%$ decrease at $\Delta = 0.5$. Although all divergence times remain below those of the optimal point, an increase in τ_ϵ is nonetheless observed as Δ grows.

The existence of these thresholds, beyond which performance declines, can be explained by the broader distribution of $\eta(t)$ or $\beta(t)$, which increases the likelihood of deviating from the optimal operating region or entering a chaotic regime, thereby degrading reservoir performance.

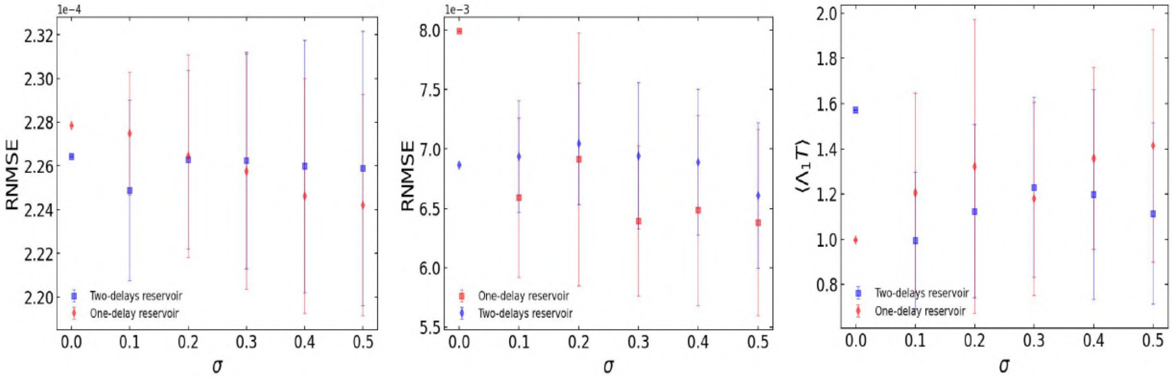

Figure 7: Results for the single-delay reservoir and two-delays reservoir governed respectively by Eq. (2.14) and by Eq. (2.15), with $\eta(t,\sigma)$ sampled from a normal distribution $\mathcal{N}(0.85,\sigma)$. Left: Average RNMSE of the one-step-ahead prediction (Eq. (3.1)) over 15 experiments for each value of σ. Center: Average RNMSE of the autonomous prediction over the same 15 experiments. Right: Average divergence time τ_ϵ obtained from 15 autonomous reconstruction experiments for each σ. The threshold is set to $\epsilon = 0.015$ and $K = 10$

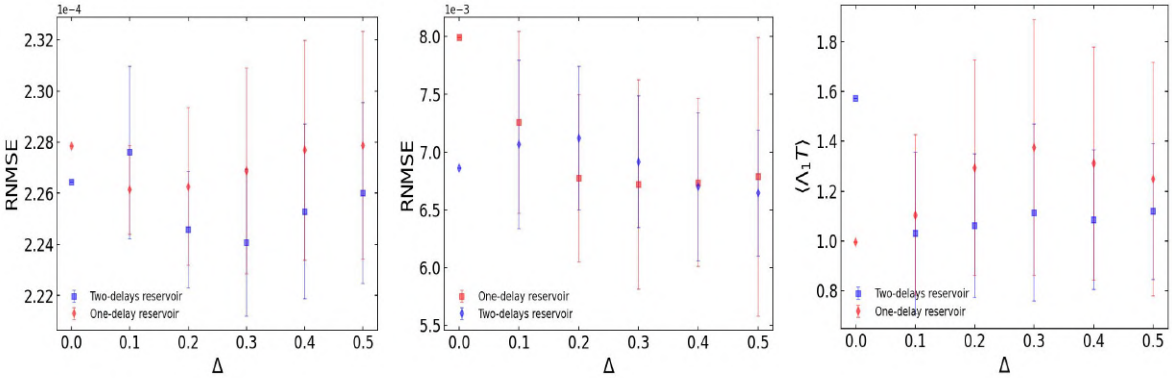

Figure 8: Results for the single-delay reservoir and two-delays reservoir governed respectively by Eq. (2.14) and by Eq. (2.15), with $\eta(t,\sigma)$ sampled from a uniform distribution $\mathcal{U}(0.85-\Delta, 0.85+\Delta)$. Left: Average RMSE of the one-step-ahead prediction (Eq. (3.1)) over 15 experiments for each value of Δ. Center: Average RMSE of the autonomous prediction over the same 15 experiments. Right: Average divergence time τ_ϵ obtained from 15 autonomous reconstruction experiments for each Δ. The threshold is set to $\epsilon = 0.015$ and $K = 10$.

The plots above illustrate the average effect of introducing a random time modulation in $\eta(t)$; however, the large deviations indicated by the error bars in Figures 7 and 8, together with the results in Figures 10 and 11, reveal that different realizations of $\eta(t)$ do not affect the reservoir dynamics uniformly. In several cases, the autonomous reconstructions remain stable for up to 5 Lyapunov times and accurately reproduce the Mackey–Glass attractor (Figs.10, 12). Moreover, some realizations, such as the best ones obtained for$\sigma = 0.5$ for the single delay reservoir (Fig.11), exhibit no divergence over the entire 1000-step test set, achieving prediction horizons beyond 5 Lyapunov times, i.e., $\tau_\epsilon > 5$. These results indicate that introducing variability in $\eta(t)$ and $\beta(t)$

can improve the robustness of the reservoir; however, the effect strongly depends on the type of variability considered. In particular, certain realizations of $\eta(t)$ and $\beta(t)$ yield reservoirs that are both more precise in short-term predictions and more robust in sustaining long-term autonomous reconstructions of the underlying attractor dynamics.

Moreover, Figures 11 and 8 and Figures 10, 12) show that not only is the expected performance of the reservoir with $\eta(t)$ and $\beta(t)$ generated with a uniform distribution worse than that with $\eta(t)$ and $\beta(t)$ generated with a gaussian distribution, but the best experiment obtained for each value of Δ in uniform distributions is also worse than the Gaussian one. This suggests that despite introducing variability in the weights improve the performance, the majority of the weights should be close to the optimal value.

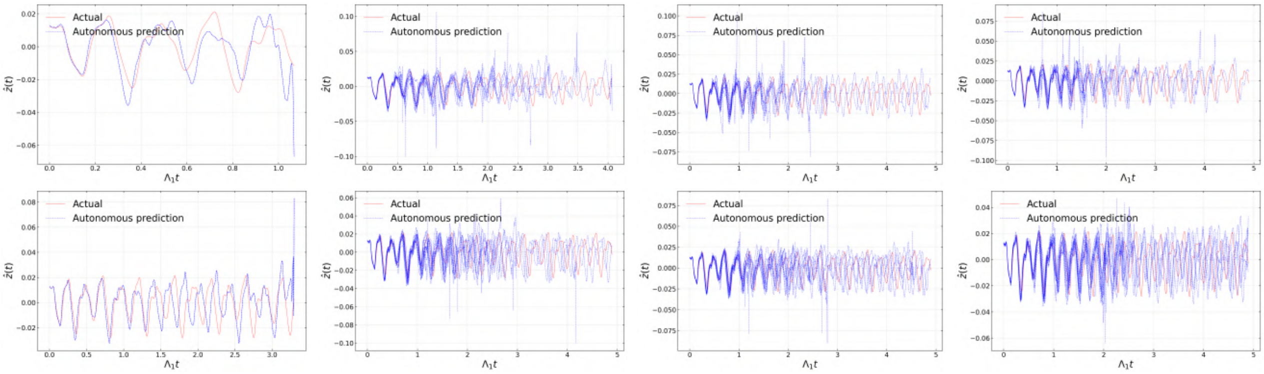

Figure 9: Autonomous prediction of the Mackey–Glass-17 system using the single-delay reservoir and two-delays reservoir governed by Eq. (3.3) (first row) and Eq. (3.3) (second row), with $\eta(t;\sigma)$ drawn from a normal distribution $\mathcal{N}(0.85,\sigma)$. Each panel corresponds to the autonomous reconstruction obtained for a specific value of σ. The panels are ordered from left to right. The first on the left corresponds with $\sigma = 0$ and the next ones with σ increasing from $\sigma = 0.3$ to $\sigma = 0.5$ in steps of 0.1.

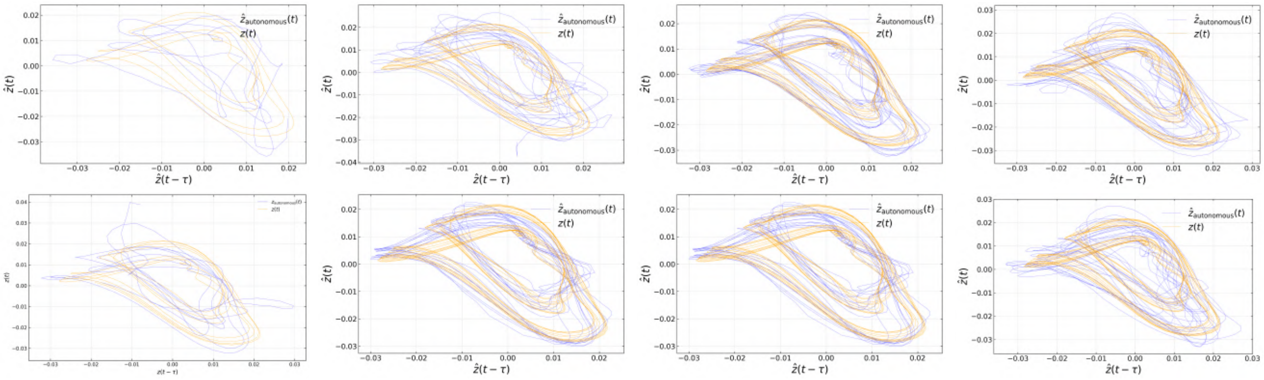

Figure 10: Atractor reconstruction from autonomous prediction of the Mackey–Glass-17 system using the single-delay reservoir and two-delays reservoir governed by Eq. (3.3) (first row) and Eq. (3.3) (second row), with $\eta(t;\sigma)$ drawn from a normal distribution $\mathcal{N}(0.85,\sigma)$. Each panel corresponds to the Mackey–Glass attractor for the best autonomous reconstruction obtained for a specific value of σ. The panels are ordered from left to right. The first on the left corresponds with $\sigma = 0$ and the next ones with σ increasing from $\sigma = 0.3$ to $\sigma = 0.5$ in steps of 0.1.

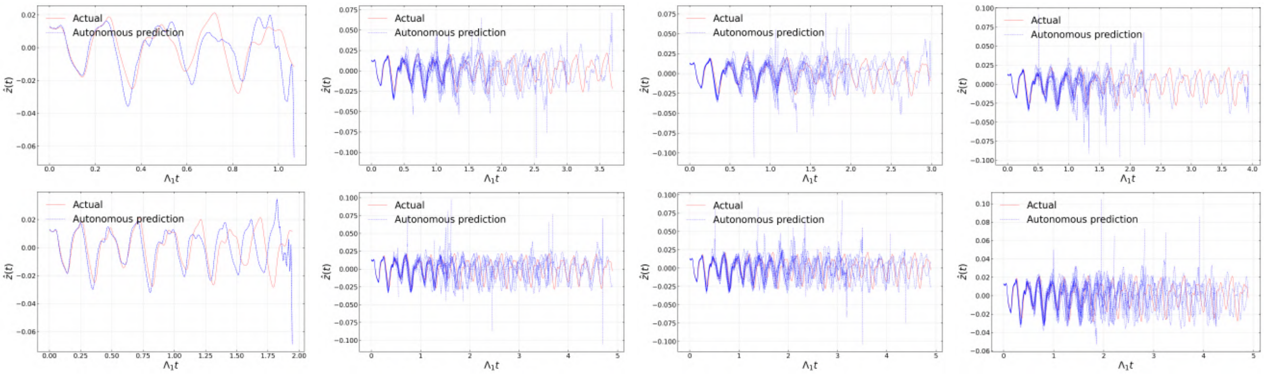

Figure 11: Autonomous prediction of the Mackey–Glass-17 system using the single-delay reservoir and two-delays reservoir governed by Eq. (3.3) (first row) and Eq. (3.3) (second row), with $\eta(t;\Delta)$ drawn from a uniform distribution $\mathcal{U}(0.85-\Delta, 0.85+\Delta)$. Each panel corresponds to the autonomous reconstruction obtained for a specific value of Δ. The first on the left corresponds with $\Delta = 0$ and the next ones with Δ increasing from $\sigma = 0.3$ to $\sigma = 0.5$ in steps of 0.1.

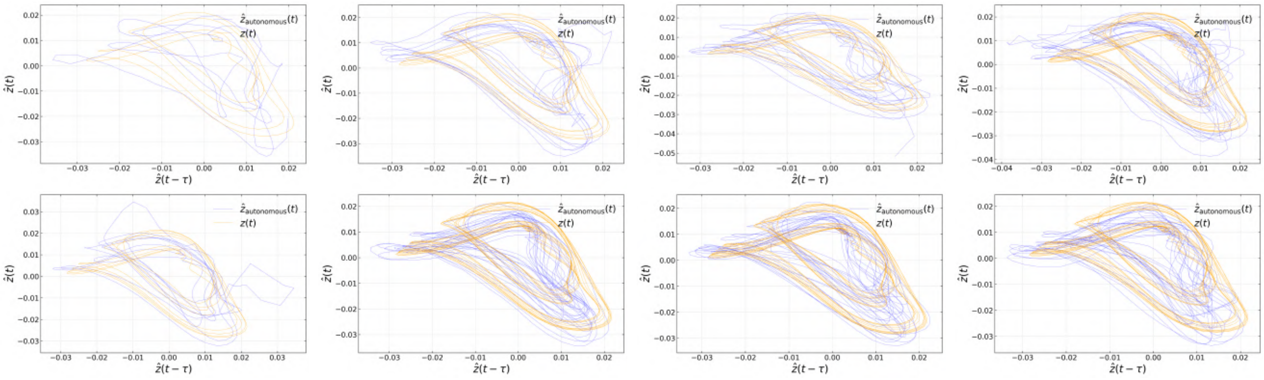

Figure 12: Atractor reconstruction from autonomous prediction of the Mackey–Glass-17 system using the single-delay reservoir and two-delays reservoir governed by Eq. (3.3) (first row) and Eq. (3.3) (second row), with $\eta(t;\Delta)$ drawn from a uniform distribution $\mathcal{U}(0.85-\Delta, 0.85+\Delta)$. Each panel corresponds to the Mackey–Glass attractor for the best autonomous reconstruction obtained for a specific value of Δ. The first on the left corresponds with $\Delta = 0$ and the next ones with Δ increasing from $\Delta = 0.3$ to $\Delta = 0.5$ in steps of 0.1.

To investigate the origin of the differing autonomous prediction performances observed when $\eta(t)$ is drawn from a Gaussian distribution—in single-delay reservoirs, where the performance improvement due to variability is more pronounced—we analyzed the distribution of $\eta(t)$ values assigned to virtual neurons across multiple experiments (Fig.13). Although the results are not entirely conclusive, the analysis indicates that the best-performing reservoirs tend to contain a smaller fraction of neurons with extreme parameter values, i.e., $\eta(t) \leq \eta_0 - \sigma$ or $\eta(t) \geq \eta_0 + \sigma$. This trend is illustrated in Fig.14 (first row), where lower RMSE values are generally associated with experiments in which the proportion of neurons outside the central interval $(\eta_0 - \sigma, \eta_0 + \sigma)$ is minimized. Furthermore, Fig. 14 (second row) shows the output layer weights plotted against η for all neurons in the worst-performing experiments with $\sigma = 0.4$ and $\sigma = 0.5$. The results reveal that neurons with extreme η values typically acquire vanishing output weights, suggesting that they contribute negligibly to the computation of the desired output.

This behavior may be partly explained by the role of $\eta(t)$ in modulating the nonlinear term in Eq. (2.14). For $\eta = 0$ the system exhibits a fixed point; as η increases, the system remains at a fixed point until it transitions through periodic dynamics and, eventually, into deterministic chaos [7, 19]. Thus, when $\eta(t)$ attains large values at certain times, the resulting modulation can destabilize the system.

Moreover, because $\eta(t)$ multiplies the nonlinear term in Eq.(2.14), it simultaneously regulates both the recurrent feedback connections—via the nonlinear function's argument—and the effective inter-neuron couplings, since in Eq.(2.9) the term $\eta_i \Delta_{ij}$ can be interpreted as an effective connection weight. Consequently, the distribution of $\eta(t)$ directly shapes the reservoir's internal connectivity structure [10]. In echo state networks, it is well established that the spectral radius of the recurrent weight matrix must satisfy $\rho(\mathbf{W}_{\text{res}}) \leq 1$ to preserve the Echo State Property [6, 8], while increasing the spectral radius pushes the reservoir toward a chaotic regime, raising the conditional Lyapunov exponent and enhancing memory capacity [7]. By analogy, large η values may effectively increase the spectral radius, risking destabilization, whereas very small values may suppress recurrent contributions and weaken memory. Reservoirs with fewer extreme $\eta(t)$ values, therefore, may strike a more favorable balance, maintaining stability while preserving sufficient memory capacity to achieve accurate autonomous predictions.

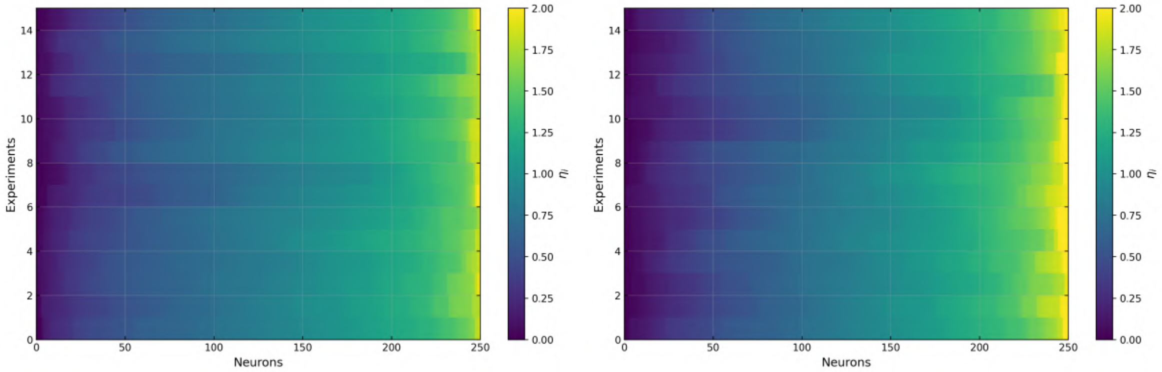

Figure 13: $\eta(t)$ values drawn from a Gaussian distribution and assigned to each virtual neuron across 15 experiments for $\sigma = 0.4$ Left: and $\sigma = 0.5$. Right: Experiments are ordered according to their one-step prediction RMSE, with index 0 corresponding to the best performance (lowest RMSE) and index 14 to the worst performance (highest RMSE).

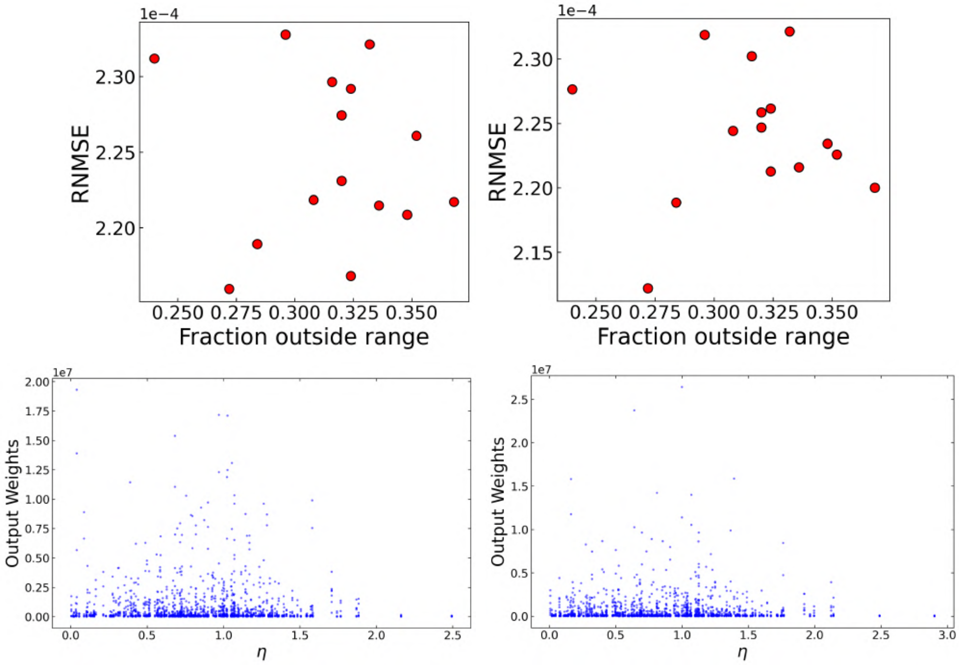

Figure 14: First Row: Root mean square error (RMSE) of one-step-ahead predictions for single-delay reservoir experiments, where $\eta(t)$ is drawn from a normal distribution. The RMSE is plotted against the fraction of virtual neurons with η values outside the central range $(0.85 - \sigma, 0.85 + \sigma)$, for two cases: $\sigma = 0.4$ (left) and $\sigma = 0.5$ (right). Second Row: Output layer weights as a function of η for neurons in the reservoir. Left: worst-performing experiment (highest RNMSE) with $\sigma = 0.4$. Right: worst-performing experiment (highest RNMSE) with $\sigma = 0.5$.

3.4 Lorenz-63 system

The third time series used to evaluate feedback time-modulation is the Lorenz system, defined by the set of differential equations:

$$\dot{x} = \sigma(x - y), \tag{3.9}$$

$$\dot{y} = x(\rho - z) - y, \tag{3.10}$$

$$\dot{z} = xy - \beta z, \tag{3.11}$$

where the parameters σ, ρ, and β govern the system's dynamics. In this work, the canonical Lorenz-63 parameters are employed: $\sigma = 10$, $\rho = 28$, and $\beta = 8/3$ [16]. With this parameter set, the largest Lyapunov exponent is $\Lambda_1 = 0.906$, confirming that the system exhibits strongly chaotic behavior.

To generate the time series, Eq. (3.9) was integrated using a fourth-order Runge–Kutta scheme with a time step of $dt = 0.002$ for $N = 60{,}000$ points. To reduce redundancy and match the treatment of previous benchmarks, only every tenth value was retained, yielding an effective sequence of $N = 6{,}000$ data points. The initial conditions were set to $x_0 = 0.9$, $y_0 = 1.0$, and $z_0 = 1.1$. As in the Mackey–Glass case, the input was normalized according to Eq. (3.8), and white noise with amplitude $\alpha = 1 \cdot 10^{-7}$ was added. Finally, the dataset was divided into training, test, and validation subsets, with $N_{\text{train}} = 4{,}000$, $N_{\text{test}} = 1{,}000$, and $N_{\text{validation}} = 1{,}000$ points, respectively.

Simulations are performed with a reservoir of $D = 350$ neurons. Only one delay reservoir has been tested since it has shown more significant effects with the introduction of feedback in time modulation. Other reservoir parameters are kept as described in Section 3.1.

Hyperparameter optimization The γ, η_0 optimization has been done as in the Mackey-Glass system through exploration of the RMSE for one-step prediction in parameter space and checking that it can reproduce autonomously the dynamics of the attractor for approximately a one lyapunov time. Figure 15 shows the RMSE across the explored parameter space. The point that minimizes the RMSE of one-step ahead prediction has been found at $(\gamma, \eta) = (1.1, 0.36)$.

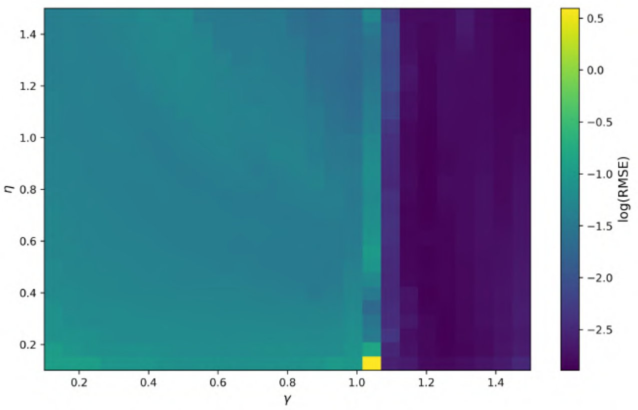

Figure 15: One-step ahead prediction of Lorenz time series in the parameter space (γ, η) of one-delay reservoir.

Results The overall results for the Lorenz time series obtained with the one-delay reservoir (Eq.(2.14)) are presented in Figures16 and 17 for the cases $\eta(t) \sim \mathcal{N}(0.36, \sigma)$ and $\eta(t) \sim \mathcal{U}(0.36 - \Delta, 0.36 + \Delta)$, respectively. In both cases, the RNMSE of the one-step-ahead prediction decreases for $\sigma \leq 0.2$ and $\Delta \leq 0.2$, indicating improved reservoir performance. For the Gaussian case, the expected improvement at $\sigma = 0.2$ is $(28 \pm 11)\%$ with respect to the optimal point, while for the uniform case the corresponding improvement at $\Delta = 0.2$ is $(25 \pm 20)\%$. Regarding divergence time, the Gaussian distribution shows a trend similar to that observed in the two-delay Mackey–Glass reservoir: although the expected divergence time decreases compared to the optimal point, it nevertheless increases with σ up to $\sigma = 0.3$, and in some realizations surpasses the performance of the optimal case. In contrast, for the uniform distribution, the expected divergence time decreases with Δ.

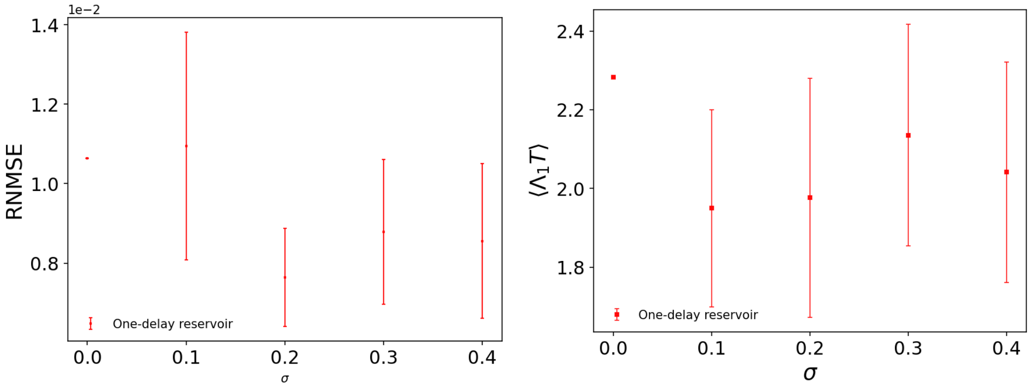

Figure 16: Results for the single delay reservoir (Eq. (2.14) with $\eta(t;\sigma)$ sampled from a normal distribution $\mathcal{N}(0.36,\sigma)$. Left: Average RNMSE of one-step ahead prediction (Eq. (3.1) over 15 experiments for each value of σ. Right: Average divergence time τ_ϵ obtained from 15 autonomous reconstruction experiments for each σ with $\epsilon = 0.01$ and $K = 10$.

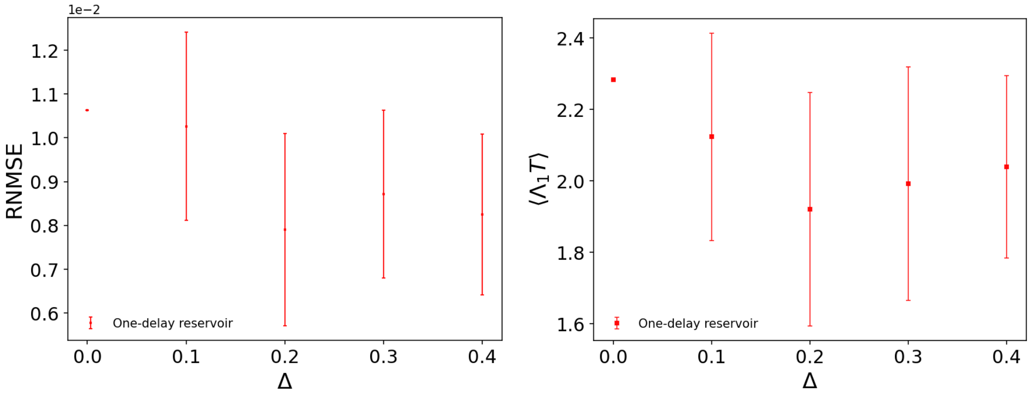

Figure 17: Results for the single delay reservoir (Eq. (2.14)) with $\eta(t;\sigma)$ sampled from a normal distribution $\mathcal{U}(0.36-\Delta, 0.36+\Delta)$. Left: Average RNMSE of one-step ahead prediction (Eq. (3.1)) over 15 experiments for each value of σ. Right: Average divergence time τ_ϵ obtained from 15 autonomous reconstruction experiments for each σ with $\epsilon = 0.01$ and $K = 10$.

As in the Mackey–Glass case, there are particular instances where temporal feedback modulation through $\eta(t)$ produces reservoirs that surpass the performance of the optimal point, as shown in Fig.18 and Fig.19. In the best cases, the reservoir was able to follow the Lorenz dynamics for up to $\sim 3\Lambda_1^{-1} \approx 3.3$ time units, but not beyond. Reservoirs with $\eta(t)$ drawn from a normal distribution generally exhibited higher stability than those with $\eta(t)$ drawn from a uniform distribution. However, full reconstruction of the Lorenz dynamics and attractor was not achieved beyond this timescale. As noted in [8, 13], improving reconstruction performance likely requires explicitly embedding the symmetries of Eq. (3.9) into the reservoir.

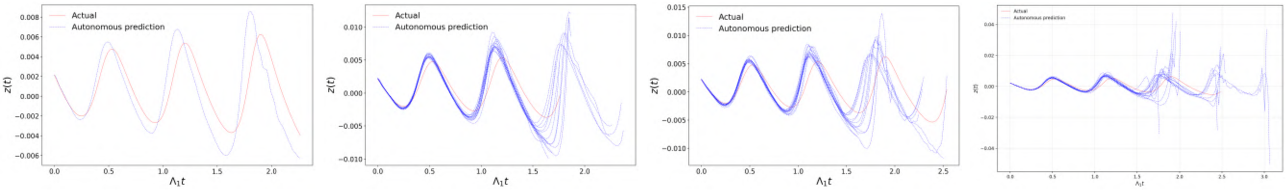

Figure 18: Autonomous prediction of the Lorenz-63 system using the single delay reservoir (Eq. (2.14) with $\eta(t;\sigma)$ drawn from a normal distribution $\mathcal{N}(0.36, \sigma$. The first plot on the left corresponds with $\sigma = 0$ and the next ones with σ increasing in steps of 0.1.

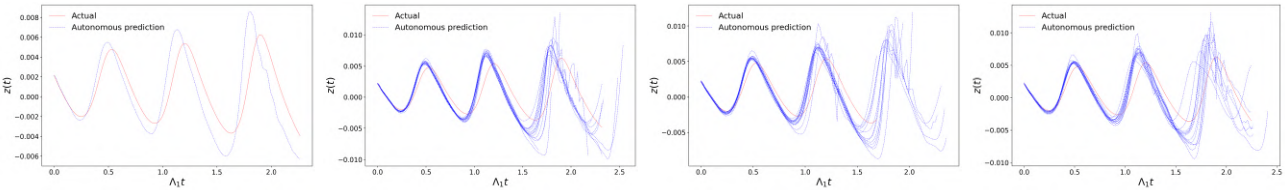

Figure 19: Autonomous prediction of the Lorenz-63 system using the single delay reservoir (Eq. (2.14) with $\eta(t;\sigma)$ drawn from a uniform distribution $\mathcal{U}(0.36, \sigma)$. The first plot on the left corresponds with $\sigma = 0$ and the next ones with σ increasing in steps of 0.1.

4 Conclusions

In this work, we have investigated the effect of temporally modulated feedback in a single-node time-delayed reservoir across several benchmark tasks. We found that introducing variability in the feedback modulation through the nonlinear term in a single-delay reservoir consistently improved the accuracy of one-step-ahead predictions for NARMA-10, Mackey–Glass, and Lorenz-63 when $\eta(t)$ was sampled from either a uniform or a normal distribution. In all three cases, the maximal improvement in prediction due to the introduction of variability is observed when $\eta(t)$ is drawn from a normal distribution. By contrast, direct modulation of the feedback coefficients in a two-delay reservoir yielded no improvement for NARMA-10 and only a reduction in RNMSE for Mackey–Glass at specific values of the modulation strength $\beta(t)$.

For autonomous dynamics reconstruction, nonlinear feedback modulation proved particularly beneficial in the Mackey–Glass system, where it enhanced both prediction accuracy and divergence time. In the best-performing experiments, temporal modulation enabled the reservoir to reproduce the system dynamics for up to five Lyapunov times, substantially surpassing the performance of the optimal modulation-fixed reservoir. Consistent with the results for the next-step prediction task, the largest improvements—both in terms of experiment averages and individual realizations—were obtained when $\eta(t)$ was sampled from a normal distribution. In the Lorenz system, an increment in average divergence time was also observed exclusively when $\eta(t)$ followed a Gaussian distribution. It should be studied how the introduction of symmetry consideration in the reservoir affects these results. By contrast, direct modulation of the feedback coefficients in a two-delay reservoir showed no systematic improvement: while certain experiments outperformed the optimal case in Mackey–Glass, no consistent gains with respect to the optimal case were observed on average.

Taken together, these results indicate that performance gains are most pronounced when variability in the feedback is introduced within a controlled range, avoiding extreme values of $\eta(t)$ that destabilize the reservoir.

Further research should investigate the effects of temporal feedback modulation for different values of θ, which define the effective feedback connectivity between virtual neurons, as well as for varying numbers of virtual neurons. In addition, the influence of temporal modulation in multiple-delay reservoirs should be systematically analyzed in the context of the Lorenz system. More broadly, future work is required to identify the specific characteristics of $\eta(t)$ that are responsible for enhancing reservoir performance, and to clarify the mechanisms by which temporal modulation alters the reservoir dynamics.

Acknowledgments

I would like to express my deepest gratitude to my supervisor, Silvia Ortín, for her invaluable guidance, constant support, and encouragement throughout this project. Her expertise and mentorship have been fundamental to the completion of this work. I am also sincerely grateful to the friends I have made during the SURF fellowship, whose companionship and enthusiasm made this experience truly unforgettable. I would also like to thank the SURF coordinators for their dedication and support in organizing this fellowship. This work was supported by the SURF@IFISC fellowship.

References

[1] Guoqi Li et al. “Brain-Inspired Computing: A Systematic Survey and Future Trends”. English. In: *Proceedings of the IEEE* 112.6 (2024). Publisher Copyright: © 1963-2012 IEEE., pp. 544–584. ISSN: 0018-9219. DOI: `10.1109/JPROC.2024.3429360`.

[2] Wolf Singer. “The Cerebral Cortex: A Delay-Coupled Recurrent Oscillator Network?” In: *Reservoir Computing: Theory, Physical Implementations, and Applications*. Ed. by Kohei Nakajima and Ingo Fischer. Singapore: Springer Singapore, 2021, pp. 3–28. ISBN: 978-981-13-1687-6. DOI: `10.1007/978-981-13-1687-6_1`. URL: `https://doi.org/10.1007/978-981-13-1687-6_1`.

[3] Herbert Jaeger and Harald Haas. “Harnessing Nonlinearity: Predicting Chaotic Systems and Saving Energy in Wireless Communication”. In: *Science* 304.5667 (2004), pp. 78–80. DOI: `10.1126/science.1091277`. eprint: `https://www.science.org/doi/pdf/10.1126/science.1091277`. URL: `https://www.science.org/doi/abs/10.1126/science.1091277`.

[4] Michael te Vrugt. *An introduction to reservoir computing*. 2024. arXiv: `2412.13212 [cs.ET]`. URL: `https://arxiv.org/abs/2412.13212`.

[5] Peter Dominey, Michael Arbib, and Jean-Paul Joseph. “A Model of Corticostriatal Plasticity for Learning Oculomotor Associations and Sequences”. In: *Journal of Cognitive Neuroscience* 7.3 (July 1995), pp. 311–336. ISSN: 0898-929X. DOI: `10.1162/jocn.1995.7.3.311`. eprint: `https://direct.mit.edu/jocn/article-pdf/7/3/311/1932498/jocn.1995.7.3.311.pdf`. URL: `https://doi.org/10.1162/jocn.1995.7.3.311`.

[6] David Verstraeten and Benjamin Schrauwen. “On the Quantification of Dynamics in Reservoir Computing”. In: *Artificial Neural Networks – ICANN 2009*. Ed. by Cesare Alippi et al. Berlin, Heidelberg: Springer Berlin Heidelberg, 2009, pp. 985–994. ISBN: 978-3-642-04274-4.

[7] Masanobu Inubushi et al. “On the Characteristics and Structures of Dynamical Systems Suitable for Reservoir Computing”. In: *Reservoir Computing: Theory, Physical Implementations, and Applications*. Ed. by Kohei Nakajima and Ingo Fischer. Singapore: Springer Singapore, 2021, pp. 97–116. ISBN: 978-981-13-1687-6. DOI: `10.1007/978-981-13-1687-6_5`. URL: `https://doi.org/10.1007/978-981-13-1687-6_5`.

[8] Joseph D. Hart. “Attractor reconstruction with reservoir computers: The effect of the reservoir’s conditional Lyapunov exponents on faithful attractor reconstruction”. In: *Chaos: An Interdisciplinary Journal of Nonlinear Science* 34.4 (Apr. 2024), p. 043123. ISSN: 1054-1500. DOI: `10.1063/5.0196257`. eprint: `https://pubs.aip.org/aip/cha/article-pdf/doi/10.1063/5.0196257/19869739/043123\_1\_5.0196257.pdf`. URL: `https://doi.org/10.1063/5.0196257`.

[9] L. Appeltant et al. “Information processing using a single dynamical node as complex system”. In: *Nature Communications* 2.1 (Sept. 2011), p. 468. ISSN: 2041-1723. DOI: `10.1038/ncomms1476`. URL: `https://doi.org/10.1038/ncomms1476`.

[10] Daniel Brunner, Miguel C. Soriano, and Guy Van der Sande, eds. *Optical Recurrent Neural Networks*. Berlin, Boston: De Gruyter, 2019. ISBN: 9783110583496. DOI: `doi:10.1515/9783110583496`. URL: `https://doi.org/10.1515/9783110583496`.

[11] Silvia Ortín et al. “A Unified Framework for Reservoir Computing and Extreme Learning Machines based on a Single Time-delayed Neuron”. In: *Scientific Reports* 5 (Oct. 2015), p. 14945. DOI: `10.1038/srep14945`.

[12] Tobias Hülser et al. “Role of delay-times in delay-based photonic reservoir computing”. In: *Opt. Mater. Express* 12.3 (Mar. 2022), pp. 1214–1231. DOI: `10.1364/OME.451016`. URL: `https://opg.optica.org/ome/abstract.cfm?URI=ome-12-3-1214`.

[13] Jaideep Pathak et al. "Using machine learning to replicate chaotic attractors and calculate Lyapunov exponents from data". In: *Chaos: An Interdisciplinary Journal of Nonlinear Science* 27.12 (Dec. 2017), p. 121102. ISSN: 1054-1500. DOI: `10.1063/1.5010300`. eprint: `https://pubs.aip.org/aip/cha/article-pdf/doi/10.1063/1.5010300/14614073/121102\_1\_online.pdf`. URL: `https://doi.org/10.1063/1.5010300`.

[14] J. -P. Eckmann and D. Ruelle. "Ergodic theory of chaos and strange attractors". In: *Rev. Mod. Phys.* 57 (3 July 1985), pp. 617–656. DOI: `10.1103/RevModPhys.57.617`. URL: `https://link.aps.org/doi/10.1103/RevModPhys.57.617`.

[15] Anwar Sadath, Thomas K. Uchida, and C. P. Vyasarayani. *Approximating strange attractors and Lyapunov exponents of delay differential equations using Galerkin projections*. 2018. arXiv: `1810.01016 [physics.comp-ph]`. URL: `https://arxiv.org/abs/1810.01016`.

[16] Chester Wringe, Martin Trefzer, and Susan Stepney. *Reservoir Computing Benchmarks: a tutorial review and critique*. 2025. DOI: `https://doi.org/10.1080/17445760.2025.2472211`. arXiv: `2405.06561 [cs.ET]`. URL: `https://arxiv.org/abs/2405.06561`.

[17] Michael C. Mackey and Leon Glass. "Oscillation and Chaos in Physiological Control Systems". In: *Science* 197.4300 (1977), pp. 287–289. DOI: `10.1126/science.267326`. eprint: `https://www.science.org/doi/pdf/10.1126/science.267326`. URL: `https://www.science.org/doi/abs/10.1126/science.267326`.

[18] J.Doyne Farmer, Edward Ott, and James A. Yorke. "The dimension of chaotic attractors". In: *Physica D: Nonlinear Phenomena* 7.1 (1983), pp. 153–180. ISSN: 0167-2789. DOI: `https://doi.org/10.1016/0167-2789(83)90125-2`. URL: `https://www.sciencedirect.com/science/article/pii/0167278983901252`.

[19] Miguel C. Soriano et al. "Delay-Based Reservoir Computing: Noise Effects in a Combined Analog and Digital Implementation". In: *IEEE Transactions on Neural Networks and Learning Systems* 26.2 (2015), pp. 388–393. DOI: `10.1109/TNNLS.2014.2311855`.

Decoding the Brain: How Neuronal Morphology Shapes Dynamics and Function

Nuria Balbás, Dimitrios Chalkiadakis, Leonardo Lyra Gollo
Instituto de Física Interdisciplinar y Sistemas Complejos, IFISC (CSIC-UIB)
Campus Universitat de les Illes Balears, E-07122 Palma de Mallorca, Spain

Abstract

Neurons, the fundamental building blocks of the brain, exhibit diverse morphologies that critically shape their dynamics and function. Alterations of neuronal structure, such as those arising from aging or neurological disorders, raise the key neurophysics question of how morphology influences information processing. In this work, we address this problem using a biologically plausible computational model of a pyramidal neuron, implemented with compartmentalized dendrites. By systematically applying dendritic pruning, we analyze how changes in morphology affect three core functional parameters: energy consumption, firing rate and dynamic range. These results provide mechanistic insights into the role of dendritic complexity in neural coding and offer a framework for interpreting the functional consequences of morphological alterations in health and disease.

1 Introduction

Neurons are the fundamental processing units of the brain. They receive information from thousands of synaptic contacts, integrate these inputs through their complex dendritic trees, and generate action potentials or spikes that travel along the axon to communicate with other neurons. A spike represents the basic unit of neuronal output, and can be defined as a rapid depolarization of the membrane potential, encoding the neuron's decision to respond to its inputs. This output is typically measured as the firing activity at the soma and across dendritic compartments, linking dendritic integration to neuronal communication.

Despite their central role, the function and behaviour of dendritic trees is not yet fully uderstood. Traditional neuron models often simplify dendrites as passive conductive cables or reduce them to point neurons, thereby underestimating their contribution to computation. However, accumulating evidence has revealed that dendrites exhibit active properties, including local dendritic spikes and nonlinear integration, which strongly influence somatic profiling profiles [1]. While previous studies have examined dendritic function using simplified models [2, 3, 4], none have systematically investigated how dendritic pruning affects neuronal dynamics in a multicompartmental model operating in continuous time, a framework that more closely reflects biological conditions.

In this work, we address this gap by simulating a multicompartmental pyramidal neuron model from Figure 1 implemented using the Dendrify [5] library on top of the Brian2 [6] simulator. The model explicitly represents multiple dendritic branches, each capable of receiving synaptic input and eliciting subthreshold responses or dendritic spikes. To assess how dendritic complexity shapes neuronal function, we systematically prune by reducing the number of dendritic branches, thereby generating simplified morphologies of the same neuron. Computational modeling offers precise control over these manipulations, enabling direct monitoring of how structural changes alter function, even in highly complex dendritic trees [1]. An example of the spiking rate output across the different dendritic compartments and soma can be seen in Figure 2, illustrating the compartmental behaviour under varying Poisson input frequencies.

We focus on three fundamental parameters: the firing rate, dynamic range and energy consumption. Studying these parameters in relation to dendritic morphology provides insight into the trade-offs between efficiency and computational power in neurons. By comparing models with different degrees of pruning, we examine how structure supports function, and how simplification

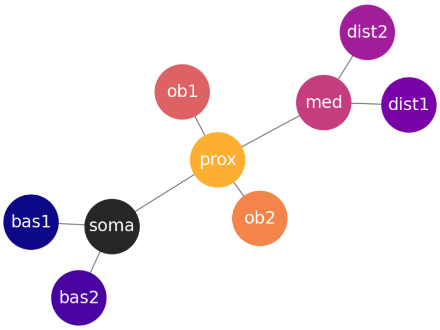

Figure 1: Schematic of the pyramidal multicompartmental neuronal model with the compartments and implemented connections.

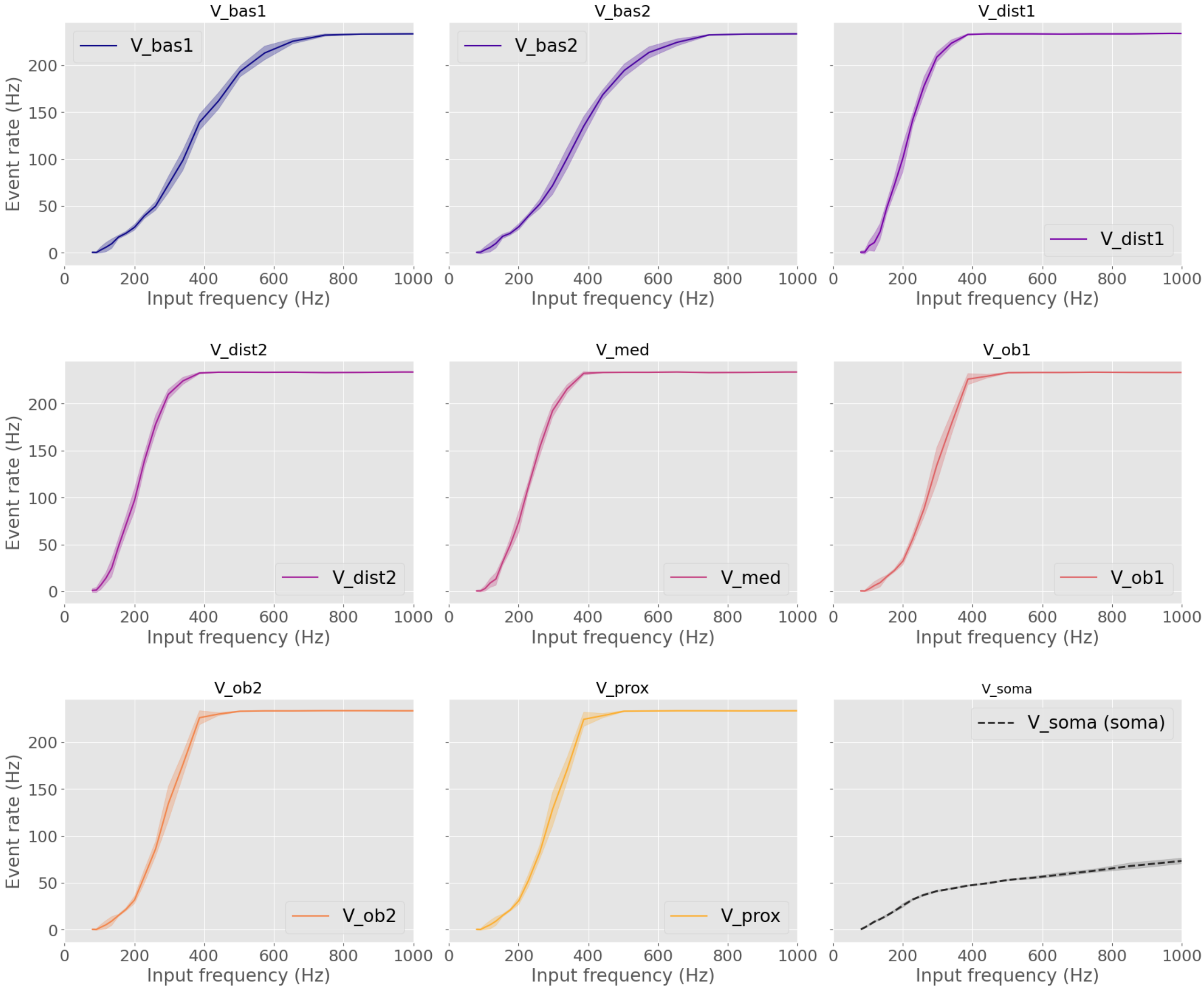

Figure 2: Spiking rate of the different compartments and the soma for varying input with the standard deviation from 10 trials.

degrades specific aspects of neuronal dynamics.

The main objective of this project was therefore to analyze how different dendritic morphologies affect neural dynamics and function in a continuous timescale, using computational simulations of a biophysical compartmental neural model based on Dendrify and Brian2. To illustrate the modeling approach, Figure 3 shows the compartmental structure of the model and the pruning strategies applied. It was seen that pruning reduces dendritic complexity, resulting in a trade-off: the decrease of metabolic cost at the expense of a lower dynamic range.

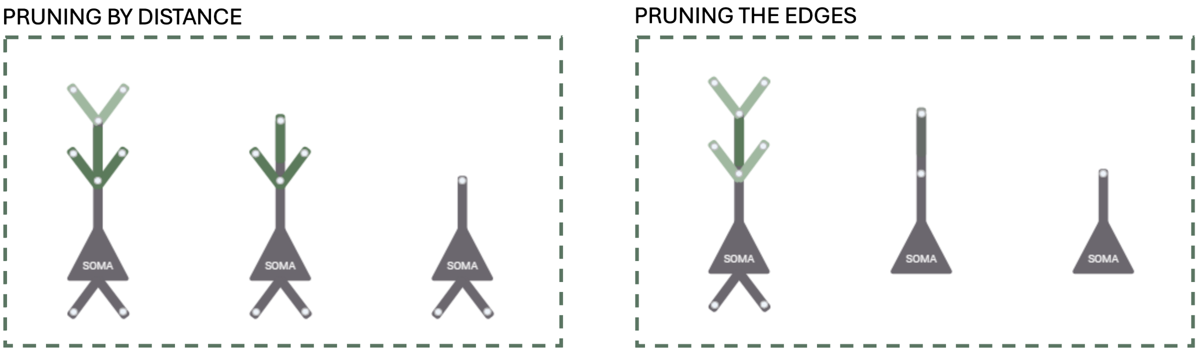

Figure 3: Pruning steps implemented for the different pruning techniques used.

2 Theoretical Model

The simulations were conducted using a 9-compartmental pyramidal model designed to emulate the behaviour of excitatory neurons from the CA1 area of the hippocampus, with 1 soma and 8 dendritic branches. The initial experimentally validated model was obtained from [5], however for this study, Poisson inputs with different frequencies were fed to all of its compartments (Equation 2.1), where ($\delta t = 1ms$) is an arbitrary time step, as defined in [2].

$$p_h \equiv 1 - \exp(-h\delta t) \tag{2.1}$$

The equations from the model are described from Eq. 2.2 to Eq. 2.11 obtained from [5].The neuron model and equations were implemented using the Dendrify library on top of the Brian2 simulator (and forward Euler integration), which enabled explicit represenntation of dendritic branches with active ionic conductances. each of the 9 compartments of the model (1 soma and 8 dendrites), had biophysically motivated parameters (membrane capacitance, leak conductance, and reversal potentials), derived from experimental pyramidal cell data. Whilst the soma captured spike-frequency adaptation, dendritic compartments allowed the generation of local dendritic spikes. The compartments were coupled through axial currents to ensure realistic electrotonic interactions between soma and dendrites.

The somatic compartment modeled was an integrate and fire (I&F) model Eq. (2.2), that had conductance-based adaptation Eq. (2.3).

$$C_m^s \frac{dV_m^s}{dt} = -g_L^s \left(V_m^s - E_L^s\right) - g_A \left(V_m^s - E_A\right) + \sum_{i \in C^s} \Gamma_a^{i,s} + \sum_{j \in S^s} \Gamma_{\text{syn}}^{j,s} + I_{\text{ext}}^s \tag{2.2}$$

$$\tau_A \frac{dg_A}{dt} = \bar{g}_A \left|V_m^s - V_A\right| - g_A \tag{2.3}$$

After a spike generation, a first reset drove the voltage to a high value (biological spike amplitude), whilst the conductance of the adaptation current incrementally increased by a constant amount (spike-triggered adaptation). Then, after a short decay, the voltage was reset. This is described in Eq. (2.4), (2.5)

$$\text{if } V_m^s > V_{th} \text{ then } \begin{cases} V_m^s \leftarrow V_{spike} \\ g_A \leftarrow g_A + b \\ t_{spike} \leftarrow t \end{cases} \tag{2.4}$$

$$\text{if } t = t_{spike} + 0.5 \text{ ms then } V_m^s \leftarrow V_{reset} \tag{2.5}$$

In the case of the dendritic compartments, instead of the adaptation current from the soma, a sodium current for initiation and potassium current for repolarization, governed by Eq. (2.6) and Eq. (2.7) respectively, controlled the dynamics of the dendritic spikes.

For the sodium current to be activated, two conditions had to be met: a voltage threshold had to be crossed for fna to be 1, and the time had to be outside of the refractory period of the sodium current.

$$\text{if } \begin{cases} V^d > V^d_{th} \\ f_{Na} = 1 \\ t > t^d_{spike} + t^d_{ref} \end{cases} \quad \text{then } \begin{cases} g^d_{Na} \leftarrow g^d_{Na} + \bar{g}^d_{Na} \\ f_{Na} \leftarrow 0 \\ f_K \leftarrow 1 \\ t^d_{spike} \leftarrow t \end{cases} \tag{2.6}$$

On the other hand, the potassium current is generated once a delayed time has passed from the activation of the sodium current.

$$\text{if } \begin{cases} t > t^d_{spike} + t^{Kdr}_{offset} \end{cases} \quad \text{then } \begin{cases} g^d_{Kdr} \leftarrow g^d_{Kdr} + \bar{g}^d_{Kdr} \\ f_{Na} \leftarrow 1 \\ f_{Kdr} \leftarrow 0 \end{cases} \tag{2.7}$$

As the soma and dendrites are connected, in this multicompartemntal neural model each of the compartments receives a current (”axial current”) from connected compartments (Ck), defined by Equation2.8.

$$I^k_a = \sum_{i \in \mathcal{C}^k} I^{i,k}_a \tag{2.8}$$

It is of importance to note that the specific-axial-current is defined by the coupling conductance, and is dependent on the morphological properties assigned to each compartment.

The synaptic currents flowing to each compartment were AMPA and NMDA, being the mathematical description Equation 2.9, and syn the type of synapse (AMPA or NMDA).

$$s^i_{syn}(t) = H(t - t_{pre}) \left(\exp\left(\frac{t - t_{pre}}{\tau^{decay}_{syn}} \right) - \exp\left(\frac{t - t_{pre}}{\tau^{rise}_{syn}} \right) \right) \tag{2.9}$$

While for the AMPA current, the voltage dependence was neglected, the NMDA currents (voltage-dependent due to a magnesium blockade, captures nonlinear dendritic integration) followed Equation 2.10

$$\sigma(V^i_m) = \frac{1}{1 + \left[\frac{[Mg^{2+}]}{\beta}\right] \cdot \exp\left(-\alpha(V^i_m - \gamma)\right)} \tag{2.10}$$

Finally, the total synaptic current of a compartment (i), is obtained from the summation of all incoming currents (Equation 2.11) from its presynaptic connections, which can be of different or the same type of synapses, and can be received simultaneously.

$$\begin{aligned} I^i_{syn}(t) = {} & \bar{g}^i_{AMPA}(V^i_m - E_{AMPA}) f_{AMPA} \sum_{j \in \mathcal{S}^i_{AMPA}} s^{j,i}_{AMPA}(t) \\ & + \bar{g}^i_{NMDA}(V^i_m - E_{NMDA}) f_{NMDA} \sum_{j \in \mathcal{S}^i_{NMDA}} s^{j,i}_{NMDA}(t) \\ & + \bar{g}^i_{GABA}(V^i_m - E_{GABA}) \sigma(V^i_m) f_{GABA} \sum_{j \in \mathcal{S}^i_{GABA}} s^{j,i}_{GABA}(t) \end{aligned} \tag{2.11}$$

The dendritic spikes properties and geometry of the compartments was maintained throughout the simulations, as well as the synaptic properties, which were all defined to be ca3 for both AMPA and NMDA synapses. All simulations had a simulated time of 1200ms, with the first 200ms discarded to avoid transient initialization effects. A timestep of 0.1ms was used, and each condition was repeated for 10 independent Poisson realizations to obtain average responses and variability.

3 Results and discussion

3.1 Firing Rates

The firing rate was calculated as the number of spikes per unit time at soma and dendrites, giving information of the excitability and integration efficiency. This parameter was obtained for the soma and dendritic compartments for each of the proposed neural models. Figure 4 shows the firing rate

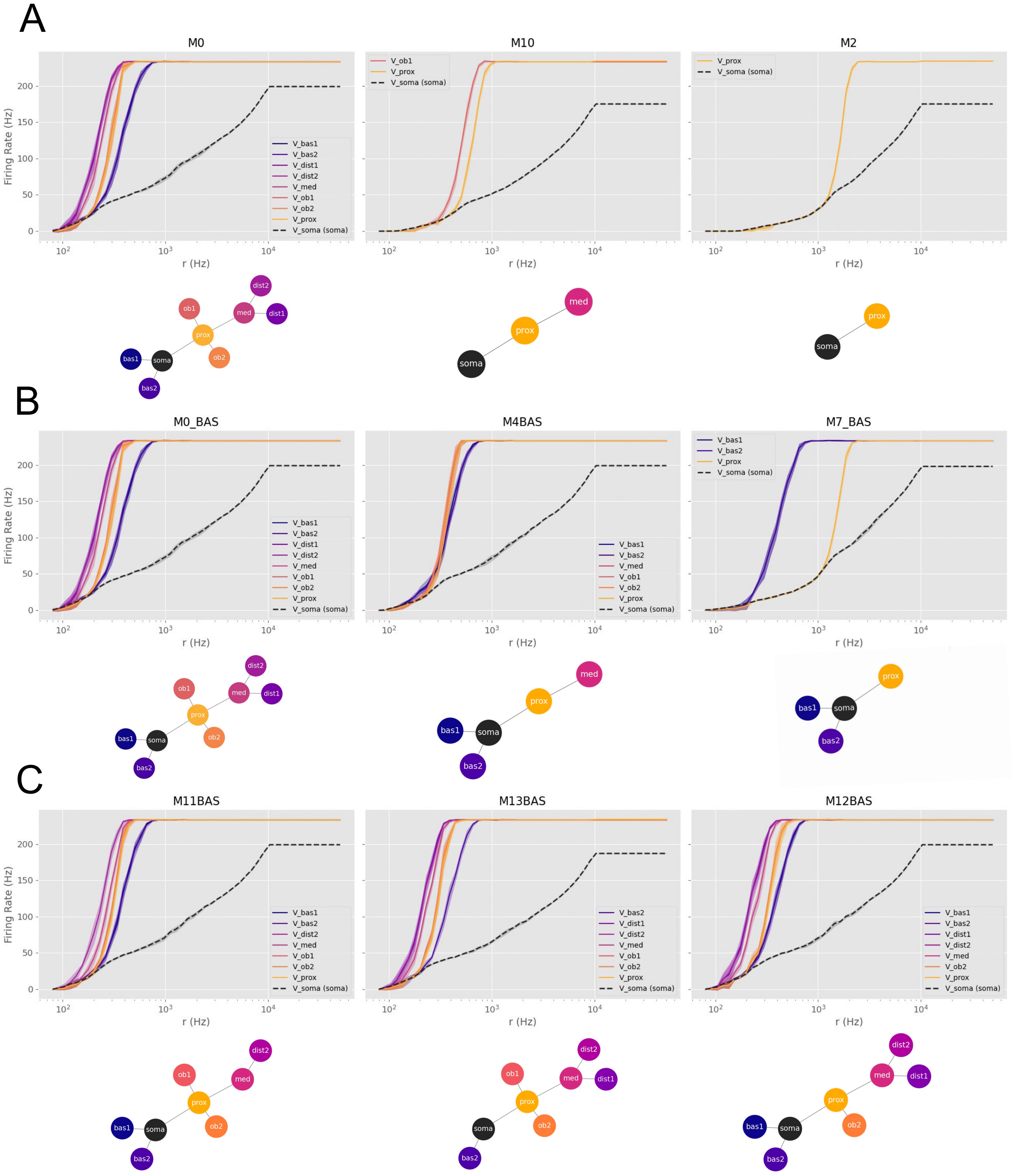

Figure 4: Dendritic and somatic firing rates across pruning stages. Row A shows the models corresponding to the pruning steps of distal pruning, row B shows the models corresponding to the pruning steps of edges pruning, and row C shows the models corresponding to the pruning steps of different pruning.

of each compartment based on the input frequency. The multicompartmental model reveals distinct firing profiles in this figure for dendritic compartments and the soma under increasing input frequencies. In the intact model (first model, ”M0”), the dendritic compartments display heterogeneous response curves, with the medial and distal branches saturating before the proximal, oblique and basal branches. Furthermore, the soma shows a more gradual sigmoidal increase, reflecting integration of distributed dendritic activity.

As dendritic pruning is applied (second and third columns), most dendritic compartments have similar, highly saturated response profiles, while the somatic response shows lower slope and reduced maximum frequency, suggesting that pruning diminishes the efficiency of somatic integration when it involves the removal of the basal dendritic compartments

Furthermore, Figure 5, showing the comparison between somatic firing rate functions across the three pruning strategies, highlights that pruning also reduces the capacity of the neuron to differentiate input regimes of small frequencies. Thus the neuron is less sensitive to small frequencies with less dendritic compartments.

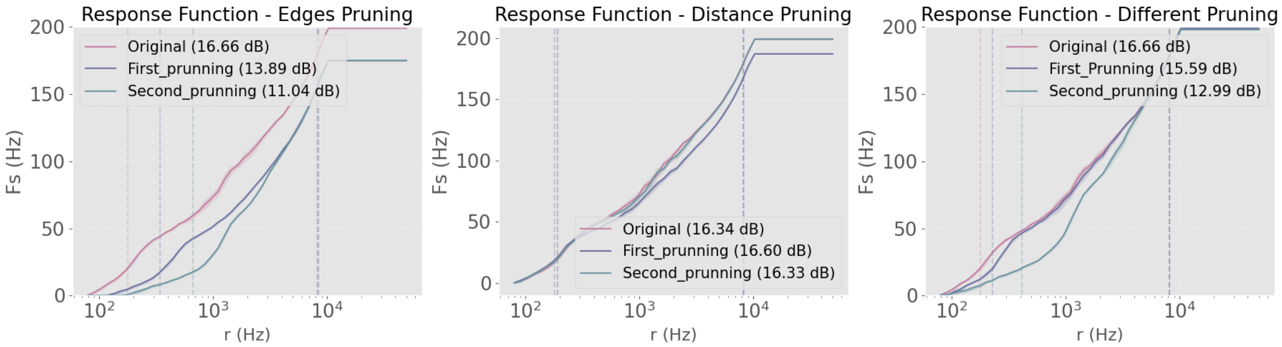

Figure 5: Somatic response functions under different pruning strategies.

3.2 Dynamic Range

The dynamic range, defined as the input frequencie values over which the neuron can distinguish changes in input intensity, was used as a measure of coding capacity. This parameter was calculated by obtaining the input frequency range that corresponded to the 10 % and 90% total somatic firing rate. A visual representation of an example of the response curve and limits for the dynamic range have been represented in Figure 6. The example shows a saturation band where the compartment cannot further distinguish input frequencies, as there is no change in the somatic firing rate, and the dynamic range, with the input frequencies that can be distinguished based on the somatic firing rate produced.

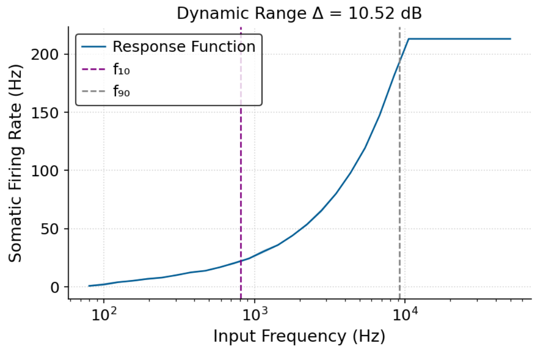

Figure 6: Example of the response function obtained for each of the models and compartments for a 1-compartmental neuron, showing the somatic firing rate for each input frequency value on a logarithmic scale.

After obtaining the response function and dynamic range for each of the multi-compartmental models, the dynamic range was seen to diminish throughout pruning steps, thus indicating that dendritic compartments increase the dynamic range of the neuron, shown in Figure 7, which agrees with the predictions from [2] and [3], which found that bifurcations played a major role in the increase of the dynamic range in neurons. This figure also shows that whilst the decrease in the dynamic range from the first pruning step is present in both pruning techniques, it is more noticeable in the edges technique. When observing the morphology, one of the possible hypothesis that would arise is that there are indeed less dendrites in the model with less dynamic range, thus being this characteristic the one to define the property and decrease, however, whilst the second step of edges pruning is greater than the third step of distance pruning, the model has two dendrites whilst the latter has three.

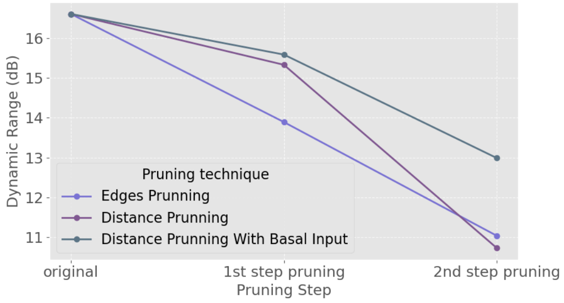

Figure 7: Dynamic range comparison between pruning steps within different pruning strategies.

Moreover, when representing the bar plots with the dynamic ranges of different compartments, it was seen that the dendritic dynamic ranges were also affected by the pruning, as seen in Figure 8, where the absence of dendritic compartments such as the oblique compartment, increased the dynamic range of the proximal dendritic compartment, seen in the third pruning step of the pruning of the edges. However, not all of the dendritic compartments are shown to change throughout pruning steps, an example being the oblique compartment, which does not vary throughout any pruning step of all three pruning techniques.

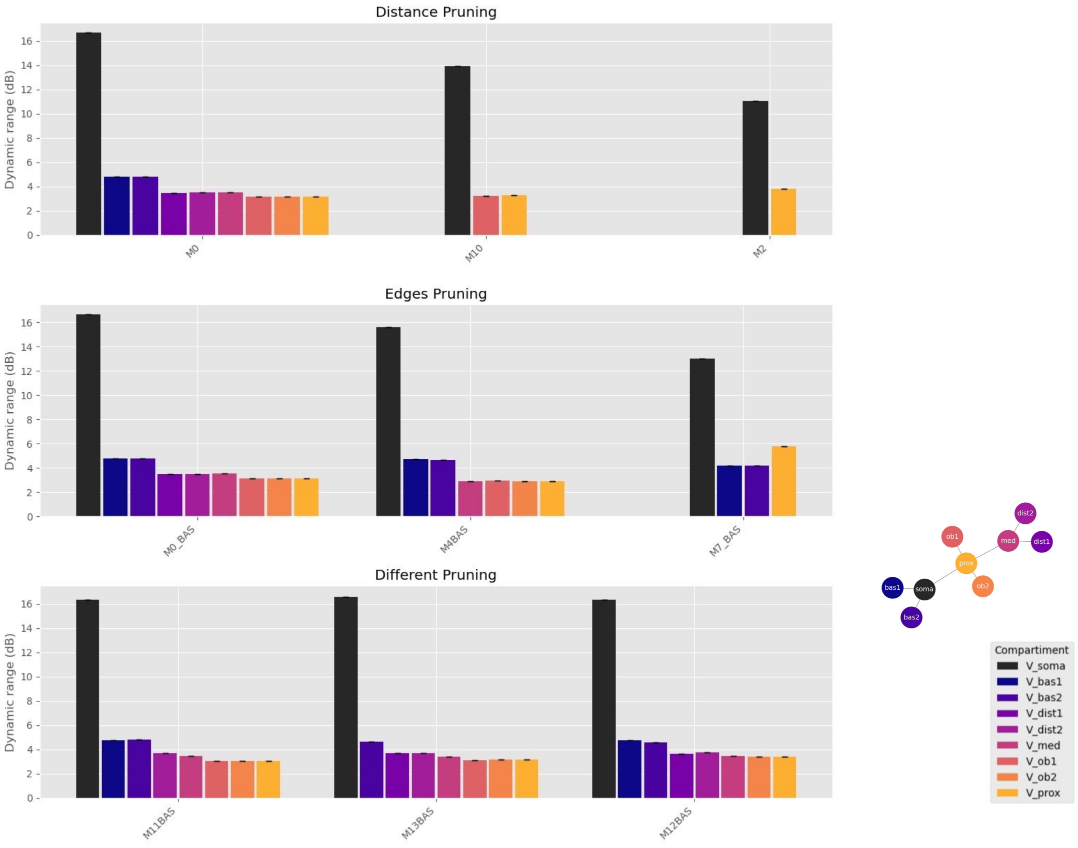

Figure 8: Compartmental dynamic range between different compartments, pruning steps and strategies.

3.3 Energy Consumption

Defined as the estimation from the ratio of dendritic spikes to somatic spikes, the parameter of energy consumption represents the metabolic cost of generating spikes relative to the effective output. A comparison of the energy consumption throughout different pruning steps has been represented in Figure 9. This figure suggests that the somatic firing rate does not only depend on the average dendritic firing rate, as even though this value becomes stagnant at somatic frequencies of 100Hz, the somatic firing rate keeps increasing. Moreover, when observing Figure 8, there may be a change in the morphology on the somatic response function once the dendritic response function saturates, suggesting a change in one of the factors that determines the somatic firing rate (the dendritic spike rate).

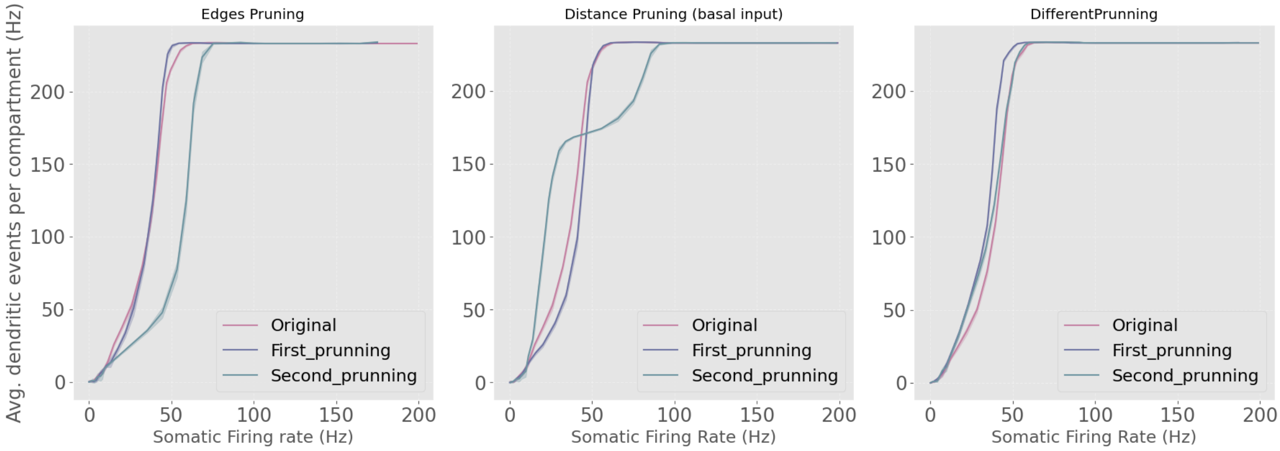

Figure 9: Energy consumption throughout pruning steps and pruning strategies.

When only observing the somatic firing rate range where there are variations on the average dendritic firing rate in Figure 10, the results suggest that, depending on the compartment that is being pruned, the energy consumption will be higher or lower (Figure 10C). The energy consumption shows to be higher when the basal compartment is removed, than when the medial or distal compartments are pruned for most of the somatic firing range where the dendritic firing rate varies. This is more clearly shown in Figure 11, that obtains the area under the curve before the dendritic spiking rate stagnation.

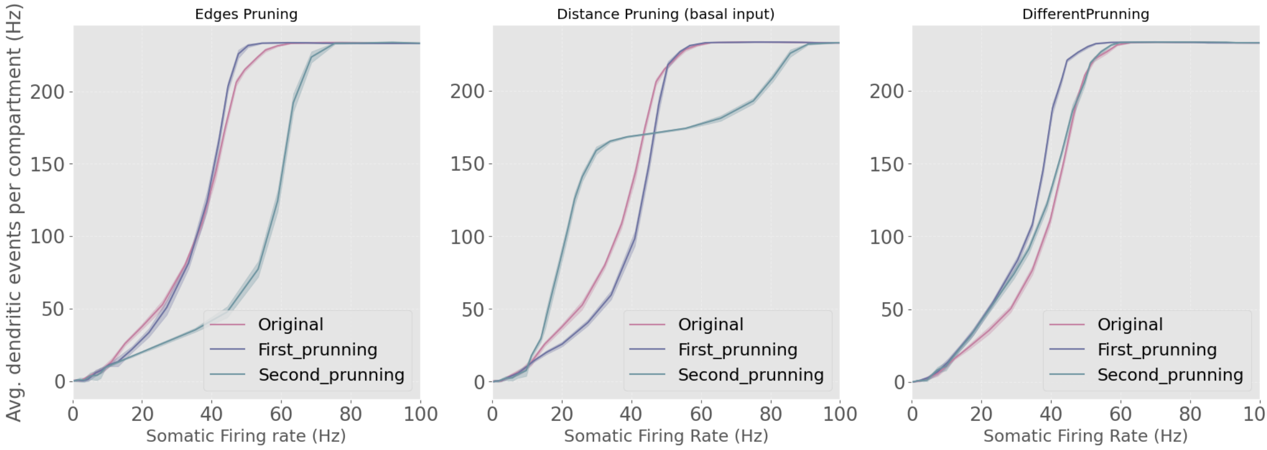

Figure 10: Zoomed graph of energy consumption throughout pruning steps and pruning strategies for somatic firing rate range of 0-100Hz.

Moreover, even though when pruning the neuron the energy consumption decreases, seen in the subplots of the first two pruning techniques for Figures 9 and 10 for the first two pruning steps, an abnormality is seen in the third pruning step of the distance pruning strategy. The energy consumption seems to increase at lower somatic firing rates, and decrease at higher somatic firing rates.

Interestingly, whilst in both the second pruning step of the edges pruning technique and the

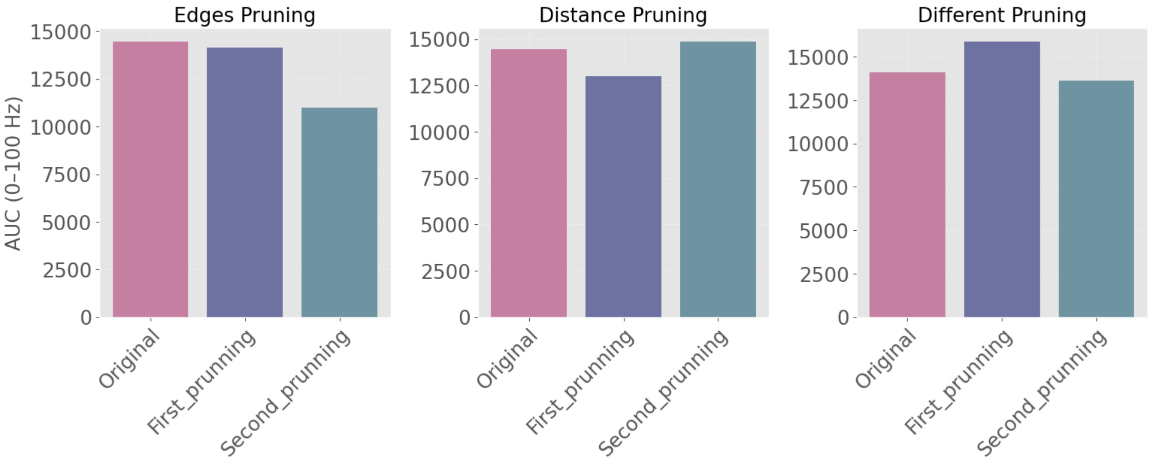

Figure 11: Area under the curve for the energy consumption throughout pruning steps and strategies for somatic firing rate range of 0-100Hz.

second pruning step of the distance pruning technique the only change between steps is the removal or the medial compartment, the change in the morphology of the energy consumption curve is different.

4 Conclusions

In this study, we investigated how dendritic morphology influences neural computation by systematically pruning branches of a multicompartmental pyramidal neuron model. By analyzing firing rates, dynamic range and energy consumption, we demonstrated that dendritic complexity plays a critical role in shaping neuronal dynamics and coding capacity. Specifically, pruning lowered the somatic dynamic range, altered the trade-off between integration efficiency and metabolic cost. Our results suggest that the presence of multiple dendritic compartments not only enhances sensitivity to weak inputs, but also broadens the range over which input intensities can be distinguished, thereby increasing the computational power of the neuron. At the same time, this comes at the expense of higher energetic demands, highlighting an evolutionary balance between efficiency and capacity. Moreover the results presented from the multi-compartmental model agree with the findings from simplified models such as [4]

Altogether, these findings support the view that dendritic structure is not a redundant anatomical detail, but a key determinant of neuronal function. Computational simplification via pruning revealed how morphology constrains both the efficiency and richness of neuronal computations. Furute work could extend this approach by incorporating different inputs, plasticity mechanisms and larger-scale network models such as [7], to better understand how dendritic architecture contributes to collective dynamics and information processing in cortical circuits.

Acknowledgments

This work was supported by the SURF@IFISC fellowship.

5 Appendix

References

[1] Panayiota Poirazi and Athanasia Papoutsi. "Illuminating dendritic function with computational models". In: *Nature Reviews Neuroscience* 21.6 (June 2020), pp. 303–321. ISSN: 1471-0048. DOI: `10.1038/s41583-020-0301-7`. URL: `https://www.nature.com/articles/s41583-020-0301-7`.

[2] Leonardo L. Gollo, Osame Kinouchi, and Mauro Copelli. “Active Dendrites Enhance Neuronal Dynamic Range”. In: *PLoS Computational Biology* 5.6 (June 2009), e1000402. ISSN: 1553-734X. DOI: `10.1371/journal.pcbi.1000402`. URL: `https://www.ncbi.nlm.nih.gov/pmc/articles/PMC2690843/`.

[3] Christoph Kirch and Leonardo L. Gollo. “Spatially resolved dendritic integration: towards a functional classification of neurons”. In: *PeerJ* 8 (Nov. 2020), e10250. ISSN: 2167-8359. DOI: `10.7717/peerj.10250`. URL: `https://peerj.com/articles/10250`.

[4] Christoph Kirch and Leonardo L. Gollo. “Single-neuron dynamical effects of dendritic pruning implicated in aging and neurodegeneration: towards a measure of neuronal reserve”. In: *Scientific Reports* 11 (Jan. 2021), p. 1309. ISSN: 2045-2322. DOI: `10.1038/s41598-020-78815-z`. URL: `https://www.ncbi.nlm.nih.gov/pmc/articles/PMC7809359/`.

[5] Michalis Pagkalos, Spyridon Chavlis, and Panayiota Poirazi. “Introducing the Dendrify framework for incorporating dendrites to spiking neural networks”. In: *Nature Communications* 14.1 (Jan. 2023), p. 131. ISSN: 2041-1723. DOI: `10.1038/s41467-022-35747-8`. URL: `https://www.nature.com/articles/s41467-022-35747-8`.

[6] Marcel Stimberg, Romain Brette, and Dan FM Goodman. “Brian 2, an intuitive and efficient neural simulator”. In: *eLife* 8 (), e47314. ISSN: 2050-084X. DOI: `10.7554/eLife.47314`. URL: `https://www.ncbi.nlm.nih.gov/pmc/articles/PMC6786860/`.

[7] Jacopo Bono and Claudia Clopath. “Modeling somatic and dendritic spike mediated plasticity at the single neuron and network level”. In: *Nature Communications* 8.1 (Sept. 2017), p. 706. ISSN: 2041-1723. DOI: `10.1038/s41467-017-00740-z`. URL: `https://doi.org/10.1038/s41467-017-00740-z`.

Spatiotemporal Dynamics of a Two-Species Model in a Flowing Environment

Ismaele Visentini, Nathan Silvano,
Instituto de Física Interdisciplinar y Sistemas Complejos, IFISC (CSIC-UIB)
Campus Universitat de les Illes Balears, E-07122 Palma de Mallorca, Spain

Abstract

The aim of the study is to explore the effects of space and advection in the spatiotemporal population dynamics of rivers. Treating the river as a 2D rectangular domain with periodic boundary condition we can observe the behavior of a two species system with interspecific competition related to space, diffusion and advection. Most of the work will focus on the Gray Scott model exploring pattern formation, Hops bifurcation and the role of advection in the stability of the steady states. For the Predator-Prey, we show that diffusion and advection don't have any role in the 2D extension, except for a phase shift. Instead we illustrate in the 2D Grey Scott that diffusion is crucial for the formation of spatial patterns and advection shifts the stability regions allowing the population to persists in areas where otherwise it would have gone extinct.

1 Introduction

Rivers are complex and dynamic systems, exhibiting significant variability in temperature, morphology, chemical and biological composition. The ecosystem dependency of so many parameters indicates that multiple studies are needed to fully comprehend these phenomena and their deviation from a normal behavior. Nowadays extreme events like severe drought and eutrophication are effecting the river species population worldwide causing the extinction of most of them [1] [3].
A classical approach would be using a 0D model between two interacting species in order to determine the effects from competition and the struggle for food. If we want to consider some space elements there exist two typical ways on how to model a segment of the river in the transfer zone. The cross sectional profile is used to describe the different behavior of the species varying the zone in deepness using a 1D model: from a bottom static benthic to a surface where the risk of washout is larger[4].

Instead we have adopted a top view (planform) approach that permits to focus on the interspecific interactions enlightening the role of a 2D space in the distribution and survival chance of the two species. The river domain will be a rectangle of sides $\{L_x, L_y\}$ with periodic boundary condition with the intention of eliminating spurious effects associated with external boundary variations, focusing on the bulk of the river. The flowing of the river $\bar{g}_x$ will be represented by a constant advection parallel to the x axis.

The first model is the Predator-Prey proposed by Vito Volterra between the two world wars in 1926 which tried to describe the behavior of preys like anchovies and sardines and predators like sharks and rays in the Mediterranean sea. It's a classical and well known conservative model which can't reproduce most of the dissipative behavior occurring in nature, but permitted to analyze the cycling temporal pattern and the counterintuitive effects of massive fishing.
The second is the Grey Scott which is a remarkable example of reaction diffusion model producing a big amount of different spatial patterns: dots, stripes, spirals, gliders, solitons and mazes. The instability analysis provides hints in order to find and classify the patterns, but most of the work is possible via computational methods.

2 Theoretical model

2.1 The 0D Predator-Prey model

It's a coupled ordinary differential equation system in which there are two terms that make preys grow and the predators die exponentially r and m and two terms of interspecific competition c and b. The 0D model is presented below:

$$\begin{cases} \frac{dN}{dt} = rN - cNP \\ \frac{dP}{dt} = -mP + bNP \end{cases} \tag{2.1}$$

where N is the number of prey and P the number of predator with $r, c, m, b > 0$ and $r, c, m, b \in \mathbb{R}$. With the following change of variables it is possible to reduce the free parameters of the model from 4 to 2 obtaining:

$$\begin{cases} x = \frac{b}{m}N \\ y = \frac{c}{r}P \end{cases} \tag{2.2}$$

$$\begin{cases} \frac{dx}{dt} = r(1-y)x \\ \frac{dy}{dt} = m(x-1)y \end{cases} \tag{2.3}$$

Now it is possible to calculate the nullclines obtaining 4 different stationary points: $(0, 0)$, $(0, 1)$, $(1, 0)$, $(1, 1)$. The nature of these points is mostly clear if we see the stability matrix that corresponds to the Jacobian matrix of the terms to the right.

$$A = \begin{pmatrix} r(1-y) & rx \\ my & m(x-1) \end{pmatrix} \tag{2.4}$$

That valued in the four steady states produce:

$$A_1 = A\Big|_{q^*=(0,0)} = \begin{pmatrix} r & 0 \\ 0 & -m \end{pmatrix} \tag{2.5a}$$

$$A_2 = A\Big|_{q^*=(1,0)} = \begin{pmatrix} r & r \\ 0 & 0 \end{pmatrix} \tag{2.5b}$$

$$A_3 = A\Big|_{q^*=(0,1)} = \begin{pmatrix} 0 & 0 \\ m & -m \end{pmatrix} \tag{2.5c}$$

$$A_4 = A\Big|_{q^*=(1,1)} = \begin{pmatrix} 0 & r \\ m & 0 \end{pmatrix} \tag{2.5d}$$

Calculating the trace and the determinant of each steady state we can determine the nature of the equilibria points:

$$\mathrm{tr}(A_1) = r - m > 0 \ \ \forall r > m > 0 \tag{2.6a}$$

$$\det(A_1) = -mr < 0 \ \ \forall m, r \tag{2.6b}$$

The point (0,0) is saddle because the trace is positive and the determinant is always negative.

$$\mathrm{tr}(A_2) = r > 0 \ \ \forall r \tag{2.6c}$$

$$\det(A_2) = 0 \ \ \forall m, r \tag{2.6d}$$

The point (1,0) cannot be easily determined because the determinant is null.

$$\mathrm{tr}(A_3) = -m < 0 \ \ \forall m \tag{2.6e}$$

$$\det(A_3) = 0 \ \ \forall m, r \tag{2.6f}$$

The point (0,1) cannot be easily determined because the determinant is null.

$$\mathrm{tr}(A_4) = 0 \ \ \forall m, r \tag{2.6g}$$

$$\det(A_3) = -rm < 0 \ \ \forall m, r \tag{2.6h}$$

The point (1,1) is a stable center because the trace is zero and the determinant is negative. We expect circular orbits near this point. The phase diagram for the 0D model is the following:

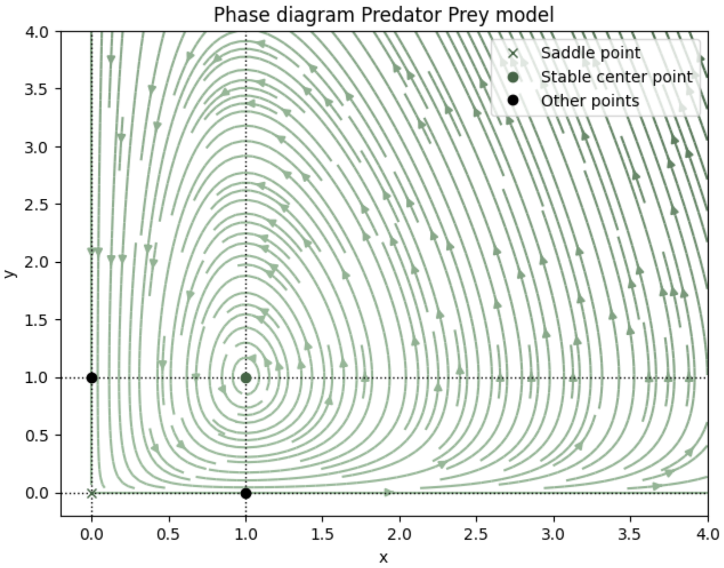

Figure 1: Phase diagram of the Predator Prey model. The nature of the points is specified in the legend. It is possible to see circular orbits near the stable point.

Integrating numerically with an Explicit Euler method it is possible to reconstruct the periodic orbits for an arbitrary initial point (x_0, y_0):

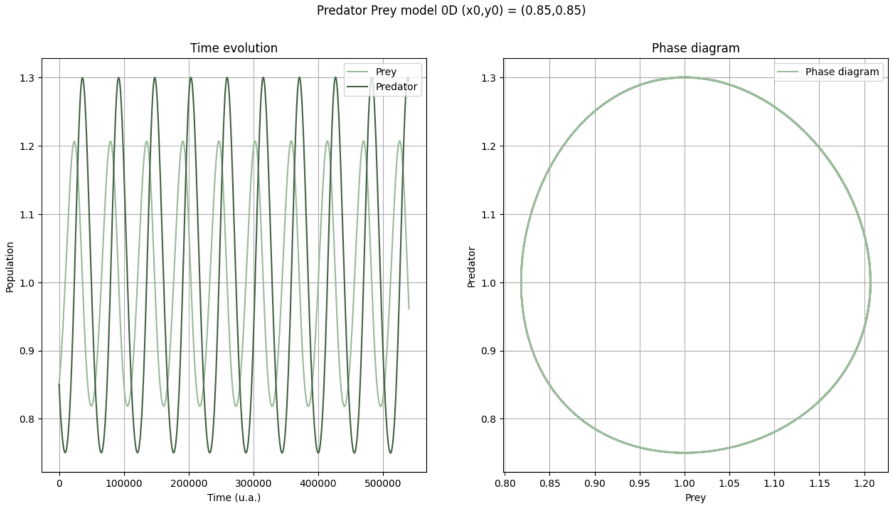

Figure 2: Time evolution of the predators and the preys for the initial point $(x_0, y_0) = (0.85, 0.85)$ and representation of the orbit in the phase diagram.

2.2 The 0D Grey Scott model

The Gray Scott is a autocatalytic model that brings to the formation of spatial patterns mostly used for describing pattern formation in chemical compounds or in cluster of living organisms [5]. The chemical origin resides in the following reactions:

$$\begin{cases} U + 2V \rightarrow 3V \\ U \rightarrow \emptyset \end{cases} \tag{2.7}$$

Which can lead to another coupled differential equation system with the presence of cubic non linear terms:

$$\begin{cases} \frac{du}{dt} = -uv^2 + F(1-u) = f(u,v) \\ \frac{dv}{dt} = uv^2 - (F+K)v = g(u,v) \end{cases} \tag{2.8}$$

The only two parameters of the model are: $F > 0$, feeding constant supplement of u and $K > 0$, killing the product v with $F, K \in \mathbb{R}$. We will associate with u the preys and with v the predator with continuity respect to the first model used.
Repeating the process we calculate the nullclines imposing in 2.8 $(f, g) = (0, 0)$. Three steady points are obtained:

$$(u^*, v^*) = (1, 0) \tag{2.9}$$

$$(u^+, v^-) = \left(\frac{1}{2}\left(1 + \sqrt{1 - \frac{4(F+K)^2}{F}}\right), \frac{F}{2(F+K)}\left(1 - \sqrt{1 - \frac{4(F+K)^2}{F}}\right)\right) \tag{2.10}$$

$$(u^-, v^+) = \left(\frac{1}{2}\left(1 - \sqrt{1 - \frac{4(F+K)^2}{F}}\right), \frac{F}{2(F+K)}\left(1 + \sqrt{1 - \frac{4(F+K)^2}{F}}\right)\right) \tag{2.11}$$

Where the point 2.9 exists $\forall F, K > 0$ and the other two 2.10 and 2.11 exist if and only if are satisfied the following conditions:

$$\begin{cases} 0 < F < \frac{1}{4} \\ 0 < K < \frac{\sqrt{F} - 2F}{2} \end{cases} \tag{2.12}$$

Computing the stability matrix and substituting the steady points to determine their nature:

$$B = \begin{pmatrix} -v^2 - F & -2uv \\ v^2 & 2uv - (F+K) \end{pmatrix} \tag{2.13}$$

$$B_1\Big|_{q^*=(1,0)} = \begin{pmatrix} -F & 0 \\ 0 & -(F+K) \end{pmatrix} \tag{2.14a}$$

$$B_2\Big|_{q^*=(u^+,v^-)} = \begin{pmatrix} -(v^-)^2 - F & -2u^+v^- \\ (v^-)\ ^2 & 2u^+v^- - (F+K) \end{pmatrix} \tag{2.14b}$$

$$B_3\Big|_{q^*=(u^-,v^+)} = \begin{pmatrix} -(v^+)^2 - F & -2u^-v^+ \\ (v^+)\ ^2 & 2u^-v^+ - (F+K) \end{pmatrix} \tag{2.14c}$$

Calculating the trace and the determinant:

$$\mathrm{tr}(B_1) = -(2F - K) < 0 \ \ \forall F, K > 0 \tag{2.15a}$$
$$\det(B_1) = F(F+K) > 0 \ \ \forall F, K > 0 \tag{2.15b}$$

Concluding that the trivial point is always stable in each region.

$$\mathrm{tr}(B_2) = -(v^-)^2 + 2u^+v^- - (2F + K) \tag{2.15c}$$
$$\det(B_2) = -((v^-)^2 + F)(2u^+v^- - (F+K)) + 2u^+(v^-)^3 \tag{2.15d}$$

$$\mathrm{tr}(B_3) = -(v^+)^2 + 2u^-v^+ - (2F + K) \tag{2.15e}$$
$$\det(B_3) = -((v^+)^2 + F)(2u^-v^+ - (F+K)) + 2u^-(v^+)^3 \tag{2.15f}$$

Solving for F,K we obtain the following condition:

$$F > \frac{1}{2}(-\sqrt{k - 4k^{\frac{3}{2}}} - 2k + \sqrt{k}) \tag{2.16}$$

The point (u^+, v^-) is always a saddle point and the point (u^-, v^+) is stable if and only if the inequality 2.16 is satisfied. The intersection between the previous condition and equation 2.12 exist and is called a Bogdanov-Taken point of codimension two. Codimension is the difference between the dimension of the parameter space and the dimension of the corresponding bifurcation boundary. The classification is made using the definitions of Elements of Applied Bifurcation Theory [6] as reference.
The following picture summarize what was said about the parameter space.

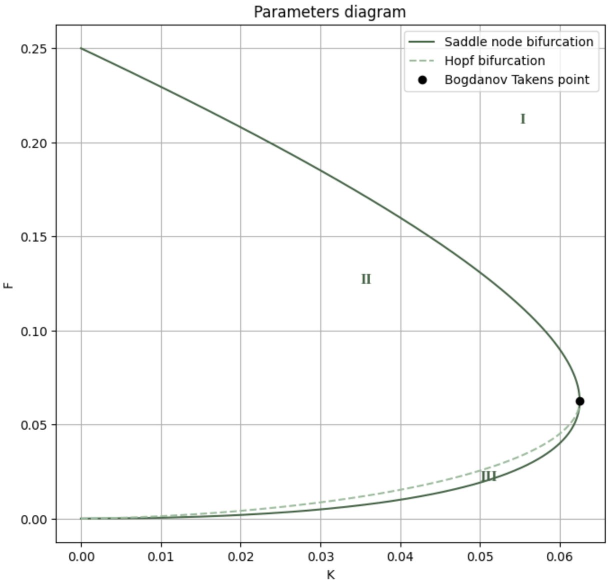

Figure 3: Parameter space of the 0D Gray Scott model. The saddle node and the Hopf bifurcation are visible. It's possible to notice also the Bogdanov-Taken point

Three examples of phase diagrams are shown below with a set of parameters respectively from the I, II and III zone.

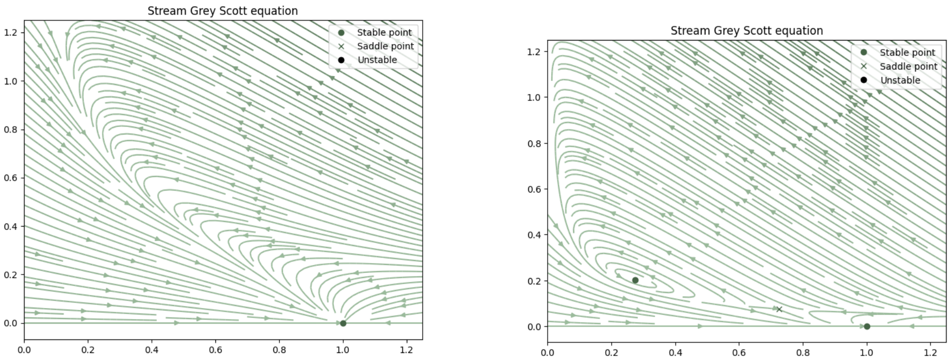

(a) Phase diagram I: F=0.2, K=0.06 (b) Phase diagram II: F=0.0155, K=0.04

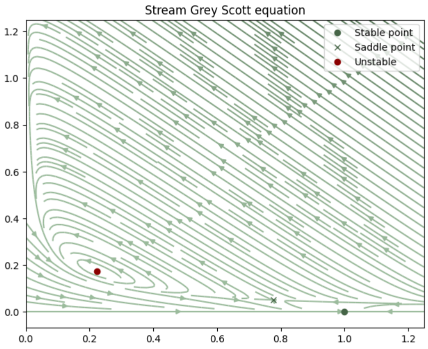

(c) Phase diagram III: F=0.0857, K=0.03

Figure 4: Phase diagrams. The trivial point always exists instead the other two are visible only in the phase diagram II e III. The nature of the third point changes from II (stable) to III (unstable)

The point (u^{-}, v^{+}) in the type II phase diagram is a stable focus as it's possible to see in the trajectory example 5, but thanks to Hopf bifurcation it forms in type III phase diagram a limit cycle as in figures 6a and 6b:

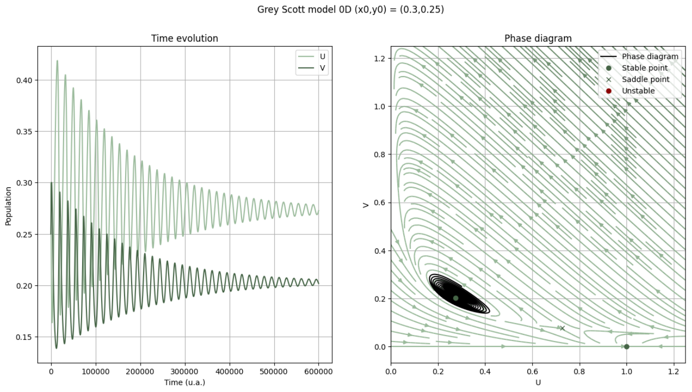

Figure 5: Time evolution in the phase diagram II and example of trajectory: F=0.0857, K=0.03. The stable focus is shown.

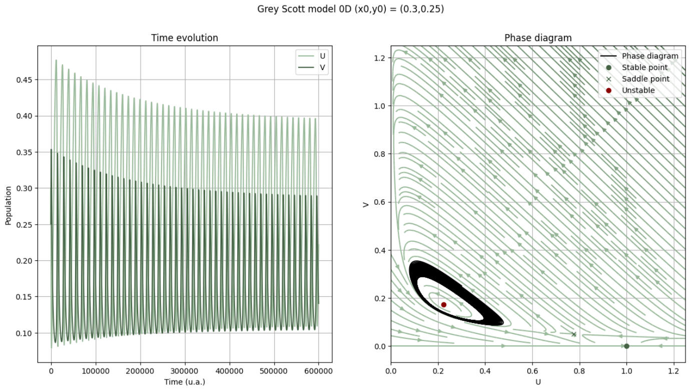

(a) The limit cycle is a topological barrier for the outside.

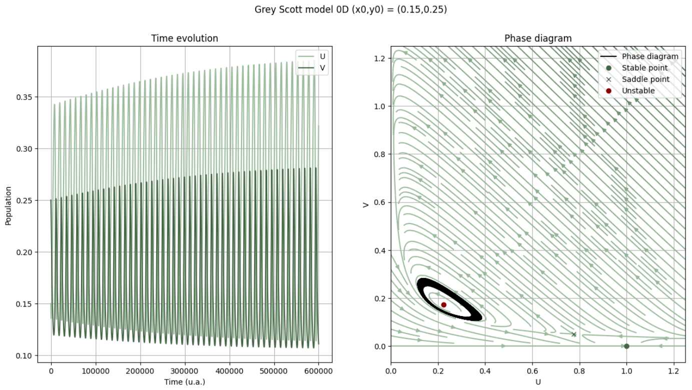

(b) The limit cycle is a topological barrier for the inside.

Figure 6: Time evolution in the phase diagram III and example of trajectory: F=0.0857, K=0.03.

3 Results and discussion

3.1 The 2D Predator-Prey model

We introduce a 2D rectangle of sides (L_x, L_y) with periodic boundary condition on both sides. $P(\bar{x}, t)$ and $N(\bar{x}, t)$ will now be probability density functions with domain the rectangle. Adding diffusion and advection we obtain the following formula:

$$\begin{cases} \frac{dN(\bar{x},t)}{dt} = D_N \nabla^2 N(\bar{x},t) - \bar{g}_{Nx} \cdot \overline{\nabla} N(\bar{x},t) + rN(\bar{x},t) - cN(\bar{x},t)P(\bar{x},t) \\ \frac{dP(\bar{x},t)}{dt} = D_P \nabla^2 P(\bar{x},t) - \bar{g}_{Px} \cdot \overline{\nabla} P(\bar{x},t) - mP(\bar{x},t) + bN(\bar{x},t)P(\bar{x},t) \end{cases} \tag{3.1}$$

Where D_N and D_P are the diffusion constants for Preys and Predators, $\bar{g}_{ix}$ is a constant velocity directed on the x axis. For all the practical purposes we will consider the difference between the two velocities $\bar{g}_x = \Delta\bar{g}$. As initial condition is reasonable to choose a constant value with noise added over the domain:

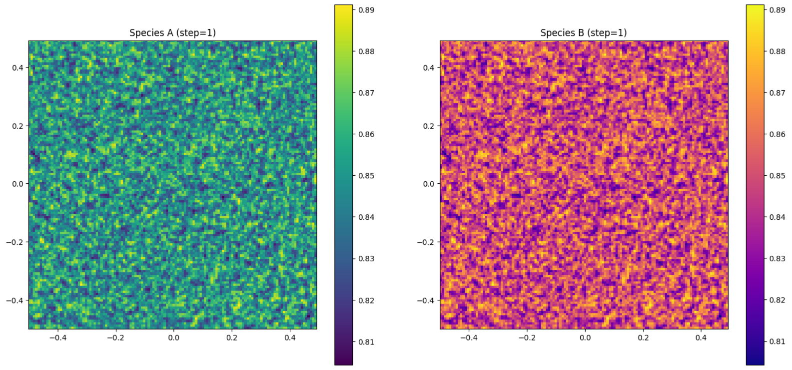

Figure 7: Initial conditions of the predators and the preys distributions for the initial point $(x_0, y_0) = (0.85, 0.85)$ with ±0.04 of uniform noise.

Similarly to the 0D case, we compute the stability matrix as in the chapter 3 of the book "Pattern formation and dynamics in nonequilibrium systems" [2]:

$$A_q = \begin{pmatrix} -D_N q^2 - iqg_x + r - cP & -cN \\ bP & -D_P q^2 - iqg_x - m + bN \end{pmatrix} \tag{3.2}$$

$$A_1 = Re\{A_q\}\Big|_{(x^*,y^*)=(r/c,m/b)} = \begin{pmatrix} -D_N q^2 & -cm/b \\ br/c & -D_P q^2 \end{pmatrix} \tag{3.3}$$

Ignoring for the moment advection and focusing on the real part of the $(r/c, m/b)$ point, it's possible to calculate the trace and the determinant.

$$\mathrm{tr}(A_1) = -(D_N + D_P)q^2 < 0 \quad \forall D_N, D_P, q > 0 \tag{3.4a}$$

$$\det(A_1) = D_N D_P q^4 + mr > 0 \quad \forall D_N, D_P, q, m, r > 0 \tag{3.4b}$$

So the point is stable for every value considered. In fact time evolving the system with a fourth order Runge-Kutta we can obtain the following graphs that directly compare with the 0D case:

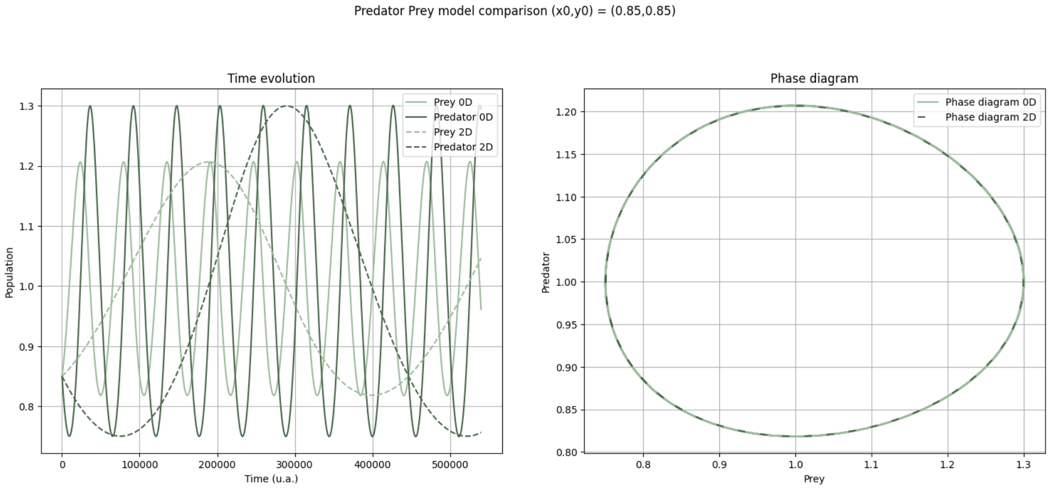

Figure 8: Time evolution of the mean of the predators and the preys for the initial point $(x_0, y_0) = (0.85 \pm 0.04, 0.85 \pm 0.04)$ and representation of the orbit in the phase diagram. Comparison with 0D and the 2D model. It is possible to notice the difference in frequency, but not in amplitude of the two systems

A further investigation is conducted trying to verify a correlation between the diffusion constants and the oscillation frequency. The result is negative.

3.2 The 2D Grey Scott model

Introducing the 2D rectangle with periodic boundary conditions on both sides, we proceed with some analytical result for diffusive case first and advection case then. Upgrading $u(\bar{x}, t)$ and $v(\bar{x}, t)$ to probability density functions, the 2D model is the following :

$$\begin{cases} \frac{\partial u(\bar{x},t)}{\partial t} = D_u \nabla^2 u(\bar{x}, t) - \bar{g}_{ux} \cdot \bar{\nabla} u(\bar{x}, t) - u(\bar{x}, t) v(\bar{x}, t)^2 + F(1 - u(\bar{x}, t)) \\ \frac{\partial v(\bar{x},t)}{\partial t} = D_v \nabla^2 v(\bar{x}, t) - \bar{g}_{vx} \cdot \bar{\nabla} v(\bar{x}, t) + u(\bar{x}, t) v(\bar{x}, t)^2 - (F + K) v(\bar{x}, t) \end{cases} \tag{3.5}$$

Where D_u and D_v are the diffusion constants for Preys and Predators, $\bar{g}_x$ is a constant velocity directed on the x axis. For all the practical purposes we will consider the difference between the two velocities $\bar{g}_x = \Delta \bar{g}$.

We calculate the stability matrix, the trace and the determinant for the trivial point.

$$B_q = \begin{pmatrix} -v^2 - F - D_1 q^2 - iqg_{ux} & -2uv \\ v^2 & 2uv - (F + K) - D_2 q^2 - iqg_{vx} \end{pmatrix} \tag{3.6}$$

$$B_1 = \mathrm{Re}\{B_q\}\Big|_{q^*=(1,0)} = \begin{pmatrix} -F - D_1 q^2 & 0 \\ 0 & -(F + K) - D_2 q^2 \end{pmatrix} \tag{3.7}$$

$$\mathrm{tr}(B_1) = -(2F + K) - (D_u + D_v) q^2 < 0 \quad \forall D_u, D_v, F, K, q > 0 \tag{3.8a}$$

$$\det(B_1) = (F + D_u q^2)(F + K + D_v q^2) > 0 \quad \forall D_u, D_v, F, K, q > 0 \tag{3.8b}$$

It follows that the point (1,0) is always stable for every case included the constant advection one:

$$B_2 = \mathrm{Im}\{B_q\}\Big|_{q^*=(1,0)} = \begin{pmatrix} -qg_{ux} & 0 \\ 0 & -qg_{vx} \end{pmatrix} \tag{3.9}$$

Because the matrix is non zero we expect an oscillatory behavior near the stable point.

The simulation is made with a square grid of $(n_x, ny) = (128, 128)$, alternative $(256, 256)$ for precision purposes, with $L_x = L_y = 64$ and respectively a $\Delta x = \{0.5, 0.25\}$. The biological constants are $D_u = 2D_v = 0.02$ and $g_x \in [0, 0.04]$. The time evolution is made with a fourth order Runge-Kutta in the Fourier space using the FFT. To facility pattern formation the initial conditions are 2 squares distributions in the middle of the grid with $u(\bar{x},0) = 1 - v(\bar{x},0)$.

The zones explored in the parameter space are defined in four blocks for practical purposes. Most of the results were found in blocks 1 and 2. For each block about (10x10) parameter points where uniformly taken to launch the respective simulations.

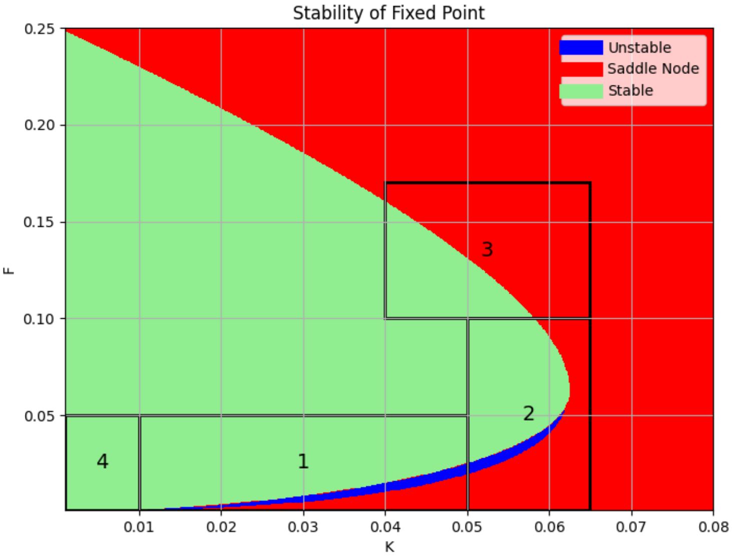

Figure 9: Parameters space with stability enlightened. It's possible to see the division in blocks

A big amount of spatial patterns have been discovered:

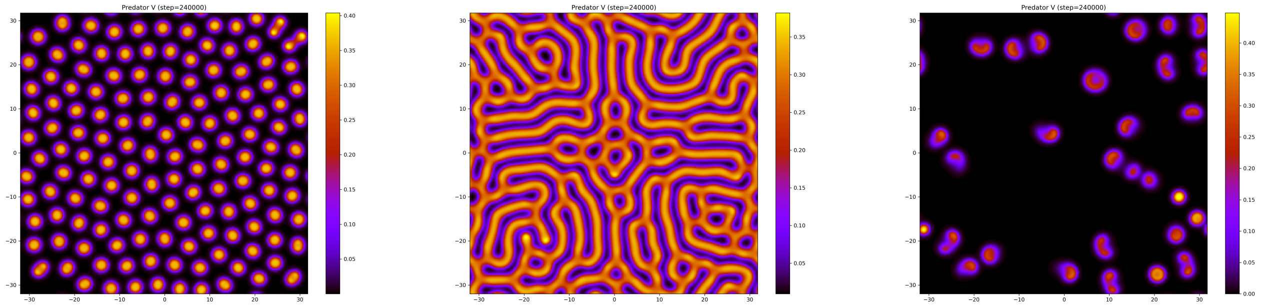

(a) Pattern type λ (self replicating spots). F=0.036, K=0.065

(b) Pattern type κ (maze). F=0.041, K=0.06

(c) Pattern type α (moving spots). F=0.011, K=0.0525

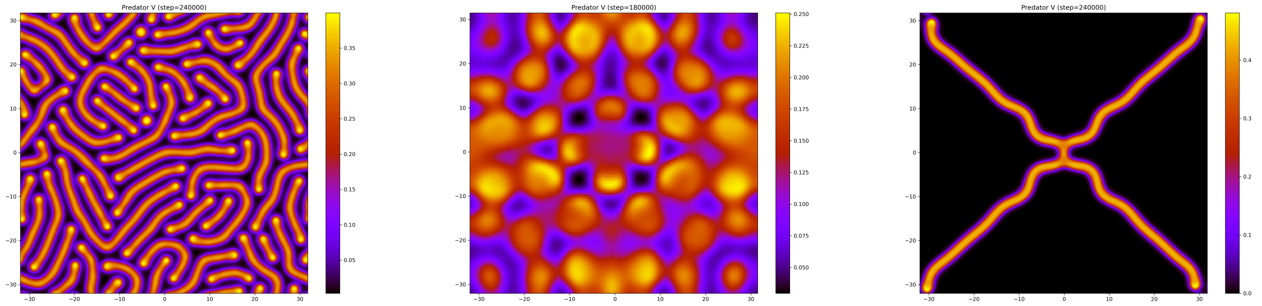

(d) Pattern type μ (worms). F=0.041 K=0.0625

(e) Pattern type β (chaos). F=0.006 K=0.025

(f) Pattern type κ (worms join into maze). F=0.081 K=0.06

Figure 10: Some examples of patterns discovered. Same initial condition applied for different F and K. The classification is made using Pearson's and Munafo's [7] [8] as references

Trajectories in the phase diagram are also diversified:

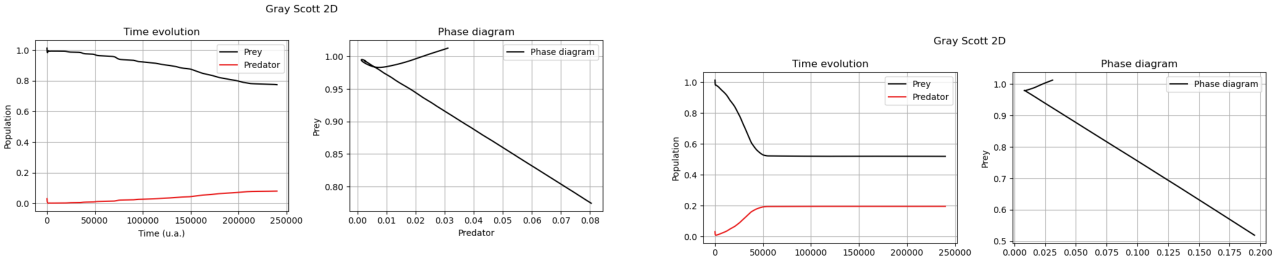

(a) Type λ (self replicating spots). F=0.036, K=0.065. Stable.

(b) Type κ (maze). F=0.041, K=0.06. Stable.

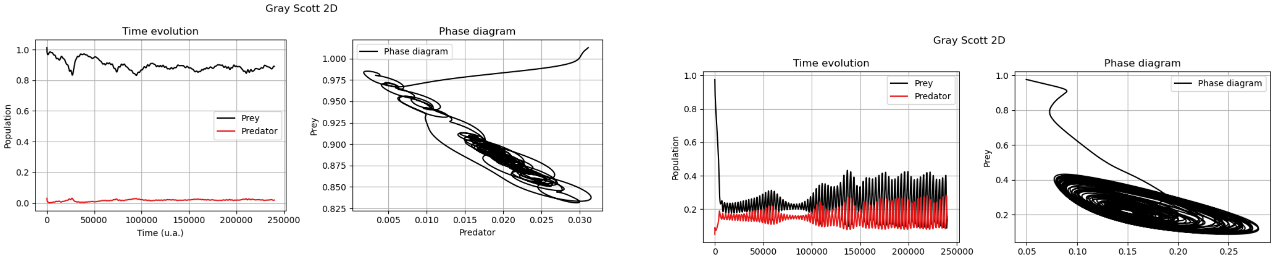

(c) Type α (moving spots). F=0.011, K=0.0525. Chaotic.

(d) Type β (chaos). F=0.006 K=0.025. Chaotic.

Figure 11: Phase diagrams of four pattern types. In some cases the system is led to chaotic instability

Turning on advection and decreasing it at about half the simulation we see a rapid change in the position of the stable point and consequently the collapsing to the trivial point (1,0).

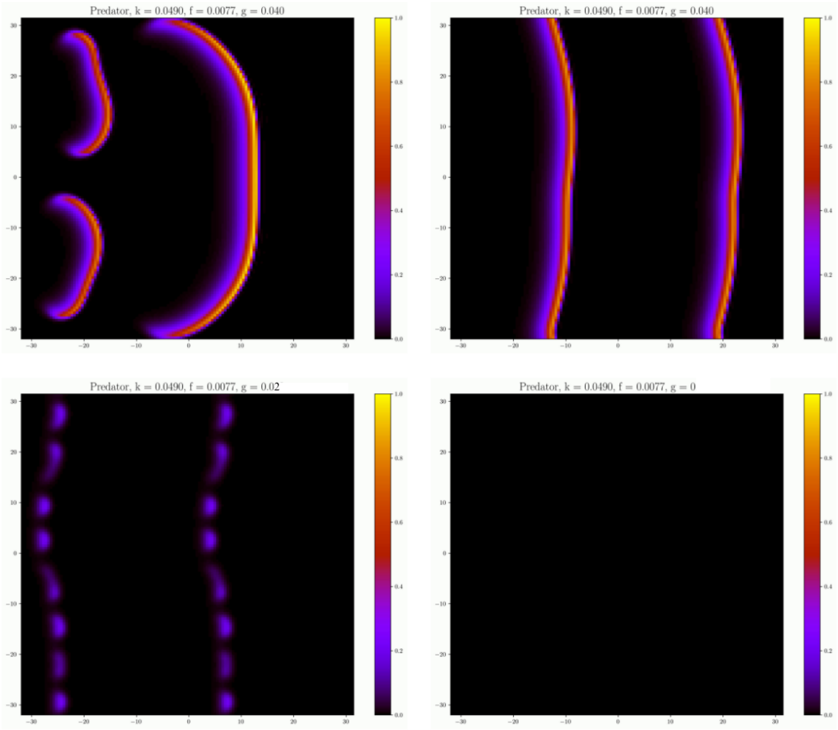

Figure 12: From the initial condition the system forms a pattern called glider (F=0.0077, K=0.049) that is completely stable around 20000 time steps (upper right). At 24000 the advection from $g = 0.04$ is progressively decreased (bottom left) until it reaches the value $g = 0$. At 36000 ts the system has reached the point (1,0) and the predators are all extinct.

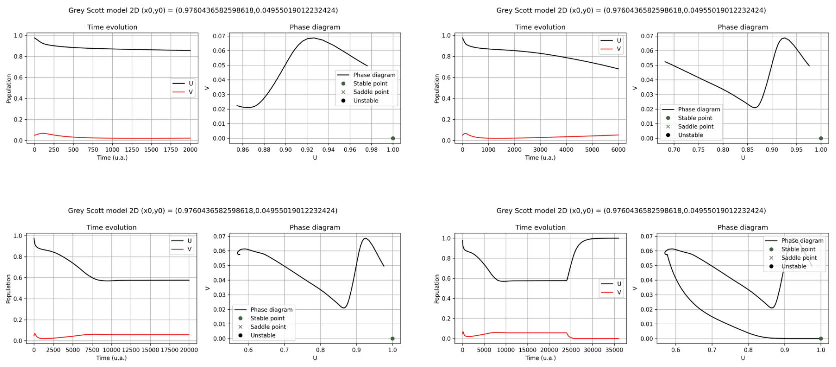

Figure 13: The phase diagram and time evolution of a glider formation and extinction. At 24000 time steps is possible to notice the angular point both in the time evolution and in the phase diagrams due to the discontinuity caused by the parameter g. The predators are led to extinction.

It has been shown that decreasing the difference in velocity between the two species can force to extinction one of them. A preliminary study on the Block 1 shows that thanks to advection the areas in the parameter space where predators survive in the glider pattern are much wider than the case with only diffusion. Even when the pattern doesn't form in the first case, the formation of the gliders is still possible with advection. On the other hand gliders seems to be the only possible pattern that a constant advection forms breaking the ones seen in figure 10.
For what we have just seen there seems to be strong suggestion of g as an instability type III critical parameter as described in [2], but further study are needed.

4 Conclusions

Simple two species models like Predator-Prey are not affected by spatial considerations or constant advection. Otherwise the Grey Scott model, that presents cubic terms, can reproduce a large variety of patterns that mimic chemical and biological phenomena. For example, the λ pattern (10a) exhibits strong analogies with mitotic behavior. In its chaotic regime, recurrent break–reconstruction cycles can be identified, reminiscent of processes typically observed in organic tissues.
It has been shown that a difference in constant advection between species is a critical parameter for the system and enhances widely the stability and consequently the survival of the species. Further studies are needed both in terms of analytical and numerical approaches in order to identify quantitatively the critical parameter g and its capability to modify patterns and stability respect to the diffusion regime. An extended research and classification of all patterns could delimit more precisely the area interested by pattern formation and its relative change varying g. In addition testing the system with more complex fluxes like gyres or parabolic flow and changing the boundary conditions (reflective) could lead to an improved and more realistic model that permits a direct confrontation with simplified but realistic natural cases.

Acknowledgments

Acknowledge support and useful discussions:
This work was supported by the SURF@IFISC fellowship.

References

[1] `https://www.iaea.org/newscenter/news/linking-nutrient-fluxes-eutrophication-and-harmful-algal`

[2] M.Cross H.Greenside, Pattern formation and dynamics in nonequilibrium systems, Cambridge University Press, 2009

[3] Nicole Cristine Laureanti, Priscila da Silva Tavares, Matheus Tavares, Daniela Carneiro Rodrigues, Jorge Luís Gomes, Sin Chan Chou and Francis Wagner Silva Correia, Extreme Seasonal Droughts and Floods in the Madeira River Basin, Brazil: Diagnosis, Causes, and Trends, Climate 2024

[4] Chen Yuan, Jinfeng Wang, Dynamics of a periodic benthic-drift model for two species competition, J. Math. Anal. Appl. 527 (2023)

[5] Demi L. Gandy and Martin R. Nelson, Analysing pattern formation in the gray-scott model: an xppaut tutorial, SIAM Review, 2022

[6] Yuri A. Kuznetsov, Elements of Applied Bifurcation Theory, Second Edition, Springer, 1998

[7] J. Pearson, Complex patterns in a simple system, Science 261 (1993) 189-192.

[8] R. Munafo, Stable localized moving patterns in the 2-D Gray-Scott model (2009)